

Advanced linear models for gyro-backward wave instabilities in gyrotrons

Thèse N° 9503

Présentée le 3 mai 2019

à la Faculté des sciences de base
SPC - Physique du Tokamak TCV
Programme doctoral en physique

pour l'obtention du grade de Docteur ès Sciences

par

Jérémy GENOUD

Acceptée sur proposition du jury

Prof. F. Mila, président du jury
Dr S. Alberti, directeur de thèse
Prof. I. G. Tigelis, rapporteur
Dr S. Jawla, rapporteur
Dr S. Brunner, rapporteur

2019

Abstract

Parasitic oscillations excitation is one of the main point hindering high-power gyrotron operation for fusion application. These instabilities, besides being dangerous for the gyrotron components, could possibly degrade the electron beam quality before it enters the cavity. In order to study the instabilities that may occur in a realistic beam duct upstream of the gyrotron cavity, the self-consistent linear and spectral code TWANGlinspec has been modified. The large inhomogeneities in the smooth-wall beam duct geometry or in the magnetic field profile required the implementation of a numerical approach using a hybrid finite element method. The new model allows to characterize a large number of potentially spurious transverse electric (TE) modes.

Compared to previous studies on gyrotron beam duct instabilities, an extended interaction space including also the gyrotron cavity has been considered. The role of the connecting part called spacer between the beam duct and the cavity is highlighted and it is shown that the gyro backward-wave TE modes excited in this region generally have their minimum starting current. The backward-wave nature of the parasitic oscillations is responsible to their strong electron velocity spread dependency, as shown with the new code TWANGlinspread. Nonlinear models were also used and allowed to evaluate the effect of the parasitic oscillations on the electron beam quality. These parasitic oscillations induce a large electron beam energy spread and subsequently a significant reduction of the gyrotron efficiency. However, the competition between the parasitic and the operating mode could play an important role and a multimode model should be used to fully study the situation in one single simulation.

For the first time, a self-consistent electron beam wave interaction is simulated in the presence of a lossy dielectric layer in the smooth-wall beam duct. In TWANGlinspec, the transverse structure of the TE mode is adapted to the solution of the complex cold dispersion relation of an infinite homogeneous dielectric coated cylindrical waveguide. Before considering the realistic situation, the dispersion relation formulation had to be adapted for dielectric materials with very high losses and the validity of the TE pure mode ($E_z = 0$) assumed in TWANGlinspec had to be assessed for SiC or BeOSiC materials. The effect of the dielectric layer on the parasitic starting current is large for parasitic oscillations localized at the end of the beam duct and in the spacer region.

For a real case, the dual frequency gyrotron for the Tokamak à Configuration Variable (TCV), but with a smooth-wall SiC dielectric layer and with a realistic electron beam including velocity spread, the parasitic oscillations starting current is increased to a level higher than the operating beam current. The excitation of these parasitic oscillations is thus not expected to

occur.

The new code TWANGlinspec, convenient for starting current calculations, has also been applied to high-power gyrotron start-up studies. These gyrotrons often suffer from the excitation of competing modes excited in the cavity during the start-up phase, when the electron beam parameters are varying to reach their nominal values. For a realistic start-up situation for the TCV dual-frequency gyrotron, the simulations with TWANGlinspec are in a remarkable agreement with the experiments, additionally validating the code TWANGlinspec.

keywords: gyrotron, beam duct, parasitic oscillation, backward-wave, lossy dielectric layer

Résumé

Parmi les entraves au développement de gyrotrons de haute puissance destinés aux applications de fusion nucléaire, on peut citer l'excitation d'oscillations parasites dans le conduit à électrons. Ces instabilités sont non seulement dangereuses pour les composants des gyrotrons mais peuvent également dégrader la qualité du faisceau électronique avant son entrée dans la cavité résonante, réduisant ainsi l'efficacité globale du gyrotron. Afin d'étudier ces instabilités le code linéaire et spectral TWANGlinspec simulant l'interaction entre le faisceau électronique et l'onde électromagnétique de manière auto-cohérente, a été développé. Un tel code est utilisé pour la première fois afin de simuler une zone d'interaction étendue comprenant un conduit à électron lisse, la cavité, et la zone intermédiaire les séparant. Cette région étendue contient de larges inhomogénéités dans la géométrie et le champ magnétique, contraignant à une adaptation de l'approche numérique basée sur une formulation d'éléments finis. L'approche spectrale est numériquement efficace pour le calcul du courant d'accrochage des modes pouvant être excités. Des études incluant une importante quantité de modes ont été conduites.

Pour une situation réelle, mais avec un faisceau électronique parfait (mono-énergétique et mono-vitesse), de nombreuses oscillations parasites ont leur courant d'accrochage inférieur au courant d'opération du gyrotron, signifiant qu'elles peuvent être excitées. Ces instabilités sont excitées dans une région étroite, située entre la dernière partie du conduit à électrons et la cavité. Elles sont dues à des interactions dans un régime appelé rétrograde, car elles se propagent dans le sens opposé au faisceau électronique et doivent être traitées de manière auto-cohérente, par un modèle tel que TWANGlinspec. Un nouveau modèle, TWANGlinspread a été développé et a permis d'étudier la forte dépendance des parasites à une déviation en vitesse des électrons du faisceau. L'effet délétère des parasites sur l'excitation du mode d'opération du gyrotron a été mis en évidence par le truchement d'un modèle nonlinéaire. Une approche multimodale capable de traiter la compétition entre les modes transverses serait néanmoins nécessaire pour ce genre de considérations.

L'originalité de cette thèse tient également dans la présentation de simulations auto-cohérente d'interactions dans un conduit à électrons diélectrique. Pour ce faire, la structure transverse du mode transverse électrique (TE) est évaluée en résolvant la relation de dispersion pour le cas d'un cylindre homogène infini avec une couche de diélectrique. Avant de traiter le cas réel, l'hypothèse de mode TE pur a été vérifiée pour les cas d'intérêt. Les simulations avec TWANGlinspec ont montré qu'une couche de SiC permet d'augmenter considérablement le courant d'accrochage des parasites dont l'interaction est localisée dans le conduit à électron

et dans la partie intermédiaire qui précède la cavité.

Dans le cas réel du gyrotron bi-fréquence pour le Tokamak à Configuration Variable (TCV), mais avec un conduit à électron lisse en SiC, l'effet combiné du diélectrique et d'une déviation en vitesse du faisceau électronique permet d'augmenter le courant d'accochage au-delà du courant d'opération. Aucune excitation d'oscillations parasites n'est donc prévue par le code.

mots-clés : gyrotron, conduit à électrons, oscillation parasite, onde rétrograde, couche de diélectrique avec pertes

Contents

Abstract (English/Français)	iii
1 Introduction	1
1.1 The gyrotron-oscillator	1
1.1.1 Principle	3
1.1.2 The beam-wave interaction, phenomenology	4
1.2 Parasitic oscillations	11
1.2.1 Experimental facts	11
1.2.2 Numerical models	12
1.3 Thesis outline	13
2 Models	15
2.1 TWANGlinspec-cavity	15
2.1.1 Derivation	15
2.1.2 Numerical implementation	21
2.1.3 Validations	23
2.1.4 Advantages of a spectral model	27
2.2 TWANGlinspec-beam-duct	31
2.2.1 Model adaptation	31
2.3 TWANGlinspec-dielectric	36
2.3.1 Model adaptation	36
2.3.2 Dielectric dispersion relation	36
2.3.3 Formulation with Hankel functions	39
2.4 Linear model TWANGlinspread	40
2.5 Non-linear model TWANG and TWANG-PIC	41
3 Metallic smooth-wall beam duct	43
3.1 Systematic studies	44
3.1.1 Magnetic field profile	45
3.1.2 Wall radius tapering	47
3.1.3 Magnetic field profile position	50
3.2 Realistic geometry	51
3.3 Nonlinear simulations	58
3.3.1 Effect on the electron beam quality	58

Contents

3.3.2	Velocity spread effect	64
3.3.3	Multimode simulations	65
3.4	Velocity spread effect on the starting current	68
3.5	Distributed losses	73
3.6	Conclusion	76
4	Dielectric coated smooth-wall beam duct	79
4.1	Validation of the dielectric dispersion relation solver	79
4.2	Effect of coating thickness	85
4.3	Validity of the model	86
4.4	Systematic studies	88
4.5	Realistic geometry	95
4.6	Conclusion	99
5	Start-up scenario studies	101
5.1	SPC 118-GHz gyrotron	103
5.2	MIT 110-GHz gyrotron	105
5.3	SPC dual-frequency gyrotron	108
6	Conclusion	113
A	Mode conversion calculation	115
B	Surface impedance needed to suppress the parasitic oscillations	119
C	Dielectric permittivity measurements for BeOSiC and SiC materials	121
C.1	Measurement method	121
C.1.1	Measurement setup	122
C.1.2	Error analysis	122
C.2	Dielectric properties measurements for BeOSiC samples	123
C.2.1	Frequency dependencies	124
C.2.2	Temperature dependencies	128
C.2.3	Characteristic penetration depth and reflection coefficient	130
C.3	Dielectric properties measurements for SiC samples	131
C.3.1	Frequency dependencies	131
C.3.2	Temperature dependencies	133
C.3.3	Characteristic penetration depth and reflection coefficient	134
C.4	Resistivity measurements	135
C.5	Conclusions	137
D	Low-power gyrotron for DNP-NMR spectroscopy, the Temperature-Jump experiment	139
E	Dispersion relation with dielectric layer, formulation with Hankel functions	141
	Bibliography	153

	Contents
Publications and Conferences	155
Acknowledgements	157
Curriculum Vitae	159

1 Introduction

1.1 The gyrotron-oscillator

Gyrotrons are vacuum electronic devices capable of generating high-power coherent electromagnetic waves (EM) at RF power levels in Continuous Wave (CW) in excess of 1MW [1, 2]. Their development was mainly driven by their application for heating magnetically confined plasmas in experimental fusion reactors. In order to reach a relevant fusion reaction rate for a reactor, the electron and ions in the plasma need to be heated to temperatures up to 10keV. The Ohmic heating, generated by the inductive electric current, is not sufficient to reach these temperatures as it becomes less and less effective with the temperature increase. Additional plasma heating are needed. For a future reactor, and in particular for the International Thermonuclear Experimental Reactor (ITER), a combination of Neutral Beam Heating (NBH), Ion Cyclotron Resonance Heating (ICRH), Lower Hybrid (LH) and Electron Cyclotron Resonance Heating (ECRH) is developed [3]. Compared to the other heating systems, the EC-waves propagate seamlessly from free space to the plasma and have the added potential to very locally deposited energy and eventually control instabilities of a fusion plasma as well as heating it.

The plasma heating is performed via ECRH [4]. In order for the EC-wave to effectively couple with the plasma electrons and transfer its energy, its frequency has to match the electron cyclotron frequency, which is given by $f_{\text{cycl}} = 28 \cdot B$ GHz for non-relativistic electrons. As the magnetic field profile varies strongly from the core to the edge of the tokamak, the condition is localized in a narrow frequency band. Moreover, by changing the way the EC-waves are injected inside the tokamak, in particular by injecting it with a toroidal propagation component, a current can be driven. This non-inductive manner to drive a current is called Electron Cyclotron Current Drive (ECCD) [4]. The ECCD location can be controlled and be used to mitigate Neoclassical Tearing Modes [5] (NTM) degrading the plasma performance and confinement. The fact that the wave propagates in vacuum allows for the launcher to be far away from the plasma, avoiding possible heat damages. In magnetically confined fusion plasmas, the gyrotrons are also used as coherent sources for Collective Thomson Scattering

(CTS) diagnostics for confined alpha-particle [6].

Concerning ECRH, the ITER tokamak requires devices delivering 1MW of rf-power at 170GHz to the plasma for one hour. Only gyrotrons are available for this application, as can be seen in Figure 1.1 (source: [7]). Solid state devices are not capable to reach such power level, while other vacuum electronic devices are either producing waves with lower frequency or lower power. Recently, the progress in gyrotrons permitted to reach such power level and frequencies in European [8–10], American [11], Russian [12] or Japanese [13] gyrotrons.

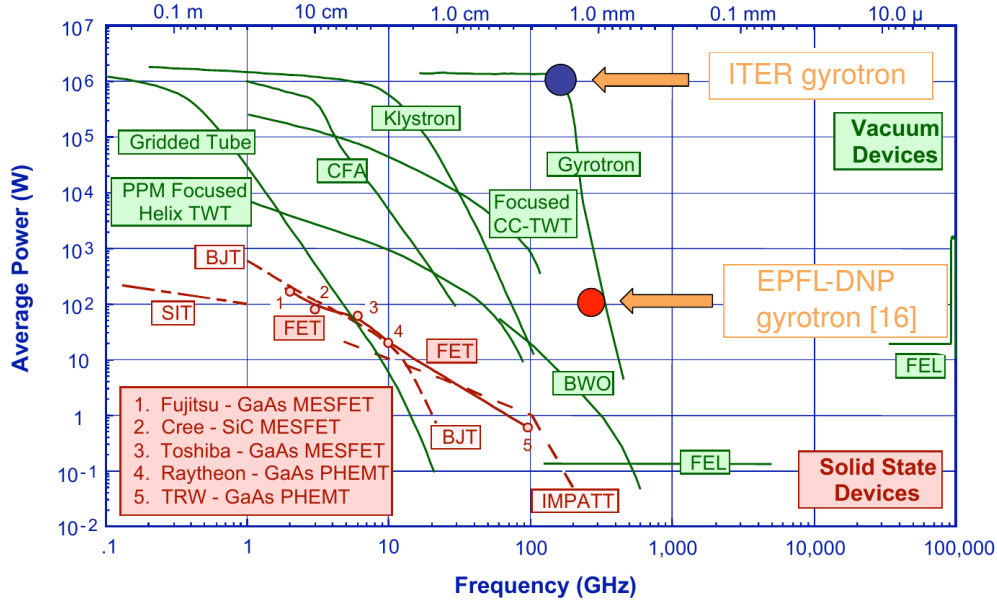


Figure 1.1 – Vacuum and solid state devices sorted in the power versus frequency plane. The ITER specifications as well as the low power DNP gyrotron tube are located with the blue and red circles (Source: [7]).

Beside this main application, gyrotrons are also used for Dynamic Nuclear Polarization enhanced Nuclear Magnetic resonance (DNP-NMR) spectroscopy [14, 15]. A DNP gyrotron has been designed at the Swiss Plasma Center (SPC) for this application [16–18] and outstanding NMR signal improvement were obtained [19, 20]. The simulations done with our models permitted to properly set the gyrotron and as this work was also part of this thesis, a more detailed discussion is given in appendix D. This permits as well to demonstrate the flexibility of the gyrotron. Gyrotrons are also used for remote detection of concealed radioactive materials [21, 22], materials processing [23] and their application to rocket propulsion is the subject of a recent project [24]. A list of high-power gyrotrons can be found in [25, 26].

1.1.1 Principle

The gyrotron oscillator is based on the Electron Cyclotron Maser (ECM) instability, where a weakly relativistic electron beam interacts with an electromagnetic wave supported by a cylindrical structure. A simplified scheme of the gyrotron cross section is shown in Figure 1.2, featuring the main elements. Starting from the bottom, the Magnetron Injection Gun (MIG) is composed by the cathode and the filament, where the hollow electron beam is emitted by thermionic emission. The electrons are accelerated in a crossed electric and magnetic field. They are guided by the magnetic field lines, created by the external magnet, towards the beam duct and the resonant cavity. Along their path, the increasing magnetic field compresses the electron beam, converting part of their longitudinal kinetic energy to their rotational kinetic energy. In the cavity, the wave-particle interaction takes place, transferring a large part of the electron kinetic energy to the rf-wave. The spent electron beam is eventually collected at the top part of the gyrotron, called the collector. The rf-wave exits the cavity in the same direction as the electron beam and is converted to a free-space Gaussian mode by the launcher part. A set of three quasi-optical mirror directs the rf-wave in the direction of the diamond window, where it exits the gyrotron.

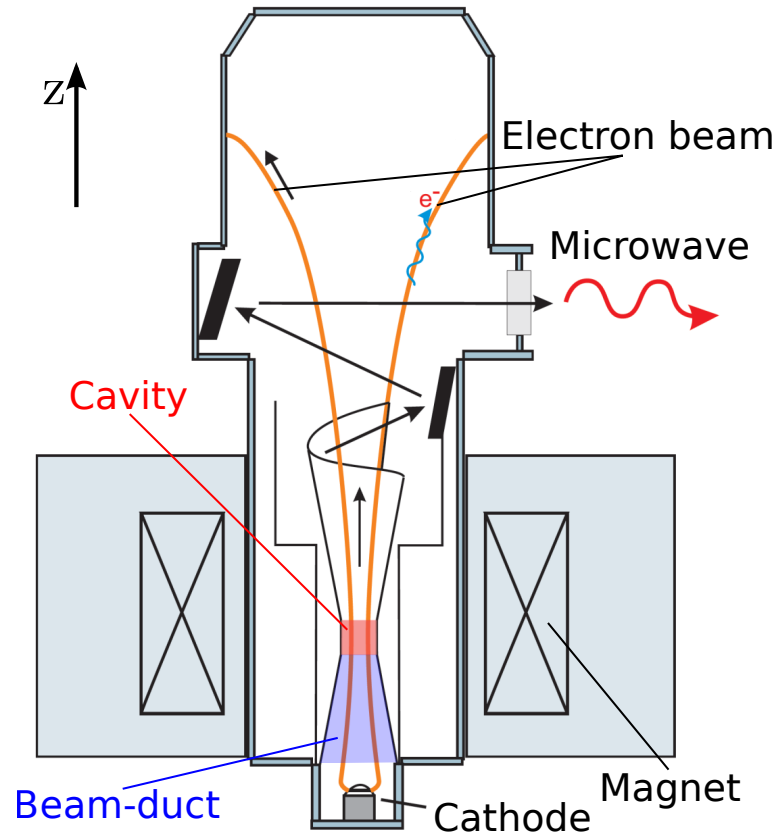


Figure 1.2 – Schematic of gyrotron oscillator. The electron beam trajectory is indicated with orange lines and the rf-beam trajectory is shown with the black arrows. The cavity and beam ducts parts, highlighted in blue and red are the parts of interest in this work.

1.1.2 The beam-wave interaction, phenomenology

In the resonant cavity, the interaction takes place between the weakly relativistic electron beam and the transverse electric $TE_{m,p,q}$ mode supported by the cavity. A TE mode has no longitudinal electric field component ($E_z = 0$). The three indices m , p and q are the azimuthal, radial and longitudinal mode numbers. As an example, the electric field of the Tokamak à Configuration Variable (TCV) dual-frequency gyrotron $TE_{26,7,1}$ operating mode is shown in Figure 1.3 in the transverse cross section (left) and in the axial direction (right). In the right figure, the variation of the phase indicates that the wave is practically a standing wave in the cavity, the constant radius part highlighted with the blue shading, and is a propagating wave in the uptaper following the cavity. The beam radius R_b is shown in black in the two figures, it is chosen such that the electrons experience the maximum electric field in order to maximize the beam-wave coupling.

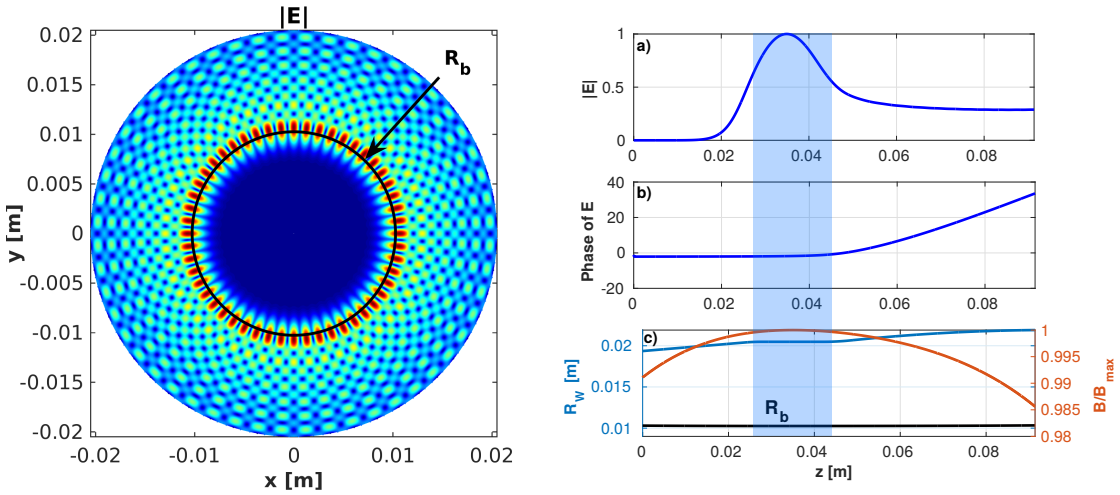


Figure 1.3 – (Left) Amplitude of the electric field profile in the transverse cross-section for the $TE_{26,7}$ mode of the TCV dual-frequency gyrotron. (Right) a) and b) Amplitude and phase of the electric field profile in the axial direction for the same mode. c) Cavity wall radius (in blue), beam radius R_b (in black) and magnetic field profile (in red) for the TCV dual-frequency gyrotron [27].

If the electrons remain in phase with the wave, the Cyclotron Maser Instability (CMI) can take place. Under the action of the electromagnetic (EM) field, the electrons are either accelerated or decelerated, depending on their relative phase with the wave. Because of the relativistic dependence of the cyclotron frequency ($\Omega_c = \frac{qB}{\gamma m}$), the accelerated electrons rotate slower, as their energy increase (γ increases), while the decelerated electrons rotates faster, as their energy decrease. This leads to a bunch in the effective cyclotron phase space [28], called "phase bunching". If the electrons are exactly in phase with the wave, no net energy exchange between the electrons and the wave is observed, as half of the electrons is accelerated and the other half is decelerated.

In order to get a net electron beam-wave energy exchange, the idea is to operate at a cyclotron frequency slightly different than the wave frequency. If the wave frequency is slightly larger than the cyclotron frequency or its harmonics, the bunching takes place in a decelerating phase. Statistically, more electrons are decelerated and transfer their kinetic energy to the wave EM energy. This is how a high-power gyrotron is operated. Inversely, if the wave frequency is slightly lower than the cyclotron frequency or its harmonics, the bunching takes place in the accelerating phase. The EM wave energy is ceded to the electrons. In order for a rf-wave to be excited, another condition need to be fulfilled. It can be shown that the current need to exceed a threshold value, called starting current [29–32]. In the studies presented in this thesis, the starting current is the key element as it permits to assess under which conditions the wanted (operating) or unwanted (parasitic) modes are excited.

To apprehend the complex interaction, the simple uncoupled dispersion relations for the electron beam and the EM wave are convenient. The different cases treated during the thesis are discussed in the next sections, using the uncoupled dispersion relations.

Infinite homogeneous cylinder with perfectly-conducting metallic wall

In the most simplified model, consisting of an infinite homogeneous perfectly-conducting metallic cylinder (cf. Figure 1.4), the beam-wave interaction takes place at the intersection between the electron beam and the wave dispersion relations (cf. Figure 1.5).

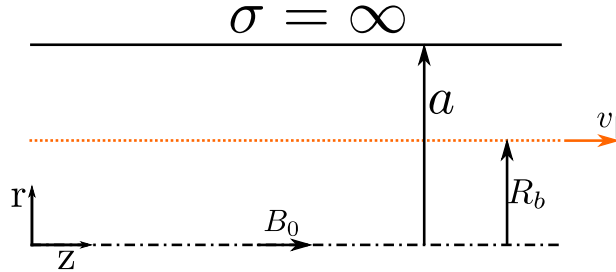


Figure 1.4 – Schematic of the infinite homogeneous cylinder with perfectly-conducting metallic wall. a is the wall radius, R_b the beam radius, $v_{||}$ is the electron parallel velocity and B_0 is the external magnetic field.

The Doppler-shifted electron beam dispersion relation is given by

$$\omega_{\text{beam}} = \frac{\Omega_c}{\gamma} + v_{||} k_z, \quad (1.1)$$

where Ω_c is the electron cyclotron angular frequency, γ is the relativistic factor and $v_{||}$ and k_z are the parallel electron velocity and wave-vector respectively. The $\text{TE}_{m,p}$ mode dispersion relation is given by

$$\omega_{\text{wave}} = c \sqrt{k_{\perp}^2 + k_z^2}, \quad (1.2)$$

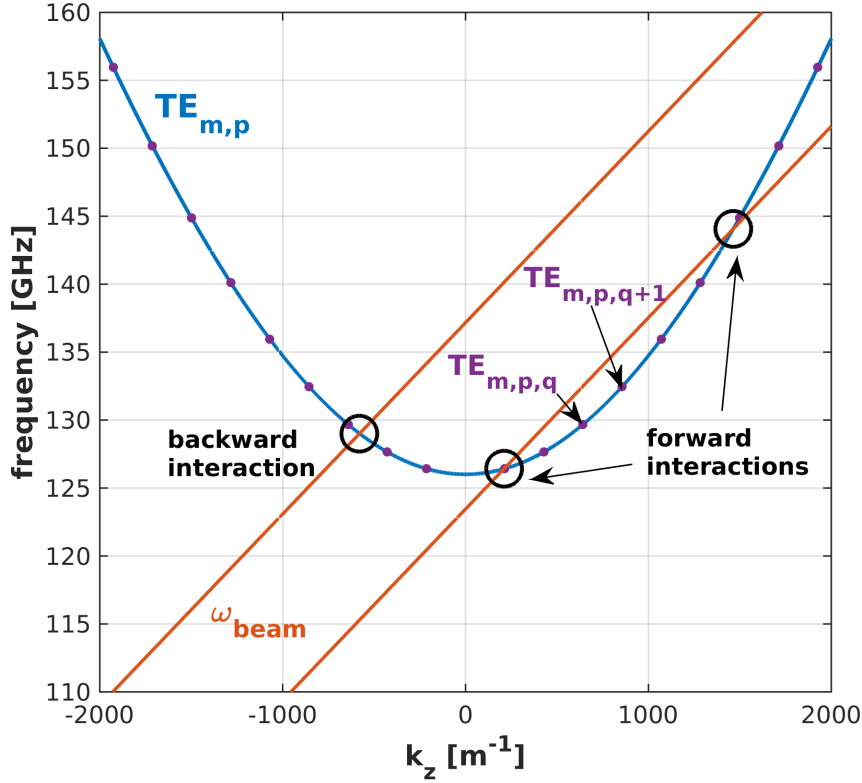


Figure 1.5 – Simplified uncoupled dispersion relation in the $\omega - k_z$ space. The blue line is the cavity dispersion relation, while the red lines are two beam dispersion relations for two different cyclotron frequencies. The purple points indicate the solutions for a finite interaction length. The parameters correspond to the TCV dual-frequency gyrotron.

where c is the speed of light and k_\perp and k_z are the perpendicular and parallel wave-vectors respectively. For a metallic boundary condition, the perpendicular wave-vector is given by the ratio between $v_{m,p}$, the p^{th} root of the derivative of the Bessel function J_m and the wall radius a . In Figure 1.5, the wave dispersion relations corresponding to the $\text{TE}_{26,7}$ mode is shown in blue for parameters of the TCV dual-frequency gyrotron. The two red lines are the beam dispersion relations for two different magnetic fields, thus for two different cyclotron frequencies. The beam line on the right intersects the wave dispersion relation for two positive k_z , indicating two possible interactions in the forward regime. The second beam line (on the left), intersects the wave in the negative k_z plane. The wave phase velocity is negative and the interaction is called a backward wave interaction. Also this line has a second intersection (not shown in the figure), which is in the forward regime

The physics of forward and backward wave interactions is intrinsically different and both have their own properties. These properties are listed in Table 1.1. While the forward wave interaction leads to a convective instability, where the amplification of the wave is achieved while propagating with the beam, the backward wave interaction leads to an absolute in-

stability, where the feedback mechanism between the forward propagating beam and the backward propagating wave is governing the interaction. This feedback mechanism involves much stronger self-consistent effects, allowing a large frequency tunability. This property is exploited by gyro-backward-wave oscillator (gyro-BWO), operating in the backward-wave regime, further away from cutoff than gyrotrons. The forward wave interaction is stronger and leads to higher efficiency. The high-power gyrotron are operated in this regime, close to the cutoff, while gyro-Travelling Wave Tube (gyro-TWT) are also operated in the forward regime, but further away to the cutoff, for example the second intersection indicated for a large positive k_z . An important advantage of operating close to the cutoff is the low dependency to a velocity spread in the electron beam. The Doppler shift contribution in the beam dispersion relation ($v_{\parallel} k_z$) is minor close to the cutoff and the interaction is almost insensitive to a velocity spread. This is not the case for the gyro-BWO, strongly sensitive to a velocity spread, as will be shown in Sections 3.3.2 and 3.4.

Table 1.1 – Forward and backward interaction properties.

Interaction type	Forward ($k_z > 0$)	Backward ($k_z < 0$)
instability	convective	absolute
self-consistent effects	weak	strong
frequency tunability	small	large
interaction	strong	weak
efficiency	high	low

Not shown in Figure 1.5, the interaction with a transverse magnetic (TM) mode is also possible [33]. They are neglected as the beam coupling between the electron beam and the wave is much weaker than for a TE mode [34]. Nevertheless, recent studies showed that the axial bunching mechanism, caused by the E_z component of the TM mode, could cooperate with the azimuthal bunching from the TE mode for backward wave interactions [35].

The boundary conditions for a cylinder of finite length L leads to a discretization of the dispersion relation solutions. The solutions of the discretized dispersion relation

$$\omega_{\text{wave}} = c \sqrt{k_{\perp}^2 + \left(\frac{q\pi}{L}\right)^2}, \quad (1.3)$$

are called the longitudinal modes and are indexed with q . The discrete solutions, considering for L the TCV dual-frequency gyrotron cavity length, are shown in Figure 1.5 with the purple points. The intersection in the forward regime crosses one specific longitudinal mode. In this case, it corresponds to the $\text{TE}_{26,7,1}$ operating mode which has the largest quality factor.

During this thesis, the parasitic modes simulated are essentially due to gyro-backward wave interactions. Due to this fact, a self-consistent treatment is indispensable and a study on the electron beam velocity spread is done. Many studies of parasitic oscillations in gyrotrons, regardless whether of backward-wave or forward-wave interaction, are based on a non self-consistent model.

Infinite homogeneous system with a dielectric layer

In order to avoid parasitic oscillations, dielectric loading of the waveguide walls is often considered by placing a layer of lossy material on the conducting surface with a complex dielectric permittivity [36–41]. This same technique is also used in particle accelerators for suppressing high order modes [42]. The complexity of the problem increases when a dielectric boundary condition is considered. For the infinite homogeneous cylinder shown in Figure 1.6, two solutions of the wave dispersion relation are shown in Figure 1.7. The solution with a metallic boundary condition at $r = a$ (as in Figure 1.5) is reported in black. The red curves are the solutions with a dielectric layer between $r = a$ and $r = b$ without losses ($\epsilon_r = \epsilon'_r + i\epsilon''_r$, with $\epsilon''_r = 0$).

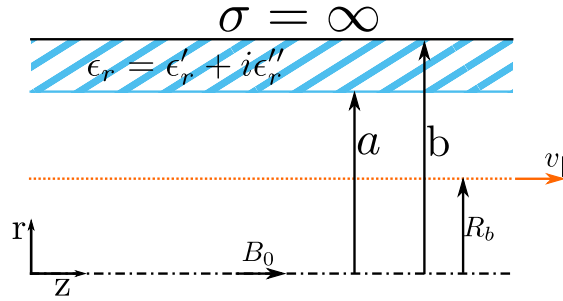


Figure 1.6 – Schematic of the infinite homogeneous cylinder with a dielectric layer between $r = a$ and $r = b$.

For azimuthally symmetric transverse modes ($TE_{0,p}$ or $TM_{0,p}$) the modes are pure TE or TM modes. Except for these cases, whenever a dielectric layer is introduced, the modes become hybrid HE or EH modes [43]. Close to the cutoff the HE or EH modes have negligible E_z or H_z components and are thus called TE-like or TM-like modes respectively. On the contrary, further away from the cutoff the TE or TM mode purity decreases and the longitudinal electric or magnetic field components, respectively, become significant.

With the addition of the dielectric region, additional modes appear. This is seen in Figure 1.7 where two solutions exist, while only one exists in the metallic boundary condition case. Depending on the dielectric permittivity, its frequency and its longitudinal wave-number, the electric field could penetrate in the dielectric layer. In this situation, it is the case for example for larger k_z . The mode, penetrating in the dielectric layer, is referred to as a surface mode.

Whenever a lossy dielectric material is considered ($\epsilon_r = \epsilon'_r + i\epsilon''_r$, with $\epsilon''_r < 0$), the solution of the dispersion relation with dielectric become complex [43]. In this work, a careful study of the model hypothesis is performed when the lossy dielectric layer is added. The self-consistent studies including a lossy dielectric layer is novel in the thesis and necessitate an adaptation of the model to account for the complex dispersion relation solutions.

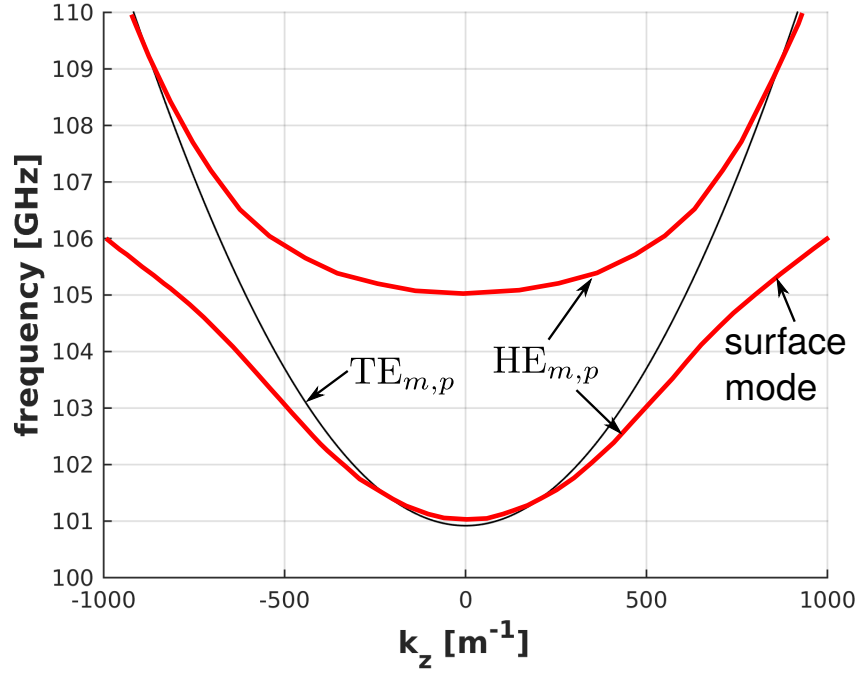


Figure 1.7 – Simplified uncoupled dispersion relation in the $\omega - k_z$ space. The black line is the dispersion relation solution for a metallic case for one given $TE_{m,p}$ mode ($m = 10, p = 7$). The red lines are the corresponding hybrid $HE_{m,p}$ solutions of the dispersion relation with a (non lossy) dielectric layer ($\epsilon_r = \epsilon'_r \neq 1$) (cf. Figure 1.6).

Finite inhomogeneous system with a dielectric layer

The novelty in this work is the self-consistent treatment of the interaction in the extended region including the beam duct and the cavity (and the part between the two regions called the spacer). Commonly, the studies focus on the cavity region, where much less inhomogeneities in the geometry or in the magnetic field exist. This can be seen in Figure 1.8, including the extended interaction region considered in this work. Except the envelope smooth-wall approximation of the beam duct, this case corresponds to the a real extended interaction space of a high-power gyrotron, as it is for instance the case for the TCV dual-frequency gyrotron [27]. The self-consistent treatment including the dielectric layer in the smooth-wall beam duct is also performed for the first time in this thesis.

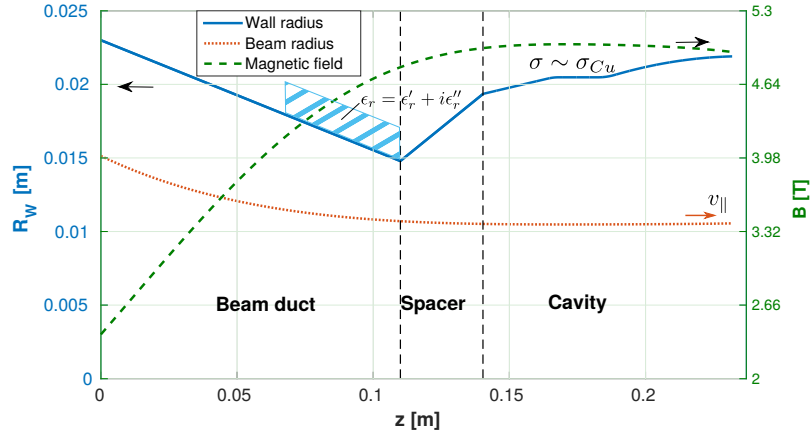


Figure 1.8 – Geometry of the smooth-wall beam duct approximation, spacer and cavity of the TCV dual-frequency gyrotron (in continuous blue). A lossy dielectric layer is considered in the last part of the beam duct. For the rest, a high but finite conductivity, on the order of the copper conductivity, is considered. Magnetic field profile and electron beam radius are plotted in dashed green and dotted red line respectively.

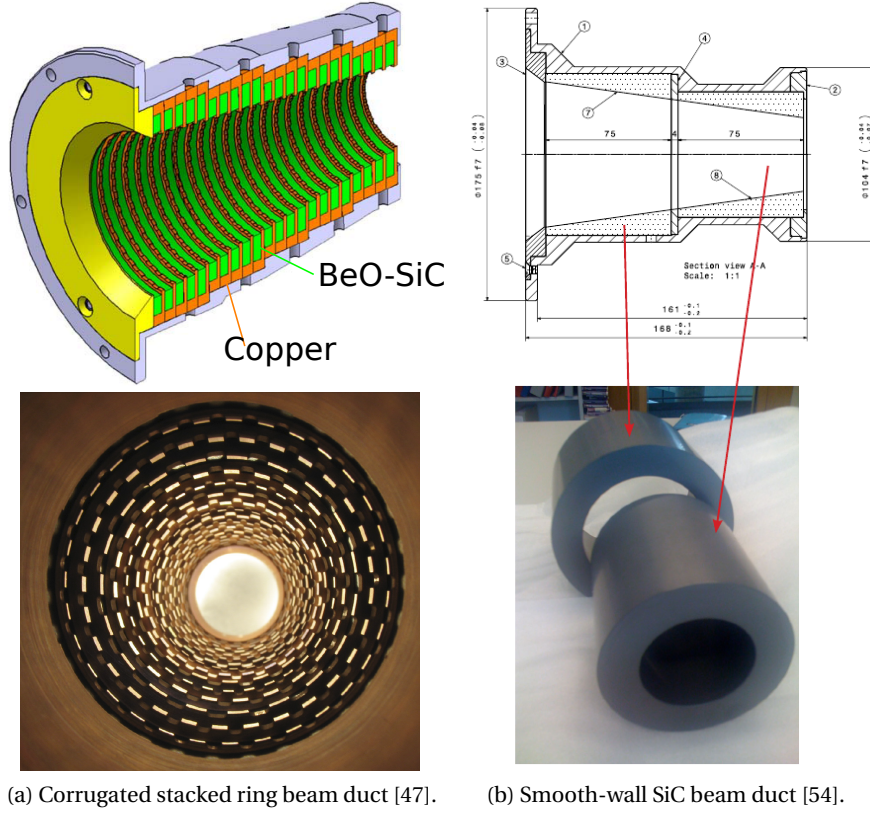
1.2 Parasitic oscillations

Parasitic oscillations have been observed in high-power gyrotrons and their generation is commonly attributed to a beam-wave interaction in the gyrotron beam-duct situated before to the cavity. The instability responsible for the excitation of the beam-duct parasitic oscillations is generally a gyro-backward wave. If excited, it introduces significant electron beam velocity and energy spreads inducing a significant degradation of the gyrotron interaction efficiency. For high-power gyrotron above the 1 MW power level, a significant increase of the beam current above the present typical level of 40A is foreseen and could significantly worsen the situation by increasing the risk of parasitic excitation. These reasons motivated this thesis.

1.2.1 Experimental facts

A notable effort has been devoted to the theoretical and experimental study of these parasitic oscillations. Based on these studies [44–53], essentially three different strategies for suppressing spurious instabilities in gyrotron beam ducts have been studied and implemented. The first one is to use a smooth-wall dielectric loaded beam duct, made from Silicon Carbide (SiC) [45]. Such beam ducts are already used in Japan Atomic Energy Agency (JAEA) high-power gyrotrons and have been proven to be a good option for the ITER high-power gyrotrons [54]. A schematic of the smooth-wall beam ducts and the two conical SiC parts are shown in Figure 1.9b. The second strategy, used in Russian high-power gyrotrons at the Institute of Applied Physics (IAP), is the use of a metallic beam duct with a random surface [44, 55]. The third one is the stacked ring beam duct, composed by rings of copper and dielectric material, like BeOSiC. This option is used in the European or American high-power gyrotrons [8, 27, 56]. In [47], indented copper rings are introduced in order to reduce the parasitic oscillations of beam ducts with smooth-wall copper rings (cf. Figure 1.9a). Despite these efforts, gyrotrons with stacked rings beam-tunnel have often experienced parasitic oscillations. This type of structure has also the drawbacks to be challenging and costly to manufacture and, so far, no exploitable self-consistent model exist for studying the parasitic oscillations.

The question of absorbing material in a cylindrical beam pipe is also relevant in high-energy accelerator physics [57, 58]. The relativistic charged particles travelling through the pipe form bunches of particles. The particles in the front of the bunch generate wake-fields, which in turn exert forces on the particles in the tail of the bunch, leading to the so called head-tail instability. The wake-field depends strongly on the geometry and wall material. One possibility to reduce the head-tail instabilities is the use of absorbing materials to damp the wake-fields [42].



(a) Corrugated stacked ring beam duct [47]. (b) Smooth-wall SiC beam duct [54].

Figure 1.9

1.2.2 Numerical models

Theoretically, various models exist to describe the beam-wave interaction inside a gyrotron oscillator. A distinction can be made between the models treating the beam-wave interaction self-consistently or not. Among the non self-consistent models, some are assuming a fixed field profile of the mm-wave electric field [44]. They compute the electric field profile in an empty structure and evaluate afterwards its effect on the beam [59]. Other non self-consistent models are using the empty-cavity (i.e. without electron beam) longitudinal eigenmode for the interaction simulation [60, 61]. Such models are suitable for simulating the main cavity interaction in gyrotrons, when the excitation takes place in the forward regime and the interaction is mainly governed by the electromagnetic properties of the empty cavity geometry. However, the necessity of using a self-consistent model has been discussed in several publications [30, 62–65], especially for backward wave interactions where self-consistent effects are essential.

The full description of the interaction requires nonlinear models [28, 66] and several codes have been developed worldwide [67–71]. Some of the models are monomode, treating a single

transverse $TE_{m,p}$ mode, it is the case for TWANG [72], while others take into account mode competition between the transverse modes and are called multimode [68, 70]. However, to describe the linear phase and in particular to calculate the starting current, linear models are adequate [30–32, 73–78].

When dielectric loadings are used, in many papers, their effect is based on non self-consistent models [79]. For stacked-rings beam ducts, the extremely complicated electromagnetic system does not allow a self-consistent model so far [59, 80]. Another approach to approximate the dielectric loading is to define an equivalent model in which the effect of the dielectric is described by a complex surface impedance [76, 81, 82]. However, this type of model fails to be used in generic dielectric loading with arbitrary thickness and dielectric permittivity properties. The less restrictive approach is a self-consistent approach considering the correct boundary condition in the presence of the dielectric coating, as discussed in [43] and extensively used throughout the thesis.

1.3 Thesis outline

The thesis backbone is made of four chapters. In chapter 2, the three numerical models used along the thesis are presented. The development, adaptation, validation and application of the first model, TWANGlinspec constitute the main effort in the thesis. The code development is separated in three parts. The first part is the development of the basis TWANGlinspec code. The second part is dedicated to the adaptation of TWANGlinspec to treat the electron beam-wave interaction in the beam-duct region. The third part involves the modification to include the effect of the dielectric layer with arbitrary thickness and complex dielectric permittivity. A complementary code, used to calculate the transverse field structure of the wave in the presence of the dielectric layer is also presented. In the last part of the chapter, the other two models are introduced. First, the new linear model TWANGlinspread, developed to study the velocity spread effect, and second the non-linear model TWANG [72].

In chapter 3, the application of these three models on non-homogeneous smooth-wall beam duct cases with a metallic boundary condition are presented. First, the simulations with the code TWANGlinspec are presented, starting with systematic studies to assess the effect of inhomogeneities and continuing with the most realistic situation shown in Figure 1.8 but with a metallic boundary condition. When the extended interaction space is treated, even with a linear model, a very large amount of modes has to be considered in order to determine the mode which has the minimum starting current. The non-linear simulations with the monomode code TWANG, to study the parasitic radiated power and their effect on the main gyrotron efficiency are discussed, together with a study on the electron beam velocity spread effect. Additionally, non-linear multimode simulations with EURIDICE [68] are shown, assessing the mode-competition effect between parasitic oscillations. In the following section, the results from TWANGlinspread, demonstrates the important velocity spread effect on the self-excitation conditions of parasitic oscillations. Eventually, the effect of distributed Ohmic

losses in the wall is concluding the chapter.

The third chapter is dedicated to the studies of smooth-wall beam duct parasitics modes in the presence of a dielectric layer. First, the validations of the complementary code, solving the transverse structure of the electric field profile with the dielectric layer, are detailed. Secondly, a singular effect of the dielectric coating thickness is discussed. Before the presentation of the results from TWANGlinspec, a discussion about the validity of our approach is carried out. The most realistic situation, for the situation shown in 1.4, is treated at the end of the chapter.

The model TWANGlinspec, developed in the thesis, became appropriate for the starting current calculations, especially for situations where a scan over some parameters or over a list of modes has to be performed. This is the case for instance for gyrotron start-up studies, focusing on the interaction in the gyrotron cavity, where the starting current has to be calculated for a list of modes and for a set of time-varying parameters. The code was applied for start-up simulation studies for high-power gyrotron. Three of these studies are presented in chapter 5, first for the 500kW/118GHz gyrotron for TCV [83], then for the MIT 1.5MW/110GHz gyrotron [84] and finally for the TCV 1MW dual-frequency gyrotron 84/126GHz [27]. This last simulation, being in excellent agreement with the experiment, provides another validation of the model.

In the appendices, first an additional study to evaluate the mode conversion level for a typical case studied in this thesis is presented. The second appendix is a study performed during the development of TWANGlinspec, where the surface impedance needed to suppress the parasitic oscillation in the beam duct is evaluated and compared to the results published in [76]. The report on dielectric permittivity measurements of BeOSiC and SiC materials is given in appendix C. These results are used in chapter 4, where the dielectric layer effect is studied. In appendix E the derivation of the dispersion relation with a dielectric layer, but using a different formulation essential for dielectric with very high losses, is presented. The last appendix is a presentation of the "Temperature-Jump" DNP-NMR experiment performed with the SPC DNP gyrotron at EPFL.

2 Models

The self-consistent linear and spectral model TWANGlinspec has been developed first to study cyclotron maser instabilities occurring in the cavity of a gyrotron oscillator. The model derivation, its numerical implementation and its validation are presented in 2.1. In order to study parasitic oscillations in smooth-wall beam duct, the model has to be adapted. This is described in detail in 2.2. The last development of TWANGlinspec includes the possibility to treat self-consistently the instability in the beam duct region including a layer made from a lossy dielectric material. This is presented in 2.3. Complementary to the model TWANGlinspec, two other models are used for the parasitic studies, TWANGlinspread, a time-dependent linear code including velocity spread, and TWANG, a self-consistent non-linear model. They are introduced in 2.4 and 2.5.

2.1 TWANGlinspec-cavity

2.1.1 Derivation

TWANG

The model TWANGlinspec is a self-consistent linear and spectral model derived from the self-consistent model TWANG [72]. The fundamental equations describing the electrons and the wave evolution are the relativistic equation of motion for the electrons with a Lorentz force,

$$\frac{d\vec{p}_i}{dt} = -e \left(\vec{E} + \frac{\vec{v}_i}{c} \wedge (\vec{B}_0 + \vec{B}) \right) \quad (2.1)$$

and the wave equation derived from Maxwell's equations neglecting the space-charge effect and including the source term:

$$\frac{1}{c^2} \frac{\partial^2 \vec{E}}{\partial t^2} - \vec{\nabla}^2 \vec{E} = -\mu_0 \frac{\partial \vec{J}}{\partial t}. \quad (2.2)$$

Chapter 2. Models

In the momentum equation, $\vec{p}_i = m_e \gamma \vec{v}_i$ is the relativistic electron momentum, with m_e , γ and \vec{v}_i being the electron rest mass, Lorentz factor and velocity, respectively. e is the electron charge and c the speed of light. E and B are the rf-field and \vec{B}_0 is the external magnetic field. In the wave equation, μ_0 is the vacuum permeability and \vec{J} is the current density defined as

$$\vec{J} = \sum_{i=1}^{N_p} -e \vec{v}_i \delta(\vec{x} - \vec{x}_i). \quad (2.3)$$

These fundamental equations are adapted to the cylindrical geometry (cf. Figure 1.3b) and timescale separations are assumed in order to reduce the problem. First, a reference frequency ω_0 is chosen close to the actual oscillation frequency ω_{rf} in order to separate the electric field expression between a fast oscillation $e^{-i\omega_0 t}$ and a slow-varying field amplitude $F(z, t)$:

$$\vec{E}(z, t) = \text{Re} \left(F(z, t) \hat{e}_{m,p}(r, \phi) e^{-i\omega_0 t} \right). \quad (2.4)$$

$\hat{e}_{m,p}(r, \phi)$ is the fixed normalized transverse field profile of a transverse electric $\text{TE}_{m,p}$ mode (cf. Figure 1.3a). No mode coupling between transverse modes is assumed and only one transverse $\text{TE}_{m,p}$ mode is treated. The second timescale separation assumed in TWANG is the assumption that the electric field profile F is varying on a timescale much longer than the electron transit time through the cavity. These different time scales are shown in Figure 2.1 in the case of a DNP gyrotron [85]. The derivation leading to the model used in TWANG is described in [66].

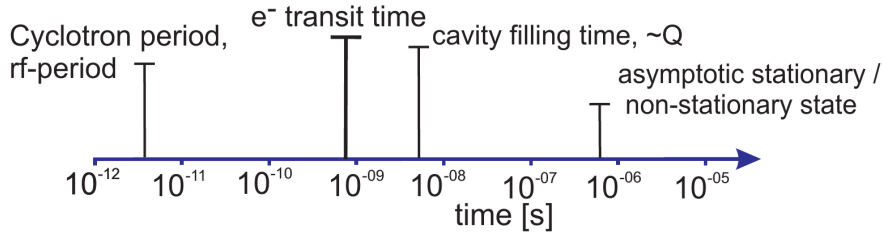


Figure 2.1 – Relevant time-scales in gyrotron. The different time scales were evaluated for a gyrotron used for DNP-NMR spectroscopy [85].

The reduced equations of motion for the perpendicular and parallel electron momentum are given below.

$$\frac{d\mathcal{P}}{d\hat{z}} = \left(-i \frac{\gamma - s \frac{\Omega_c}{\omega_0}}{p_z} + \frac{s}{2} \frac{d(\ln B_0)}{d\hat{z}} \right) \mathcal{P} + s(-\gamma F^* + i p_z F'^*) C_0 \frac{p_{\perp}^{2s-2}}{p_z}, \quad (2.5a)$$

$$\frac{dp_z}{d\hat{z}} = -\frac{C_0}{p_z} \text{Im}(F' \mathcal{P}) - \frac{1}{2} \frac{p_{\perp}^2}{p_z} \frac{d(\ln B_0)}{d\hat{z}}. \quad (2.5b)$$

The wave equation for the wave electric field envelope $F(\hat{z}, \tau)$ is

$$\left(2i\frac{\partial}{\partial\tau} + \frac{\partial^2}{\partial\hat{z}^2} + \kappa_{\parallel}^2\right)F = i\mathcal{J}\langle C_0\frac{\mathcal{P}^*}{p_z}\rangle. \quad (2.5c)$$

The boundary conditions at the beginning (\hat{z}_{in}) and end (\hat{z}_{out}) of the interaction space are:

$$\left.\frac{\partial F}{\partial\hat{z}}\right|_{\hat{z}_{\text{in/out}}} = \mp i\frac{k_{\parallel}}{k_0}F(\hat{z}_{\text{in/out}}, t). \quad (2.6)$$

In these equations, the two variables are the normalized axial position $\hat{z} = \frac{\omega_0}{c}z = k_0z$ and the normalized time $\tau = \omega_0 t$. $\mathcal{P} = p_{\perp}^s \exp(-i\Psi)$ is the complex perpendicular momentum, p_{\perp} and p_z the perpendicular and parallel electron momentum, respectively, and Ψ the slow-timescale electron phase. $F = \frac{e}{m_e c^2} \frac{s^s}{2^s s!} \frac{E}{k_{\perp}}$ is the normalized rf-field envelope. Ω_c the non-relativistic cyclotron angular frequency and s cyclotron resonance harmonic number. $B_0 = B_0(z)$ is the external imposed magnetic field amplitude. k_0 , k_{\parallel} and k_{\perp} are the wave number and its parallel and perpendicular components. The three quantities C_0 , κ_{\parallel} and \mathcal{J} are given by:

$$C_0 \equiv \left(\frac{k_{\perp}}{k_0}\right)^s \left(\frac{s\Omega_c}{\omega_0}\right)^{1-s} J_{m-s}(k_{\perp}R_g), \quad (2.7)$$

$$\kappa_{\parallel}^2 \equiv 1 - \frac{k_{\perp}^2}{k_0^2} \left[1 - (1+i) \left(1 + \frac{m^2}{v_{mp}^2 - m^2} \right) \frac{\delta_{sk}}{R_w} \right], \quad (2.8)$$

and

$$\mathcal{J} \equiv \frac{eZ_0}{m_e c^2} \frac{I_b}{C_{mp}} \left(\frac{s^s}{2^s s!} \right)^2, \quad (2.9)$$

with the geometrical coupling factor C_{mp} given by

$$C_{mp} \equiv \frac{\pi}{2} (v_{mp}^2 - m^2) J_m^2(v_{mp}). \quad (2.10)$$

In these expressions, R_g is the guiding center radius, R_w the wall radius, Z_0 the vacuum impedance, I_b the electron beam current, m and p the azimuthal and radial mode numbers for a transverse mode $\text{TE}_{m,p}$. v_{mp} is the p^{th} root of the derivative of the Bessel function J_m . In this model, the Ohmic dissipation due to a metallic boundary condition is taken into account via a surface impedance boundary term correcting the parallel wave number κ_{\parallel} , depending on the skin depth $\delta_{sk} = \sqrt{\frac{2}{\omega_0 \mu_0 \sigma}}$, with μ_0 the vacuum permeability and σ the wall conductivity. In the wave equation, the average of the source term is defined as: $\langle V \rangle = \frac{1}{N} \sum_{j=1}^N V_j$ for N electrons at a given \hat{z} and τ , where V stands for any electron beam dynamical quantity. In equation 2.5a, the first term on the right hand side is a term proportional to the difference between the wave and relativistic cyclotron frequency, called detuning. The second term accounts for the compression effect due to the longitudinal variation of the magnetic field. The terms

proportional to F and F' are the effects of the electric and magnetic fields, respectively.

Linearization

From this set of equations, various linear models have been developed. They have been named TWANGlin [30, 85], TWANGlinspec [31, 32] and TWANGlinspread [86]. The linearization has been done considering the amplitude of the electric field F as a first order perturbation on the electron motion. More details on the linearization can be found in [85]. In the following equations, the equilibrium quantities are indexed with a zero and the perturbed quantities with a one. The zero-order equations are:

$$\frac{d}{d\hat{z}} \mathcal{P}_0 = \left(-i \frac{\gamma_0 - s \frac{\Omega_c}{\omega_0}}{\hat{p}_{z0}} + \frac{s}{2} \frac{d(\ln B_0)}{d\hat{z}} \right) \mathcal{P}_0 \quad (2.11)$$

$$\frac{d\hat{p}_{z0}}{d\hat{z}} = -\frac{1}{2} \frac{p_{\perp 0}^2}{\hat{p}_{z0}} \frac{d(\ln B_0)}{d\hat{z}} \quad (2.12)$$

The conservation of the magnetic moment and kinetic energy can be derived from these equations. The linearized first-order equations are:

$$\begin{aligned} \frac{d}{d\hat{z}} \mathcal{P}_1 &= \left(-i \frac{\gamma_0 - s \frac{\Omega_c}{\omega_0}}{\hat{p}_{z0}} + \frac{s}{2} \frac{d(\ln B_0)}{d\hat{z}} \right) \mathcal{P}_1 \\ &\quad + i \frac{(\gamma_0 - s \frac{\Omega_c}{\omega_0}) \frac{\hat{p}_{z1}}{\hat{p}_{z0}} - \gamma_1}{\hat{p}_{z0}} \mathcal{P}_0 \\ &\quad + s \left(-\gamma_0 F^* + i \hat{p}_{z0} F'^* \right) C_0 \frac{\hat{p}_{\perp 0}^{2s-2}}{\hat{p}_{z0}} \end{aligned} \quad (2.13a)$$

$$\begin{aligned} \frac{d}{d\hat{z}} \hat{p}_{z1} &= -\frac{C_0}{\hat{p}_{z0}} \text{Im}(F' \mathcal{P}_0) \\ &\quad + \left(\frac{\frac{1}{2} p_{\perp 0}^2 \frac{\hat{p}_{z1}}{\hat{p}_{z0}} - p_{\perp 0} p_{\perp 1}}{\hat{p}_{z0}} \right) \frac{d(\ln B_0)}{d\hat{z}} \end{aligned} \quad (2.13b)$$

$$\left(2i \frac{\partial}{\partial \tau} + \frac{\partial^2}{\partial \hat{z}^2} + \kappa_{\parallel 0}^2 \right) F = i \mathcal{J} \left\langle C_0 \left(\frac{\mathcal{P}_1^*}{\hat{p}_{z0}} - \frac{\mathcal{P}_0^* \hat{p}_{z1}}{\hat{p}_{z0}^2} \right) \right\rangle. \quad (2.13c)$$

Moment approach

In a second step, the model has been simplified, considering no spread in the electron energy or velocity and neglecting the rf-magnetic field (proportional to dF/dz), implying that the perturbed electron momentum $p_{z1} = 0$. Thanks to these simplifications, the system of $2N + 1$ equations (2.13) for the N electrons and the field F can be reduced to three partial differential equations (PDEs) by using a moment approach. This is done by defining two moments of the electron distribution function $\pi_1(\hat{z}, \tau) = \langle \mathcal{P}_1^* \rangle$, $\pi_2(\hat{z}, \tau) = \langle \mathcal{P}_1 e^{2i\Psi_0} \rangle$, and the electric field envelope $F(\hat{z}, \tau)$. Considering an electron distribution function $\mathcal{F}(\mathcal{P}_1, \Psi_0, \hat{z}, \tau)$ depending explicitly on the three dynamic variables $\mathcal{P}_1, \Psi_0, \hat{z}$ and on the evolution variable τ , the assumption usually done of a constant electric field during the electron transit-time can be relaxed. The average of the spatial derivative of a function $\mathcal{G}(\mathcal{P}_1, \Psi_0)$ can be expressed as

$$\left\langle \frac{d\mathcal{G}}{d\tau} \right\rangle = \frac{\partial}{\partial \tau} \langle \mathcal{G} \rangle + \frac{\partial}{\partial \hat{z}} \langle \mathcal{G} v_z \rangle. \quad (2.14)$$

This expression can be derived starting from the phase-space continuity equation:

$$\frac{\partial \mathcal{F}}{\partial t} + \frac{\partial}{\partial \mathcal{P}_1} \left(\mathcal{F} \frac{d\mathcal{P}_1}{dt} \right) + \frac{\partial}{\partial \Psi_0} \left(\mathcal{F} \frac{d\Psi_0}{dt} \right) + \frac{\partial}{\partial z} (\mathcal{F} v_z) = 0. \quad (2.15)$$

For a function $\mathcal{G}(\mathcal{P}_1, \Psi_0)$, the average of the time derivative is :

$$\begin{aligned} \left\langle \frac{d\mathcal{G}}{dt} \right\rangle &= \iint d\mathcal{P}_1 d\Psi_0 \frac{d\mathcal{G}}{dt} \mathcal{F} \\ &= \iint d\mathcal{P}_1 d\Psi_0 \left[\frac{\partial \mathcal{G}}{\partial \mathcal{P}_1} \frac{d\mathcal{P}_1}{dt} \mathcal{F} + \frac{\partial \mathcal{G}}{\partial \Psi_0} \frac{d\Psi_0}{dt} \mathcal{F} \right] \\ &= - \iint d\mathcal{P}_1 d\Psi_0 \mathcal{G} \left[\frac{\partial}{\partial \mathcal{P}_1} \left(\mathcal{F} \frac{d\mathcal{P}_1}{dt} \right) + \frac{\partial}{\partial \Psi_0} \left(\mathcal{F} \frac{d\Psi_0}{dt} \right) \right] \\ &= \iint d\mathcal{P}_1 d\Psi_0 \mathcal{G} \frac{\partial}{\partial t} \mathcal{F} + \iint d\mathcal{P}_1 d\Psi_0 \mathcal{G} \frac{\partial}{\partial z} (\mathcal{F} v_z) \\ &= \frac{\partial}{\partial t} \iint d\mathcal{P}_1 d\Psi_0 \mathcal{G} \mathcal{F} + \frac{\partial}{\partial z} \iint d\mathcal{P}_1 d\Psi_0 \mathcal{G} \mathcal{F} v_z \\ &= \frac{\partial}{\partial t} \langle \mathcal{G} \rangle + \frac{\partial}{\partial z} \langle \mathcal{G} v_z \rangle. \end{aligned} \quad (2.16)$$

For the first three steps respectively, the chain rule, an integration by parts and the continuity equation (2.15) have been used. With this relation, the system of $2N + 1$ equations is reduced to a closed system of 3 partial differential equations for the two complex moments $\pi_1(\hat{z}, \tau)$, $\pi_2(\hat{z}, \tau)$ and the electric field envelope $F(\hat{z}, \tau)$:

$$\frac{\partial \pi_1}{\partial \tau} + \frac{\partial}{\partial \hat{z}} (\pi_1 \beta_z) = A_1 \pi_1 + i C_1 \pi_2 - C_2 C_0 F \quad (2.17a)$$

$$\frac{\partial \pi_2}{\partial \tau} + \frac{\partial}{\partial \hat{z}} (\pi_2 \beta_z) = A_2 \pi_2 - i C_1 \pi_1 \quad (2.17b)$$

$$\left(2i \frac{\partial}{\partial \tau} + \frac{\partial^2}{\partial \hat{z}^2} + \kappa_{\parallel 0}^2 \right) F = i C_3 C_0 \pi_1. \quad (2.17c)$$

In these equations, new notations have been introduced for clarity:

$$A_1 = i\Delta_0 + iC_1 + \beta_z\delta, \quad (2.18)$$

$$A_2 = i\Delta_0 - iC_1 + \beta_z\delta, \quad (2.19)$$

$$C_1 = \frac{p_{\perp 0}^2}{2s\gamma_0^2}, \quad (2.20)$$

$$C_2 = sp_{\perp 0}^{2s-2}, \quad (2.21)$$

$$C_3 = \frac{eZ_0}{m_e c^2 p_{z0}} \frac{I_b}{C_{mp}} \left(\frac{s^s}{2^s s!} \right)^2, \quad (2.22)$$

$$\beta_z = \frac{p_{z0}}{\gamma_0}, \quad (2.23)$$

$$\Delta_0 = 1 - \frac{s\Omega_c}{\gamma_0\omega_0}, \quad (2.24)$$

$$\delta = \frac{s}{2} \frac{d}{d\hat{z}} \ln(B_0). \quad (2.25)$$

Finally, by Fourier transforming equations (2.17) in time, the partial differential equations (PDEs) can be rewritten as ordinary differential equations (ODEs). The Fourier transformation is done assuming $F \sim e^{-i\Omega\tau}$ and $\pi_{1,2} \sim e^{-i\Omega\tau}$, with $\Omega = (\omega_{\text{rf}} - \omega_0)/\omega_0$ being the normalized difference between the rf-frequency ω_{rf} and the reference frequency ω_0 . The system of equations in its spectral form is given by:

$$i\Omega\pi_1 = \frac{d}{d\hat{z}} (\pi_1\beta_z) - A_1\pi_1 - iC_1\pi_2 + C_2C_0F \quad (2.26a)$$

$$i\Omega\pi_2 = \frac{d}{d\hat{z}} (\pi_2\beta_z) - A_2\pi_2 + iC_1\pi_1 \quad (2.26b)$$

$$-2\Omega F = \frac{d^2 F}{d\hat{z}^2} + \kappa_{\parallel 0}^2 F - iC_3C_0\pi_1. \quad (2.26c)$$

The boundary conditions for the two moments π_1 and π_2 and the electric field at the entry of the cavity correspond to homogeneous Dirichlet boundary conditions:

$$\pi_1(\hat{z}_{\text{in}}, \tau) = 0, \quad (2.27a)$$

$$\pi_2(\hat{z}_{\text{in}}, \tau) = 0, \quad (2.27b)$$

$$F(\hat{z}_{\text{in}}, \tau) = 0. \quad (2.27c)$$

The boundary condition for the field at the cavity entry is set to 0 as the gyrotron cavity modes are in cutoff at the entry of the cavity. The boundary condition for the electric field at the output of the cavity is a radiation boundary conditions:

$$\left. \frac{dF}{d\hat{z}} \right|_{\hat{z}_{\text{out}}} = i \frac{k_{\parallel}}{k_0} F(\hat{z}_{\text{out}}, \tau). \quad (2.27d)$$

An important point to be noted is that in equation 2.27d, k_{\parallel} depends on Ω since

$$k_{\parallel}^2 = \frac{\omega_{\text{rf}}^2}{c^2} - k_{\perp}^2 = \frac{\omega_0^2(1 + \Omega^2)^2}{c^2} - k_{\perp}^2. \quad (2.28)$$

2.1.2 Numerical implementation

Different discretizations schemes of equations (2.26) have been studied and the discretized model can be expressed as a general eigenvalue problem:

$$A\mathbf{X} = \Omega B\mathbf{X}. \quad (2.29)$$

This is not a standard eigenvalue problem, since the matrix A depends on the eigenvalue Ω , via the boundary conditions (2.27d) as k_{\parallel} depends on the eigenvalue Ω . The real and imaginary parts of the eigenvalue Ω are respectively the frequency and the growth rate of the wave with $\text{Im}(\Omega) > 0$ for an unstable mode. The eigenvectors \mathbf{X} are composed by the three complex fields $\pi_1(z)$, $\pi_2(z)$ and $F(z)$.

The first discretization in space scheme considered is a finite difference scheme for the first and second-order derivatives. It is expressed here for an equidistant discretization for more clarity ($\Delta\hat{z} = \hat{z}_i - \hat{z}_{i-1}$, $\forall i \in [2, N_z]$):

$$\left. \frac{d\pi}{d\hat{z}} \right|_{i-\frac{1}{2}} \simeq \frac{\pi_i - \pi_{i-1}}{\Delta\hat{z}} + \mathcal{O}(\Delta\hat{z}^2) \quad \forall i = 1, \dots, N_z. \quad (2.30)$$

Here, i and $i - 1$ are indices denoting points on the discretization grid and $i - \frac{1}{2}$ denotes a point centered between the two former points. N_z is the number of points. The second-order spatial derivative is:

$$\left. \frac{d^2 F}{d\hat{z}^2} \right|_i \simeq \frac{F_{i+1} - 2F_i + F_{i-1}}{(\Delta\hat{z})^2} + \mathcal{O}(\Delta\hat{z}^2) \quad \forall i = 1, \dots, N_z. \quad (2.31)$$

For an index $i \in]1, N_z[$, the two first equations of (2.26) become:

$$\pi_{1_{i-1}} \left(-\frac{\beta_z}{\Delta\hat{z}} + \frac{\beta'_z}{2} - \frac{A_1}{2} \right) + \pi_{1_i} \left(\frac{\beta_z}{\Delta\hat{z}} + \frac{\beta'_z}{2} - \frac{A_1}{2} \right) + \pi_{2_{i-1}} \left(-\frac{iC_1}{2} \right) + \pi_{2_i} \left(-\frac{iC_1}{2} \right) \quad (2.32)$$

$$+ F_{i-1} \left(\frac{C_2 C_0}{2} \right) + F_i \left(\frac{C_2 C_0}{2} \right) = \pi_{1_{i-1}} \left(\frac{i\Omega}{2} \right) + \pi_{1_i} \left(\frac{i\Omega}{2} \right), \quad (2.33)$$

and

$$\pi_{2_{i-1}} \left(-\frac{\beta_z}{\Delta\hat{z}} + \frac{\beta'_z}{2} - \frac{A_2}{2} \right) + \pi_{2_i} \left(\frac{\beta_z}{\Delta\hat{z}} + \frac{\beta'_z}{2} - \frac{A_2}{2} \right) + \pi_{1_{i-1}} \left(\frac{iC_1}{2} \right) \quad (2.34)$$

$$+ \pi_{1_i} \left(\frac{iC_1}{2} \right) = \pi_{2_{i-1}} \left(\frac{i\Omega}{2} \right) + \pi_{2_i} \left(\frac{i\Omega}{2} \right), \quad (2.35)$$

Chapter 2. Models

where all the indices, related to position along z , for the elements β_z , $\beta'_z = \frac{\partial \beta_z}{\partial \hat{z}}$, A_1 , A_2 , C_0 , C_1 and C_2 have been omitted. Those elements are evaluated at $\hat{z}_{i-\frac{1}{2}}$. The third equation (2.26c), becomes:

$$F_{i-1} - F_i \left(2 - \Delta \hat{z}^2 \kappa_{\parallel 0}^2 \right) + F_{i+1} - \pi_{1_i} \left(i \Delta \hat{z}^2 C_3 C_0 \right) = -2 \Delta \hat{z}^2 \Omega F_i \quad \forall i = 1, \dots, N_z. \quad (2.36)$$

Here, the elements $\kappa_{\parallel 0}$, C_0 and C_3 are evaluated at \hat{z}_i . The value of F_{N_z+1} is needed in the wave equation (2.36). It is expressed as function of F_{N_z} and F_{N_z-1} , using the radiation boundary condition (2.27d):

$$F_{N_z+1} = 2i \Delta \hat{z} \frac{k_{\parallel}(\Omega)}{k_0} F_{N_z} + F_{N_z-1}. \quad (2.37)$$

As k_{\parallel} depends on the eigenvalue Ω , the matrix A in (2.29) depends on Ω . The boundary conditions at the entry (2.27a), (2.27b) and (2.27c) impose:

$$\pi_{1_1} = 0, \quad \pi_{2_1} = 0, \quad F_{1_1} = 0. \quad (2.38)$$

With this discretization, the eigenvalue problem (2.29) takes the form

$$\begin{pmatrix} A_{11} & A_{12} & A_{13} \\ A_{21} & A_{22} & 0 \\ A_{31} & 0 & A_{33}(\Omega) \end{pmatrix} \begin{pmatrix} \Pi_1 \\ \Pi_2 \\ \mathbf{F} \end{pmatrix} = \Omega \begin{pmatrix} B_{11} & 0 & 0 \\ 0 & B_{22} & 0 \\ 0 & 0 & B_{33} \end{pmatrix} \begin{pmatrix} \Pi_1 \\ \Pi_2 \\ \mathbf{F} \end{pmatrix}, \quad (2.39)$$

where $\Pi_1 = (\pi_{1_1}, \pi_{1_2}, \dots, \pi_{1_{N_z}})$, $\Pi_2 = (\pi_{2_1}, \pi_{2_2}, \dots, \pi_{2_{N_z}})$ and $\mathbf{F} = (F_1, F_2, \dots, F_{N_z})$ are the three complex fields on a discretized vector form. The matrices A_{ij} contain at most three non-zero terms by row. Hence, sparse matrices are used to optimize numeric performance.

Two methods have been tested to solve the eigenvalue problem. The first method, which will be retained, solves the problem using the iterative method "eigs" available from the ARPACK library [87]. Since the very last term of the matrix A depends on the eigenvalue Ω , the eigenvalue problem is solved iteratively, starting for the first iteration with $\Omega = 0$, i.e. from the arbitrary reference frequency ω_0 . The second method to solve the eigenvalue problem consists in searching the roots of $\det(A(\Omega) - \Omega B)$ using the Muller's method [88]. As this method uses quadratic interpolation, three initial guesses are needed. One iteration of the first method gives for example those three guesses. In Figure 2.2 are reported the time needed by the two methods to perform 10 iterations, solving only the wave equation and for an equidistant discretization in the longitudinal direction z . The first method is faster for large number of points N_z ($N_z > 600$), and thus for larger matrices. Moreover, by adding the time needed to compute the eigenvector in the second method, the first method is faster for $N_z > 400$. For this reason, the first method, calculating the eigenvalues with the methods from the ARPACK library has been retained.

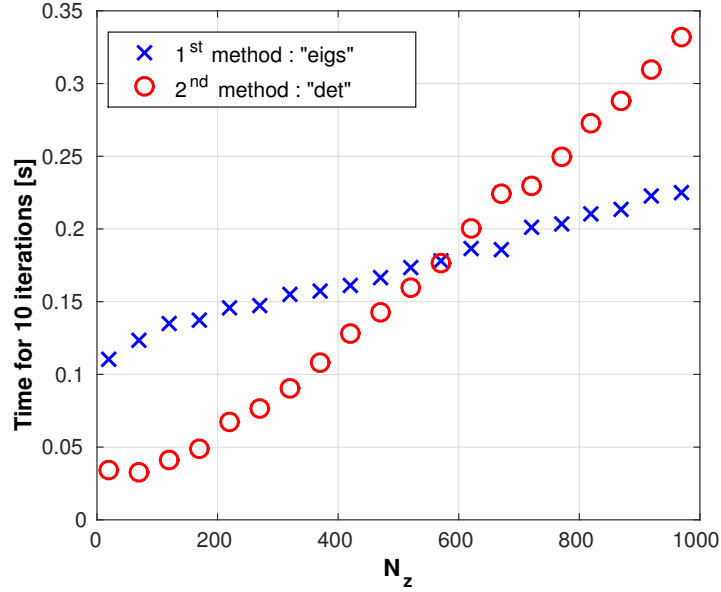


Figure 2.2 – Time needed by the two methods to solve the eigenvalue problem with 10 iterations (average on 10 runs).

Starting current calculation

In gyrotrons, the starting current is the self-excitation condition, i.e. a threshold current above which a mode is excited. The starting current is the most important parameter, especially for the parasitic oscillation studies. If the minimum starting current of a mode exceeds the operational gyrotron beam current, it would not be excited. The spectral approach is convenient for the computation of starting current. Indeed, as the field is expressed as $e^{-i\omega_r f t}$, the imaginary part of $\omega_r f$ is the wave growth rate and the current for which its value is zero is the starting current. In our formulation, $\omega_{rf} = \omega_0(1 + \Omega(I_b)) = \omega_0(1 + \text{Re}(\Omega(I_b)) + i \text{Im}(\Omega(I_b)))$. The starting current, I_{start} is thus defined as the current I_b for which $\text{Im}(\Omega(I_b)) = 0$.

2.1.3 Validations

Code benchmarking with other codes

The first code validations were done with the cavity of a low power gyrotron for DNP-NMR spectroscopy [17, 18]. The cavity longitudinal profile and the magnetic profile are shown in Figure 2.3. TWANGlinspec was first tested without current ($I_b = 0$), i.e. without beam-wave interaction, also called cold-cavity model. It was benchmarked against Cavity, a cold-cavity code solving only the wave equation and based on a finite elements method (see Table 2.1) using B-splines of arbitrary order. For the comparison $N_z = 4225$ points for the discretization were chosen as well as 10 iterations in order to achieve a numerical convergence. The reference frequency ω_0 was set to the cutoff-frequency of the flat section of the cavity.

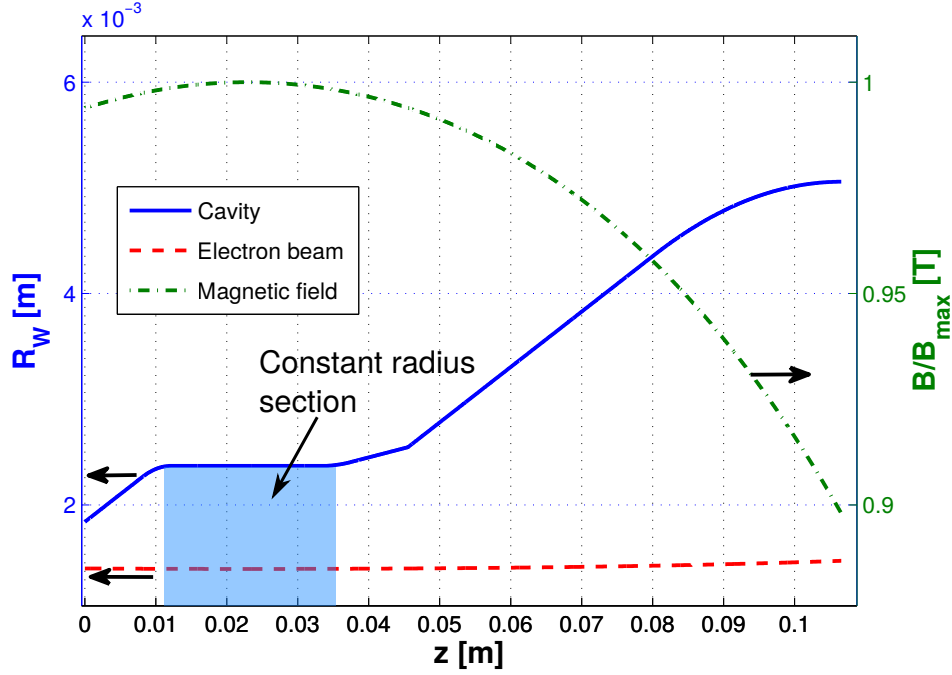


Figure 2.3 – Longitudinal profile of the DNP-cavity (in blue), average guiding center radius (in red, dashed) and normalized magnetic field profile (in green, dashed-dotted).

The relative difference between the first eigenvalue given by the two codes never exceeds 0.09% for both the real and imaginary parts. The discrepancies for higher modes are slightly larger, as expected, as a higher number of points is needed for the sampling (according to the Nyquist-Shannon sampling theorem).

Table 2.1 – Model and numerical implementation for the cold-cavity code “Cavity” and the time-evolution linear code “TWANGlin”, both used to benchmark the new spectral code “TWANGlinspec”. These three codes have been developed at SPC. FEM, FDM and RK stand for Finite Element Method, Finite Difference Method and Runge-Kutta, respectively.

Code	Model	Numerical implementation
Cavity (cold-cavity)	spectral	FEM
TWANGlin	temporal	FEM + RK
TWANGlinspec	spectral	FDM

A second validation step consisted in adding the self-consistent interaction with the electron beam. For this case, the comparison was done with the results of the code TWANGlin [30] (see Table 2.1). To solve the equations, the code TWANGlin uses a fourth order Runge-Kutta method for the two beam equations related to the moments π_1 and π_2 and a finite element method based on B-splines of arbitrary order for the wave equation. The boundary conditions are solved either by adapting iteratively the reference frequency ω_0 in order to obtain zero

reflection in the case of a single frequency oscillation, or by solving an integro-differential type boundary condition [89] in the case of multi-frequency or broadband-spectrum oscillation. The frequency and growth rates are calculated respectively with a Fourier transform and with an exponential fit of the electric field time-evolution. The frequency and growth rates computed with the TWANGlin and TWANGlinspec are shown in Figure 2.4, for different average step size $\langle dz \rangle$ of the non-equidistant spatial discretization. As expected, the convergence is faster with the code TWANGlin, using a third-order finite element method for the wave equation, whereas a first-order finite difference method is used in this first version of TWANGlinspec.

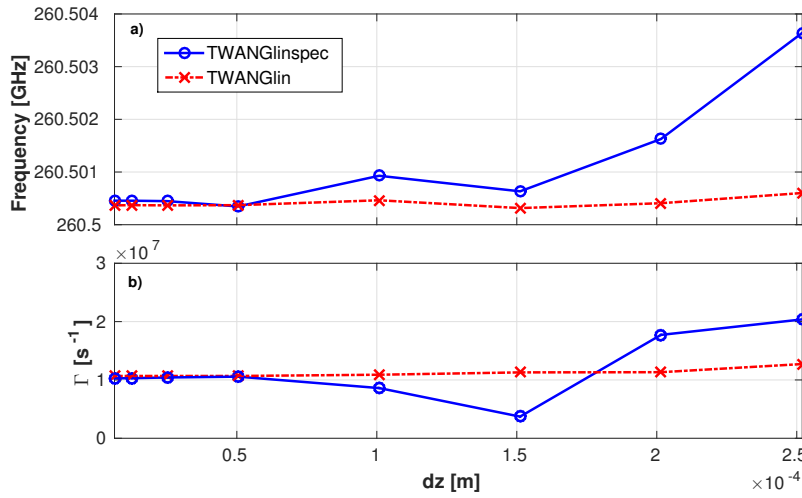


Figure 2.4 – Frequency (a) and growth rate (b) versus the average step size $\langle dz \rangle$ computed with the spectral code TWANGlinspec (in blue) and the time-dependent code TWANGlin.

Model validation against experiments

The model in TWANGlinspec allows to consider real experimental system parameters with all the spatial inhomogeneities, such as magnetic field or cavity radius inhomogeneities. An additional validation is done comparing the starting current calculated with TWANGlinspec with experimental measurements. The results of TWANGlinspec for the DNP-gyrotron [17, 18] are presented in Figure 2.5 along with experimental results. The simulation parameters are listed in the first part of Table 2.2. The agreement between TWANGlinspec and the experimental results is remarkably good over the whole range of magnetic field.

Most of the start-up scenarios in gyrotron operations are based on non-self-consistent starting current calculation. Such simplification allows to find an analytic expression for the starting current [60, 61]. The starting current of the analyzed DNP-gyrotron was calculated with such a fixed-field model and added in Figure 2.5. A significant discrepancy is found between the starting current calculated with TWANGlinspec and the non-self consistent model. For

example for magnetic field lower than 9.52T, corresponding to the positive detuning ($\Delta_0 > 0$) regime in which high-power gyrotrons are operated. The detuning, defined in equation (2.24), is the normalized difference between the wave frequency ω_{rf} and the electron cyclotron frequency Ω_c . It is indicated at the top of Figure 2.5. An operation in the positive detuning leads to the excitation of a forward wave, while an operation in the negative detuning leads to a backward wave excitation. A fully self-consistent model is thus significantly more accurate for start-up scenarios studies, as it has already been mentioned in several publications [30, 62–65, 85, 90].

Table 2.2 – Simulation parameters. The magnetic field, beam radius and pitch angle values are set in the middle of the constant radius section of the cavity (cf. Figure 2.3).

Parameter	Value
Transverse mode	TE _{7,2}
Beam radius	1.394 mm
Pitch angle	1.9
Acceleration voltage	15.5 kV
Wall conductivity	$2.9 \cdot 10^7$ S/m
Magnetic field	9.55 T
Beam current	15 mA

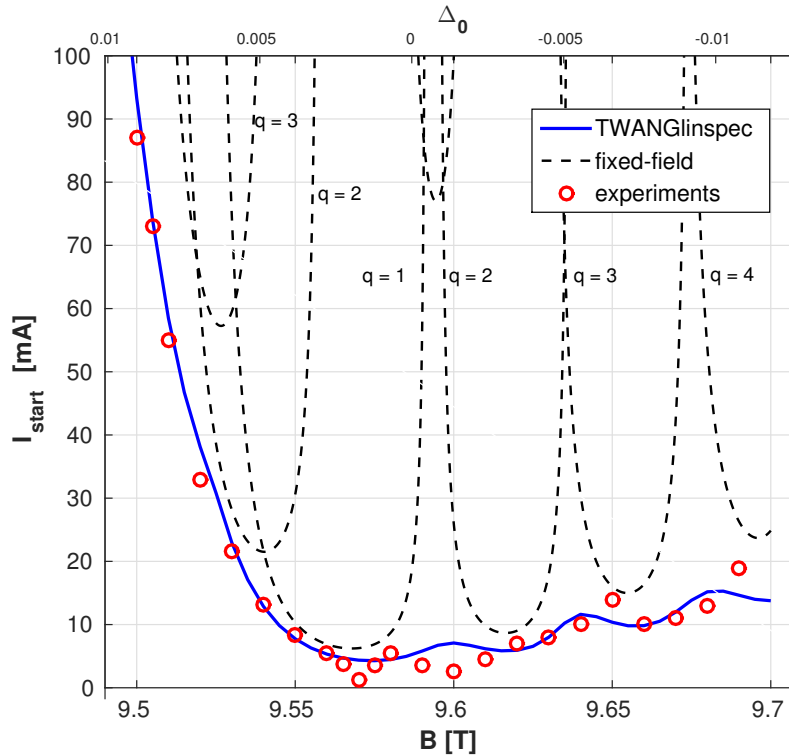


Figure 2.5 – Starting current calculated with TWANGlinspec (in blue) and with a fixed-field code (in black, dashed) and measured (red points).

2.1.4 Advantages of a spectral model

In the spectral approach, the computation time does not depend on the systems physical parameters, while in a time-evolution code it depends on the growth rate, as a longer simulation time is needed for lower growth rates to correctly describe the initial linear phase. The difference in computation time between the time-evolution code TWANG and the spectral code TWANGlinspec are reported in Table 2.3 for two beam currents. The operating point is at $B = 9.55$ T, where the starting current is $I_{\text{start}} = 7.7$ mA. This advantage is decisive for parasitic instabilities studies, which require a large number of starting current calculations, as will be shown later.

Table 2.3 – TWANG and TWANGlinspec (Finite difference discretization) runtimes for two different beam currents on an Intel Haswell i7 quad core processor. The code TWANG is written in FORTRAN and makes effectively use of the four cores using MPI communications, whereas TWANGlinspec is a serial Matlab program running in a single core.

Code	TWANG	TWANGlinspec (FD)
$I_b = 8.1$ mA	228 s	5 s
$I_b = 15.5$ mA	19 s	5 s

With a time-dependent model, only the most unstable mode evolution is described. The spectral approach gives more physical insight, since it computes the growth rate of both stable, $\text{Im}(\Omega) < 0$, and unstable modes, $\text{Im}(\Omega) > 0$. This is illustrated in Figure 2.6, for the simulation parameters given in Table 2.2. The horizontal axis represents the real part of the eigenvalues, corresponding to the wave frequency, whereas the vertical axis represents the imaginary part of the eigenvalues, corresponding to the wave growth rate. In this case, only one longitudinal mode is unstable ($\Gamma > 0$). The field profiles corresponding to these eigenmodes are obtained via the eigenvector \mathbf{X} in Eq.(2.29). The amplitude and phase of the electric field profile for the four modes highlighted in Figure 2.6 are shown in Figures 2.7 and 2.8. For the unstable mode, the electric field profile corresponds to the mode with one axial variation ($\text{TE}_{7,2,1}$). The closest mode in the complex plane in Figure 2.6 is the mode with two axial variations ($\text{TE}_{7,2,2}$) and by following the same direction in the complex plane, all the “usual” modes with increasing axial variations are found.

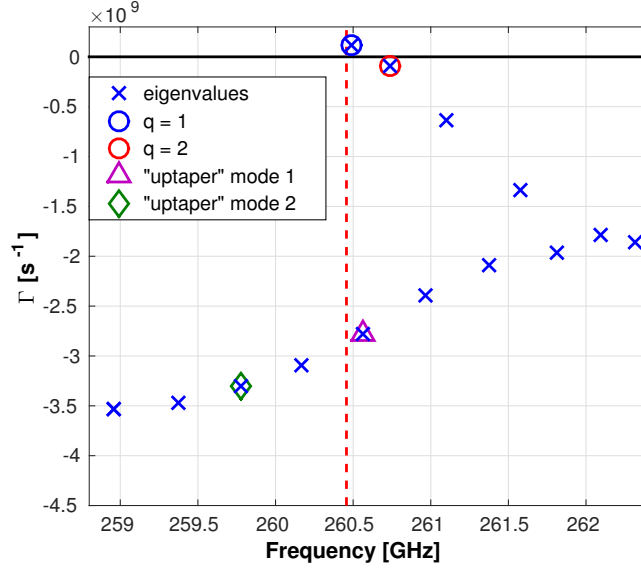


Figure 2.6 – Real (frequency) and imaginary (growth rate) parts of the first 14 eigenvalues ($TE_{7,2,q}$) computed with TWANGlinspec. The dashed vertical red line indicates the cutoff frequency in the constant radius cavity part. The horizontal continuous black line indicates the limit between stable ($\Gamma < 0$) and unstable ($\Gamma > 0$) modes. The four symbols indicate which modes are considered in Figures 2.7 and 2.8. (cf. Table 2.2 for parameters).

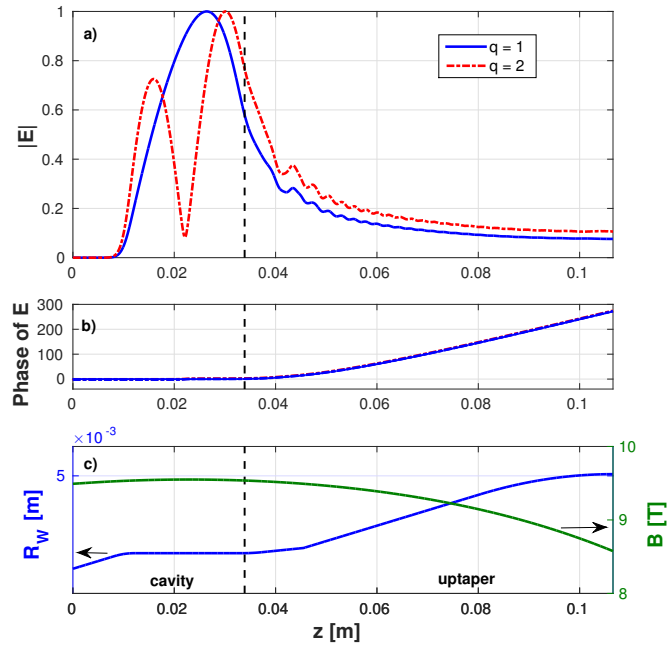


Figure 2.7 – (a) and (b) Amplitude and phase of the electric field profile along the longitudinal direction, calculated with TWANGlinspec for two of the modes highlighted in Figure 2.6 ($TE_{7,2,q}$). (c) Cavity and magnetic field profile. The dashed black line indicates the end of the cavity constant radius part. (cf. Table 2.2 for parameters).

On the other hand, all the modes situated in the bottom part of the complex plane in Figure 2.6, with $\Gamma < -2 \cdot 10^9 \text{ s}^{-1}$, have their electric field profile mainly situated in the uptaper following the constant radius section of the cavity, as can be seen in Figure 2.8. They are called "uptaper" modes.

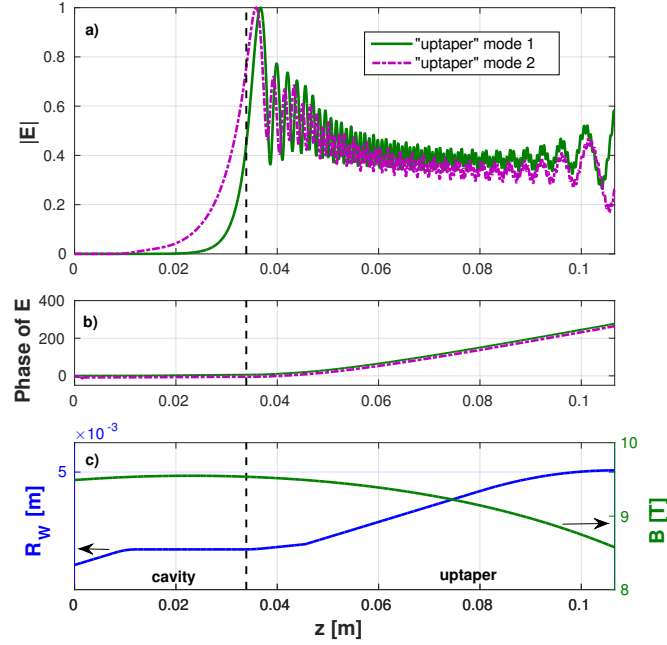


Figure 2.8 – (a) and (b) Amplitude and phase of the electric field profile along the longitudinal direction, calculated with TWANGlinspec for two of the modes highlighted in Figure 2.6. (c) Cavity and magnetic field profile. The dashed black line indicates the end of the cavity constant radius part. (cf. Table 2.2 for parameters).

Another asset of the spectral approach is the possibility to follow each eigenvalue individually when one parameter is changed. As an illustration, the eigenvalues computed for different beam current values between 0 mA (no electron beam) and 20 mA are shown in Figure 2.9. The difference with respect to the results shown in Figure 2.6 is the value of the magnetic field maximum: $B = 9.62 \text{ T}$. For this magnetic field, the first mode to be excited is the mode $\text{TE}_{7,2,3}$ with three axial variations, a result that could be expected by examining Figure 2.5.

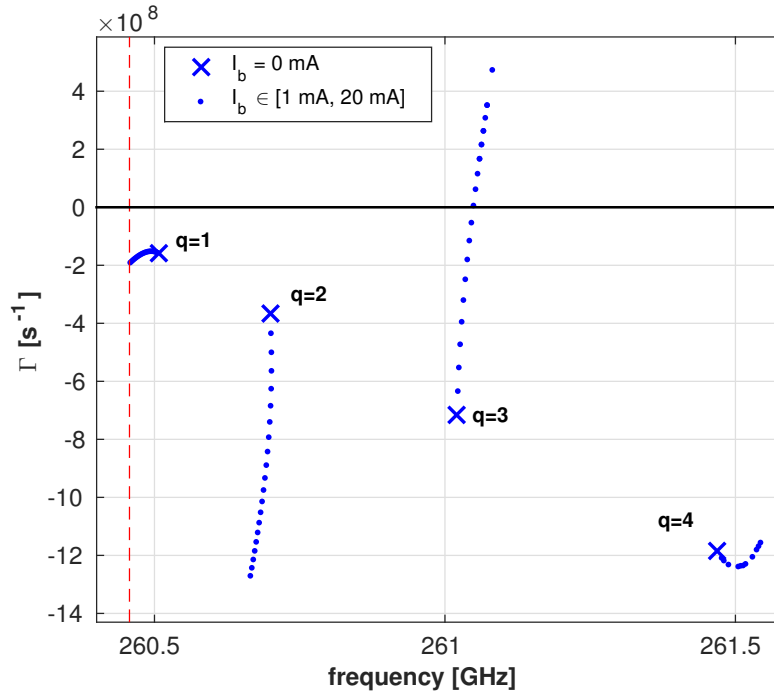


Figure 2.9 – Real (frequency) and imaginary (growth rate) parts of the first 4 eigenvalues computed with TWANGLinspec. The dashed vertical red line indicates the cutoff frequency in the constant radius cavity part. The horizontal continuous black line indicates the limit between stable ($\Gamma < 0$) and unstable ($\Gamma > 0$) modes. The crosses are the eigenvalues computed without electron beam and the points are the eigenvalues for different beam current values (cf. Table 2.2 for parameters, $B = 9.62$ T).

2.2 TWANGlinspec-beam-duct

2.2.1 Model adaptation

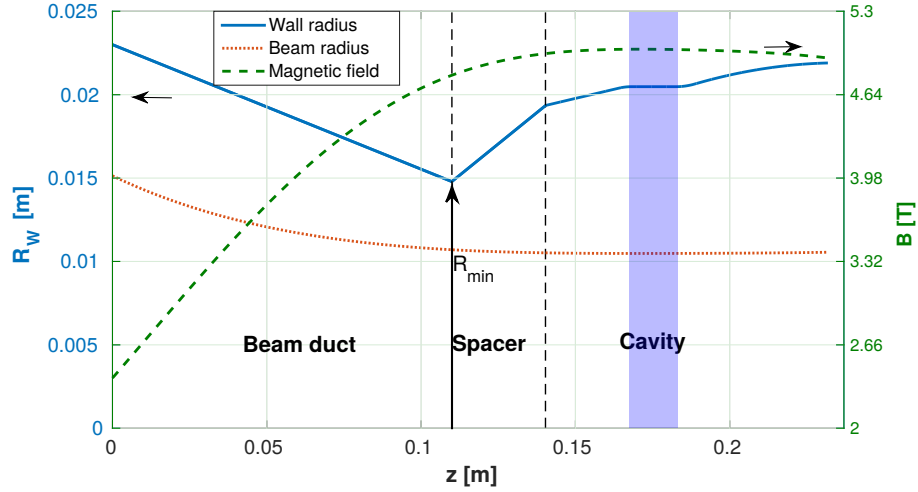


Figure 2.10 – Example of geometry considered. The usual interaction zone considered is the cavity, the constant radius part highlighted in blue, and its uptaper and downtaper.

In order to treat oscillations in smooth-wall beam ducts, some modifications of the model had to be made. First the boundary conditions for the electric field (2.27) had to be adapted to radiation boundary conditions at both extremities:

$$\left. \frac{dF}{dz} \right|_{\hat{z}_{in/out}} = \mp i \frac{k_{\parallel}}{k_0} F(\hat{z}_{in/out}, \tau). \quad (2.40)$$

The first tests involving a conical interaction region (e.g. the part labelled "Beam duct" in Figure 2.10) with radiation boundary conditions at both extremities revealed a limitation in our numerical model. The finite difference scheme used was insufficient to simulate this interaction region with a sufficient accuracy.

Discretization using finite element methods

This led us to reformulate the model with a finite element method (FEM), based on B-Splines of arbitrary order and has been the subject of a master student semester project [91]. At this stage, the code has been rewritten in FORTRAN. The numerical approach adopted is in fact based on hybrid FEMs [92]. Due to the two different type of problems in equations (2.26), including a first order initial value problem (IVP) for the equations for π_1 (2.26a) and π_2 (2.26b) and one second order boundary value problem (BVP) for the field F (2.26c), a hybrid FEM scheme has to be used. Indeed, using a finite element method formulation based on test functions of the same order as the basis functions for the IVP leads to numerical instabilities.

Using test functions one order lower than the basis functions for (2.26a) and (2.26b), allows to solve this issue. For (2.26c), a conventional FEM formulation is used. A convergence study is reported in Figure 2.11 for a conical interaction region comparable to a gyrotron smooth-wall beam duct. The three curves are the real part of the frequency ω_{rf} of a given $TE_{m,p,q}$ mode in a cylindrical geometry calculated with three different discretization methods. The benefit of using a finite element method of second order is evident.

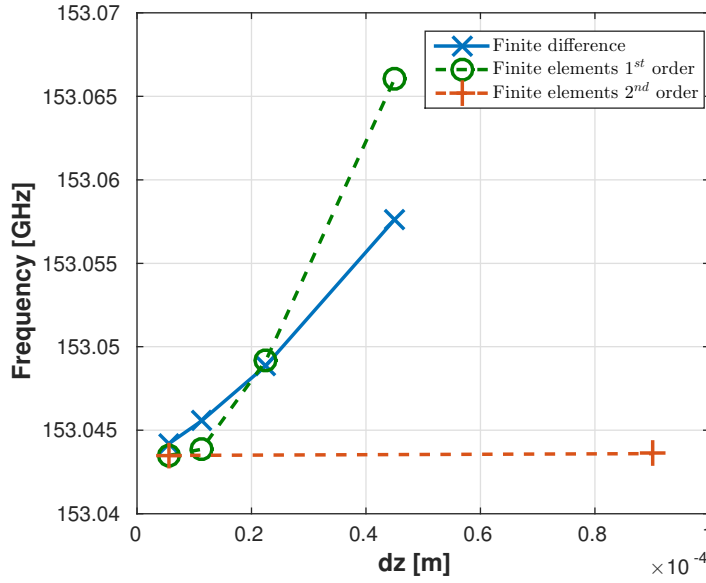


Figure 2.11 – Frequency of a given $TE_{m,p,q}$ eigenmode calculated with the code TWANGlinspec for different step size for the discretization and for different numerical scheme. The situation treated is a conical structure equivalent to a gyrotron smooth-wall beam duct (cf. the conical section between $z = 0$ and $z = 0.11$ m in Figure 2.10).

Distributed losses

As the goal was to consider a realistic situation, the code had to be adapted to treat, in the same simulation, regions with different wall conductivities. Some studies focused on the Ohmic losses effect on the instabilities, and thus the wall conductivity had to be varied. On the other hand, the cavity wall conductivity is fixed at a given value. Indeed, the cavity is usually made from a copper alloy, its conductivity is often assumed to be $\sigma_{\text{cond}} = 1.45 \cdot 10^7$ S/m. The modifications were done in order to consider a wall conductivity profile $\sigma(z)$, along the interaction region. As an illustration, a typical wall conductivity profile used in this work is shown in Figure 2.12. As a reminder, the effect of a resistive wall is taken into account via a surface impedance boundary term correcting the parallel wave vector κ_{\parallel} (cf. equation 2.8).

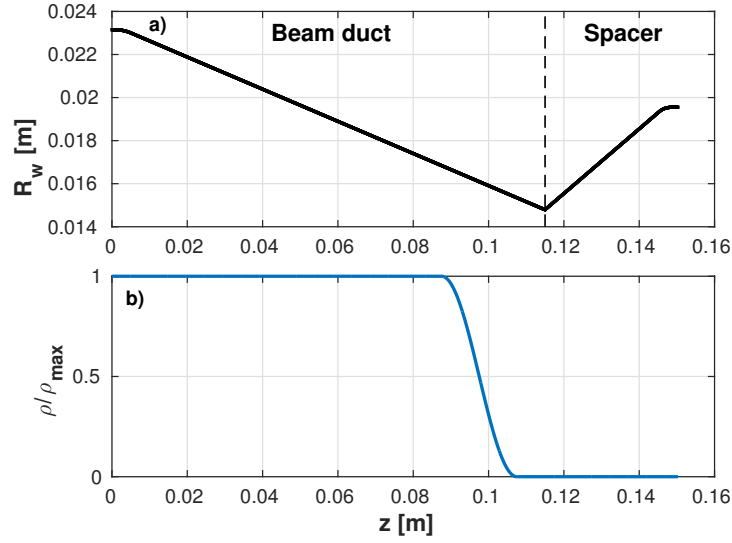


Figure 2.12 – a) Smooth-wall beam duct and spacer geometry. b) Resistivity profile considered for the simulation. The transition between the resistive part and the perfectly conducting part is made smooth to avoid reflection.

Choice of the transverse mode $TE_{m,p}$

The selection of transverse modes $TE_{m,p}$ to simulate is usually done using their geometrical beam coupling factor:

$$C_{\pm} = \frac{J_{m\pm s}(k_{\perp} R_g)^2 J_m(v_{mp})^2}{v_{mp}^2 - m^2}, \quad (2.41)$$

where $k_{\perp} = \frac{v_{mp}}{R_w}$ and the signs \pm stand for the co- or counter-rotating waves (with respect to the electron rotation) respectively. Thus, for a given $TE_{m,p}$ mode, the coupling factor depends explicitly only on the wall and beam radii. For a usual cavity interaction study, these two parameters are almost constant along the interaction region (see Figure 2.10) and the choice of the transverse mode is straightforward. As an illustration, the coupling factor (normalized to the nominal mode coupling factor) for four different modes are reported in Figure 2.13 according to their cutoff frequency ($\omega_{co} = k_{\perp} c$). The mode $TE_{7,2}$ is the operating mode and the other three modes are potential competing modes. The points are the counter-rotating modes ($m < 0$) whereas the other symbols are the co-rotating waves ($m > 0$).

On the other hand, when the wall or beam radii are varying along the interaction region, as is the case for the beam-duct (cf. Figure 2.10), the choice of the relevant set of transverse modes is more intricate. Various methods were unsuccessfully tested. Eventually, as the numerical efficiency of the spectral method allows, it was decided to scan over all the possible transverse $TE_{m,p}$ modes.

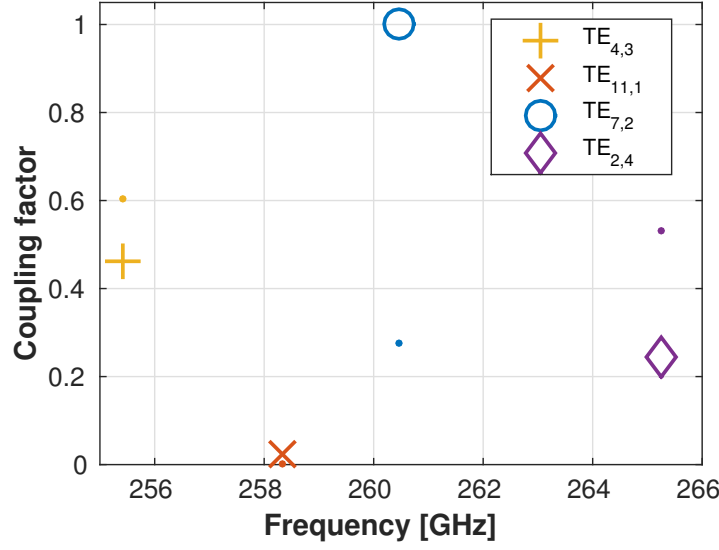


Figure 2.13 – Beam coupling factor for four different transverse $TE_{m,p}$ modes for the DNP gyrotron cavity parameters ($R_b = 1.39$ mm, $R_w = 2.37$ mm) The operating mode is the co-rotating $TE_{7,2}$.

Choice of the reference frequency

The reduced simulations require the choice of a reference frequency ω_0 . In the spectral approach, the complex eigenvalue calculated (cf. equation (2.29)) is the normalized difference between the rf-frequency and the reference frequency. As the model accuracy decreases for large value of Ω , the reference frequency has to be chosen close to the actual rf-frequency of the wave. For ordinary gyrotron interactions, the resonance condition occurs close to the cutoff ($\omega_{rf} = s\Omega_c/\gamma + k_z v_{\parallel} \simeq s\Omega_c/\gamma$). The reference frequency is then chosen at the cutoff frequency, depending only on the mode considered and the wall radius of the cavity ($\omega_{co} = v_{mp}c/R_w$). For beam duct interactions, it will be shown later that interactions could occur for larger Doppler shift ($k_z v_{\parallel}$). Moreover, the variation of the magnetic field amplitude along the beam duct (cf. Figure 2.10) strongly affects the electron cyclotron frequency $\Omega_c = eB/m$. The choice of the reference frequency becomes complicated. The solution adopted is to scan over a range of acceptable reference frequency for every transverse $TE_{m,p}$ modes.

Optimization and parallelization for the starting current calculation

Even though the spectral approach is numerically significantly more efficient than a time evolution approach, the decisions to scan over a large number of transverse modes and over different reference frequencies requires an important optimization effort. For instance, for a study on the operating mode for the DNP gyrotron 8 different transverse modes (4 co-rotating and 4 counter rotating, see Figure 2.13) are included, leading to 8 starting current calculations. For a beam duct parasitic study, a scan over 1420 transverse modes and 200 reference frequencies is usually done, leading to 284000 starting current calculations.

The first measure was to improve the method used for carrying out the zero-search of $\text{Im}(\Omega)$ by combining a fast adaptive trial and error method giving a coarse first guess for the subsequently applied second method based on either a Newton [88] or Illinois algorithm [93], the combination of both algorithms in case one fails, for instance due to a bad initial first guess, permits to have a reliable result.

The second measure was to parallelize the code using Message Passing Interface (MPI) [94] for communication between processes. The strategy adopted is a standard distribution of sub-tasks from one master process to different slave processes. The simplest scheme has been adopted and is shown in Figure 2.14 for a typical starting current calculation. First, the master process P0 distributes the different starting current requests to the slave processes P1-4. Then whenever a slave process completes its starting current calculation, the result is sent back to the master.

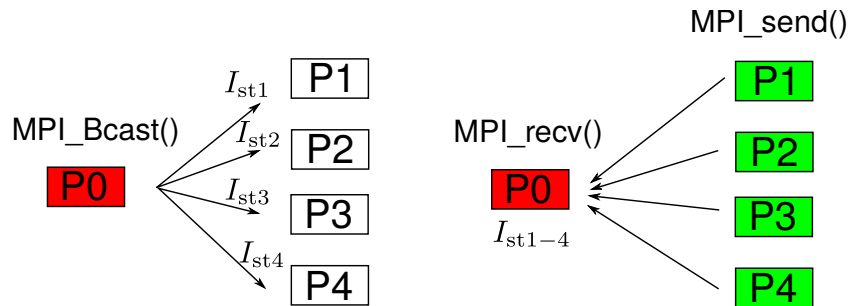


Figure 2.14 – Schematic of the communication between the master process and the four slave processes (P1-4) for a typical starting current calculation.

2.3 TWANGlinspec-dielectric

The code has been extended to include the effect of a dielectric loading in the interaction region. The approach considered here is to use the self-consistent model TWANGlinspec with the minimum number of simplifications. The modes simulated are assumed to remain pure transverse $TE_{m,p}$ modes. However, the transverse profile of the mode is adapted, accounting for the correct boundary condition in the presence of the dielectric layer [43].

2.3.1 Model adaptation

In the model, the expression of the perpendicular electric field component is:

$$\vec{E}_\perp(\vec{r}, t) = \frac{1}{2} E(z, \tau) \left[-\frac{im}{k_\perp r} J_m(k_\perp r) \vec{e}_r + J'_m(k_\perp r) \vec{e}_\phi \right] e^{-i(\omega t - m\phi)} + \text{c.c.} \quad (2.42)$$

where c.c. stands for the complex conjugate of the expression. The perpendicular wavenumber is $k_\perp = \frac{v_{mp}}{R_w}$ for an ideal metallic boundary condition. For a dielectric boundary condition, the wavenumber k_\perp is calculated by solving the dispersion relation of an infinitely long cylindrical waveguide with a dielectric coating [43]. The dispersion relation derivation is described in [43] and is recalled here.

2.3.2 Dielectric dispersion relation

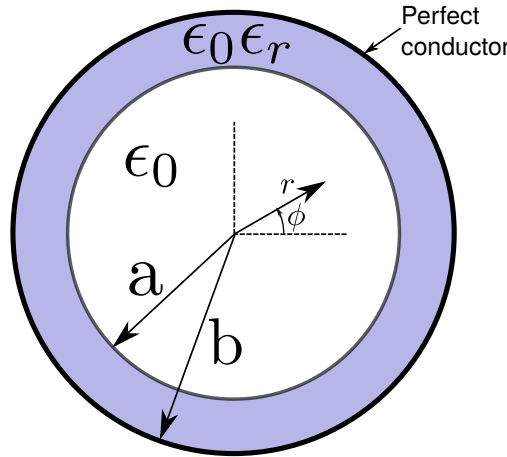


Figure 2.15 – Transverse section of the geometry considered, a cylindrical waveguide of radius a surrounded by a layer of material with a complex dielectric permittivity $\epsilon_0 \epsilon_r$ and a perfect conductor for $r > b$. The layer thickness is $b - a$.

For an infinitely long cylindrical waveguide with a dielectric layer (see Figure 2.15), the electric

and magnetic fields solutions to Maxwell's equations are :

$$E_{r_{1,2}} = \left[-\frac{m}{r} (A_{1,2} J_m(k_{\perp,2} r) + B_{1,2} Y_m(k_{\perp,2} r)) - \frac{k_z k_{\perp,2}}{\omega \epsilon_{1,2}} (C_{1,2} J'_m(k_{\perp,2} r) + D_{1,2} Y'_m(k_{\perp,2} r)) \right] \cos(m\phi) \exp(-i k_z z), \quad (2.43a)$$

$$E_{\phi_{1,2}} = \left[k_{\perp,2} (A_{1,2} J'_m(k_{\perp,2} r) + B_{1,2} Y'_m(k_{\perp,2} r)) + \frac{m k_z}{\omega \epsilon_{1,2} r} (C_{1,2} J_m(k_{\perp,2} r) + D_{1,2} Y_m(k_{\perp,2} r)) \right] \sin(m\phi) \exp(-i k_z z), \quad (2.43b)$$

$$E_{z_{1,2}} = \frac{k_{\perp,2}^2}{i \omega \epsilon_{1,2}} (C_{1,2} J_m(k_{\perp,2} r) + D_{1,2} Y_m(k_{\perp,2} r)) \cos(m\phi) \exp(-i k_z z), \quad (2.43c)$$

$$H_{r_{1,2}} = \left[-\frac{k_{\perp,2} k_z}{\omega \mu_0} (A_{1,2} J'_m(k_{\perp,2} r) + B_{1,2} Y'_m(k_{\perp,2} r)) - \frac{m}{r} (C_{1,2} J_m(k_{\perp,2} r) + D_{1,2} Y_m(k_{\perp,2} r)) \right] \sin(m\phi) \exp(-i k_z z), \quad (2.43d)$$

$$H_{\phi_{1,2}} = \left[-\frac{m k_z}{\omega \mu_0 r} (A_{1,2} J_m(k_{\perp,2} r) + B_{1,2} Y_m(k_{\perp,2} r)) - k_{\perp,2} (C_{1,2} J'_m(k_{\perp,2} r) + D_{1,2} Y'_m(k_{\perp,2} r)) \right] \sin(m\phi) \exp(-i k_z z), \quad (2.43e)$$

$$H_{z_{1,2}} = \frac{k_{\perp,2}^2}{i \omega \mu_0} (A_{1,2} J_m(k_{\perp,2} r) + B_{1,2} Y_m(k_{\perp,2} r)) \sin(m\phi) \exp(-i k_z z). \quad (2.43f)$$

$$H_{r_{1,2}} = \left[-\frac{k_{\perp,2} k_z}{\omega \mu_0} (A_{1,2} J'_m(k_{\perp,2} r) + B_{1,2} Y'_m(k_{\perp,2} r)) - \frac{m}{r} (C_{1,2} J_m(k_{\perp,2} r) + D_{1,2} Y_m(k_{\perp,2} r)) \right] \sin(m\phi) \exp(-i k_z z), \quad (2.43g)$$

$$H_{\phi_{1,2}} = \left[-\frac{m k_z}{\omega \mu_0 r} (A_{1,2} J_m(k_{\perp,2} r) + B_{1,2} Y_m(k_{\perp,2} r)) - k_{\perp,2} (C_{1,2} J'_m(k_{\perp,2} r) + D_{1,2} Y'_m(k_{\perp,2} r)) \right] \sin(m\phi) \exp(-i k_z z), \quad (2.43h)$$

$$H_{z_{1,2}} = \frac{k_{\perp,2}^2}{i \omega \mu_0} (A_{1,2} J_m(k_{\perp,2} r) + B_{1,2} Y_m(k_{\perp,2} r)) \sin(m\phi) \exp(-i k_z z). \quad (2.43i)$$

In these expressions, the indices 1,2 refer respectively to the vacuum and dielectric regions. The permittivity constants are respectively $\epsilon_1 = \epsilon_0$ and $\epsilon_2 = \epsilon_0 \epsilon_r$. The functions J_m and Y_m are the Bessel function of first and second kind. This system of 6 equations contains the 8 unknowns $A_{1,2}, B_{1,2}, C_{1,2}, D_{1,2}$. As the function Y_m are singular at $r = 0$, the coefficients B_1 and D_1 have to be zero. The boundary conditions the fields have to fulfill are continuous tangential field components at the interface $r = a$ and vanishing tangential electric field at the perfect conductor $r = b$:

$$E_{\phi_1}(r = a) = E_{\phi_2}(r = a), \quad (2.44a)$$

$$E_{\phi_2}(r = b) = 0, \quad (2.44b)$$

$$E_{z_1}(r = a) = E_{z_2}(r = a), \quad (2.44c)$$

$$E_{z_2}(r = b) = 0, \quad (2.44d)$$

$$H_{\phi_1}(r = a) = H_{\phi_2}(r = b), \quad (2.44e)$$

$$H_{z_1}(r = a) = H_{z_2}(r = b). \quad (2.44f)$$

With these boundary conditions, the system of equations (2.43) can be recast into the disper-

sion relation [43]:

$$\left[\frac{1}{k_{\perp 2}} \frac{\epsilon_2}{\epsilon_1} \frac{Q'(k_{\perp 2} a)}{Q(k_{\perp 2} a)} - \frac{1}{k_{\perp 1}} \frac{J'_m(k_{\perp 1} a)}{J_m(k_{\perp 1} a)} \right] \left[\frac{1}{k_{\perp 2}} \frac{\mu_2}{\mu_1} \frac{P'(k_{\perp 2} a)}{P(k_{\perp 2} a)} - \frac{1}{k_{\perp 1}} \frac{J'_m(k_{\perp 1} a)}{J_m(k_{\perp 1} a)} \right] - \frac{1}{\epsilon_1 \mu_1} \left(\frac{k_z m}{\omega a} \right)^2 \left(\frac{1}{k_{\perp 1}^2} - \frac{1}{k_{\perp 2}^2} \right)^2 = 0. \quad (2.45)$$

where

$$P(x) = J_m(x) Y'_m(k_{\perp 2} b) - Y_m(x) J'_m(k_{\perp 2} b), \quad (2.46a)$$

$$P'(x) = J'_m(x) Y'_m(k_{\perp 2} b) - Y'_m(x) J'_m(k_{\perp 2} b), \quad (2.46b)$$

$$Q(x) = J_m(x) Y_m(k_{\perp 2} b) - Y_m(x) J_m(k_{\perp 2} b), \quad (2.46c)$$

$$Q'(x) = J'_m(x) Y_m(k_{\perp 2} b) - Y'_m(x) J_m(k_{\perp 2} b). \quad (2.46d)$$

This dispersion relation is solved together with the relations

$$k_{\perp 1}^2 + k_z^2 = \omega^2 \epsilon_1 \mu_0, \quad (2.47)$$

$$k_{\perp 2}^2 + k_z^2 = \omega^2 \epsilon_2 \mu_0. \quad (2.48)$$

Note that for a mode at its cutoff frequency $k_z = 0$ or for an azimuthally symmetric mode $m = 0$, the third term in equation (2.45) is zero. In this case, the dispersion relation is uncoupled for TE and TM modes:

$$\left[\frac{1}{k_{\perp 2}} \frac{\epsilon_2}{\epsilon_1} \frac{Q'(k_{\perp 2} a)}{Q(k_{\perp 2} a)} - \frac{1}{k_{\perp 1}} \frac{J'_m(k_{\perp 1} a)}{J_m(k_{\perp 1} a)} \right] = 0, \quad \text{for TM modes}, \quad (2.49)$$

or

$$\left[\frac{1}{k_{\perp 2}} \frac{\mu_2}{\mu_1} \frac{P'(k_{\perp 2} a)}{P(k_{\perp 2} a)} - \frac{1}{k_{\perp 1}} \frac{J'_m(k_{\perp 1} a)}{J_m(k_{\perp 1} a)} \right] = 0, \quad \text{for TE modes}. \quad (2.50)$$

The equation (2.49) leads to the TM modes solutions while equation (2.50) leads to the TE modes solutions. When $k_z \neq 0$ or $m \neq 0$, the solutions of the dispersion relation (2.45) are hybrid $\text{HE}_{m,p}$ or $\text{EH}_{m,p}$ modes, as already mentioned in the introduction chapter (cf. 1.1.2).

Another parameter affected by the dielectric coating is the geometrical coupling factor used in the normalization (cf. equation (2.10)). This term comes from the volume integral of the perpendicular electric field component. With the dielectric layer, the integral has to be extended to the external boundary and this factor becomes:

$$C_{mp} = \frac{|k_{\perp 1}^2|}{2} (K_a + K_b), \quad (2.51)$$

with

$$K_a = \frac{2\pi}{|k_{\perp 1}|^2} \int_0^a \left[|J'_m(k_{\perp 1} r)|^2 + \left| \frac{m}{k_{\perp 1} r} J_m(k_{\perp 1} r) \right|^2 \right] r dr, \quad (2.52)$$

and

$$K_b = \frac{2\pi}{|k_{\perp 2}|^2} \int_a^b \left\{ \left| \alpha J'_m(k_{\perp 2} r) + \beta Y'_m(k_{\perp 2} r) \right|^2 + \left| \frac{m}{k_{\perp 2} r} [\alpha J_m(k_{\perp 2} r) + \beta Y_m(k_{\perp 2} r)] \right|^2 \right\} r dr. \quad (2.53)$$

In this last expression, α and β are given by

$$\alpha = \frac{J_m(k_{\perp 1} a) Y'_m(k_{\perp 2} b)}{P(k_{\perp 2} a)}, \quad (2.54)$$

and

$$\beta = -\frac{J_m(k_{\perp 1} a) J'_m(k_{\perp 2} b)}{P(k_{\perp 2} a)}. \quad (2.55)$$

Note that for a complex dielectric permittivity of the dielectric layer, $k_{\perp 1}$ and $k_{\perp 2}$ are complex numbers.

Numerical method

To solve the dispersion relation, the strategy used is to fix the parallel wavenumber $k_z \in \mathbb{R}$ and search for the complex frequency solution to the dispersion relations (2.45) and the relations (2.47) and (2.48). For the zero-search, a combination of two algorithms has been found to be the most reliable method. The first algorithm is used to localize roughly the zero in the complex plane, using Nyquist's method [95]. In this method, the phase variation of the function along a circular path is used to identify the number of zeros enclosed by this path as well as values of these zeros. The second algorithm is based on the Muller method [88] and is used to refine the results.

2.3.3 Formulation with Hankel functions

It is found that for a layer with a dielectric constant with a large imaginary part, the formulation used is not appropriate. The coefficients Q'/Q or P'/P in the dispersion relation 2.45 are numerically indefinite and the methods fail to find the zero. The solution to this problem is to express the electric and magnetic field with the help of Hankel functions of the first and second kind:

$$H_m^{(1)}(x) = J_m(x) + i Y_m(x), \quad (2.56a)$$

$$H_m^{(2)}(x) = J_m(x) - i Y_m(x). \quad (2.56b)$$

The details of the derivation are given in the appendix E. The dispersion relation with the Hankel formulation reads:

$$\frac{Q(k_{\perp 2} a) P(k_{\perp 2} a)}{\epsilon_2 \mu_0 H_m^{(2)}(k_{\perp 2} a) H_m'^{(2)}(k_{\perp 2} a)} \left(\frac{k_z m}{\omega a} \right)^2 \left(1 - \frac{k_{\perp 2}^2}{k_{\perp 1}^2} \right)^2 + \frac{k_{\perp 2}^2}{H_m^{(2)}(k_{\perp 2} a) H_m'^{(2)}(k_{\perp 2} a)} \zeta \lambda = 0, \quad (2.57a)$$

with

$$\zeta = \frac{k_{\perp 2}}{k_{\perp 1}} \frac{P(k_{\perp 2} a) J_m'(k_{\perp 1} a)}{J_m(k_{\perp 1} a)} - P'(k_{\perp 2} a), \quad (2.57b)$$

$$\lambda = Q'(k_{\perp 2} a) - \frac{\epsilon_2}{\epsilon_1} \frac{k_{\perp 2}}{k_{\perp 1}} \frac{Q(k_{\perp 2} a) J_m'(k_{\perp 1} a)}{J_m(k_{\perp 1} a)}. \quad (2.57c)$$

2.4 Linear model TWANGlinspread

Within a master project [86] the code TWANGlinspread was developed. The goal of this project was to develop a linear version of TWANG including the possibility to account for a non-ideal electron beam with velocity and energy spreads. This is not possible with the model TWANGlinspec due to the assumptions used in the model based on the moment approach. The idea was to step back to the linearized equations (2.13), include the spreads and study their effect on the parasitic starting current. The two equations of motion (2.13a) and (2.13b) are solved with a 4th order Runge-Kutta method, while the wave equation (2.13c) is solved using a finite element method scheme of arbitrary order in the spatial domain and a finite difference method with a predictor-corrector method in the time domain. The initial distribution functions for the electron beam velocities and/or energies can be uniform or Gaussian. Practically, the results from an electron trajectory code, such as DAPHNE [96] or ARIADNE [97], are used to approximate the velocity/energy distributions. In order to distribute the electrons, a quiet-start algorithm is used based on a Hammersley-sequence [98, 99].

The numerical implementation is identical to the one used in TWANG or TWANGlin. However, the larger inhomogeneities in the geometry or in the magnetic field profile in the beam duct case require three main adaptations, in the same way as it was done for TWANGlinspec. First, a quadratic interpolation instead of the existing linear interpolation is used to calculate the magnetic field value at any given position z . Secondly, a Simpson scheme, instead of an Euler scheme, is used to calculate the slow phase Ψ_0 . Finally, in the other time-evolution codes, the solution corresponding to the cold-cavity simulation, i.e. the case without electron-beam interaction, was used as an initial condition ($t = 0$). For interaction in the beam duct, the gyro-backward wave nature of the interaction, as will be presented later, involve stronger self-consistent effects and the result from the interaction is often significantly different than the non self-consistent case. Starting from the cold-cavity result as an initial condition, the time-dependent code could, in some cases, not converge to the correct solution. For this reason, the code has been changed to take the self-consistent result from TWANGlinspec as an initial condition for the field.

2.5 Non-linear model TWANG and TWANG-PIC

The third model used in these studies is the nonlinear code TWANG [72]. At each time-step, the equations of motion (2.5a) and (2.5b) for electrons are solved for the entire interaction region. The calculated trajectories are then used to solve the wave equation (2.5c). Actually, in this work, the code TWANG-PIC [67] is used. This model was developed in order to treat non-stationary regimes in which the field profile could change during the electron transit time along the interaction region. It has to be emphasized that in this work, as only stationary regimes are treated, the PIC-approach is not necessary. Both codes TWANG or TWANG-PIC lead to the same results.

The equations solved in the code TWANG-PIC are the following [67]:

$$\frac{d\mathcal{P}}{d\tau} = \left(-i \frac{\gamma - s \frac{\Omega_c}{\omega_0}}{p_z} + \frac{s}{2} \frac{\hat{p}_z}{\gamma} \frac{d(\ln B_0)}{d\hat{z}} \right) \mathcal{P} + s C_0 p_{\perp}^{2s-2} \left(-F^* + i \frac{\hat{p}_z}{\gamma} F'^* \right) \quad (2.58a)$$

$$\frac{d\hat{p}_z}{d\tau} = -\frac{C_0}{\gamma} \text{Im}(\mathcal{P} F') - \frac{p_{\perp}^2}{2\gamma} \frac{d(\ln B_0)}{d\hat{z}} \quad (2.58b)$$

$$\frac{d\hat{z}}{d\tau} = \frac{\hat{p}_z}{\gamma} \quad (2.58c)$$

$$\left(2i \frac{\partial}{\partial \tau} + \frac{\partial^2}{\partial \hat{z}^2} + \kappa_{\parallel}^2 \right) F = i \mathcal{J} \frac{1}{N_{\text{inj}}} \sum_{j=1}^{N_{\text{inj}}} \frac{C_{0j} \mathcal{P}_j^*}{\gamma_j} \Delta \tau \delta(\hat{z} - \hat{z}_j), \quad (2.58d)$$

where the normalized time $\tau = \omega_0 t$, is used. The numerical methods are the same as those used in TWANG. The differences, inherent to the PIC-approach, are that the equations of motion are solved in the time-domain and that the field equation is solved between each Runge-Kutta step of the electrons.

In the frame of this work, the code TWANG-PIC is used to compute the rf-power radiated by the beam duct instabilities, to evaluate their effect on the electron beam and subsequently their effect on the main cavity instability. For these purposes, the code has been slightly adapted.

Model adaptation

As already explained in the previous section, the time dependent codes need an initial condition for the field profile. The gyro-backward interaction excited in the beam duct involves strong self-consistent effects and the self-consistent profile is often significantly different than the cold-cavity profile. For this reason, it was chosen to use the self-consistent profile calculated with TWANGlinspec as an initial field profile, instead of the cold-cavity profile.

For the same reason as it is done in TWANGlinspec, the code TWANG-PIC is adapted to

consider a longitudinal profile of wall conductivity (cf. Figure 2.12).

Summary of the models used during the thesis

To summarize, the three codes used throughout this thesis are reported in Table 2.4. The model, the numerical implementation and the consideration of electron beam velocity or energy spread $\Delta\alpha$ and $\Delta\gamma$ respectively, are indicated. The model TWANGlinspec has been adapted during the thesis, the latest version is indicated.

Table 2.4 – List of codes used in this thesis and their main properties. FEM stands for finite elements method, RK for Runge-Kutta and $\Delta\alpha$ and $\Delta\gamma$ for the electron beam velocity and energy spreads, respectively.

Code	Model	Num. implementation	$\Delta\alpha \neq 0$ or $\Delta\gamma \neq 0$
TWANGlinspec	linear and spectral	hybrid FEM	no
TWANGlinspread	linear, time-dependent	FEM+RK	yes
TWANG-PIC	nonlinear, time-dependent	FEM+RK	yes

3 Metallic smooth-wall beam duct

In this chapter, the goal is to study the possible parasitic oscillations that could occur in a realistic smooth-wall beam duct geometry as shown in Figure 3.1. The models are normally applied to study the electron beam-wave interaction in the cavity region. In order to extend the interaction region to the smooth-wall beam duct and spacer regions, the strategy considered was to start with a simple symmetric situation of a cylindrical constant beam duct with a downtaper on the gun side and an uptaper on the cavity side as well as an uniform magnetic field. This situation is represented in Figure 3.2 with continuous lines. From this reference, the metallic wall and the magnetic field profiles were progressively adjusted to simulate a real smooth-wall beam duct (corresponding to a smooth-wall approximation of the TCV dual-frequency gyrotron), represented in dashed lines in Figure 3.2.

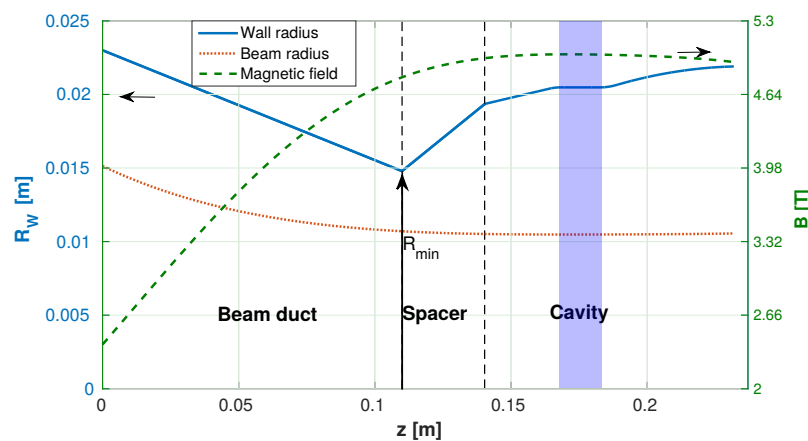


Figure 3.1 – Example of a realistic geometry considered. The usual interaction zone considered is the cavity, the constant radius part highlighted in blue, and its uptaper and downtaper. The goal in this work is to extend it to the beam duct and spacer regions.

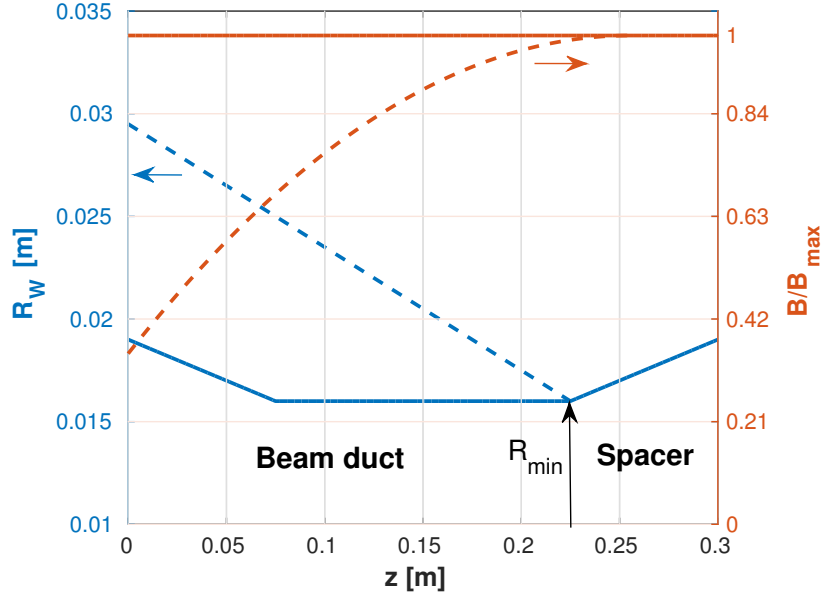


Figure 3.2 – Beam duct geometry and magnetic field profile (normalized to the maximum value B_{\max}). The continuous line corresponds to the starting point, called reference case. The dashed lines correspond to a more realistic smooth-wall beam duct situation.

3.1 Systematic studies

For each situation the starting current curves for different transverse mode were calculated using the TWANGLinspec code. To illustrate the difficulty related to the transverse mode selection, the starting current for four different transverse modes is shown in Figure 3.3 for the reference situation shown with continuous lines in Figure 3.2 and for different values of the constant magnetic field. The continuous line enlightens the minimum starting current for each magnetic field value, thus showing which transverse mode would be excited first. For clarity here, only a reduced selection of transverse modes is shown. The most complete studies, involved more than 1400 transverse modes, justifying the choice of MPI code parallelization discussed in section 2.2.1.

The parametric studies presented in the following focus only on one transverse $TE_{m,p}$ mode for simplicity. The dependencies discussed have been observed with all the transverse modes considered and thus are considered to be valid in general for all transverse modes.

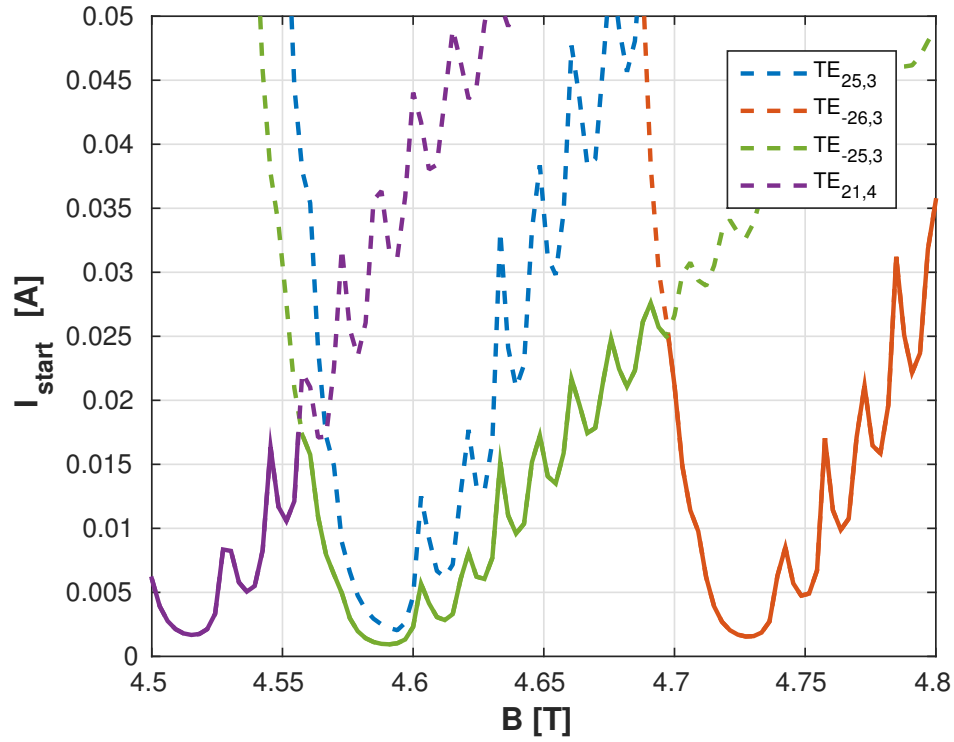


Figure 3.3 – Starting current calculated with the linear code TWANGlinspec for the situation shown in continuous line in Figure 3.2. For each transverse modes, the different local minima correspond to different longitudinal modes (Parameters: $U_c = 75\text{ kV}$, $\alpha = 1.3$, $R_b = 12\text{ mm}$).

3.1.1 Magnetic field profile

The first parametric study focused on the magnetic profile. The situation considered is shown in Figure 3.4. The geometry is kept constant, while the magnetic field profile varies from an uniform case to a more realistic one. The starting current for the transverse mode $\text{TE}_{25,3}$ (one of the mode with the lowest starting current) for these different configurations is shown in Figure 3.5 for a range of magnetic field value (value at the maximum) between 4.5 T and 4.75 T. The inhomogeneity of the magnetic field appears to have two main effects; the increase of the starting current as well as the narrowing of the excitation magnetic field range. This is attributed to the fact that the magnetic field profile reduces the electron beam-wave interaction region.

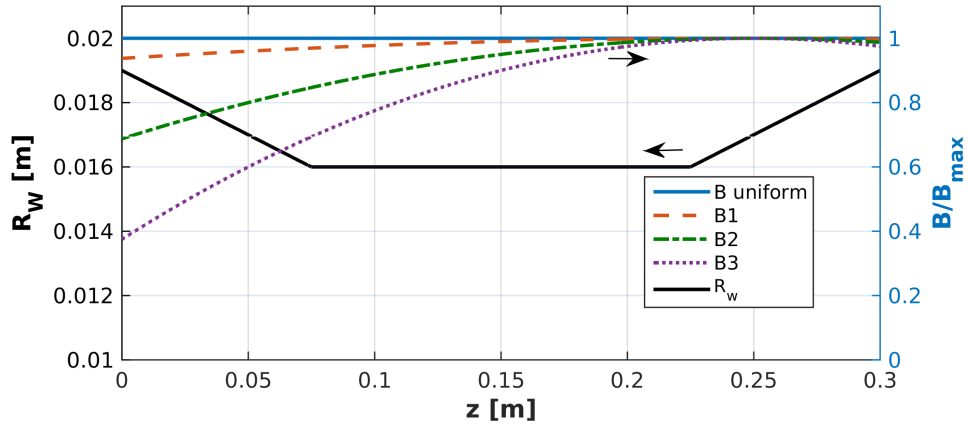


Figure 3.4 – Beam duct geometry and magnetic field profile. The different magnetic field profiles considered in Figure 3.5 are shown with the continuous blue line and the colored dashed lines.

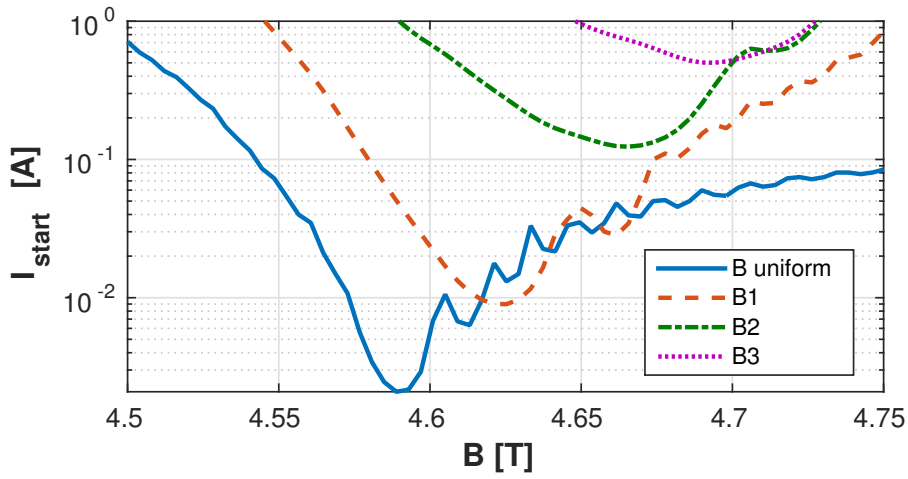


Figure 3.5 – Starting current of the transverse mode $TE_{25,3}$ for the four different magnetic field profiles shown in Figure 3.4 and for a range of external magnetic field values.

3.1.2 Wall radius tapering

An extensive study was also performed by varying the wall radius. As an illustration, the angle θ_1 of the beam duct downtaper is changed from the reference situation $\theta_1 = 0^\circ$ to a more realistic situation $\theta_1 = 5.1^\circ$ or $\theta_1 = 8.5^\circ$, as can be seen in Figure 3.6. Our model neglects the mode conversion to different transverse modes, which could be important for a steeper wall tapering with larger angle θ_1 . A scattering matrix formalism has been used to evaluate the mode conversion. As is shown in the appendix A, even considering the larger angles ($\theta_1 = 8.5^\circ$), the mode conversion is moderate. The starting current calculated for the four angles θ_1 shown in Figure 3.6 are shown for the mode $TE_{25,3}$ for a range of magnetic field between 4.6 T and 4.75 T in Figure 3.7. For this mode, the starting current increases from 500 mA for the reference geometry up to 40 A for the more realistic geometry. Increasing the spacer angle θ_2 (shown in Figure 3.6) leads to a similar increase in the starting current. In this case, this would mean that this specific transverse mode ($TE_{25,3}$) is not excited in a typical gyrotron with a nominal beam current around 40 A. This study shows that the effect of the wall tapering on the starting current is much stronger than the one due to the magnetic field profile inhomogeneity. This has been confirmed with an additional study where the magnetic field profile is kept uniform while the geometry is changed in the same way as in Figure 3.6. In this case, the starting current variation is varying from a few mA for the reference situation to 30 – 40 A for the more realistic situation ($\theta_1 = 8.5^\circ$).

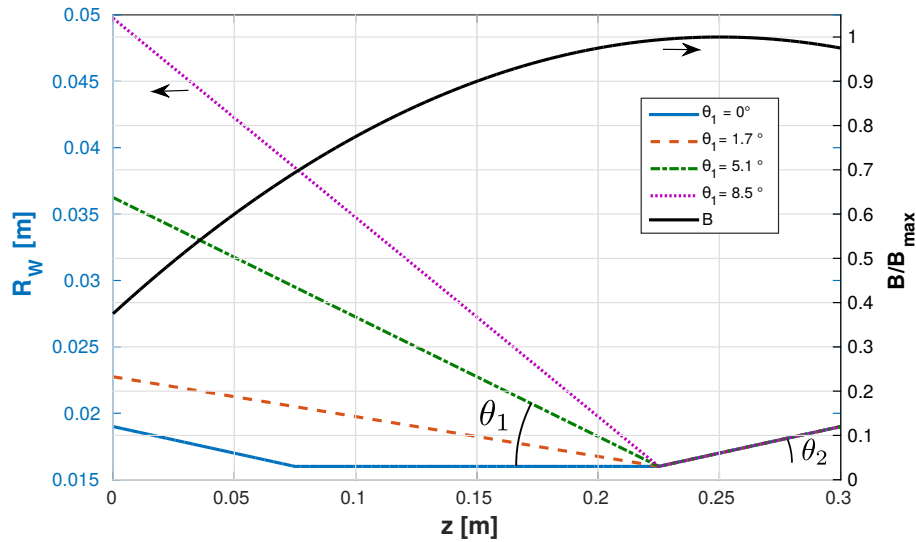


Figure 3.6 – Beam duct geometry and magnetic field profile. The different geometries considered in Figure 3.7 are shown with dashed lines ($\theta_2 = 2.3^\circ$). The magnetic field profile considered here is the magnetic field profile B_3 in figure 3.4.

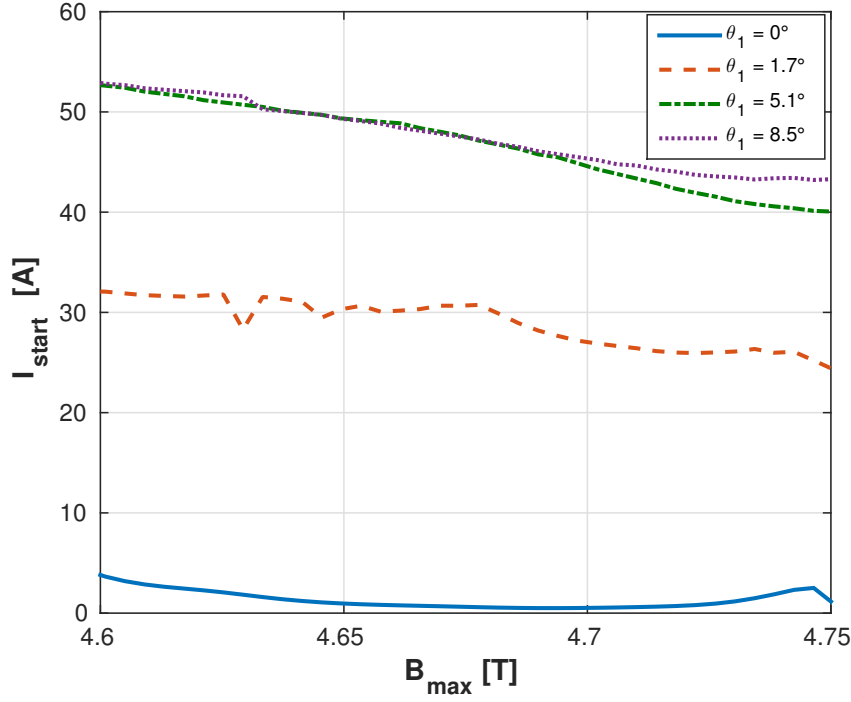


Figure 3.7 – Starting current of the transverse mode $TE_{25,3}$ for the four different geometries shown in Figure 3.6 and for a range of magnetic field values.

These systematic studies led to the more realistic situation shown in the Figure 3.8 d). For this case, and considering an electron beam with no velocity spread (consistent with the underlying assumption made in TWANGlinspec), the starting current for some transverse modes is still lower than the operating beam current of the gyrotron, meaning that they could be excited. This is the case for example for the mode $TE_{17,4}$ whose electric field amplitude and phase profiles are represented along the interaction space in Figure 3.8 a) and b). For this mode the variation of the rf-field phase, with a negative slope in the left conical section, indicates a backward wave. This is the case for all the potentially unstable modes that were found. As an illustration, the cold cavity (i.e. without electron beam) profile is shown with the green line. This profile is completely different from the self-consistent profile, as usually expected for a backward-wave interaction. This observation is very important and demonstrates the need of a self-consistent model, which is often not the case in many models used for studying parasitic oscillations in gyrotron beam ducts [44, 59]. As mentioned before, the interaction is very localized in the spacer region, defined in Figure 3.2. This can be seen in Figure 3.8 c), where the absolute value of the source term in the wave equation (2.26c) ($-iC_3C_0\pi_1$) is shown.

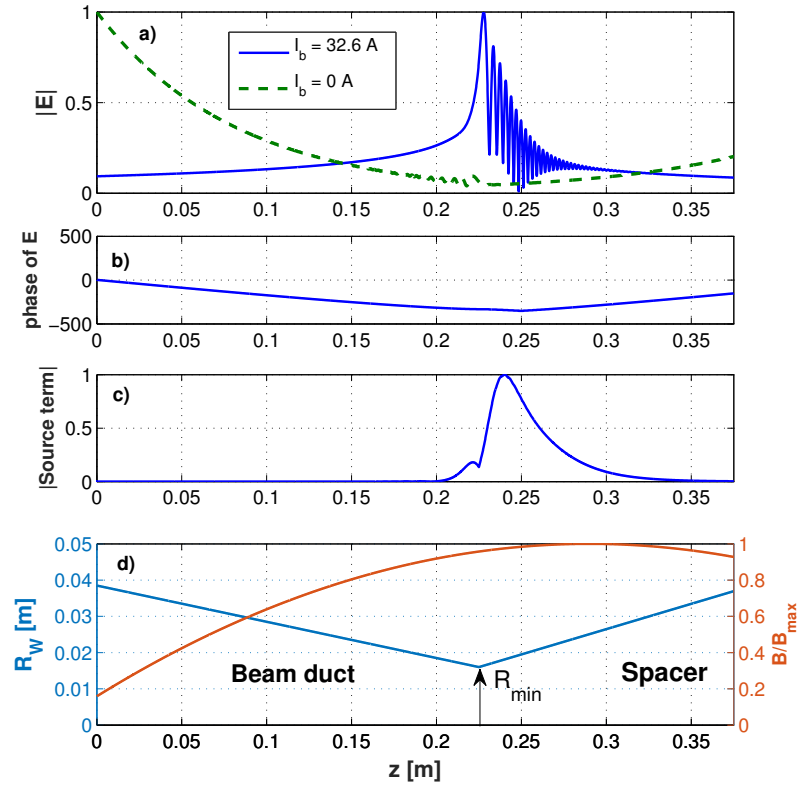


Figure 3.8 – a) and b) Amplitude and phase of the electric field profile for a beam current slightly exceeding the mode ($TE_{17,4}$) starting current. c) Profile of the amplitude of the wave equation source term (2.26c). d) Profiles of the beam-duct and magnetic field profile. (Parameters: $U_c = 75$ kV, $\alpha = 1.3$, $R_b = 10$ mm, $B_{\max} = 4.7$ T)

3.1.3 Magnetic field profile position

The fact that the potentially unstable modes are localized in a narrow region between the beam duct and the spacer suggests that the excitation of these modes strongly depends on the magnetic field value at this position. This can be evaluated by shifting the magnetic field profile in the longitudinal direction. In a real gyrotron, this could be done by translating vertically the gyrotron inside the magnet. For this study a translation of ± 10 mm is considered, as can be seen in Figure 3.9. As reported in Table 3.1, the starting current is increased from 32.6 A to 44.3 A by shifting the magnetic field profile in the direction of the cavity. On the other hand, the starting current decreases to 29.1 A, when the magnetic field profile is shifted in the direction of the beam-duct. However, considering the large number of transverse modes, as will be shown later, when the minimum starting current of a specific mode is increased, the minimum starting current of other modes is reduced. This is the case for the modes $TE_{-9,7}$ and $TE_{7,7}$, as reported in Table 3.1.

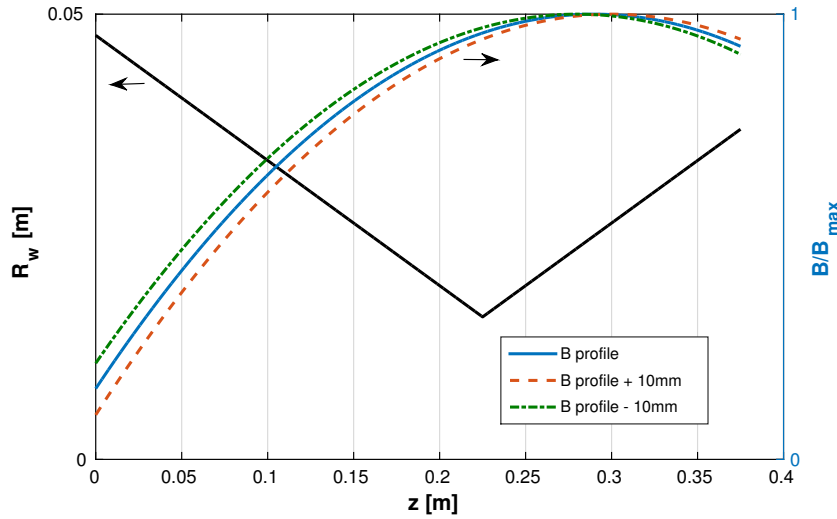


Figure 3.9 – Beam duct geometry and magnetic field profiles considered.

Table 3.1 – Starting current calculated with TWANGlinspec for three $TE_{m,p}$ transverse modes and for the three magnetic field profiles shown in Figure 3.9. The starting current below 40 A are shown in bold and represents the cases where the modes are expected to be excited for a beam current $I_b = 40$ A.

Mode	I_{start} [A]		
	B	B + 10 mm	B - 10 mm
$TE_{17,4}$	32.6	44.3	29.1
$TE_{-9,7}$	41.9	37.7	63.1
$TE_{7,7}$	88.4	43.1	36.4

3.2 Realistic geometry

The next step is to study a "real" smooth-wall situation. For this the geometry of the dual-frequency gyrotron [27] planned on the Tokamak à Configuration Variable (TCV) [100] is chosen. The beam duct implemented in this gyrotron consists of stacked copper and dielectric rings. The very complex asymmetric geometry, including strong discontinuities in the wall radius between the rings cannot be simulated with our models. For this reason, a smooth-wall approximation following the wall radius envelope is considered for the beam duct part, while the spacer and cavity wall profiles correspond to the real situation (cf. thick red line in Figure 3.10 for a gyrotron including a corrugated beam duct). The mode conversion due to the wall

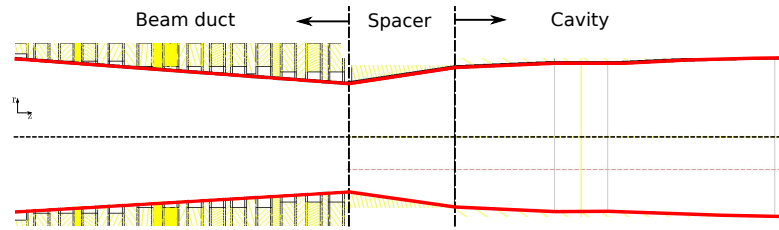


Figure 3.10 – Longitudinal cross-section for a high-power gyrotron including a stacked copper and dielectric rings beam duct. The thick red line indicates the geometry considered in the simulations: a smooth-wall approximation of the beam duct envelope and the real spacer and cavity profiles.

radius tapering has been evaluated using a scattering matrix model [101], for the geometry shown in Figure 3.11. With the spurious $TE_{23,7}$ mode excited in the spacer ($\theta = 8.5^\circ$), the mode conversion in other $TE_{23,n}$ modes is of the order of 15%. These results are detailed in appendix A. In a second phase, the exact geometry of the cavity is also included. In the following this geometry is called the extended beam duct/spacer/cavity region.

Table 3.2 – Parameters used for the starting current calculations (note that 1400 transverse modes are considered).

Parameters	Value
Magnetic field maximum	4.98 T
Cathode voltage	78 kV
Pitch angle (no pitch angle spread)	1.3
Wall conductivity	$1.45 \cdot 10^7$ S/m
Beam radius	10.48 mm
TE modes considered	$TE_{m,n}$ with $m \in [-35, 35]$ and $n \in [1, 20]$

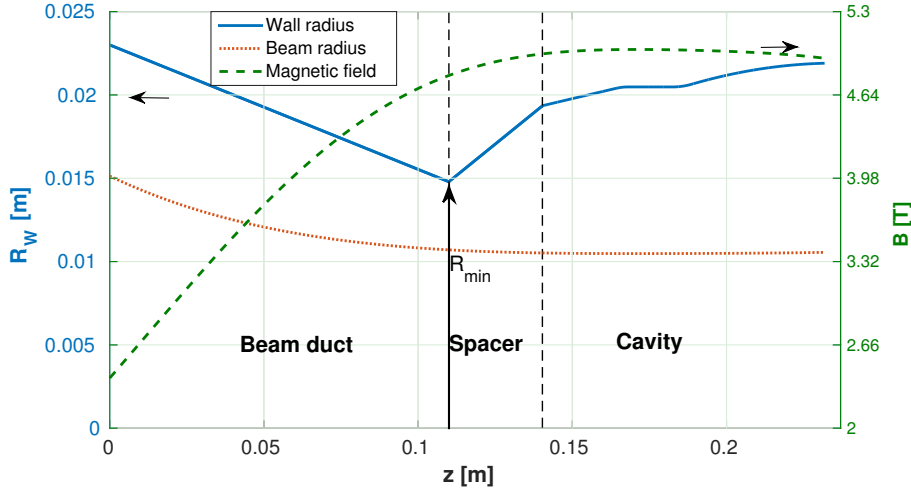


Figure 3.11 – Geometry and magnetic field profile considered. The spacer and cavity parts correspond to the geometry of the dual-frequency gyrotron for TCV. A smooth-wall approximation following the wall radius envelope of the beam duct is done. The magnetic field profile is shown in dashed lines. The beam radius profile, defined by the average guiding center radius, is shown with the red-dotted line.

Beam duct plus spacer

Concentrating first on the beam duct and spacer structure, choosing the high frequency operating point of the dual-frequency gyrotron (cavity mode $TE_{26,7}$ at 126 GHz), whose parameters are reported in Table 3.2 and scanning over more than 1400 transverse TE modes, 11 modes are found to have a starting current below 40A, the nominal operating beam current. All these modes are backward waves and have their electric field maximum situated in the spacer region as indicated in Figure 3.12. The starting currents and frequencies of these modes are shown in Figure 3.13. Their frequencies are higher than their cutoff frequencies at the minimum radius R_{min} . They are thus able to propagate through the beam duct without being reflected. The electric field profile for the transverse mode $TE_{16,4}$ with the lowest starting current (highlighted in Figure 3.13) is shown in Figure 3.14. As mentioned, the electric field amplitude is peaked close to the minimum radius part and the negative slope in the phase profile confirm the gyro-backward wave interaction type.

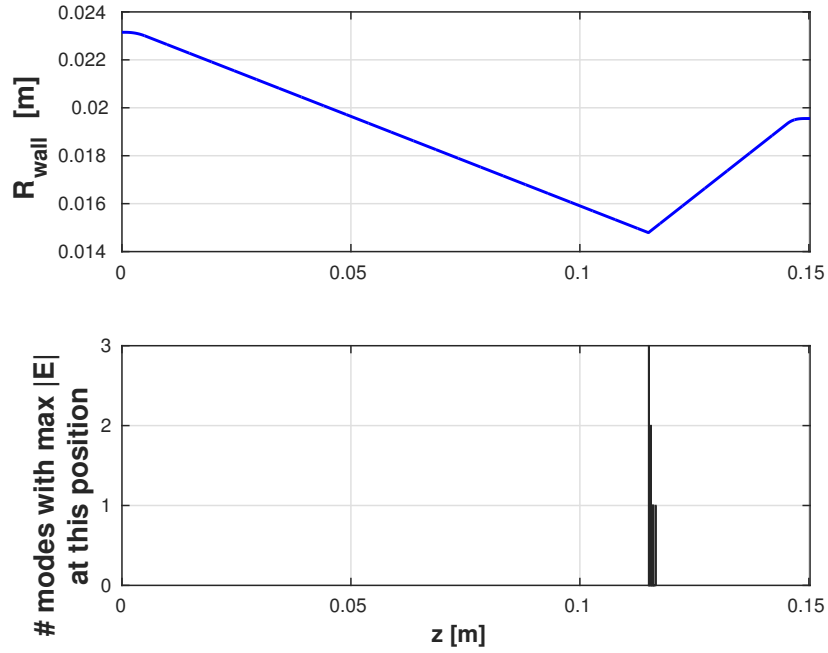


Figure 3.12 – a) Geometry of the interaction region. b) Histogram representing the position of the electric field maximum for all the transverse modes with $I_{\text{start}} < 40$ A.

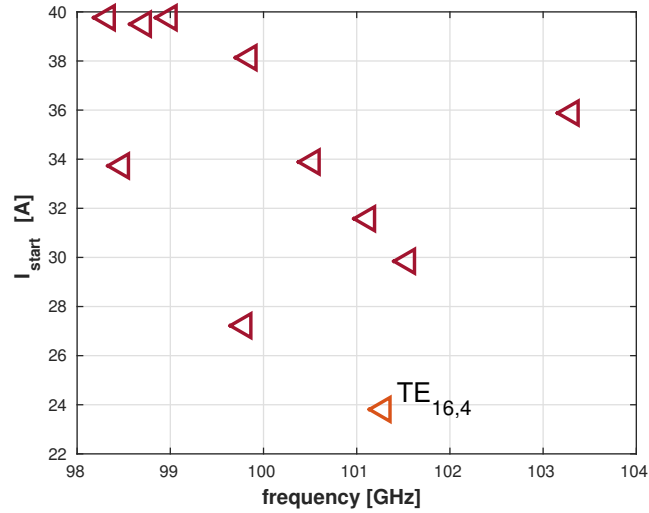


Figure 3.13 – Starting current and frequency of the modes excited in the spacer region. All these modes are gyro-backward modes and have their frequency higher than the mode cutoff frequency at the minimum radius, meaning that the backward modes are propagating towards the beam-duct direction. The mode $\text{TE}_{16,4}$ is shown with the orange triangle.

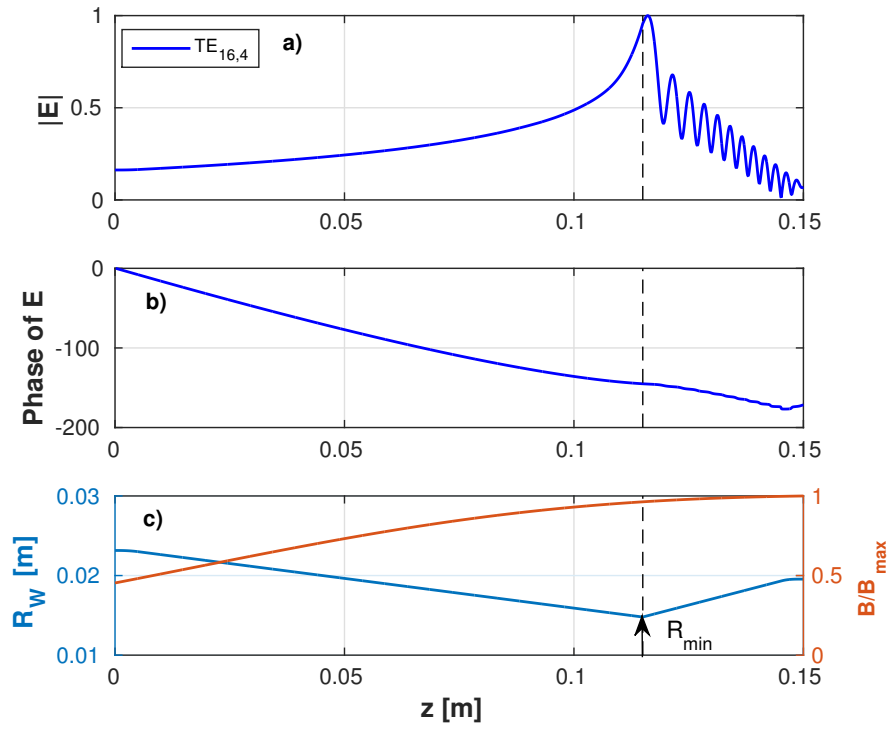


Figure 3.14 – a) Amplitude of the electric field profile for the transverse modes $TE_{16,4}$ for a current slightly exceeding its starting current ($I_{start} = 23.8A$). b) Phase of the electric field profile. c) Interaction space and magnetic field profiles.

Extended beam duct/spacer/cavity region

The same study, scanning over more than 1400 transverse TE modes, was done for the structure including the cavity. For this situation, 328 modes are found to have a starting current below 40A. Ninety-one percent of these modes are backward waves and around 70% have their electric field maximum situated in the spacer region, as indicated in Figure 3.15. The starting currents and frequencies of these 328 modes are shown in Figures 3.16 and 3.17. The modes excited in the spacer region are selected and shown in Figure 3.16. All these modes are gyro-backward modes. Most of the modes below 100 GHz have a frequency higher than their cutoff frequency at the minimum radius R_{\min} . They are thus able to propagate through the beam duct while the others are reflected back to the spacer/cavity region. The modes excited after the spacer, in the cavity region, are shown in figure 3.17. Both forward and backward propagating mode can be found. The mode indicated with the red circle is the gyrotron operating mode $TE_{26,7}$ at 126 GHz.

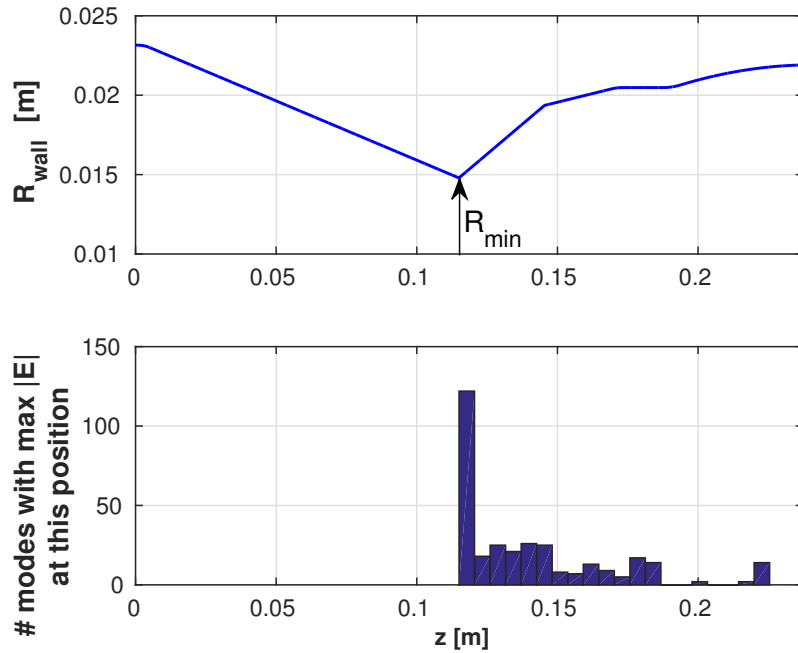


Figure 3.15 – a) Geometry of the interaction region. b) Histogram representing the position of the electric field maximum for all the transverse modes with $I_{\text{start}} < 40A$.

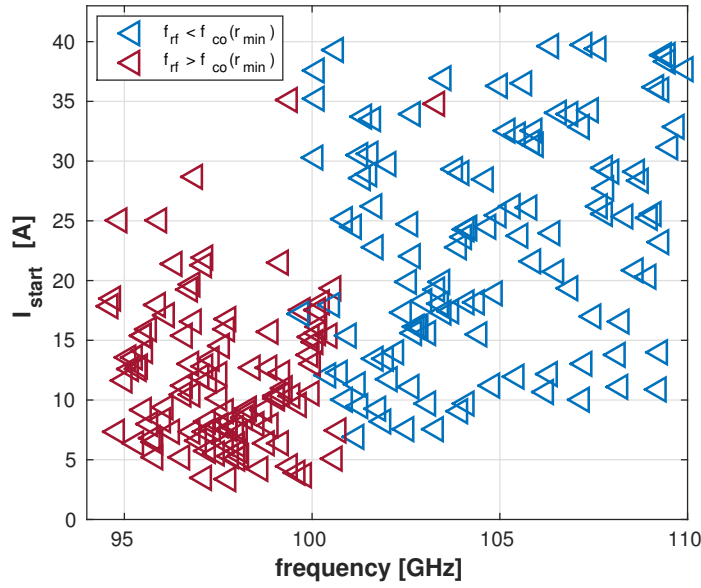


Figure 3.16 – Starting current and frequency of the modes excited in the spacer region. All these modes are gyro-backward modes. Almost all the modes below 100 GHz (indicated in red) have a frequency higher than the mode cutoff frequency at the minimum radius, meaning that they propagate towards the beam duct direction. The other are reflected towards the gyrotron cavity direction.

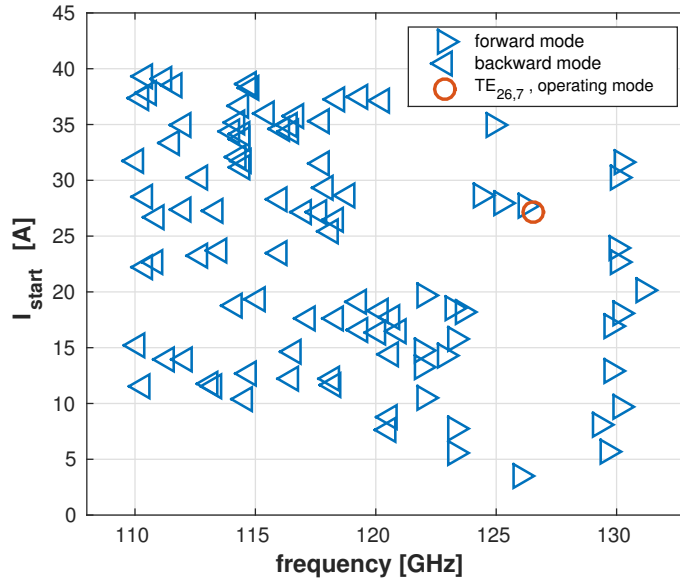


Figure 3.17 – Starting current and frequency of the modes excited in the cavity region. The direction of the arrow indicate the propagation direction. All these modes have a frequency lower than the mode cutoff frequency at the minimum radius, meaning that the backward propagating modes are reflected towards the gyrotron cavity direction. The operating mode $TE_{26,7}$ is shown with the red circle.

As an illustration, the electric field amplitude and phase for two transverse modes excited in the spacer, the $TE_{16,4}$ (at 100.7 GHz) and $TE_{19,4}$ (at 102.7 GHz) are shown in Figure 3.18 for a beam current slightly exceeding their starting current and for the parameters reported in Table 3.2 ($I_{\text{start}}(TE_{16,4}) = 7.5\text{ A}$, $I_{\text{start}}(TE_{19,4}) = 22.4\text{ A}$). Both modes have their electric field peaked in the spacer region and exhibit an oscillation with a large longitudinal wave number in the spacer/cavity region. These are backward waves but only the $TE_{16,4}$ is propagating in the beam duct. This is due to the fact that its frequency is higher than the cutoff frequency at the minimum radius ($f_{rf} = 100.7\text{ GHz} > f_{co}(r_{\min}) = 100.3\text{ GHz}$). On the contrary, the frequency of the mode $TE_{19,4}$ is lower than the cutoff frequency ($f_{rf} = 102.7\text{ GHz} < f_{co}(r_{\min}) = 111.8\text{ GHz}$) and is thus reflected back towards the cavity. Within the assumption of this model (no velocity spread), even though these modes are excited in the spacer region, they are still interacting with the beam in the cavity region. Due to this extended interaction region, the starting current for all the transverse modes is reduced. This is qualitatively consistent with the linear theory of gyro-backward waves in a homogeneous interaction space [75], where their starting current significantly decrease when the interaction length is increased.

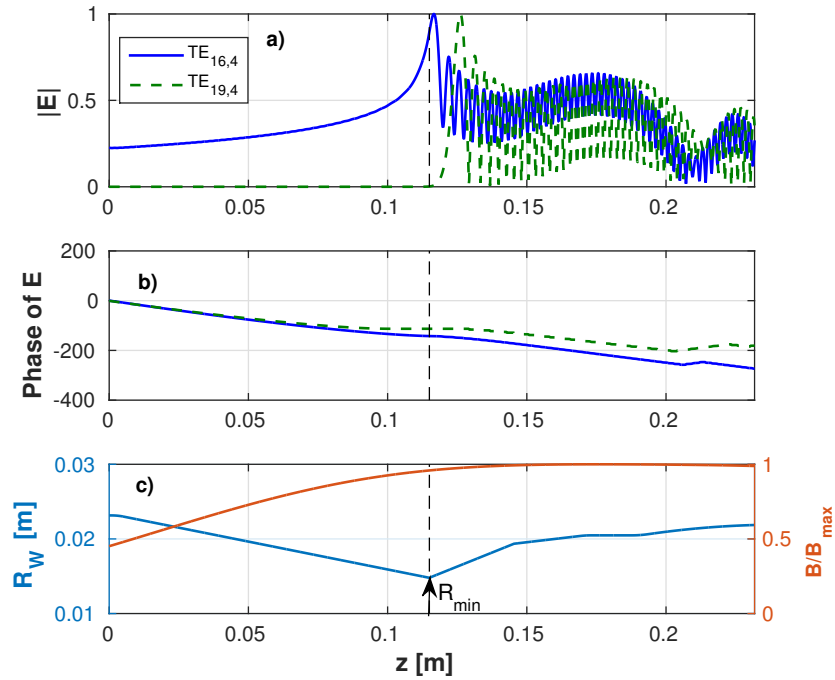


Figure 3.18 – Extended simulation: beam duct + spacer + cavity. a) Amplitude of the electric field profile for two transverse modes for a current slightly exceeding their starting current. b) Phase of the electric field profile. c) Interaction space and magnetic field profiles.

Qualitatively consistent with these observations, experimentally, damages on the last rings close to the spacer have been observed [47]. They are indications that parasitic instabilities, if excited, have the maximum rf-field in this region.

3.3 Nonlinear simulations

3.3.1 Effect on the electron beam quality

To evaluate the rf-power of the parasitic oscillations and their effect on the electron beam and on the operating mode operation, the monomode nonlinear code TWANG-PIC [67] was used. Notice that for these studies the non-linear code TWANG [72] could also be used and would lead to the same results. This study involves two consecutive simulations. First, the parasitic mode $TE_{16,4}$, which has been found to have the smallest starting current (see Figure 3.13), is simulated in either the beam duct plus spacer or the extended beam duct/spacer/cavity regions (cf. 3.11). This simulation is stopped once the non-linear stationary state is reached. The resulting particle distribution in energy and velocity at the entry of the cavity region (cf. Figure 3.11) is saved and used as an initial beam state for the second simulation. The second simulation is a usual cavity interaction calculation, considering only the cavity region and the transverse mode $TE_{26,7}$, the high-frequency (126 GHz) operating mode for the dual-frequency gyrotron. The parameters used in both simulations are listed in Table 3.3. $P_{\text{rad}}(t = 0)$ is the initial condition on the rf-power radiated. This parameter can be tuned to simulate soft-excitation regime, where the initial power is lower than the radiated power when the stationary state is reached ($P_{\text{rad}}(t = 0) < P_{\text{rad}}(t_{\text{stat}})$) or the hard-excitation regimes in the other case ($P_{\text{rad}}(t = 0) > P_{\text{rad}}(t_{\text{stat}})$). The hard-excitation regime is used to access high-efficiency regime in high-power gyrotrons [102], where the oscillation is sustained only if a sufficient rf-power is previously generated. Experimentally, this regime is reached first by operating in the soft-excitation regime, in order to get the sufficient rf-power, and then by changing the beam parameters to access the hard-excitation regime. In this study, only the soft-excitation regime is studied and a very low initial rf-power radiated is chosen $P_{\text{rad}}(t = 0) = 0.1 \text{ mW}$.

Table 3.3 – Parameters used for the nonlinear simulations. For the pitch angle and beam radius, the value is given at the middle of the cavity, where the magnetic field is maximum.

Parameters	Value
Magnetic field maximum	4.98 T
Cathode voltage	78 kV
Pitch angle (no pitch angle spread)	1.3
Beam current	40 A
Wall conductivity	$1.45 \cdot 10^7 \text{ S/m}$
Beam radius	10.48 mm
$P_{\text{rad}}(t = 0)$	0.1 mW

Beam-duct plus spacer

The beam-duct plus spacer region is considered for the first simulation. The result of the nonlinear simulation, when the saturation is reached is shown in Figure 3.19. The power radiated in the $TE_{16,4}$ mode is 28 kW. It is noteworthy that the electric field profile obtained is similar to the electric field profile obtained close to the starting current with the linear

simulation (see Figure 3.14). The particle energy and velocity distributions taken at the entry of the cavity part ($z = 0.145$ m, indicated with the dashed lines in Figure 3.19) are reported in Figure 3.20. The relative spread in energy and parallel momentum are respectively $\Delta\gamma = 0.3\%$ and $\Delta p_z = 0.5\%$ (calculated with the standard deviation: $\Delta\gamma = \sqrt{1/N \sum_{i=1}^N (\gamma_i - \bar{\gamma})^2}$, with $\bar{\gamma}$ being the mean value). These energy and velocity distributions are then used at the beginning of the cavity region to evaluate their effect on the operating mode TE_{26,7}. The radiated power simulated with these distributions is reported in Figure 3.21 along with a simulation with an ideal electron beam (without spread). The relative power reduction is around 5%.

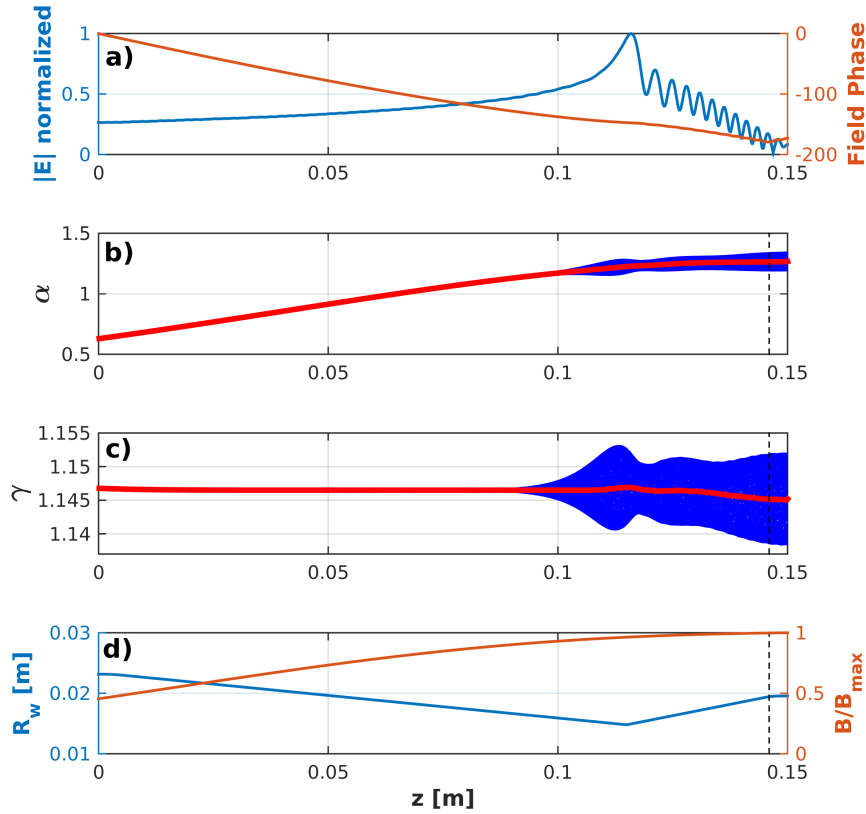


Figure 3.19 – Limited simulation: beam duct + spacer only. a) Amplitude and phase of the electric field profile of TE_{16,4} mode. b) and c) Particle distribution in the pitch angle and energy (Lorentz factor) The red lines represent the average values. d) Interaction space and magnetic field profiles. The dashed lines indicate where the particle distributions are taken for evaluating their effect on the gyrotron operating mode.

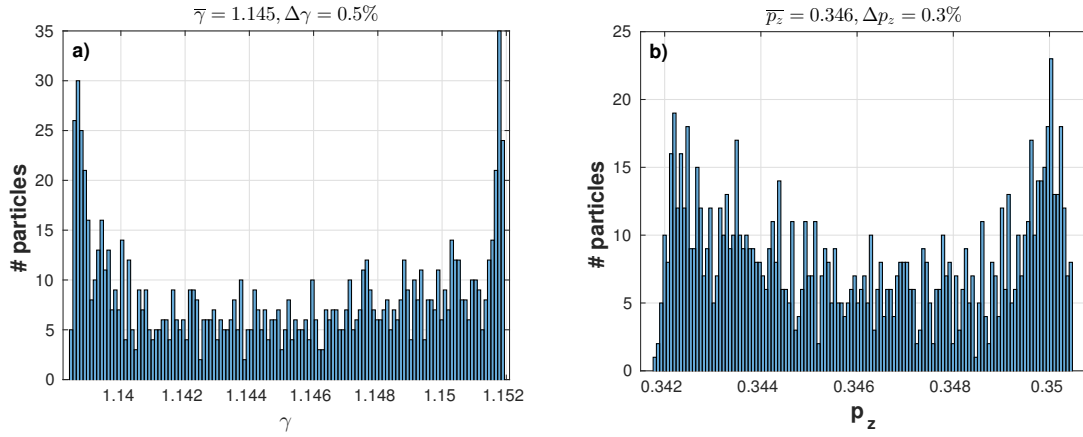


Figure 3.20 – Limited simulation: beam duct + spacer only. Energy particle distribution a) and parallel momentum particle distribution b) at $z = 0.145\text{m}$ when the saturation of the parasitic mode $\text{TE}_{16,4}$ is reached. This position corresponds to the entry of the cavity region, indicated with the dashed line on Figure 3.19.

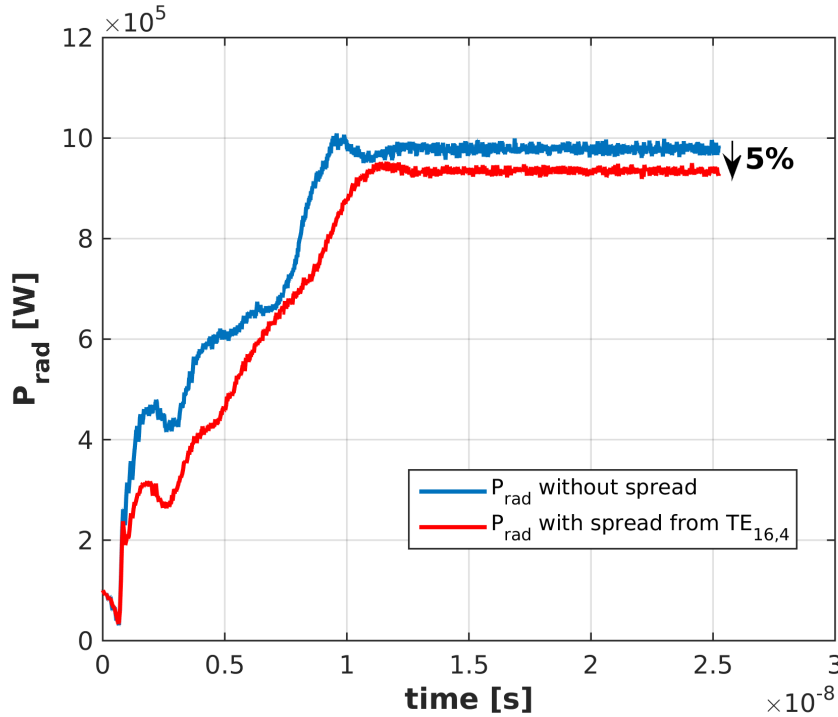


Figure 3.21 – Radiated power calculated with TWANG-PIC for the operating mode $\text{TE}_{26,7}$ of the TCV dual-frequency gyrotron. The region simulated is the cavity indicated in Figure 3.11 and the parameters are those listed in Table 3.3. The blue curve is the radiated power when an ideal electron beam is considered (without any velocity or energy spread). The red curve is the radiated power with the electron beam affected by the parasitic mode $\text{TE}_{16,4}$ shown in Figure 3.19 for the particle energy and velocity distributions reported in Figure 3.20.

Extended beam duct/spacer/cavity region

The same study is done considering the extended beam duct/spacer/cavity region (cf. Figure 3.11). The electric field profile and the energy and velocity particle distributions, once the saturation is reached, are reported in Figure 3.22. Again, the electric field profile is similar to the electric field profile from the linear simulation (cf. Figure 3.18). The energy and velocity particle distributions at the position $z = 0.145\text{ m}$ are reported in Figure 3.23. The relative spread in energy and parallel momentum are respectively $\Delta\gamma = 1.1\%$ and $\Delta p_z = 0.7\%$. The energy spread is significantly larger than in the case with the beam duct plus spacer region (cf. Figure 3.20). There is a larger number of particle with a lower energy. This indicates that more particle transferred their energy to the wave in this case. Indeed in the first case (beam duct plus spacer), the radiated power simulated is around 28 kW, while in the second case (extended region) the radiated power is around 190 kW. From the operating mode $\text{TE}_{26,7}$ simulation in the cavity part only, the expected power loss is around 40% when this distribution is taken into account (cf. Figure 3.24).

Compared to the previous case (cf. Figure 3.21), this shows that if the parasitic mode interaction region is extended to the cavity, its effect on the electron beam and thus on the gyrotron operation is much more serious. One should emphasize that this study is a rough approximation of the parasitic effect. The treatment of the interaction extended to the cavity should be treated self-consistently with a multimode code, taking into account the transverse mode competition with the operating mode. In a multimode model these modes might not be excited. Such a study is presented later, in section 3.3.3.

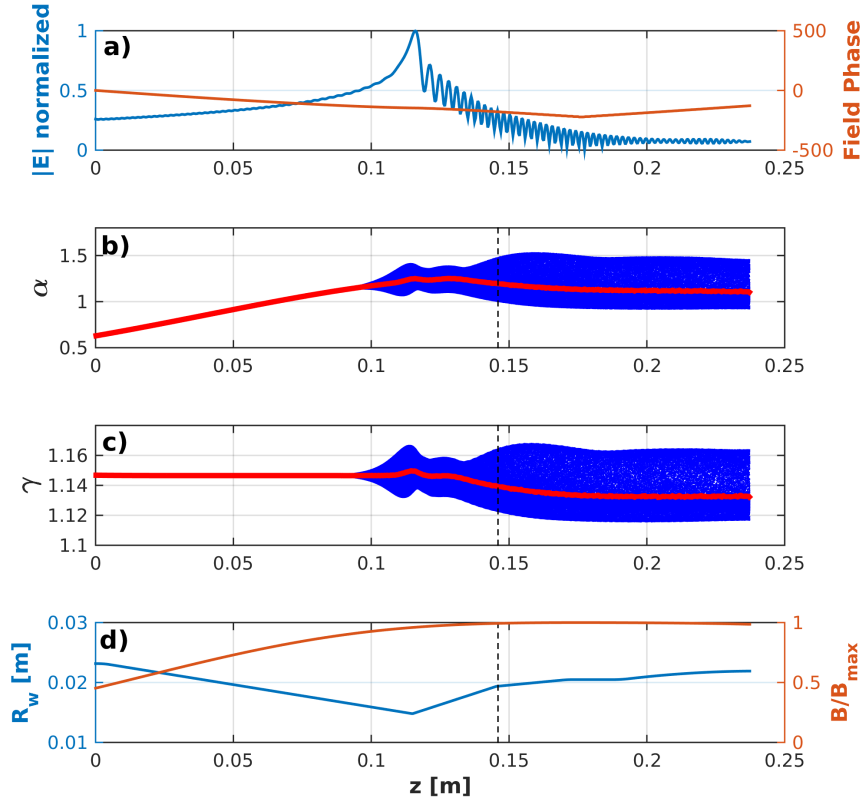


Figure 3.22 – Extended simulation: beam duct + spacer + cavity. a) Amplitude and phase of the electric field profile of $TE_{16,4}$ mode. b) and c) Particle distribution in the pitch angle and energy (Lorentz factor). The red lines represent the average values. d) Interaction space and magnetic field profiles. The dashed line indicates where the particle distribution is taken for evaluating their effect on the operating mode.

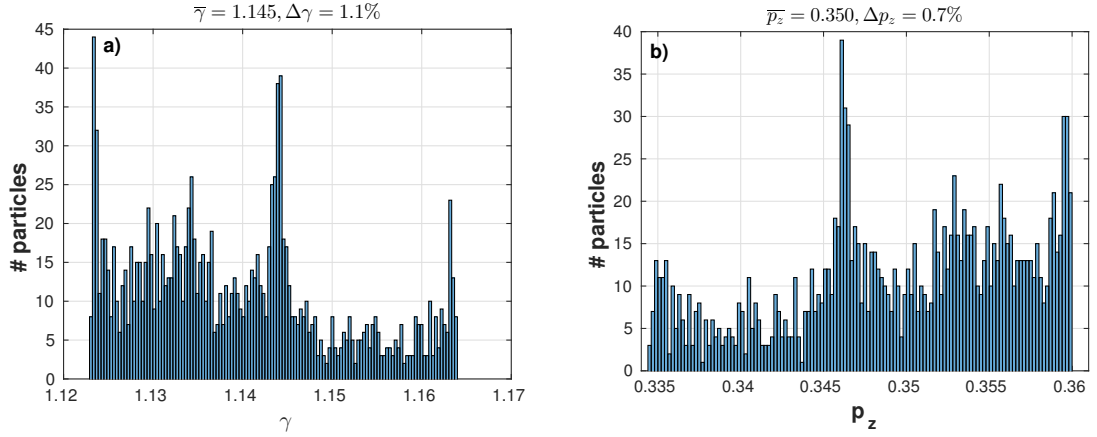


Figure 3.23 – Extended simulation: beam duct + spacer + cavity. Particle distribution in the energy a) and parallel momentum b) at $z = 0.145\text{m}$. This position corresponds to the entry of the cavity region, indicated with the dashed line on Figure 3.22, and when the saturation is reached.

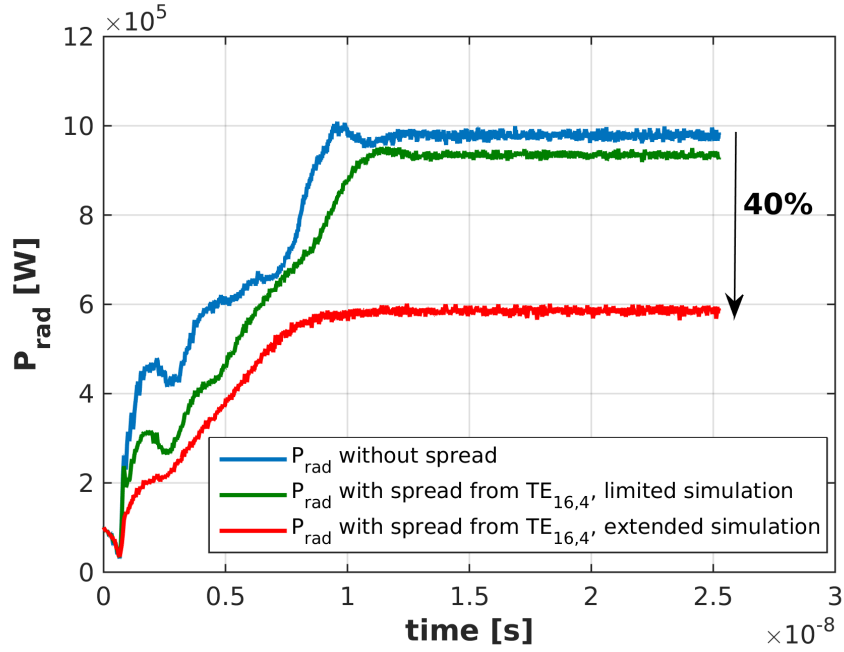


Figure 3.24 – Radiated power calculated with TWANG-PIC for the operating mode $\text{TE}_{26,7}$ of the TCV dual-frequency gyrotron. The region simulated is the cavity indicated in Figure 3.11 and the parameters are those listed in Table 3.3. The blue curve is the radiated power when an ideal electron beam is considered (without any velocity or energy spread). The red curve is the radiated power with the electron beam affected by the parasitic mode $\text{TE}_{16,4}$ shown in Figure 3.22 and with the particle energy and velocity distributions reported in Figure 3.23. To facilitate the comparison, the power radiated with the electron beam affected by the parasitic mode $\text{TE}_{16,4}$ (limited simulation) from figure 3.19 is shown in green.

3.3.2 Velocity spread effect

In the two studies presented above, the parasitic rf power is exceeding 28kW in the beam-duct plus spacer case (cf. Figure 3.19) and 190kW in the extended case (cf. Figure 3.22). Such rf-power levels from parasitic oscillations were never observed experimentally.

Compared to a gyrotron mode excited in the cavity of a gyrotron, the parasitic modes excited in the spacer region as shown in Figure 3.18 have an important parallel wave-vector component k_z . This can be directly deduced from the fast longitudinal oscillation of their electric field in the spacer plus cavity region. Recalling that the resonant frequency of the wave is given by

$$\omega_{\text{rf}} \approx \frac{\Omega_c}{\gamma} + k_z v_{\parallel}, \quad (3.1)$$

with Ω_c the cyclotron frequency, γ the Lorentz factor and v_{\parallel} the electron parallel velocity. Because of the non-negligible parallel wave-vector, the Doppler shift term could have some importance. It suggests that these modes are more sensitive to an electron velocity spread than a normal cavity mode for which k_z is very small. This was verified by using the nonlinear code TWANG-PIC to simulate the parasitic mode $\text{TE}_{16,4}$ and the operating mode $\text{TE}_{26,7}$ for the extended interaction region (cf. Figure 3.18 c), for nominal electron beam parameters ($I_b = 40\text{A}$, $\alpha = v_{\perp} / v_{\parallel} = 1.3$ in the cavity) and for different values of the electron pitch angle spread (no energy spread) at the entry of the interaction region ($z_{\text{in}} = 0$). The rf-power generated for four different spreads in the pitch angle α is shown in Figure 3.25. As expected, due to the large upshift for the parasitic mode, the rf power is much more affected by the velocity spread than the operating mode. For a relative rms alpha-spread of 3.8% at the entry of the interaction region (a typical pitch angle spread in electron gun designs) the parasitic mode is no more excited while the operating mode power is reduced by only 3%.

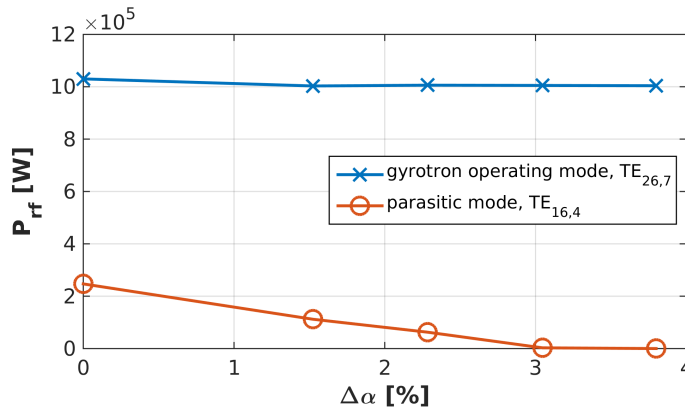


Figure 3.25 – Rf-power of the nominal $\text{TE}_{26,7}$ and the parasitic $\text{TE}_{16,4}$ modes calculated with the monomode nonlinear code TWANG-PIC for different pitch factor spread. The interaction region used is the extended beam duct/spacer/cavity region.

3.3.3 Multimode simulations

This strong dependency on velocity spread was also observed with the nonlinear and multimode code EURIDICE [68]. A multimode model permits also to potentially fully solve the problem including the whole interaction and considering both the parasitic mode excited in the spacer and the cavity modes in a single simulation. For this study, the 1MW-170GHz European gyrotron [8, 103] was considered (cf. Figure 3.26). A list of 16 spurious "spacer" modes, with frequencies around 138 GHz, have been selected with TWANGlinspec. They are listed in Table 3.4.

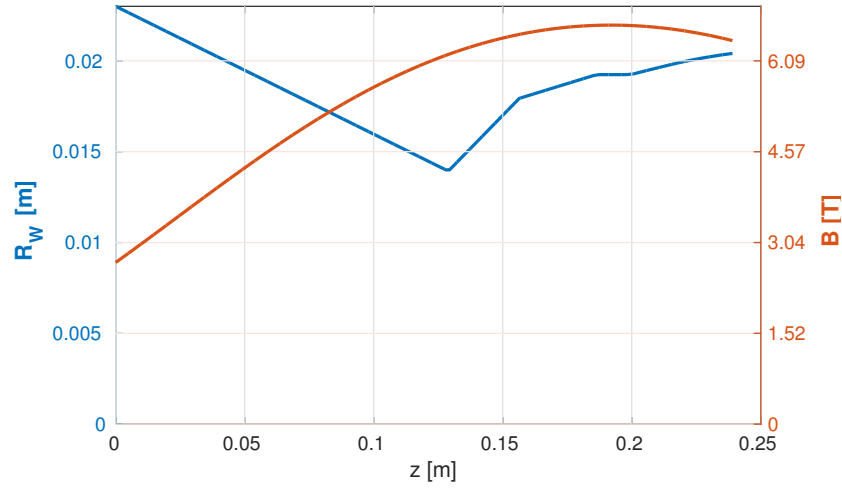


Figure 3.26 – Interaction space and magnetic field profiles corresponding to the 1MW-170GHz European gyrotron for ITER. The interaction space includes a smooth-wall approximation of the beam duct and the real spacer and cavity geometries.

Table 3.4 – List of parasitic spacer modes selected with TWANGlinspec for the multimode simulations with EURIDICE.

m,p (TE _{m,p})	20,5	-20,6	22,5	-21,6	21,5	22,6	23,5	-19,6
I _{start} [A]	4	5.1	5.1	5.3	5.5	5.5	5.7	5.9
m,p (TE _{m,p})	-12,8	-22,6	21,6	-17,7	0,13	-19,7	13,9	0,15
I _{start} [A]	6.2	6.3	9.4	9.6	10.8	12.4	19.7	24.3

The results from the EURIDICE multimode start-up simulations are reported in Figures 3.27 and 3.28 for two different pitch angle spread values. For values of the accelerating voltage ranging from 40kV to 80kV, the power radiated at the output of the cavity is calculated. In the simulations reported in Figure 3.27, 34 standard cavity competing modes have been considered. It predicts the excitation of the operating mode TE_{32,9} at the nominal acceleration voltage ($V_{\text{beam}} = 75\text{kV}$). For the simulations presented in Figure 3.28, the 16 spurious "spacer" modes listed in Table 3.4 have been added in the simulations. In this case, the spurious TE_{22,6} mode is excited together with the operating TE_{32,9} mode for the nominal acceleration voltage, leading to a decrease on the order of 200 kW in the radiated power of the operating mode (from

Chapter 3. Metallic smooth-wall beam duct

950kW to 750kW). This is another indication that the parasitic modes, if excited, could have a significant effect on the main interaction. These simulations also showed that the mode competition plays an important role and that only one of the parasitic modes is excited along with the operating mode. This surviving mode is part of the most unstable (lowest starting current) modes calculated with TWANGlinspec.

On the other hand, when a 25% spread in the pitch angle is considered, no parasitic mode is excited and no effect is seen on the operating mode.

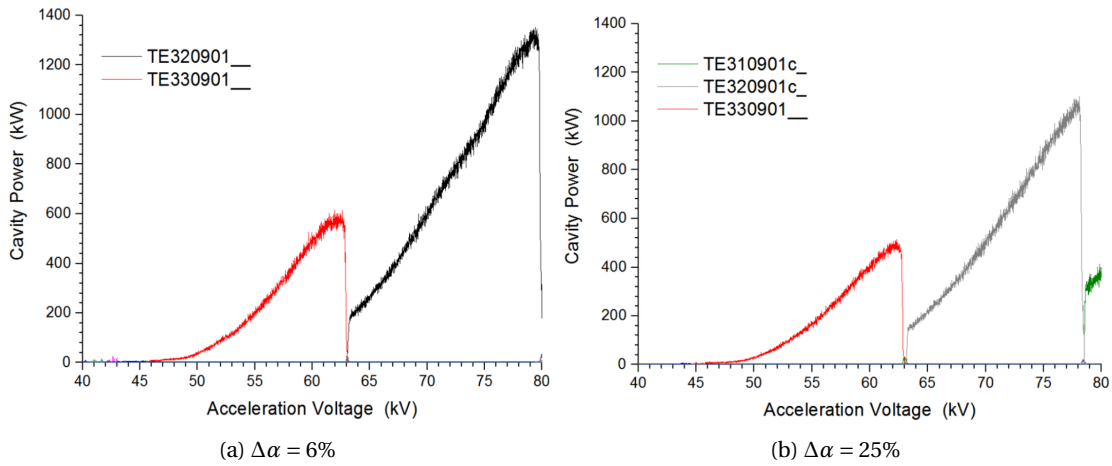


Figure 3.27 – EURIDICE simulation results. 34 standard cavity competing modes are simulated for 6% α spread (right) and 25% α spread (left).

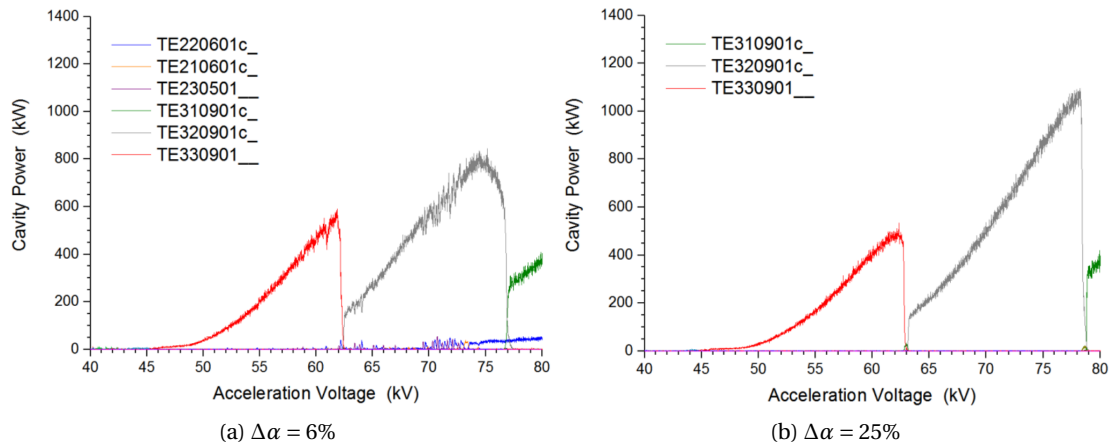


Figure 3.28 – EURIDICE simulation results. 34 standard cavity competing modes and the 16 spurious modes from Table 3.4 are simulated for 6% α spread (right) and 25% α spread (left).

Some questions still need to be investigated, such as the choice of transverse modes to include in the multimode simulations, which have an impact on the simulation results. Ideally, all

the potentially unstable parasitic modes identified with TWANGlinspec (more than 500 in this case) should be included in the simulation. This is currently not feasible in a multimode simulation.

The much larger velocity spread dependency of the parasitic, compared to the cavity modes indicates that the linear model, TWANGlinspec, neglecting this spread is underestimating the minimum starting current compared to the case in which the velocity spread would be taken into account. Based on this consideration, if for some beam duct geometry and properties, using TWANGlinspec, the minimum starting current of all possible TE modes would be above the nominal operating current, than this would be even more valid when velocity spread would be included. In order to evaluate quantitatively this dependency, the linear code TWANGlinspread was developed and the results are presented in the following section.

3.4 Velocity spread effect on the starting current

As already mentioned, the code TWANGlinspread has been developed within a master project [86]. The model used in the linear code TWANGlinspread and its numerical implementation have been presented in section 2.4. The main results are presented here as well as additional simulation results.

The code has been validated following the same strategies as in TWANGlinspec. First, cavity simulations for the DNP gyrotron have been performed and both the nonlinear code TWANG, for the wave growth rate in the linear initial phase, and TWANGlinspec, for the starting current, have been used for the validation. The details about the validation are reported in [86]. In a second phase, the code was applied for beam duct situations with an ideal electron beam and compared to the results from TWANGlinspec. For the reference geometry with a uniform magnetic field shown in Figure 3.29, the starting current calculated for the mode $TE_{25,3}$ is shown in Figure 3.30 for a range of magnetic field values. On top of the figure, the normalized detuning (defined in equation (2.24)), gives an indication on the backward (negative detuning) or forward (positive detuning) interaction regions. It has to be noted that the only difference in the model between the two codes is the rf-magnetic field neglected in TWANGlinspec. In TWANGlinspread, the effect of the rf-magnetic field could be assessed by either considering its contribution or not. It has been shown that the rf-magnetic field effect is negligible close to cut-off and becomes more important away from cutoff. Nevertheless, the starting current are in a good agreement over the whole magnetic field range considered.

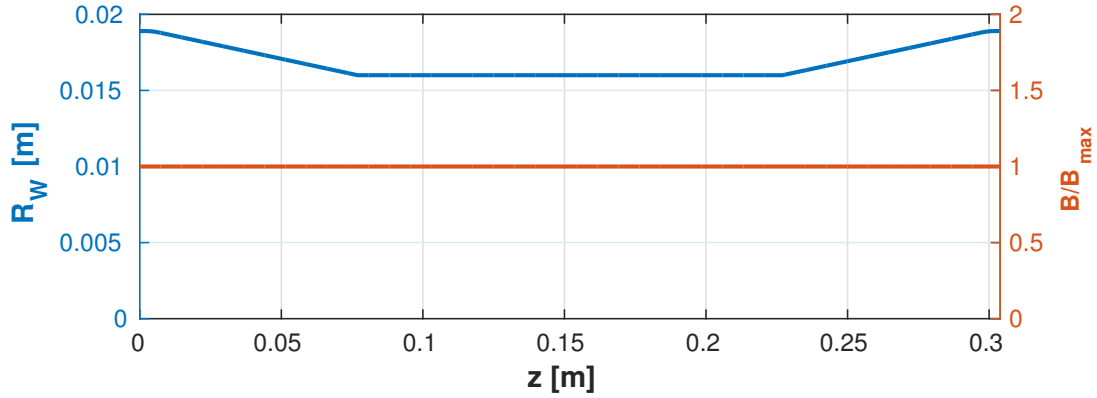


Figure 3.29 – Interaction region and magnetic field profile for the reference situation.

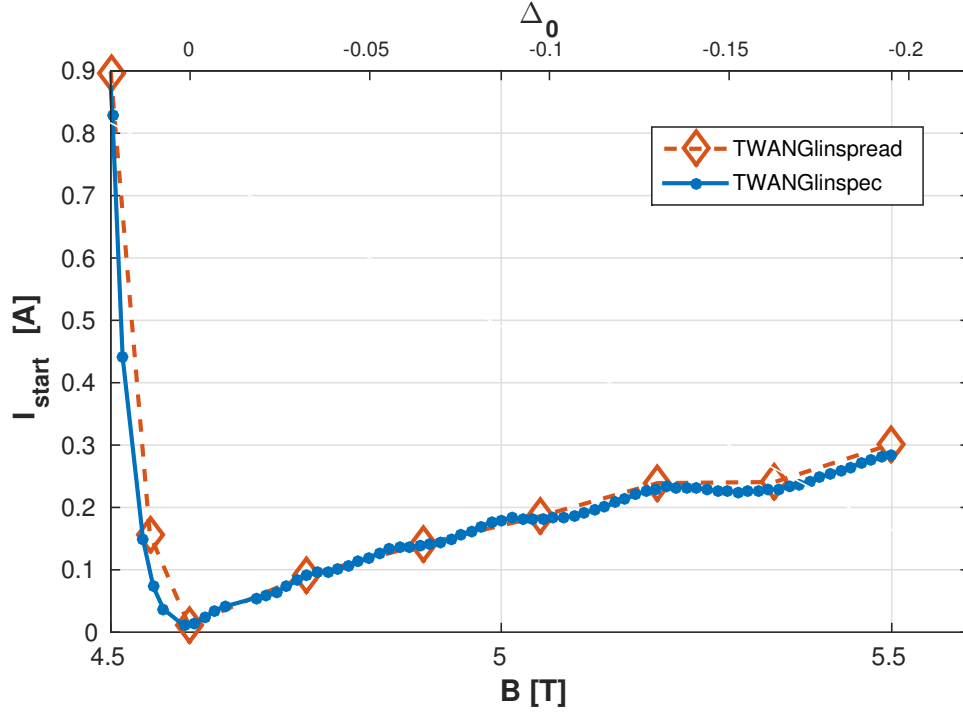


Figure 3.30 – Starting current calculated with TWANGlinspec (in continuous blue) and with TWANGlinspread (in dashed red) for a range of magnetic field values. The detuning, indicating the cut-off and the forward ($\Delta_0 > 0$) and backward ($\Delta_0 < 0$) regions is shown on the top axis. (Parameters: $TE_{25,3}$, $V_b = 75$ kV, $\alpha = 1.3$, $\Delta\alpha = 0$, $R_b = 12$ mm, $\sigma_{\text{cond}} = 2.9 \cdot 10^7$ S/m, $\Delta\gamma = 0$)

From this situation, simulations for a non-ideal electron beam parameters have been performed. The electron beam trajectory simulations from ARIADNE [97] indicate that a Gaussian approximation for the velocity distribution is reasonable. For a realistic situation, the spread in the pitch factor (defined as the relative standard deviation) is on the order of 5%, while the spread in the relativistic Lorentz factor is on the order of 0.01%. In this study, only a spread in the pitch factor (called velocity spread in the following) is considered. The starting current calculated with TWANGlinspread for different velocity spread values are reported in Figure 3.31 for the reference geometry case and for a uniform magnetic field. The two cases reported are for the mode $TE_{25,3}$ for two different magnetic field values. The case with $B = 4.75$ T (in continuous blue line) is an interaction close to the cutoff ($k_z = -220 \text{ m}^{-1}$), as can be seen in the detuning reported in Figure 3.30, while the case with $B = 5.5$ T (in dashed green line) is a case far from cutoff in the backward regime ($k_z = -940 \text{ m}^{-1}$).

The starting current dependence on the velocity spread for the interaction far from the cutoff is much larger than close to the cutoff. As already discussed in the previous section, this is expected as the modes away from cutoff have a much larger Doppler shift contribution in the resonance condition (3.1). This is also in agreement with the results presented in [75].

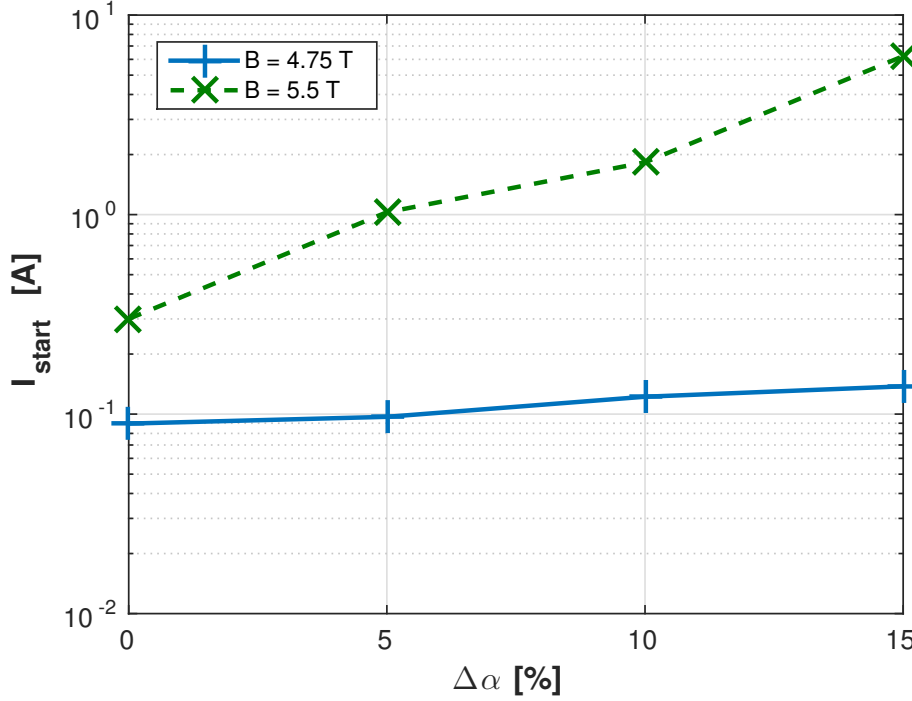


Figure 3.31 – Starting current calculated with TWANGlinspread for the reference situation (shown in Figure 3.29) for different velocity spread values and for two values of the magnetic field. The case $B = 4.75$ T is a case close to the cutoff ($k_z = -220 \text{ m}^{-1}$) while the case $B = 5.5$ T is a case away from cutoff ($k_z = -940 \text{ m}^{-1}$). (Parameters: $\text{TE}_{25,3}$, $V_b = 75 \text{ kV}$, $\alpha = 1.3$, $R_b = 12 \text{ mm}$, $\sigma_{\text{cond}} = 2.9 \cdot 10^7 \text{ S/m}$, $\Delta\gamma = 0$).

Finally, the more realistic situation for the TCV dual-frequency gyrotron is studied. The 11 modes identified with $I_{start} < I_b = 40 \text{ A}$ for the case where only the smooth-wall beam duct and the spacer were simulated (cf. Figure 3.13), are considered. In this particular case, the parasitic mode $\text{TE}_{16,4}$ has the lowest starting current.

In the following the extended interaction region, including the cavity, is considered. To be consistent, the 328 modes with $I_{start} < I_b = 40 \text{ A}$ (cf. Figure 3.16 and 3.17) should be considered. However, treating such a large number of modes with the time-dependent code TWANGlinspread is onerous and require a large amount of numerical resources. This is even worsed by the fact that a larger number of particles have to be simulated in a case including spread in velocity and/or energy.

The starting current results from TWANGlinspread for the parasitic mode $\text{TE}_{16,4}$ as well as

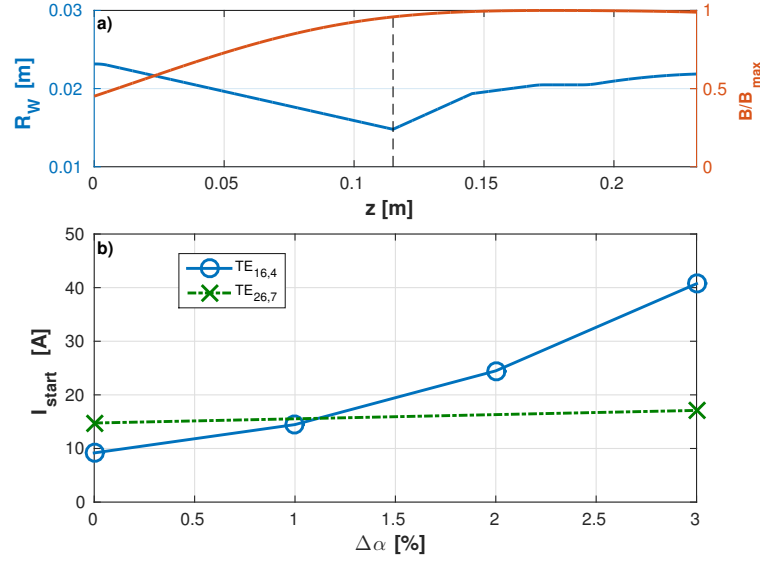


Figure 3.32 – a) Interaction region and magnetic field profile for the smooth wall beam duct, spacer and cavity of the TCV dual-frequency gyrotron. b) Starting current calculated with TWANGlinspread for different velocity spread for the parasitic mode $TE_{16,4}$ (in continuous blue) and for the operating mode $TE_{26,7}$ (in dashed green). (Parameters: $B = 4.98$ T, $V_b = 78$ kV, $\alpha = 1.3$, $R_b = 10.48$ mm, $\sigma_{cond} = 2.9 \cdot 10^7$ S/m, $\Delta\gamma = 0$).

the operating mode $TE_{26,7}$ are shown in Figure 3.32 for different velocity spread values at the entry of the interaction region (entry of the beam duct at $z = 0$ m). As expected, as the parasitic mode has a much larger Doppler shift contribution than the operating mode, the electron beam velocity spread has a much larger effect on the parasitic starting current. For a 3% velocity spread, the starting current is higher than the operating beam current ($I_b = 40$ A). As an illustration, the amplitude and phase profiles for the mode $TE_{16,4}$ with $\Delta\alpha = 0\%$ and $\Delta\alpha = 3\%$ are shown in Figure 3.33 a) and b), respectively. The beam current for the simulation are slightly above the respective starting current, $I_b = 9.3$ A for $\Delta\alpha = 0\%$ and $I_b = 40.9$ A for $\Delta\alpha = 3\%$. Note that due to the magnetic field variation along z , the spread is more important in the cavity region. For a velocity spread at the entry of the interaction region on the order of 3%, the velocity spread in the cavity is around 5.8%, which is a realistic velocity spread value in gyrotron devices.

For the other 10 modes, the calculated starting currents are reported in Table 3.5 for a 3% velocity spread. The starting current calculated with TWANGlinspec without spread is also reported. With a 3% velocity spread (5.8% in the cavity), all the modes have a starting current higher than the operating beam current ($I_b = 40$ A). They are thus not expected to be excited in this situation. Ideally, all the 328 transverse modes for many operating points should be tested. This is not feasible with a time-dependent approach (in a reasonable amount of time). Nevertheless, the systematic increase in starting current for the modes with a non-zero Doppler-shift contribution are a good indication that all the backward wave parasitic modes

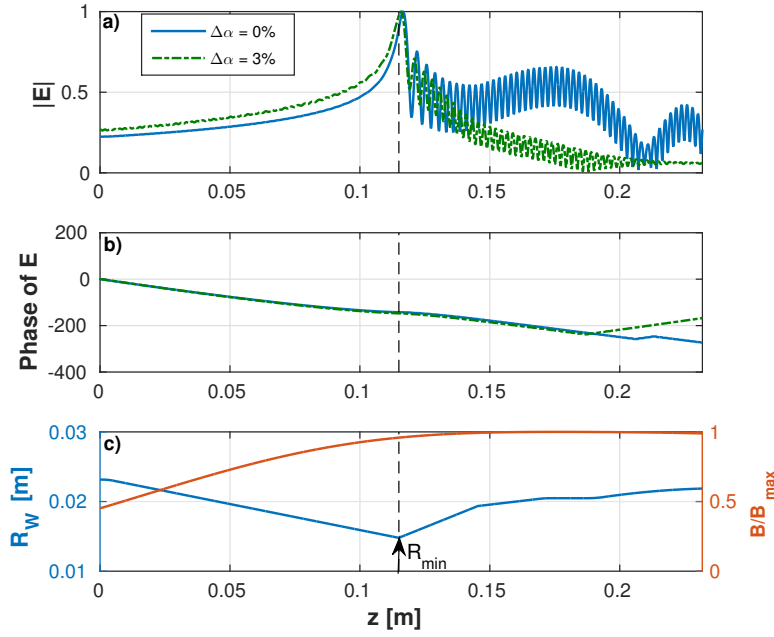


Figure 3.33 – a) and b) Amplitude and phase of the electric field profile for the mode $TE_{16,4}$ calculated with TWANGlinspread for an ideal electron beam ($\Delta\alpha = 0\%$ in continuous blue) and for a realistic velocity spread ($\Delta\alpha = 3\%$ in green). c) Interaction region and magnetic field profile. (Parameters: $B = 4.98$ T, $V_b = 78$ kV, $\alpha = 1.3$, $R_b = 10.48$ mm, $\sigma_{\text{cond}} = 2.9 \cdot 10^7$ S/m, $\Delta\gamma = 0$).

are strongly affected by the velocity spread.

Table 3.5 – Starting current calculated with TWANGlinspec, without spread, and with TWANGlinspread with a 3% velocity spread for the extended beam duct plus spacer plus geometry case.

Transverse mode	I_{start} [A]		$\frac{I_{\text{start}, \Delta\alpha=3\%}}{I_{\text{start}, \Delta\alpha=0\%}}$
	TWANGlinspec $\Delta\alpha = 0$	TWANGlinspread $\Delta\alpha = 3\%$	
$TE_{15,4}$	3.7	40.3	10.9
$TE_{14,4}$	4.5	61.8	13.7
$TE_{-13,5}$	5.1	54.4	10.7
$TE_{16,4}$	7.5	40.9	5.4
$TE_{10,5}$	7.9	112.6	14.3
$TE_{11,5}$	14.5	127.8	8.8
$TE_{-10,6}$	15.3	126.4	8.3
$TE_{-14,3}$	16.8	118.5	7.1
$TE_{19,3}$	17.5	64.5	3.7
$TE_{-9,6}$	21.5	101.2	4.7
$TE_{20,3}$	34.8	58.3	1.7

3.5 Distributed losses

Still considering a metallic smooth-wall beam duct, the objective is to study the dependency of the minimum starting current on the wall conductivity, and also to identify in which part of the beam duct plus spacer region the parasitic mode excitation takes place. This was considered for example in [76, 81], but in particular in [76] the spacer region was neglected. TWANGlinspec has been validated by reproducing the results presented in [76] with a good qualitative agreement (cf. appendix).

Beam duct plus spacer

Concentrating on a parasitic mode excited in the spacer and considering the beam duct and spacer region, the effect of the distribution of the Ohmic losses is studied. Two different wall resistivity distributions are represented in Figure 3.34. The transition between two different resistivity regions is made smoothly to minimize reflections. The two profiles ρ_1 and ρ_2 in Figure 3.34 are the two cases where the lossy part is either in the beam-duct part for ρ_1 or in the spacer part for ρ_2 . The starting currents calculated for the transverse mode $TE_{16,4}$ for different values of the resistivity and for these two different profiles are shown in Figure 3.35. For the first profile ρ_1 , there is only a small starting current variation by increasing the resistivity in the beam duct part. On the contrary, the variation is significantly more important if the resistive part is in the spacer region. This variation is almost identical as the variation when the whole structure is considered to be resistive (not presented here). As the nominal beam current is 40 A, one could see that the mode $TE_{16,4}$ is expected to be stable for a resistivity around $10^{-2} \Omega m$. Notice that in the derivation of the surface impedance model the good conductor assumption is made ($\sqrt{\frac{\sigma}{\omega\epsilon_0}} \gg 1$) [59]. This assumption is still valid in this case ($\sqrt{\frac{\sigma}{\omega\epsilon_0}} \approx 4$).

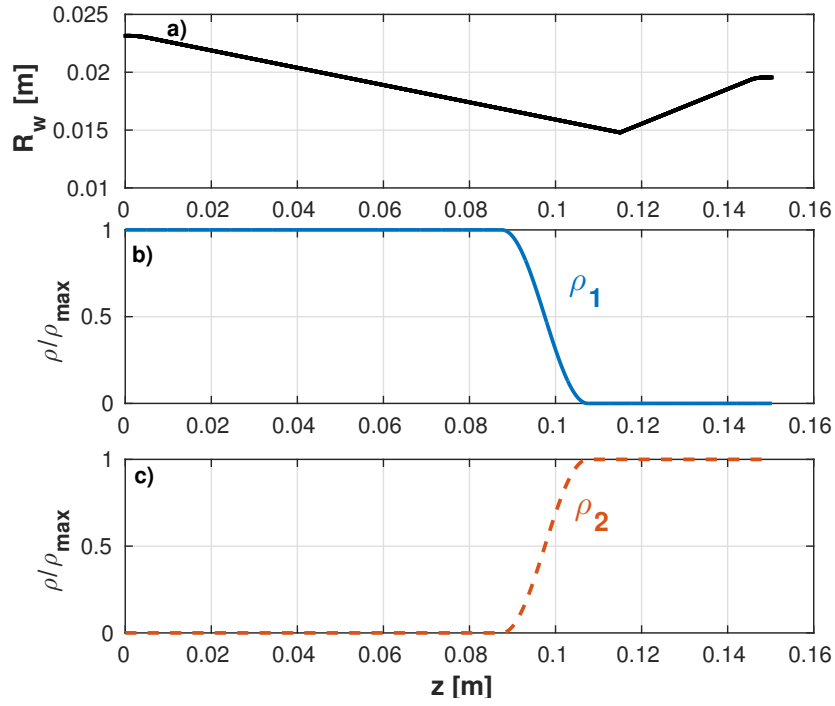


Figure 3.34 – a) Geometry considered. b) and c) Resistivity profiles considered for the starting current study in 3.35.

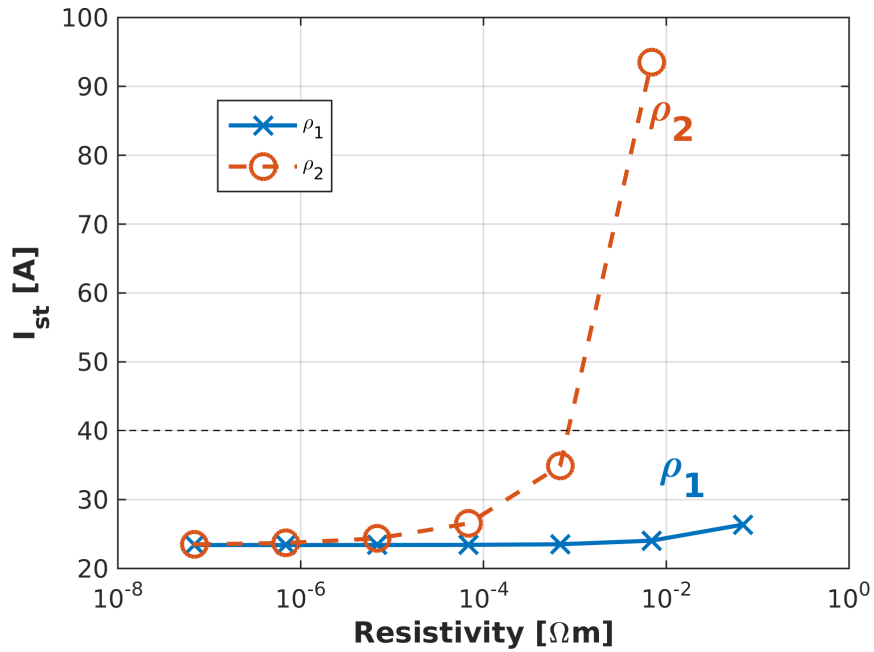


Figure 3.35 – Starting current calculated for the transverse mode $\text{TE}_{16,4}$ by varying the wall resistivity and for the two different resistivity distributions shown in Figure 3.34. The resistivity of pure copper is $1.7 \cdot 10^{-8} \Omega\text{m}$.

Extended beam duct/spacer/cavity region

The next step was to add the cavity in the interaction region. The same study was done with the two resistivity profiles reported in Figure 3.36. In this case, one could see that with the wall resistivities considered in Figure 3.37 and with no velocity spread, the $TE_{16,4}$ mode is still expected to be excited as the largest starting current is around 21A. However, for the large considered resistivity value in figure 3.37, the good conductor assumption made in the derivation of the surface impedance model is violated ($\sqrt{\frac{\sigma}{\omega\epsilon_0}} \approx 0.1$).

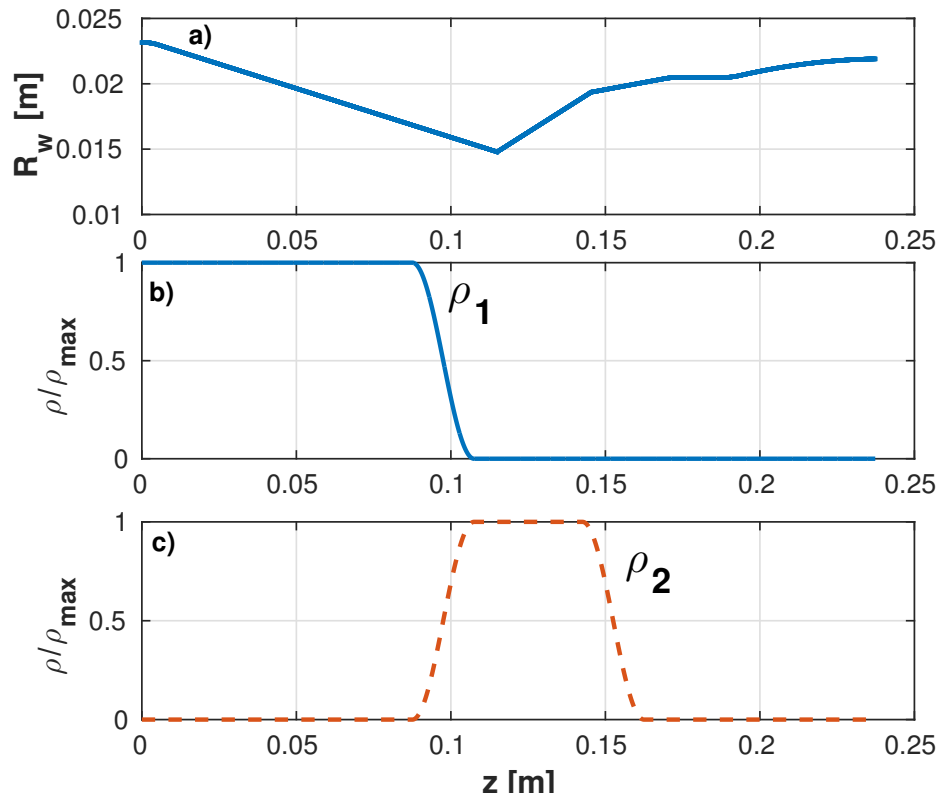


Figure 3.36 – a) Geometry considered. b) and c) Resistivity profiles considered for the starting current study in Figure 3.37.

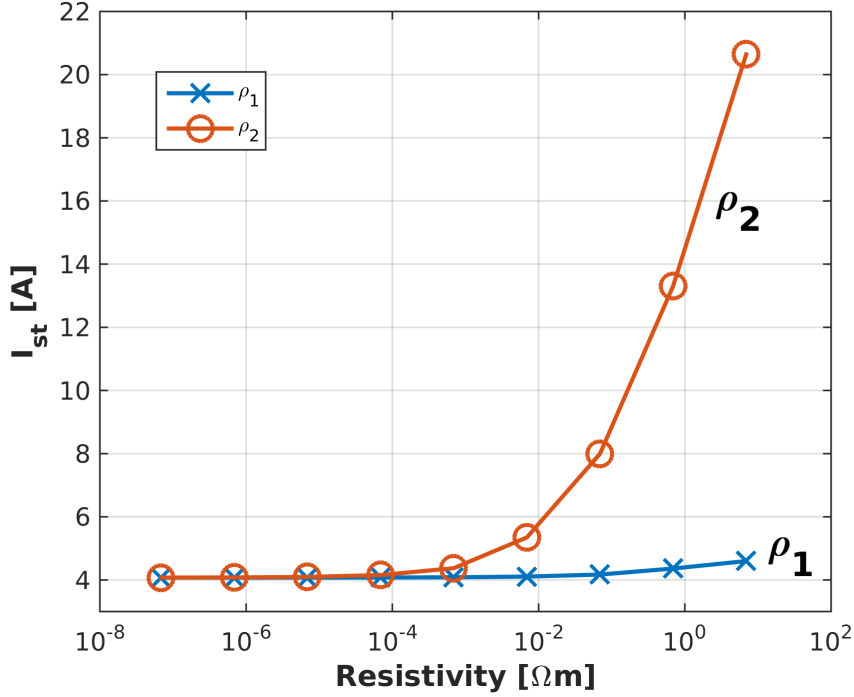


Figure 3.37 – Starting current calculated for the transverse mode $TE_{16,4}$ by varying the wall resistivity and for the two different resistivity distributions shown in Figure 3.36. The resistivity of pure copper is $1.7 \cdot 10^{-8} \Omega m$.

3.6 Conclusion

The strategy used to study the beam duct instabilities for a smooth wall metallic beam duct was to start from a simple reference situation and varying progressively the geometry and the magnetic field profile to approach a realistic situation. This shows that the tapering angles of the beam duct and the spacer are found to be the pivotal parameters impacting strongly the starting current of the parasitic modes. Due to the localized interaction region of the parasitic modes, a translation of the magnetic field profile along the longitudinal direction has also a strong influence on the self-excitation of any given modes. However, considering the large number of potentially unstable modes, when the minimum starting current of a specific mode increased, the minimum starting current of a different mode is reduced.

The extensive scans over all possible transverse modes reveal that in a realistic situation, a large number of modes could still be excited at the nominal beam current. These scans show that the spacer region, situated between the beam duct and the cavity, plays an important role in the excitation of Doppler shifted gyro-backward wave modes. The backward-wave nature of these modes demonstrates the need of a self-consistent model such as TWANGlinspec. These instabilities are peaked in the spacer region, but continue to interact with the electron beam throughout the cavity.

Non-linear monomode simulations indicate that these parasitic modes lead to an important spread in the electron energy distribution and therefore potentially affect the main interaction in the cavity. Another non-linear simulation, as well as the results from the linear code TWANGlinspread, including a realistic electron beam with spread indicate that these parasitic oscillations, unlike the gyrotron operating mode, depend strongly on the velocity spread of the electron beam. With realistic electron beam characteristics ($\Delta\alpha = 6\%$ in the cavity), the modes considered are not expected to be excited. This could explain why such parasitic oscillations with a rf-power exceeding 20kW were never observed experimentally.

This leads us to the conclusion that the model TWANGlinspec, neglecting the velocity spread, is underestimating the minimum starting current. Based on that, a situation where TWANGlinspec would not predict the excitation of any modes could be considered as a safe, free of instabilities situation in a realistic case with a non-ideal electron beam.

A solution to damp these oscillations is to add a dielectric coating in the end of the beam duct and in the spacer region. This has been approximated via a surface impedance boundary condition, as it is commonly done to evaluate Ohmic losses in the walls of gyrotron or gyrotron travelling wave amplifiers [76, 82]. As expected from the interaction localized in the spacer, an Ohmic loss distribution study shows that it is most effective to put the lossy material in the spacer region. However, the good conductor assumption made by the model is approaching its limit for wall conductivity capable of stabilizing the instabilities.

In the next chapter, the self-consistent approach to simulate the beam duct with a lossy dielectric coating of finite thickness is presented.

4 Dielectric coated smooth-wall beam duct

In this chapter, a new self-consistent approach to treat the beam-wave interaction in a waveguide covered with a dielectric layer with complex permittivity is presented. First, the validation of the dielectric dispersion relation solver detailed in chapter 2 both for the Bessel and Hankel functions formulations is presented. Then the full simulations including the dielectric layer are presented, starting from the reference geometry and eventually considering the realistic situation of the dual-frequency gyrotron.

4.1 Validation of the dielectric dispersion relation solver

The dielectric dispersion relation solving method is validated in two phases. The first phase consists in reproducing results published by other groups [43]. The frequencies of the modes satisfying the dispersion relation are shown in Figure 4.1 for the parameters listed in Table 4.1. For the three modes labelled in Figure 4.1, the normalized amplitude of the electric field azimuthal component is shown in Figure 4.2. The agreement with the results in [43] is excellent. Note that for these parameters, the field is penetrating more in the dielectric layer for modes with larger parallel wavenumber k_z .

Table 4.1 – Simulation parameters.

Parameter	Value
m ($TE_{m,p}$)	0
a	5.495 mm
b	6.905 mm
ϵ_1	ϵ_0
ϵ_2	$11\epsilon_0$

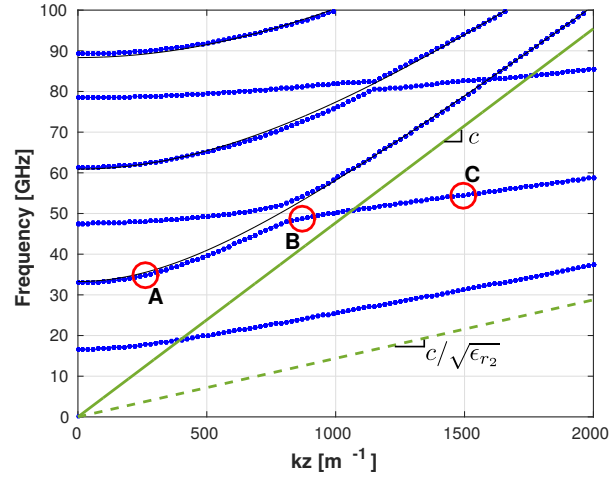


Figure 4.1 – Solution of the dispersion relation (2.45) in the frequency- k_z plane. The continuous and dashed green lines are the light dispersion relation in vacuum and in the dielectric material. The continuous black lines are the solution of the dispersion relation with an ideal metallic boundary condition at $r = a$ (cf. Figure 2.15). The three points labelled A,B,C are the points considered in Figure 4.2.

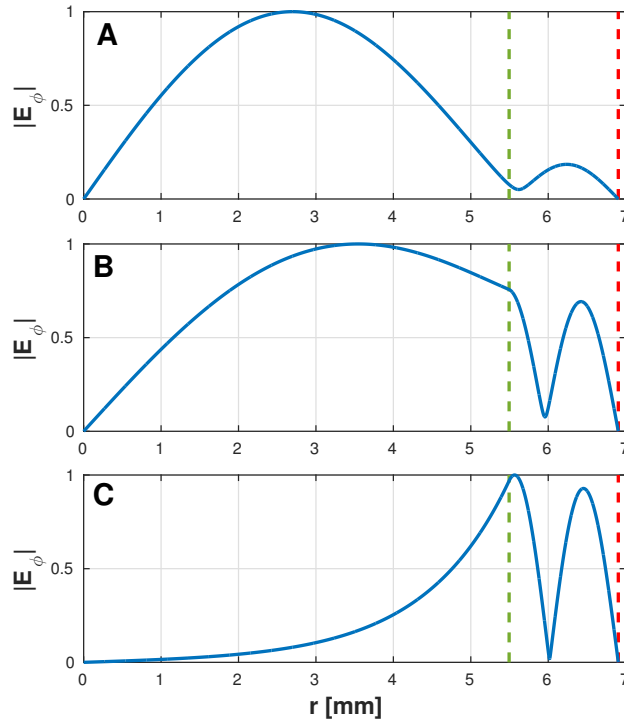


Figure 4.2 – Transverse profile of the electric field amplitude (azimuthal component) for the three dispersion relation solutions labelled in Figure 4.1. The vertical dashed lines are indicating the interface between the vacuum and the dielectric ($r = a$) and the outer boundary ($r = b$) (cf. Figure 2.15)

In [43] or [38], only azimuthally symmetric modes $TE_{0,p}$ are considered. The code has been validated for hybrid $HE_{m,p}/EH_{m,p}$ modes within a collaboration with the National and Kapodistrian University of Athens in Greece (NKUA). An example is shown in Figure 4.3 for a 10mm thick SiC layer ($\epsilon_r = 12 - 0.72i$) for the modes with $m = 25$ (cf. Table 4.2). This permittivity value was measured at SPC (cf. appendix C). In this figure, the solutions of equation (2.45) are shown with the colored points in the frequency versus parallel wavenumber plane. The continuous black lines are the solutions corresponding to $TE_{25,p}$ modes solutions to the dispersion relation with a metallic boundary condition at $r = a$ ($\omega = cv_{mp}/a$). The color of the points indicate the TM or TE mode purity. It is defined as the relative difference of the longitudinal electric or magnetic field components:

$$P = \frac{|E_{z,max}| - |cB_{z,max}|}{\max(|E_{z,max}|, |cB_{z,max}|)}. \quad (4.1)$$

A purely TE mode ($E_z = 0$) is indicated in red ($P = -1$), while a purely TM mode ($B_z = 0$) is indicated in blue ($P = 1$). It has been shown that the mode purity decreases away from the cutoff or for larger m .

As already discussed in chapter 2, when a material with a large imaginary dielectric constant is considered, the dielectric dispersion relation formulation with Bessel function of first and second kind fails to provide the solutions because of numerical round-off errors. The formulation with Hankel function (2.57a) is found to be adequate in this case. One example for a 10mm thick BeOSiC layer ($\epsilon_r = 30 - 18i$) is shown in Figure 4.4 for the parameters in Table 4.3. This dielectric permittivity value was also measured at SPC (cf. appendix).

Two different type of modes could be distinguished in Figure 4.4. The parabola labelled $TE_{25,p}$ and $TM_{25,p}$ are modes, which are marginally affected by the dielectric layer. They stay almost perfectly TE or TM modes, even for higher values of k_z . Their real frequency is very close to their corresponding mode with a metallic boundary condition at $r = a$. The radial electric field profile for the mode highlighted with the red circle in Figure 4.4 is shown in Figure 4.5. The perpendicular component of the electric field is almost identical to the corresponding mode with a metallic boundary condition. The second kind of modes are the modes with a small group velocity. These modes only exist with a dielectric layer. The radial electric field profile of the mode highlighted in green in 4.4 indicates that these modes correspond to surface modes, peaked close to the dielectric layer and with a non zero amplitude in the dielectric layer, as can be seen in Figure 4.6. These two different type of modes are found in the SiC case as well (cf. Figure 4.3). However, a stronger effect between the two type of modes is clearly seen, especially for modes with lower frequencies or larger k_z . In the BeOSiC case (cf. Figure 4.4), the second kind of modes are degenerated in frequency, between a TE-like and a TM-like mode. In Figure 4.6, the TE-like solution (hidden by the TM-like solution in Figure 4.4) has been chosen.

These results, along with a series of other simulations are reproduced with success at the NKUA. For this purpose, their in-house tools FISHBONE [33, 80, 104] is used.

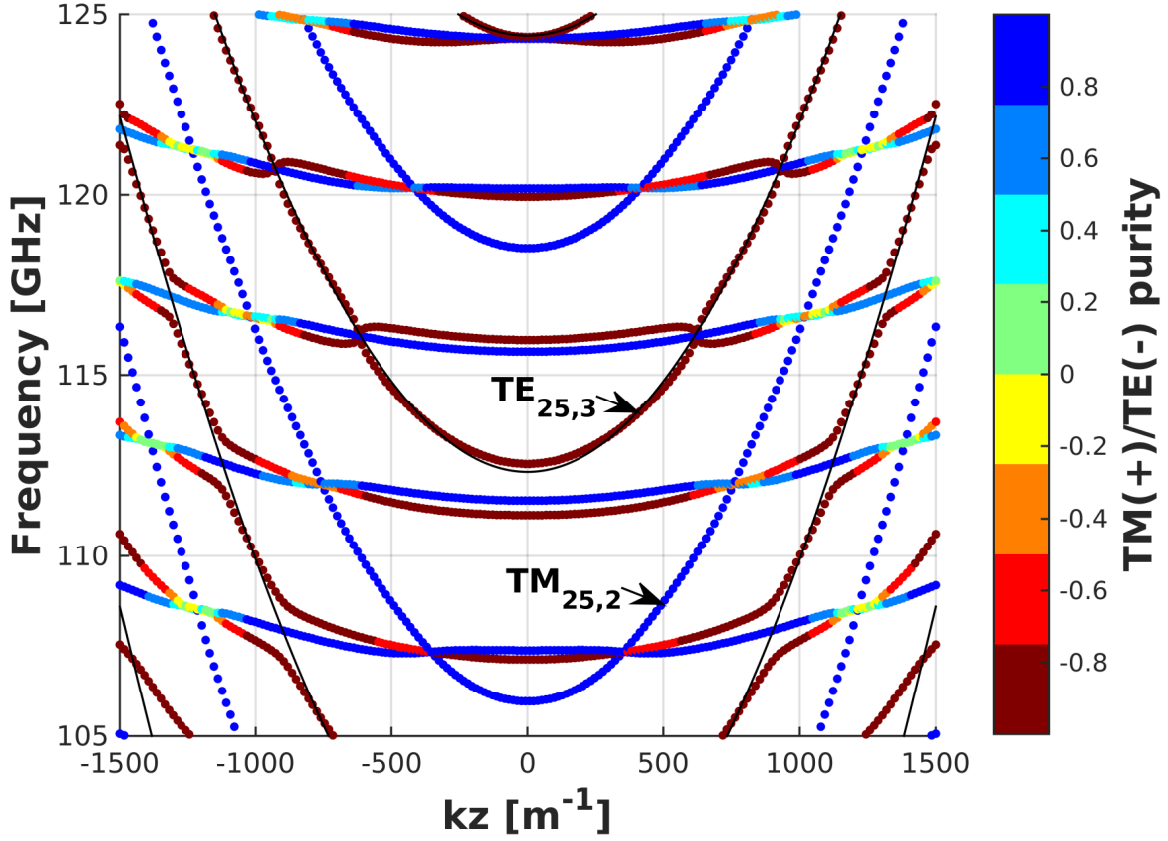


Figure 4.3 – SIC layer. Solutions of the dispersion relation (2.45) in the frequency- k_z plane for the parameters listed in Table 4.2. The color points are an indication of the TE or TM mode purity. The thin black lines are the solutions corresponding to TE modes with a metallic boundary condition at $r = a$.

Table 4.2 – Simulation parameters used for the calculation shown in Figure 4.3.

Parameter	Value
azimuthal index m	25
a	16mm
b	26mm
ϵ_1	ϵ_0
ϵ_2	$(12 - 0.72i)\epsilon_0$

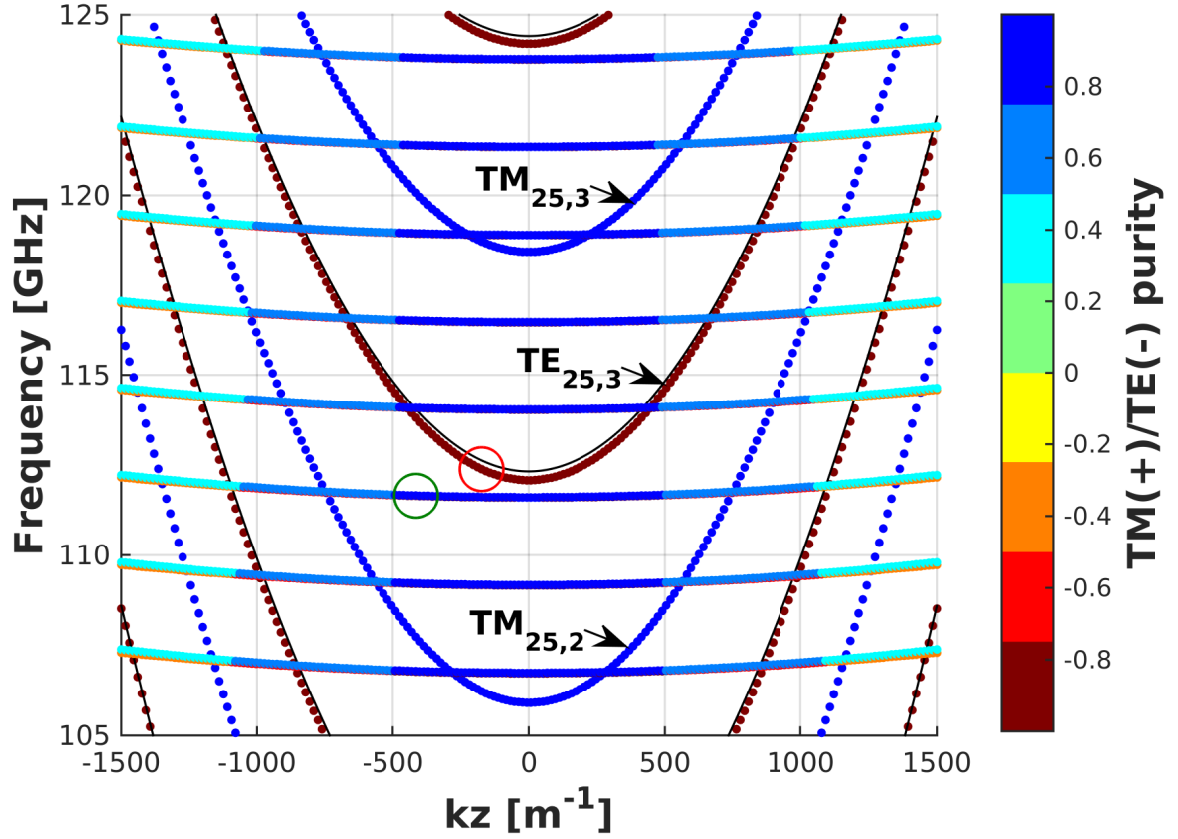


Figure 4.4 – BeOSiC layer. Solutions of the dispersion relation (2.57a) in the frequency- k_z plane for the parameters listed in Table 4.3. The color points are an indication of the TE or TM mode purity. The thin black lines are the solutions corresponding to TE modes with a metallic boundary condition at $r = a$.

Table 4.3 – BeOSiC layer. Simulation parameters used for the calculation shown in Figure 4.4.

Parameter	Value
azimuthal index m	25
a	16mm
b	26mm
ϵ_1	ϵ_0
ϵ_2	$(30 - 18i)\epsilon_0$

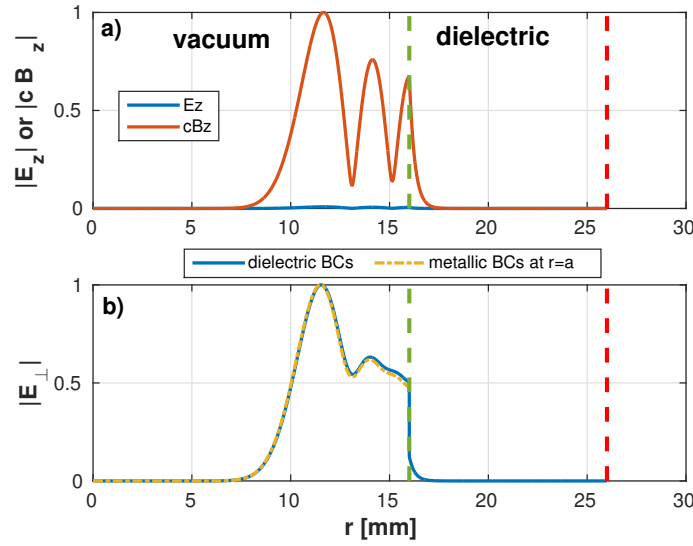


Figure 4.5 – Radial profiles of the mode highlighted with the red circle in 4.4. a) Longitudinal component of the electric and magnetic field and b) perpendicular component of the electric field. The green dashed vertical line indicates the boundary between the vacuum and the dielectric regions ($r = a$). The red dashed vertical line indicates the metallic external boundary condition ($r = b$).

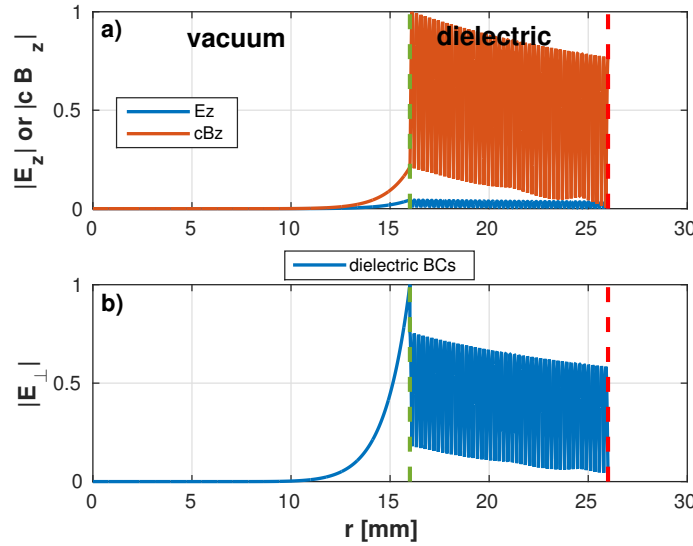


Figure 4.6 – Radial profiles of the TE-like mode highlighted with the green circle in 4.4 (hidden under the TM-like solution point). a) Longitudinal component of the electric and magnetic field and b) perpendicular component of the electric field. The green dashed vertical line indicates the boundary between the vacuum and the dielectric regions ($r = a$). The red dashed vertical line indicates the metallic external boundary condition ($r = b$).

4.2 Effect of coating thickness

During the validation phase of the dielectric dispersion relation solver, various values of the modes azimuthal index, complex dielectric permittivity and layer thickness have been used. For some layer thickness, singularities have been observed. These singularities appear when the layer thickness is on the order of the wave penetration depth.

For the case of a metallic wall with large conductivity, the skindepth is a measure of the penetration of the wave inside the wall. It corresponds to the distance at which the wave amplitude decreases by $1/e$. In the case of a purely metallic wall with finite conductivity, the skindepth δ_{sk} is calculated as

$$\delta_{\text{sk}} = \sqrt{\frac{1}{\omega \mu_0 \sigma_{\text{cond}}}}, \quad (4.2)$$

where ω is the wave frequency, μ_0 the vacuum permeability and σ_{cond} the wall conductivity.

When a dielectric with a complex permittivity constant $\epsilon = \epsilon_0 \epsilon_r (1 - i \tan \delta)$ is considered, the skindepth, called more precisely wave penetration depth, could be approximated by making the assumption $\tan \delta \ll 1$:

$$\delta_{\text{sk}} = \left[\frac{1}{2} \frac{\omega}{c} \sqrt{\epsilon_r} \tan \delta \right]^{-1}. \quad (4.3)$$

To illustrate this effect, the amplitude of the perpendicular electric field component at the external boundary ($r = b$ in Figure 2.15) for different layer thickness is shown in Figure 4.7. For very small thickness, the electric field is penetrating and does not vanish at the external wall. For layer thickness larger than the wave penetration depth (cf. equation 4.3), the wave amplitude is decaying in the layer and vanishes at the external boundary. However, for layer thickness smaller but comparable to the wave penetration depth, the value of the electric field is significantly larger.

This effect is associated to resonant phenomena due to reflections on the metallic external boundary [59]. For the same case presented in Figure 4.7, the imaginary part of the perpendicular wavenumber, an indication of the attenuation of the vacuum wave due to the dielectric, is shown in Figure 4.8 for layer thickness of the order of the wave penetration depth. The perpendicular wavelength of the wave in the dielectric for this case is $\lambda_2 = \frac{2\pi}{\text{Re}(k_{\perp 2})} = 0.47$ mm. The oscillations in the values of $\text{Im}(k_{\perp 1})$ are located at integer multiple of $\lambda_2/4$. This result has been reproduced with a really good agreement by using the formula providing the absorbed power in the dielectric for a planar geometry case (equation (4) in [59]).

This observation indicates that the dielectric layer thickness should be chosen larger than two or three times the wave penetration depth. Regardless of this effect, a dielectric with a layer

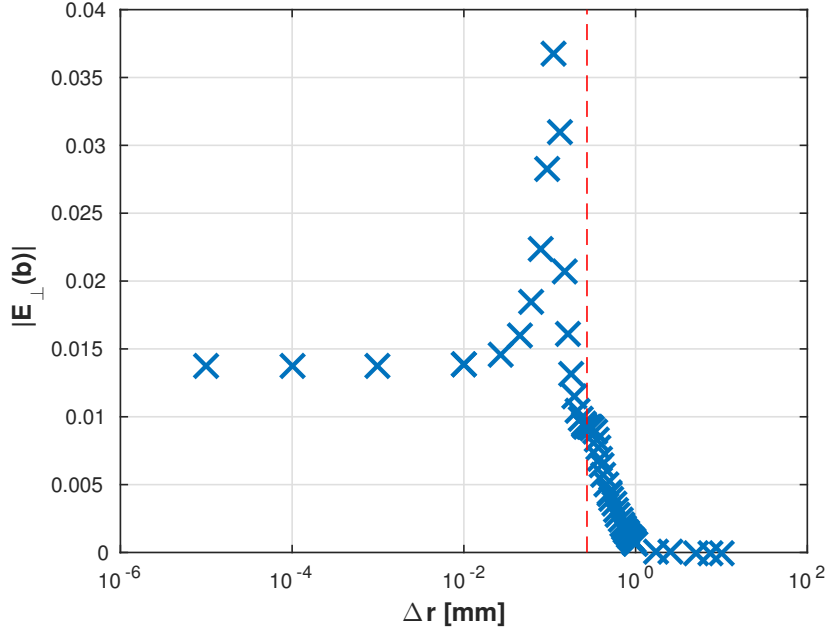


Figure 4.7 – Amplitude of the perpendicular component of the electric field at the external metallic boundary ($r = b$) for different layer thickness. The red dashed line indicates the wave penetration depth (cf. equation 4.3). (Parameters: $TE_{25,3}$, $\epsilon_r = 30 - 18i$, $a = 16\text{mm}$, $k_z = -165\text{m}^{-1}$, the red point in Figure 4.4).

thickness of a fraction of millimeter would not be practical.

4.3 Validity of the model

The model used in TWANGlinspec is based on a strong assumption. It only considers a single transverse TE mode ($E_z = 0$). With a dielectric layer, this assumption could be violated. When the resonance condition takes place with an important Doppler shift ($k_z \gg 0$), the beam-wave coupling with a TM mode could be important. It has been shown in [35] that the beam coupling to a TM mode is much stronger for backward wave interaction, due to the fact that the azimuthal and axial bunching processes cooperate with each other, while for a forward wave interaction, the two bunching processes compete against each other. In our cases, the interaction is always occurring in the backward wave regime, but the assumption of considering only TE modes is expected to be valid. Evaluating the TE and TM mode coupling coefficients in [35] for a typical case treated in this work, the TM mode coupling coefficient is found to be 3 orders of magnitude lower than the TE mode coupling coefficient.

The monomode assumption implies that no mode conversion to other transverse TE or TM modes is taken into account. In the case of a metallic boundary condition, this condition has been verified to be valid for the geometry considered (cf. appendix A). In the case of a

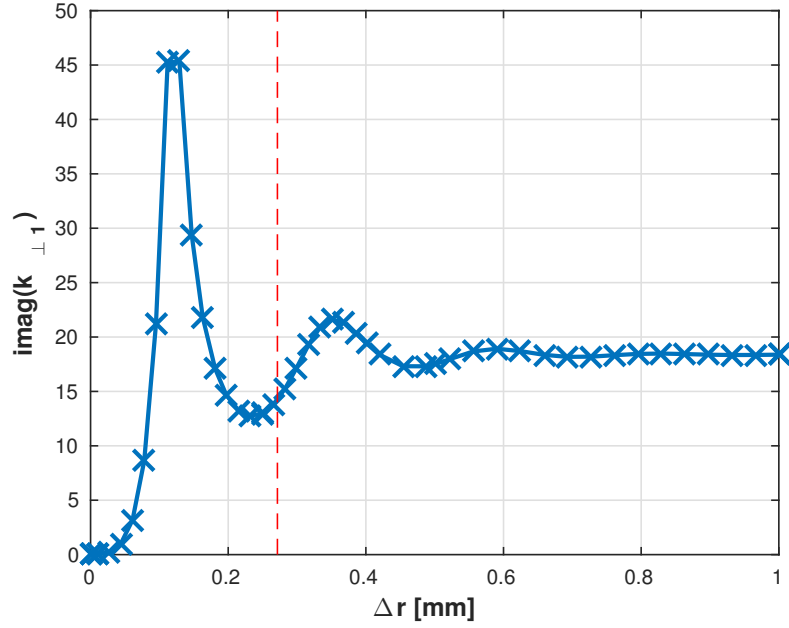


Figure 4.8 – Imaginary part of the perpendicular wavenumber inside the vacuum region for different layer thickness. The red dashed line indicates the wave penetration depth. (Parameters: $\text{TE}_{25,3}$, $\epsilon_r = 30 - 18i$, $a = 16\text{ mm}$, $k_z = -165\text{ m}^{-1}$).

dielectric boundary condition, a similar verification would be much more intricate and has not been made. As will be seen later, the electric fields for all the cases considered in these studies are similar to the electric fields in the case of a metallic boundary condition. We could then expect the mode conversion to be comparable to the mode conversion in the metallic case, thus negligible.

Finally, whenever a lossy dielectric layer is used, the modes are no longer purely TE or TM modes, but hybrid HE/EH modes (except at cutoff or for azimuthally symmetric modes with $m = 0$). For all the situations considered in this work, the modes correspond to almost pure TE mode as already seen on the results presented in Figure 4.3 or 4.4 or as will be shown in the following. This is the key point allowing the use of TWANGlinspec. A similar discussion on the validity of TE-like modes in the presence of a lossy structure is made in [105].

4.4 Systematic studies

Following the same logic as in chapter 3, a systematic parametric study has been carried-out. From the very simple geometry shown in Figure 3.2, the magnetic field profile, the wall tapering and the distribution of the dielectric layer have been changed towards the more realistic beam duct situation.

The first study consists in adding a dielectric layer to the constant radius section in the reference geometry with an uniform magnetic field profile. This situation is the most convenient to treat. Indeed, as the wall radius and magnetic field profile are constant, the solutions of the two dispersion relations, for the field in the cylinder with dielectric loading and for the electron beam, have to be calculated only once. This solution is shown in Figure 4.9 for the parameters listed in Table 4.4 for a 10mm thick BeOSiC layer. Notice that a sharp transition is considered between the dielectric layer and the metallic wall, which generates some reflection. The solution corresponding to the intersection with the electron beam dispersion relation is extracted and used in the electric field transverse structure expression in TWANGlinspec. The radial profile of the perpendicular component of the electric field is shown in Figure 4.10. The radial position of the electron beam is shown with the black dashed line. The result from the self-consistent simulation is shown in Figure 4.11. The starting current for this particular mode is increased from 57 mA, in the purely metallic case, to 53 A with the BeOSiC dielectric layer. The electric field profile indicates that the interaction is suppressed by the dielectric layer in the constant radius part. This can be seen as well by examining the wave equation source term in the same figure.

The same situation with a 10 mm thick SiC layer (not reported here) leads to a similar increase in the starting current, up to 56 A.

Table 4.4 – Simulation parameters for the dielectric dispersion relation calculation shown in Figure 4.9 and the TWANGlinspec self-consistent simulations shown in Figure 4.11.

Dielectric dispersion relation	
Parameter	Value
azimuthal index m	25
a	16 mm
b	26 mm
ϵ_2	$(30 - 18i)\epsilon_0$
TWANGlinspec	
Parameter	Value
Mode	$TE_{25,3}$
B	4.7 T
V_{beam}	75 kV
α	1.3
R_{beam}	12 mm
$\omega_0/(2\pi)$	112.672 GHz

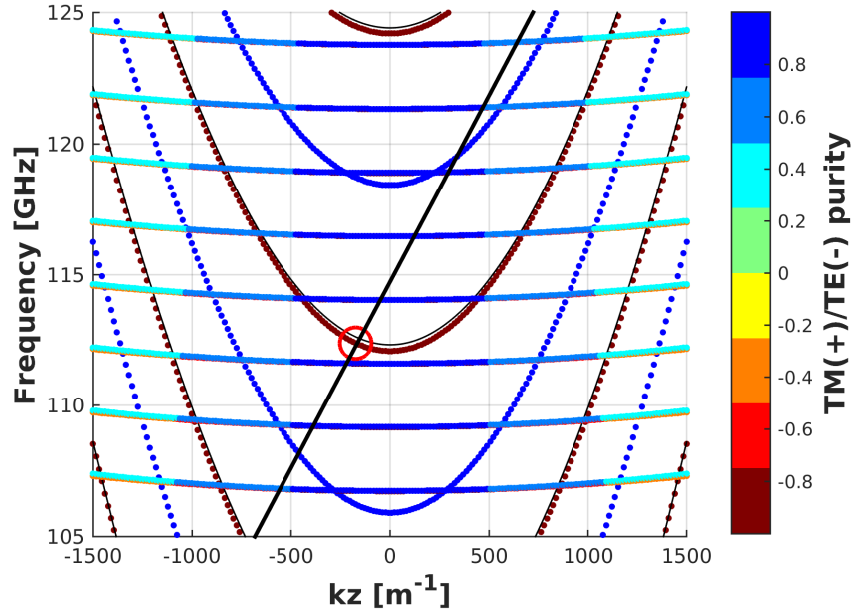


Figure 4.9 – Solutions of the dielectric dispersion relation (2.57a) in the frequency- k_z plane for the parameters listed in Table 4.4. The color points are an indication of the TE or TM mode purity. The thick black line is the solutions to the electron beam dispersion relation. The intersection, corresponding to a $TE_{25,3}$ -like mode, is highlighted with the red circle. This solution is used in the self-consistent simulation with TWANGlinspec.

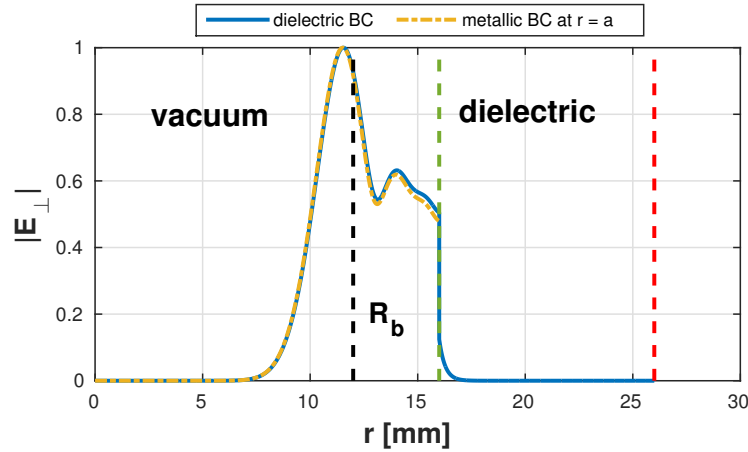


Figure 4.10 – Radial profile of the perpendicular electric field amplitude. The blue line is the solution of the dispersion relation highlighted in Figure 4.9. The dashed yellow line is the corresponding solution with a metallic boundary condition at $r = 16$ mm. The black dashed line indicates the beam radius defined as the average guiding center radius. The perpendicular electric field profile are nearly identical at this position.

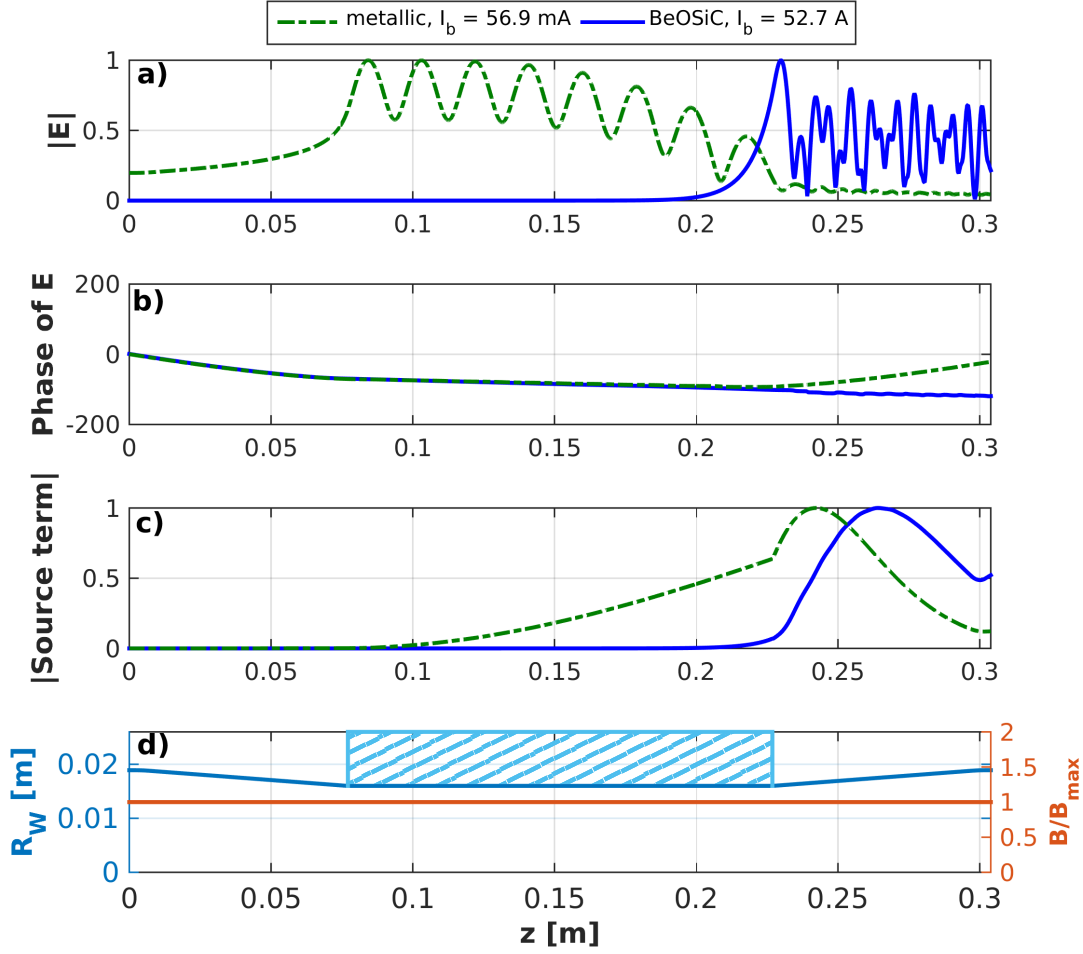


Figure 4.11 – a) and b) Longitudinal profile of the electric field amplitude and phase for the metallic boundary case (in dashed green line) and for the case with the dielectric layer in the constant radius part (continuous blue line). c) Source term of the wave equation, indicating where the interaction takes place. d) Geometry and magnetic field profile considered. The dielectric layer is shown in light blue.

Whenever a tapering in the wall radius is considered, the perpendicular wavenumber is varying along the longitudinal direction. In the case of the metallic boundary condition, the relation $k_{\perp} = v_{m,p}/R_w(z) \in \mathbb{R}$ allows a straightforward calculation. In the case of the dielectric boundary condition, the involved dispersion relation (2.45) should in principle be solved along the interaction region. However, the perpendicular wavenumber variation for different radius are smooth and an interpolation can be used to approximate their value on the grid points. As an illustration, the real and imaginary parts of the wavenumber in the vacuum ($k_{\perp 1}$) and in the dielectric ($k_{\perp 2}$) regions for different wall radius ($r = a$) are shown in Figure 4.12. For this case, a constant set of beam parameters has been chosen for the beam dispersion relation. For a more realistic situation with a varying magnetic field profile, the beam dispersion relation would be

different for each longitudinal position z , as the value of the magnetic field profile and the pitch factor value are varying along z . In this case, not shown here, the interpolation between a subset of solutions is still feasible. However, for the extreme cases with large wall radius and strongly varying magnetic field profile, there could be situations without intersection between the wave and the electron beam dispersion relations. In the most realistic study we consider, these situations only occur for the first part of the beam duct, where the wall radius is the largest and the magnetic field amplitude the lowest. This issue is avoided by not putting a dielectric layer in this location. It will be shown later that this location doesn't play a role in the parasitic suppression.

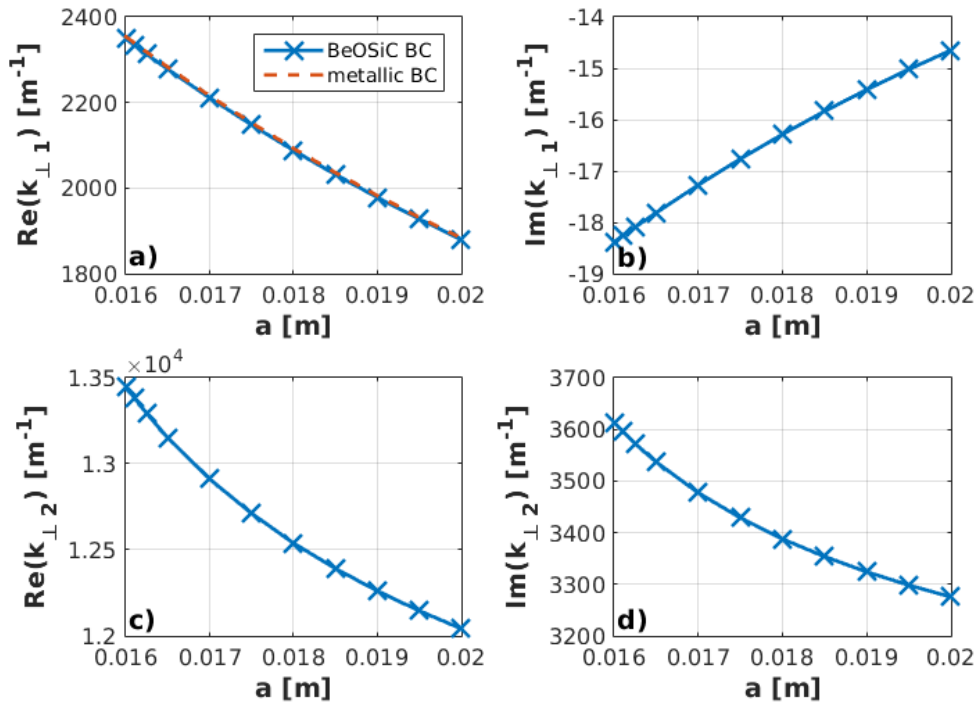


Figure 4.12 – Real and imaginary part of the perpendicular wavenumber in the vacuum region $k_{\perp 1}$ a) and b) and in the dielectric region $k_{\perp 2}$ c) and d) for different wall radius ($r = a$) and with a fixed dielectric layer thickness ($b - a = 10$ mm). The solutions correspond to the intersection with the beam dispersion relation with fixed beam parameters. In a) the solutions corresponding to a metallic boundary condition at $r = a$ are also shown.

Similar parametric studies as in chapter 3 lead to the same conclusions in the case of an interaction region with a dielectric layer. The inhomogeneity in the geometry, via the wall tapering, and the magnetic field profile have a strong effect on the transverse modes starting current. The variation on the dielectric layer location along the beam duct brings another information. The dielectric layer has a much stronger effect on the mode starting current when it is located where the interaction takes place. This can be seen on the series of Figure 4.13, where, for the reference geometry and for a 10mm thick BeOSiC layer located in the second part of the constant radius region, the magnetic field profile is changed.

For the three different magnetic field profiles, the simulation with a fully-metallic boundary condition are shown with the dashed green lines. The simulations with the BeOSiC layer are shown with the continuous blue lines. On top of each figures, the beam current slightly exceeding the starting current for each cases, are written. It is found that the most effective configuration, corresponding to the case where the mode starting current is the largest, is the situation where the magnetic field profile is peaked in the region where the dielectric layer is located. This is understandable as the beam wave interaction is favoured in this region. This result is important in view of a smooth-wall dielectric beam duct design, as it corresponds to the most realistic situation. The second best configuration (not shown here) is the situation where the magnetic field is peaked in the first part of the constant radius section and the dielectric layer is localized in the same region.

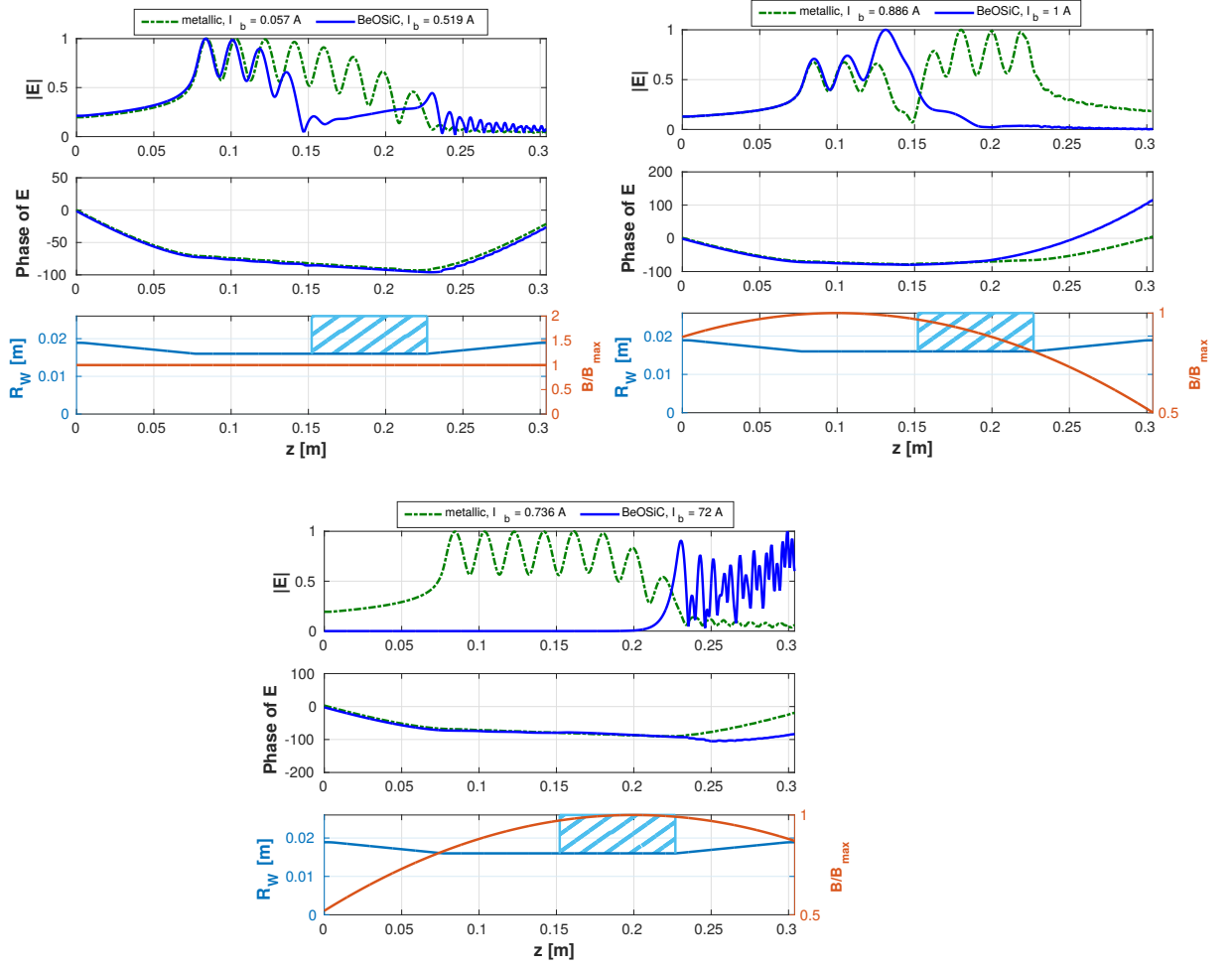


Figure 4.13 – Amplitude and phase of the electric field profile for different magnetic field profile and for a dielectric coating localized in the second part of the constant radius section. For each situation, the profile calculated with a metallic boundary condition for the entire structure is shown with the green dashed line. The beam current considered for each of these profiles (indicated at the top of each figure) is slightly exceeding the starting current for each mode.

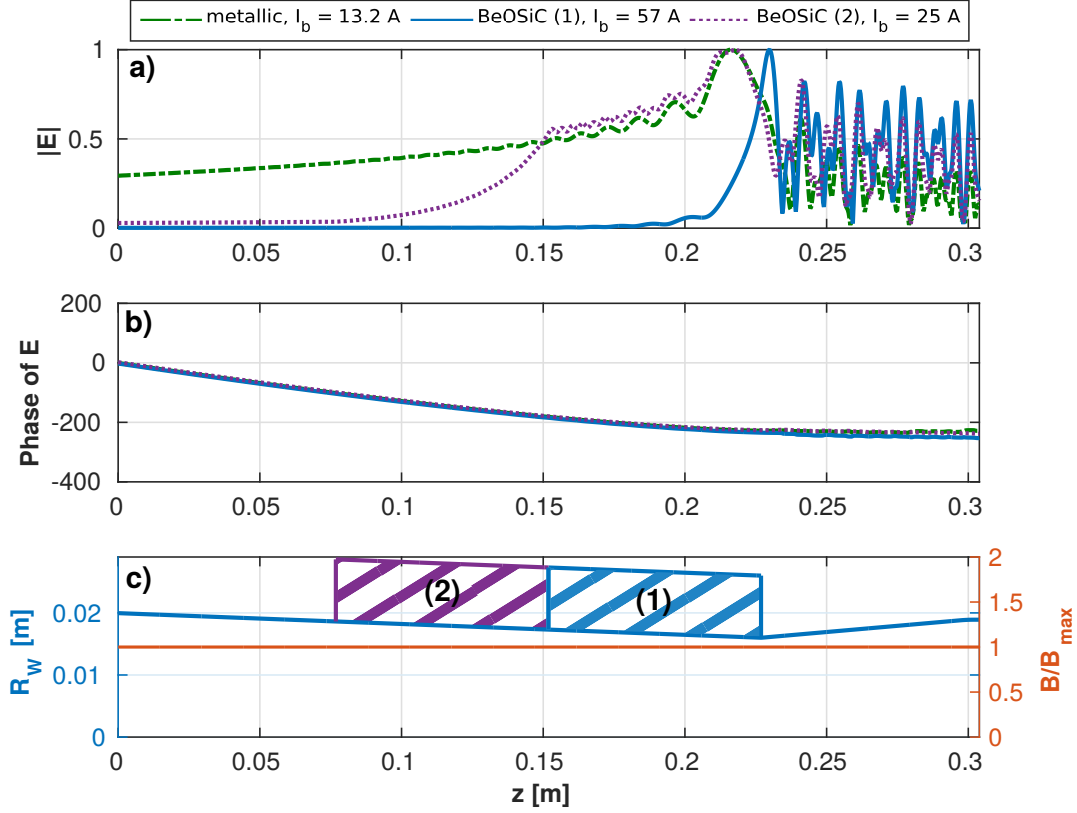


Figure 4.14 – a) and b) Amplitude and phase of the electric field profile for two different BeOSiC layer distributions (continuous blue line and purple dotted line) and for the fully metallic boundary condition (dashed green line). d) Interaction space and magnetic field profile. The beam current considered for each of these cases (indicated at the top of the figure) is slightly exceeding the corresponding starting current.

A second example, with a moderate wall tapering and a uniform magnetic field profile is shown in Figure 4.14. For this case, two different 10mm BeOSiC layer positions are considered, as well as the fully metallic boundary case (green dashed line). The situation labelled (1) is found to be the most effective to suppress the excitation, as it is the situation with the highest starting current. This is also expected as the interaction in such a structure has been found to be localized close to the minimum radius section.

Both in Figures 4.13 and 4.14, the effect of the dielectric layer on the longitudinal field profile is evident. The field is almost suppressed in the region where the dielectric is present.

4.5 Realistic geometry

The different parametric studies from the reference situation lead to the most realistic situation shown in Figure 3.11, this time including a dielectric layer. As a reminder, this situation is considering an smooth-wall envelope approximation of the beam duct, as well as the real spacer and cavity geometries for the TCV dual-frequency gyrotron [27].

For the realistic studies, the dispersion relation is solved for various z positions, taking into account the variation in the wall radius and magnetic field, thus taking into account the local conditions for both the wave and beam dispersion relations. As for the case presented in Figure 4.12, the smooth variation in the perpendicular wavenumber allows to compute the values for all the grid points along z with a simple interpolation.

Compared to the metallic case, this two-step process is by far more laborious, as it has to be done for each transverse mode and for each operating point, when a physical parameter is changed. For this reason, instead of studying all the potential modes, only a selection of modes has been analyzed. These 11 modes are the modes with a starting current lower than the operating starting current in the "realistic" situation with the metallic boundary condition, with the beam-duct plus spacer interaction region (cf. Figure 3.13). In particular the transverse mode $TE_{16,4}$ has been found to have the smallest starting current.

Again, the first step involves the resolution of the dispersion relation along the interaction region. The results are shown in Figure 4.15 for the four different longitudinal positions highlighted in Figure 4.15e and the parameters listed in Table 4.5. The four solutions extracted are highlighted with the colored circles. In Figure 4.15b and 4.15d, the solutions are well defined and separated from other solutions. However, in Figure 4.15a and 4.15c, the crossing between the wave and beam dispersion relations occurs in a region where both cavity and surface TE/TM-like modes solution exist. The surface modes, as shown in Figure 4.6, have their electric field amplitude mainly situated close to the dielectric, far from the electron beam position, therefore with a weak geometrical coupling. In addition, their wavenumber imaginary part in the vacuum ($\text{Re}(k_{\perp 1})$) is larger than for cavity modes, indicating that their losses in the dielectric is larger. These two facts suggest that these modes are unlikely to be excited. On the other hand, the mode conversion analysis between the cavity mode and the surface mode, which is not only probably cumbersome but also difficult to model, has been neglected in this model and only the TE-like cavity modes are considered in the following.

Table 4.5 – Geometry and electron beam parameters used for the dielectric dispersion relation studies shown in Figure 4.15.

Parameters	a [mm]	b[mm]	B [T]	α	V_b [keV]
(1) $z = 65$ mm	18.5	28.5	3.98	1.01	78
(2) $z = 80$ mm	17.4	27.4	4.29	1.09	78
(3) $z = 95$ mm	16.3	26.3	4.54	1.16	78
(4) $z = 115$ mm	14.8	24.8	4.77	1.23	78

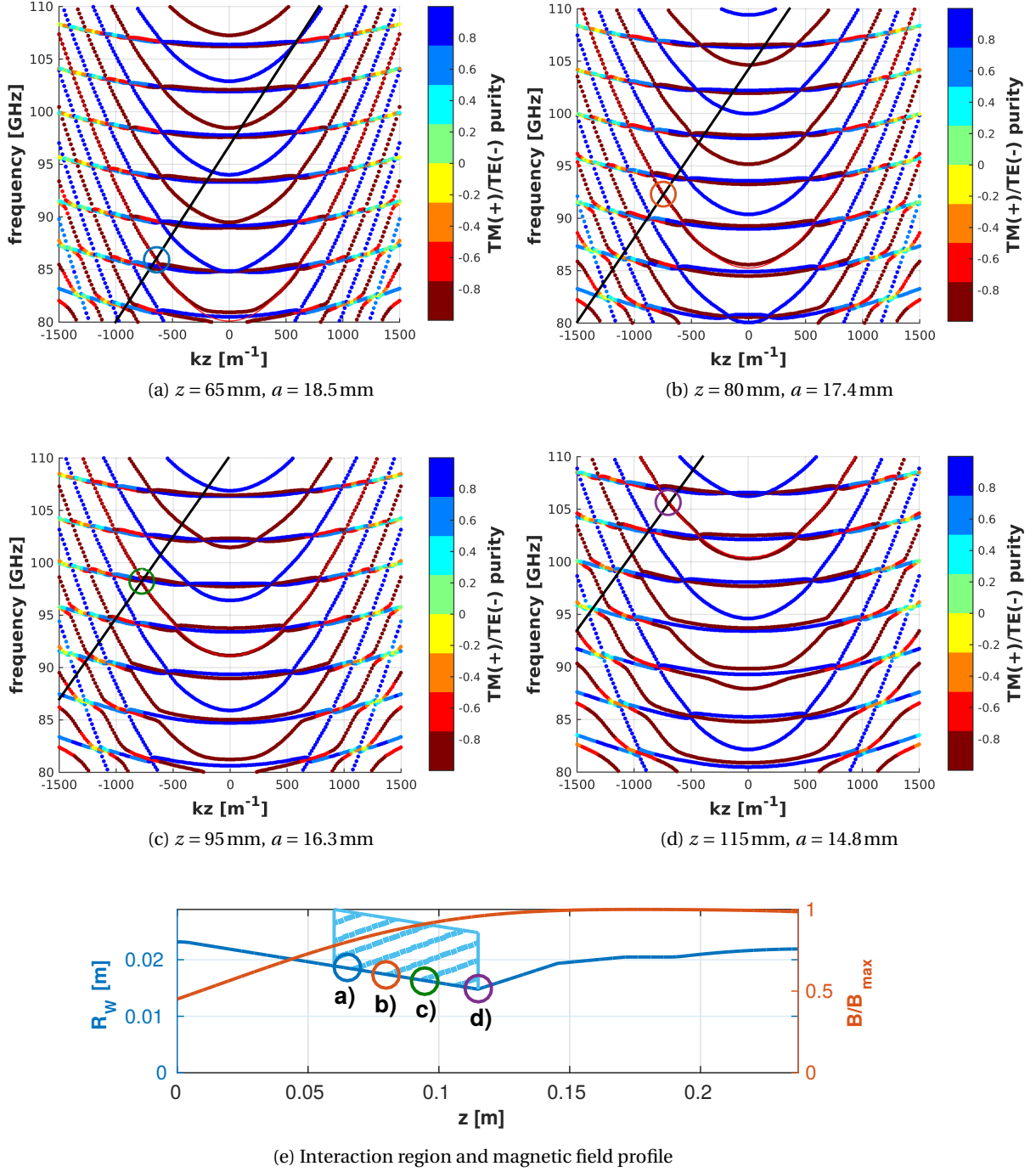


Figure 4.15 – Solutions of the dielectric dispersion relation in the frequency- k_z plane for the four points along the beam duct labelled from a) to d). For each point, the parameters are adapted to the wall radius and magnetic field variation. They are listed in Table 4.5. For each figure, the red thin line indicates the solution corresponding to the $TE_{16,4}$ mode with a metallic boundary condition. The closest electron beam wave intersections, indicated with the colored circles, are the solutions extracted that are used in the self-consistent simulations with TWANGlinspec.

With the solutions extracted from the dielectric dispersion relation, the code TWANGlinspec simulates the self-consistent case with a 10mm thick SiC layer ($\epsilon_r = 12 - 0.72i$) in the last part of the smooth-wall beam duct (cf. Figure 4.16c). Following the same logic as in the metallic case, a scan over a large range of reference frequencies is performed. The mode $TE_{16,4}$ starting current is increasing from 7.6A to 7.9A with the dielectric layer. The amplitude and phase of the electric field profile along z are shown in Figure 4.16. The limited increase in the starting current is explained by the beam-wave interaction occurring mainly in the spacer but also in the cavity. By simulating only the beam duct and the spacer region (excluding the cavity part, cf. Figure 2.10) with the same dielectric layer, the starting current is increased from 24A in the metallic case to 83A with the dielectric layer.

On the other hand, the mode $TE_{19,3}$ interaction with the beam occurs exclusively at the end of the beam duct and in the spacer regions. The effect of the SiC layer in the last part of the beam duct is much more important, increasing the starting current from 19.5A in the metallic case to 110.2A with the SiC dielectric layer. The amplitude and phase profiles in this case are shown in Figure 4.17.

For the 9 other transverse modes, the increase in starting current are reported in Table 4.6 for the case including the cavity and in Table 4.7 for the case considering only the beam duct and the spacer regions. For this later case, with the SiC layer, all the modes have a starting current higher than the operating beam current with the dielectric layer.

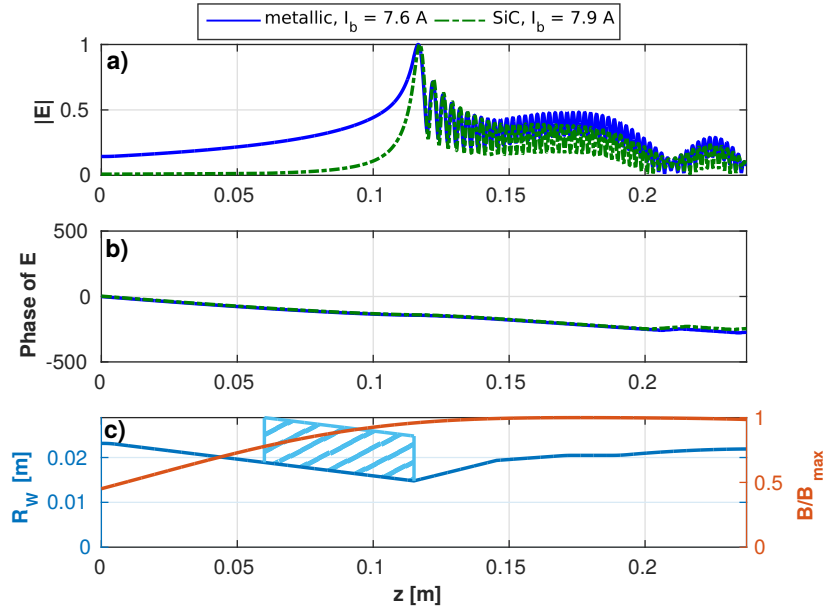


Figure 4.16 – a) and b) Amplitude and phase of the $TE_{16,4}$ mode electric field profile for the case with a 10mm SiC layer (dashed green line) and with a fully metallic boundary condition (continuous blue line). c) Interaction space and magnetic field profile.

Another study, not shown here, showed that a 10mm thick BeOSiC layer has a similar, but

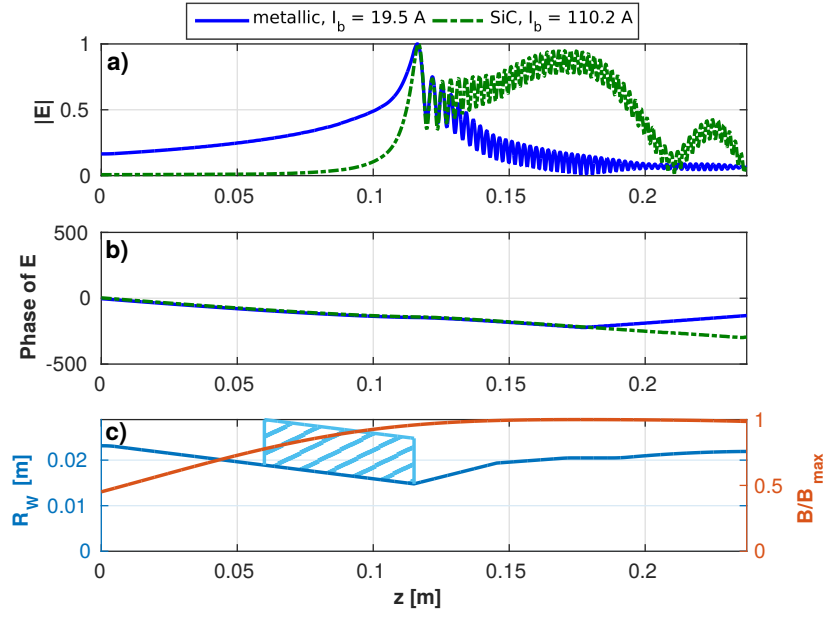


Figure 4.17 – a) and b) Amplitude and phase of the TE_{19,3} mode electric field profile for the case with a 10mm SiC layer (dashed green line) and with a fully metallic boundary condition (continuous blue line). c) Interaction space and magnetic field profile.

Table 4.6 – Starting current calculated with TWANGLinspec for the extended beam duct plus spacer plus cavity case and with a 10mm thick SiC layer in the last part of the beam duct (shown in Figure 4.16c).

Transverse mode	I_{start} [A]		$\frac{I_{start,SiC}}{I_{start,metallic}}$
	metallic	SiC	
TE _{15,4}	3.7	6.7	1.8
TE _{14,4}	4.5	4.5	1
TE _{-13,5}	5.1	6.3	1.2
TE _{16,4}	7.5	7.9	1.1
TE _{10,5}	7.9	9.7	1.2
TE _{11,5}	14.5	25.4	1.8
TE _{-10,6}	15.3	30.4	2
TE _{-14,3}	16.8	21.8	1.3
TE _{19,3}	17.5	110.1	6.3
TE _{-9,6}	21.5	43.1	2
TE _{20,3}	34.8	221.3	6.4

Table 4.7 – Starting current calculated with TWANGlinspec for the beam duct plus spacer geometry case and with a 10mm thick SiC layer in the last part of the beam duct.

Transverse mode	I_{start} [A]		$\frac{I_{\text{start,SiC}}}{I_{\text{start,metallic}}}$
	metallic	SiC	
$TE_{15,4}$	27.2	62.3	2.3
$TE_{14,4}$	33.7	58.2	1.7
$TE_{-13,5}$	31.6	70.1	2.2
$TE_{16,4}$	23.8	83	3.5
$TE_{10,5}$	39.5	49.6	1.3
$TE_{11,5}$	38.1	53.3	1.4
$TE_{-10,6}$	33.9	95.6	2.8
$TE_{-14,3}$	39.7	61.1	1.5
$TE_{19,3}$	29.9	142.3	4.8
$TE_{-9,6}$	39.8	74.2	1.9
$TE_{20,3}$	35.9	248.4	6.9

slightly weaker effect. Various dielectric layer locations have been tried. The first part of the beam-duct doesn't play a role for the suppression of parasitic oscillations, confirming the result using a non-ideal metallic boundary condition (shown in Figure 3.37). Extending the dielectric layer to the spacer region helps to increase even more the parasitic starting current. Nevertheless, the starting current of the mode still interacting in the cavity region stay lower than the operating beam current.

4.6 Conclusion

The beam-wave interaction is solved self-consistently for a realistic situation of a smooth-wall beam duct with a lossy dielectric layer. The layer thickness has to be chosen at least two to three times larger than the wave penetration depth in order to avoid resonance phenomena due to reflections inside the dielectric layer. For the situations treated in this work, the approach consisting in solving the cold dispersion relation with a dielectric boundary condition and using the solution to adapt the transverse electric field profile in TWANGlinspec has been proven to be adequate. The TE-like approximation in TWANG is still valid in all cases treated here and the coupling with TM mode is expected to be weak as the parallel wavenumber is not significant compared to the perpendicular wavenumber. However, mode conversion with surface modes is still possible and not taken into account. Ideally, a self-consistent PIC code treating the full-wave case should be used, although the complexity in treating the full case would be difficult, cumbersome and out of the scope of this thesis.

It has been shown that the dielectric layer has a strong effect on the modes, when the dielectric layer is located near the interaction region. For the modes whose interactions are located exclusively in the beam duct and spacer region, the dielectric layer located in the last part of the beam duct leads to an increase of the starting current to a level higher than the operating

beam current. For the modes with an interaction extended to the cavity, like the $TE_{16,4}$ mode, the effect is less marked. For these modes two important effects suggest that they are also not excited in a realistic situation. First, as they mainly exist in the cavity, if excited, they would likely compete and be suppressed by the main interaction in the cavity. Our monomode code could not treat this case. Secondly, it has been shown in chapter 3 that the velocity spread has a strong effect on the starting current of these modes, since they have a significant Doppler shift.

Considering this fact, in a realistic situation with a dielectric layer and a non ideal electron beam (i.e. with velocity spread), no parasitic modes are expected to be excited in the beam duct.

5 Start-up scenario studies

A start-up scenario study [65, 90] consists of predicting the modes excited during the start-up phase of a gyrotron operation. During this phase, the gyrotron parameters, such as the cathode/anode voltages or beam currents, are varying to reach their nominal value. As an illustration, the evolution of these parameters is reported in Figure 5.1 for a typical start-up with the dual-frequency gyrotron for TCV. In particular in this case, the slow evolution of the anode voltage due to the power supply characteristics leads to the excitation of a competing mode. Note that we are considering the case of a triode-gun start-up, where the control of the modulation anode voltage permits to adjust the pitch factor α value. This is not the case for an electron gun with a diode-gun configuration, thus limiting the different start-up scenarios possible. The main interaction parameters, the beam current and the pitch factor are varying slowly and reach their nominal value only after 25ms (cf. Figure 5.1 b) and c)). During their evolution, after 15ms, they are such that they reach the self-excitation condition of a competing mode. This is observed as a rf-signal is measured at this time at the output of the gyrotron, with a different frequency as the nominal mode, as shown in Figure 5.1 d). Once the nominal parameters are reached, the main mode is excited. The excitation of competing modes is an essential issue in gyrotron operation. The gyrotron, and in particular the launcher/mirror and windows parts are in general designed for one operating mode (or a finite number of mode, 2-4, for multi-frequency gyrotrons [27, 106–108]). In case a transverse mode, not part of the design modes, is excited, it is not correctly converted in the launcher and the radiated rf-power would mostly remain trapped in the gyrotron and generate strong outgassing in the ion pumps.

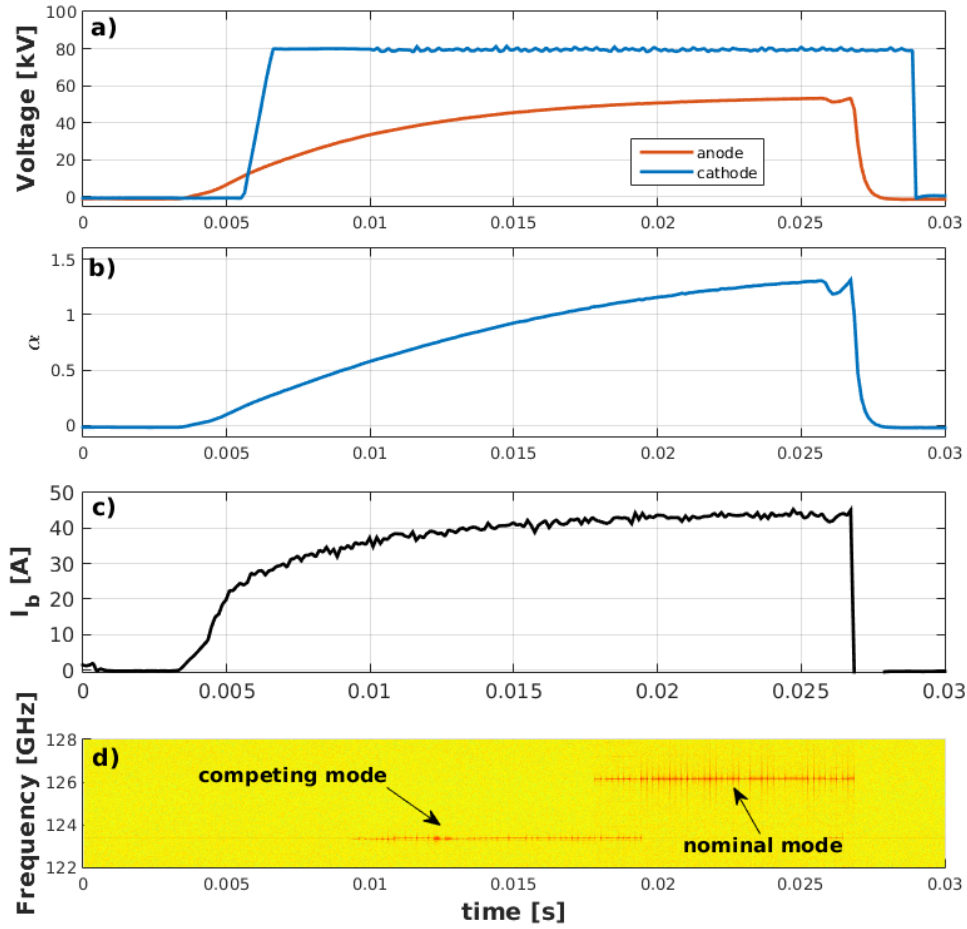


Figure 5.1 – Measurements of the anode (red) and cathode (blue) voltage (a) during the ramp-up phase of the dual-frequency gyrotron for TCV. b) Calculated pitch factor. c) Measured beam current. d) Spectrogram of the rf-signal measured with a Schottky diode located close to the window, outside of the gyrotron.

The code TWANGLinspec has been adapted to compute the starting current during the start-up phase by following the accelerating voltage and the pitch angle α for each time steps considered. The pitch angle is estimated for each time step with a first order approximation, taking into account the voltage variation and the magnetic field compression. It is first tested by comparing it with start-up studies done on the SPC 118-GHz gyrotron used for third harmonic X-mode heating in TCV. Two other studies are presented afterwards. The first one involves a 1.5MW 110-GHz gyrotron used at MIT and the second one concentrates on the dual-frequency start-up issue presented above.

5.1 SPC 118-GHz gyrotron

Following the work presented in [90, 109] on the 118-GHz gyrotron for TCV, the code TWANGlinspec has been tested for the start-up studies. It was shown that depending on the evolution of the cathode and anode voltage variation during the start-up phase, the competing mode $TE_{-19,7}$ could be excited and thus affect the excitation of the operating mode $TE_{22,6}$. Choosing the same parameters (reported in Table 5.1) and for the pitch angle variation reported in Figure 5.2, the starting current for the two modes $TE_{22,6}$ and $TE_{-19,7}$ is calculated with TWANGlinspec and shown in Figure 5.2 as a function of the beam energy. The simulations presented in [90] are based on fixed field calculation, i.e. non self-consistent simulations in which the rf-field profile is calculated solving the wave equation (2.5c) without the source term. The comparison of the starting currents calculated non-self-consistently and with TWANGlinspec is made in Figure 5.2. The agreement between the fixed field simulations and the self-consistent simulations is good in the region of interest, where the beam line first crosses the starting current line. In this situation, the operating mode $TE_{22,6}$ is expected to be excited first. Nevertheless, the fixed field and self-consistent simulations deviate for other beam energy values. A self-consistent treatment of the interaction is thus preferable.

Table 5.1 – Parameters used for the starting current calculations presented in Figure 5.2.

Parameters	Value
Magnetic field maximum	4.71 T
Wall conductivity	$1.45 \cdot 10^7 \text{ S/m}$
Beam radius	9.61 mm
Modes considered	$TE_{22,6}$ $TE_{-19,7}$
Pitch angle	varying (see Figure 5.2 b))

It is also found that the competing mode $TE_{-19,7}$ has a starting current lower than the operating mode for two ranges of beam energy, around 68 keV and 75 keV. If the start-up scenario is such that the beam line first crosses these lines, then the competing mode $TE_{-19,7}$ is expected to be excited first.

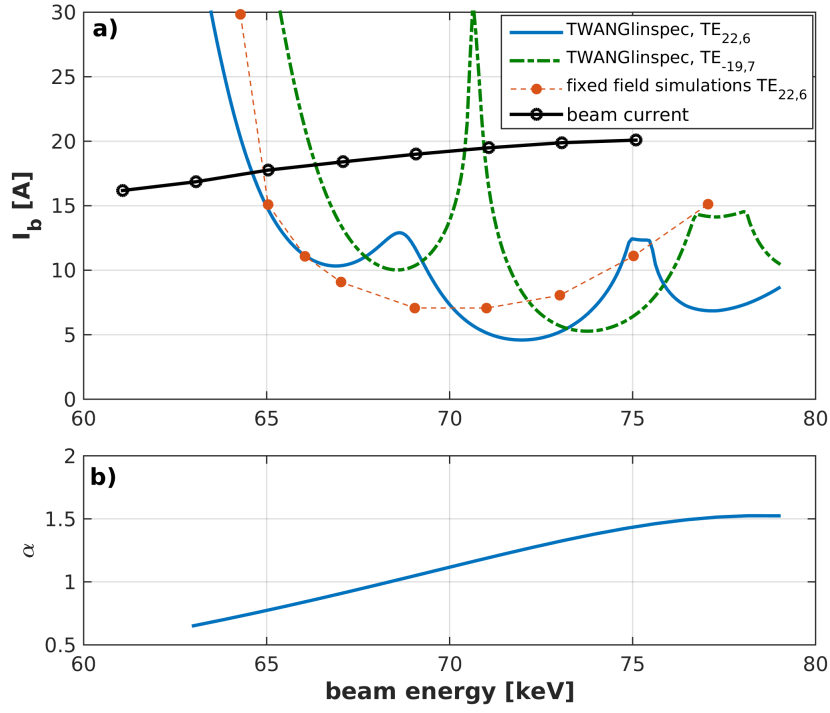


Figure 5.2 – a) Starting current calculated with TWANGlinspec for the operating mode $TE_{22,6}$ and the competing $TE_{-19,7}$ mode in function of the beam energy. The orange line with dots is the results of the fixed field calculations presented in [90], whereas the black line is the beam current. b) Pitch factor as a function of the beam energy. The parameters are listed in Table 5.1.

5.2 MIT 110-GHz gyrotron

Another start-up study has been carried out based on the experimental results obtained with the the 1.5MW, MIT 110-GHz gyrotron described in the paper by Tax *et al.* [110]. In the experimental results presented in this paper, it has been shown that during the start-up phase, the $TE_{21,6,4}$ mode is excited before the nominal $TE_{22,6,1}$ mode. As a reminder, the third index q in a transverse mode $TE_{m,p,q}$ is associated to the axial eigenmode and is called a longitudinal mode in the following. For this study, the cavity profile and the parameters described in Table 5.2 have been used. The system parameters are reported in Table 5.2, while the cathode voltage U_{cat} and the pitch factor α evolution during the start-up phase are shown in Figure 5.4a. Before considering the real magnetic field profile, a uniform magnetic field has been used for the starting current calculation. The two magnetic field profiles as well as the cavity profile are presented in Figure 5.3.

The starting current of the first longitudinal mode to be excited for the two transverse modes $TE_{21,6}$ (continuous blue line) and $TE_{22,6}$ (dashed green line) are shown in Figure 5.4b and 5.4c, respectively. The red line is the beam current measured experimentally. Following the time axis, the first intersection between the measured beam current and one of the starting current line indicates which mode is expected to be excited first. In the case of the constant magnetic field, the first mode to be excited is the $TE_{21,6,4}$. This is in good agreement with the experiment [110]. However, with the real magnetic field profiles B_{real} shown in Figure 5.3, the mode $TE_{21,6,q}$ has a larger starting current than the $TE_{22,6,q}$ mode and is not expected to be excited. Even though the magnetic field profile varies slightly in the cavity region (2% maximum relative difference), the starting current curve for the $TE_{21,6,q}$ mode is significantly different.

Table 5.2 – Parameters used for the starting current calculations.

Parameters	Value
Magnetic field maximum	4.38 T
Wall conductivity	$1.45 \cdot 10^7 \text{ S/m}$
Beam radius	10.1 mm
Modes considered	$TE_{21,6}$ $TE_{22,6}$
Cathode voltage	varying (see Figure 5.4a)
Pitch angle	varying (see Figure 5.4a)

Another aspect to consider, in particular when such parameter sensitivity is observed, is the voltage depression associated to electron beam space charge [111–113]. The results including the voltage depression indicate a strong dependence on the accelerating voltage, especially for the $TE_{21,6,q}$ modes. These two parameter studies [31] illustrate that for the start-up scenario studies, where reliable information on the starting current is needed, a precise knowledge on the experimental parameters is required. Finally, including the error bars on the system parameters one could account for any disagreement between theory and experiment.

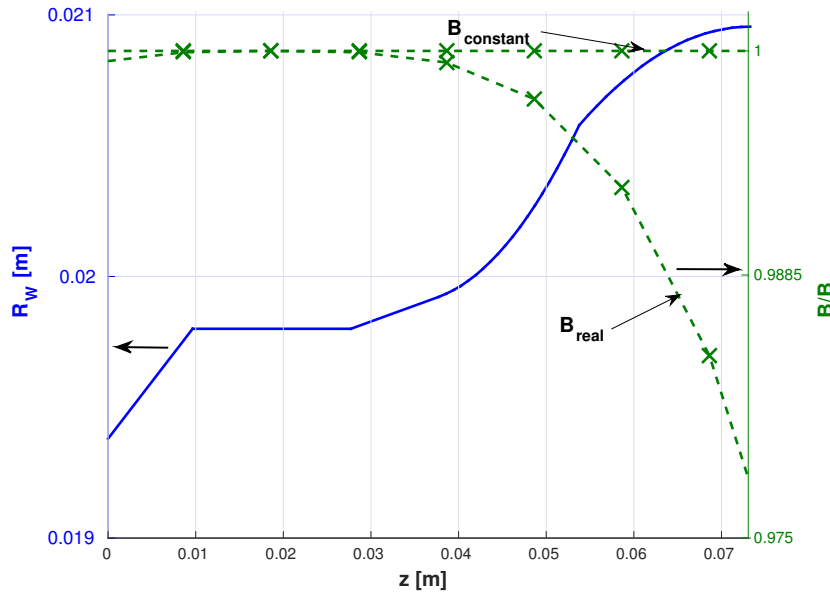


Figure 5.3 – Longitudinal profile of the MIT 110-GHz gyrotron cavity (in blue) and normalized magnetic field profiles used for the calculations (in green).

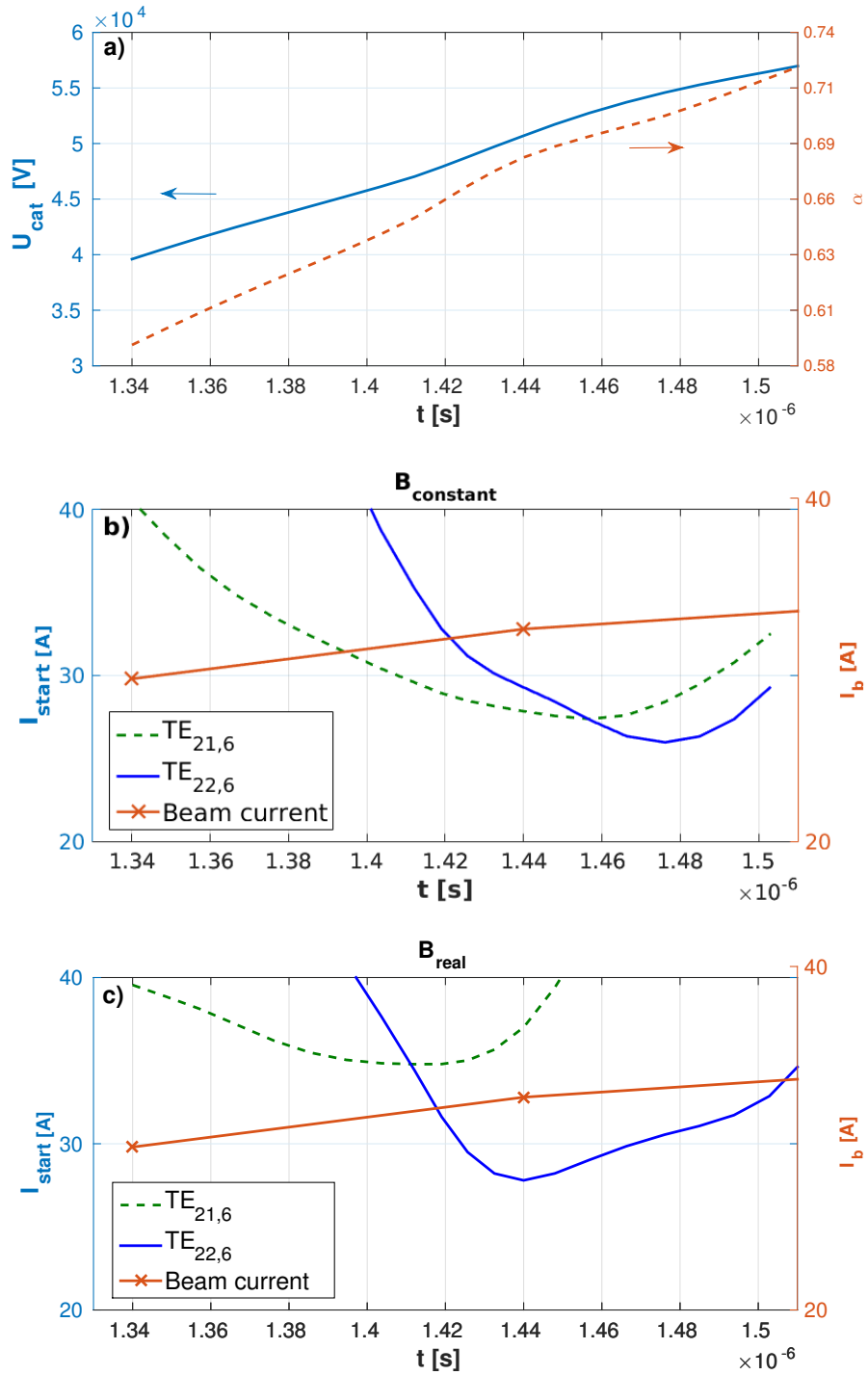


Figure 5.4 – a) Cathode voltage and pitch factor variation during the start-up phase. For this case, no voltage depression is considered. b) and c) Starting current calculated for the two modes $TE_{21,6}$ and $TE_{22,6}$ for the parameters in Table 5.2 and for the uniform b) and varying c) magnetic profiles. The red line is the experimental beam current.

5.3 SPC dual-frequency gyrotron

Finally, a start-up study has been carried-out in support of the first experimental campaign for the dual-frequency gyrotron for TCV [27]. Both for the lower (84 GHz) and higher (126 GHz) frequency, competing modes have been observed during the start-up phase. By comparing experiments and simulations, it has been found that by varying the beam radius, the effect of the competing mode on the operating mode could be reduced, but not completely avoided.

The code TWANGlinspec has been used to study a real situation, corresponding to a 20 ms, 1 MW pulse at the higher frequency (126 GHz). The simulation parameters are reported in Table 5.3 and the anode voltage variation, measured during the start-up, is shown in Figure 5.6 c). From this variation and taking into account the magnetic compression due to the magnetic field profile, the pitch angle is calculated and shown in Figure 5.6 d). As the cathode voltage nominal value ($V_k = 80$ kV) is already reached at the beginning of the start-up, a constant value is considered. The voltage depression associated with the electron beam space charge [111] is estimated to be around 7 kV, so that the beam energy is taken to be 73 kV. The starting current calculated with TWANGlinspec for a series of transverse modes selected according to their geometrical coupling factor (see Figure 5.5) are shown in Figure 5.6 a) together with the measured beam current (in black). The rf signal measured by a Schottky diode situated close to the gyrotron window is shown in Figure 5.6 b). At the same location, a heterodyne receiver scales down the frequency and permits to use a fast oscilloscope in order to perform fast spectroscopy. The spectrogram of the signal is shown in Figure 5.6 e). From the simulations, the first mode to be excited is the competing mode $TE_{25,7}$ at 125.35 GHz around $t = 10$ ms. The operating mode ($TE_{26,7}$) is expected to be excited at 126.14 GHz around 5 ms later. The measurements shown in Figure 5.6 e) are in excellent agreement with the simulations. From the measurements, it is found that there is a short period with the excitation of both the competing $TE_{25,7}$ and the operating $TE_{26,7}$ modes. After this short period, the mode competition is responsible to the suppression of the competing mode and only the operating mode is excited.

Table 5.3 – Parameters used for the starting current calculations.

Parameters	Value
Magnetic field maximum	4.97 T
Wall conductivity	$1.45 \cdot 10^7$ S/m
Beam radius	10.5 mm
Cathode voltage	80 kV
Beam energy	73 kV
Pitch angle	varying (see Figure 5.6)

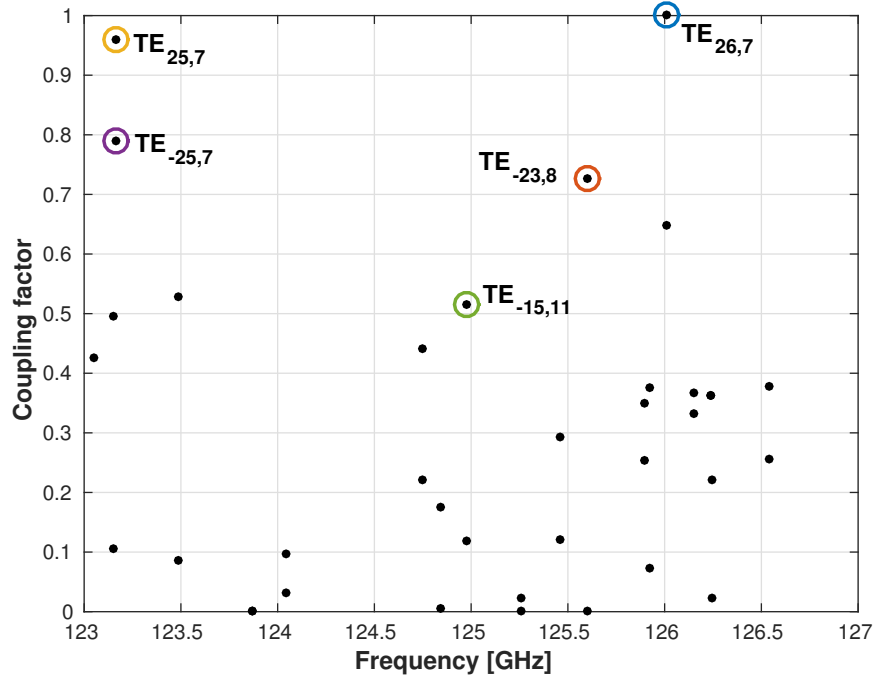


Figure 5.5 – Beam coupling factor for different transverse $TE_{m,p}$ modes for the dual-frequency gyrotron ($R_b = 10.5$ mm, $R_W = 20.48$ mm). The modes highlighted with color circles are the modes considered in the start-up studies (cf. Figure 5.6). Additional modes with large coupling factor have also been considered in the study, but as they do not play an important role and for more clarity, they are not highlighted here or shown in Figure 5.6.

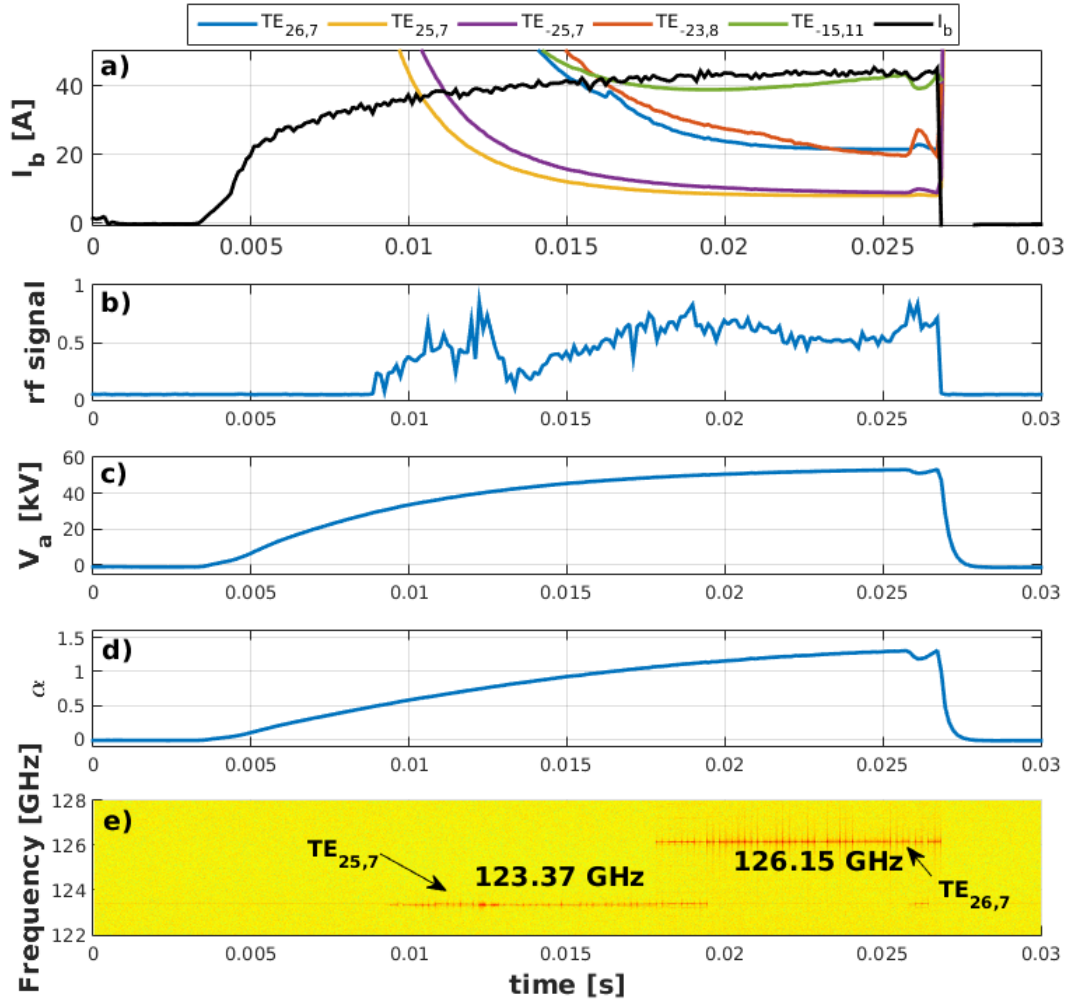


Figure 5.6 – a) Starting current calculated with TWANGlinspec for different transverse modes. The measured beam current is shown in black. b) rf signal measured. c) Anode voltage measured. d) Pitch factor estimated. e) Frequency measured with the heterodyne mixer.

From these observations, it was decided to install a solid state fast switch on the anode power supply in order to shorten the start-up. The switch allows for a very fast rise of the anode voltage, as can be seen in Figure 5.7 b). With this fast ramp-up, the competing mode is still expected to be excited first, but the excitation conditions for the operating mode are reached much faster, after 0.5 ms, as can be seen in Figure 5.7 a). The new setup has been tested successfully at the very late stage of this thesis. The beam current shown in Figure 5.7 a) has been estimated.

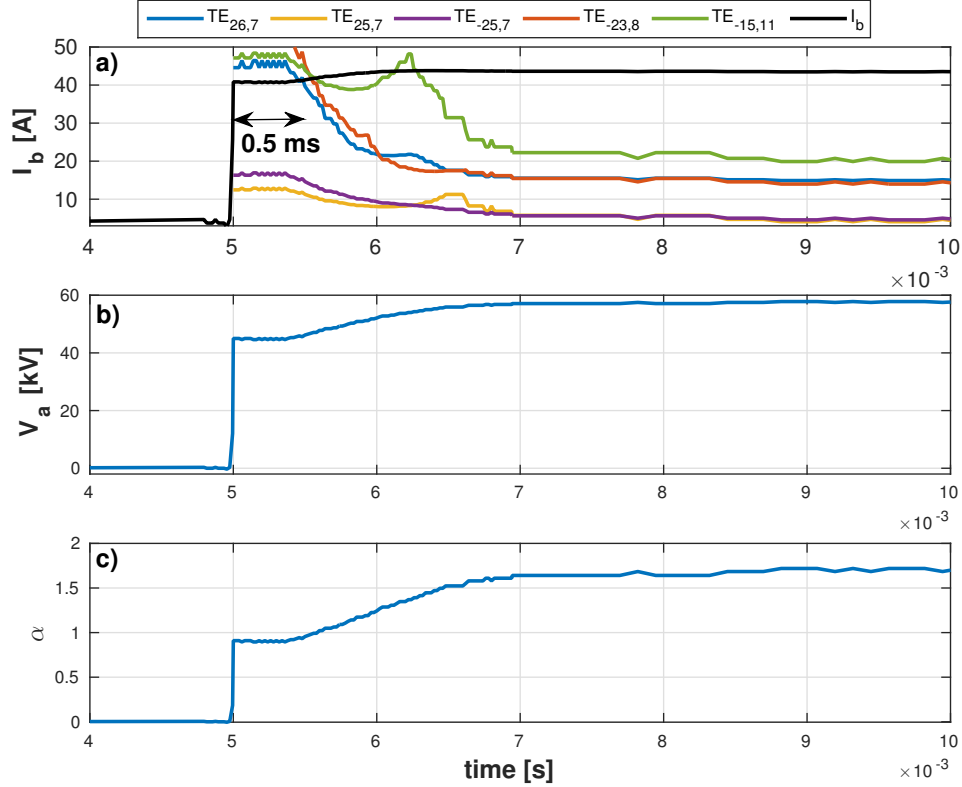


Figure 5.7 – a) Starting current calculated with TWANGlinspec for different transverse modes. The estimated beam current is shown in black. b) Anode voltage measured. c) Pitch factor calculated.

Conclusion

These three start-up studies, and in particular the last one considering the dual-frequency gyrotron for TCV, further validate TWANGlinspec. In the first study, for this specific start-up, a good agreement between the non self-consistent and the self-consistent simulations is found. Nevertheless, the discrepancies between the two models for different parameters indicate that a self-consistent treatment should be considered even for the forward-wave regime in which high-power gyrotrons are operated. The studies on the MIT 110-GHz gyrotron show

that a precise knowledge on the experimental parameters, in particular the magnetic field profile and the voltage depression associated to electron beam space charge, is required for the simulations. If this condition is fulfilled, as in the third study considering the dual-frequency gyrotron for TCV, the code TWANGlinspec can be used to simulate reliably different start-up scenario. The numerical efficiency of the code TWANGlinspec allows to perform the studies in parallel to the experiments. The code is then used to optimize the start-up scenario by determining the conditions under which the competing modes excitation is avoided or alleviated.

6 Conclusion

With the addition of the new linear and spectral code TWANGlinspec and the linear version including velocity and energy spreads in the electron beam properties TWANGlinspread [86], the modelling capabilities of gyrotron have been significantly extended. This set of codes now form a useful set of complementary codes permitting to treat self-consistently, from the linear to the non-linear regime, the beam-wave interaction in the cavity of a gyrotron, but also in the beam duct and spacer regions ahead of the cavity. For the beam-wave interaction occurring in the gyrotron cavity, TWANGlinspec has been validated several times with experiments. In particular, an excellent agreement is found between simulation and experiment for the TCV dual-frequency gyrotron [27] start-up studies. The extension of the interaction region, from the cavity to the beam duct and spacer regions, where the geometry and magnetic field are strongly inhomogeneous, constitutes a novelty. Due to these inhomogeneities, the numerical implementation of TWANGlinspec, initially developed for studying the interaction in the gyrotron cavity only, has been deeply revisited and improved. The moment and spectral approaches used in TWANGlinspec, together with the spatial discretization using hybrid finite elements, has the advantage to be numerically efficient for starting current calculations and permits extensive scan studies involving a large number of transverse modes.

For a realistic high-power gyrotron, the extended interaction region, including an envelope smooth-wall approximation of the beam duct and the real spacer and cavity geometry, starting current for more than 1400 transverse TE modes have been calculated. For the TCV dual-frequency gyrotron [27] without any spread in the electron beam and with a metallic boundary condition, more than 328 modes have a starting current value lower than the operating beam current, meaning that they could be excited. The vast majority of these parasitic modes are gyro-backward wave modes excited in the spacer between the beam duct and the cavity. The role of the spacer for parasitic oscillation studies is also an important new result of the thesis. The excitation of these modes, according to nonlinear simulations with the code TWANG shows that the parasitic modes excited in the beam duct and spacer regions are deleterious for the electron beam quality. They induce a significant spread in the electron beam energy before it enters the cavity, leading to a strong decrease in the cavity interaction efficiency. As

expected for backward-wave interaction with nonzero parallel wavenumbers, the excitation of these parasitic modes depends strongly on the electron-beam velocity spread. This has been studied with the code TWANGlinspread. Multimode simulations with the code EURIDICE [68] show that the mode competition could play an important role on the excitation of parasitics. Eventually, one of the parasitics survives and strongly affects the operating mode.

The thesis presents for the first time a self-consistent treatment of the beam-wave interaction in the beam duct region including a dielectric coating. In this work, the transverse profile of the EM field is calculated from the cold dispersion relation for an infinite homogeneous cylinder with a lossy dielectric layer. Whenever a dielectric layer is taken into account, the transverse TE/TM modes become hybrid HE/HM modes. Nevertheless, the backward wave interactions responsible for the parasitic oscillations excitation are occurring close to the cutoff and the modes remain almost pure TE or TM modes. The transverse TE mode profile is adapted accordingly in TWANGlinspec and the self-consistent treatment is performed. The effect of a SiC or BeOSiC dielectric layer on the starting current of the parasitic modes is found to be important, if the dielectric layer is placed where the main beam-wave interaction takes place. In a real case, only the beam duct part could be dielectric coated. Its effect is thus significantly larger for parasitic oscillations excited in the beam duct and spacer part than for the parasitic oscillations with an extended interaction region including the cavity. As the interaction does not take place in the first part of the beam duct, this part is found to have almost no effect on the parasitic oscillation.

With the combined effect of losses due to the dielectric coating in the beam duct and a realistic electron beam velocity spread, the starting current of the parasitic oscillations is exceeding the operating beam current. No parasitic oscillation is expected to be excited for this realistic situation.

A significant effort is still to be dedicated to avoid or suppress the parasitic oscillations in gyrotron beam ducts, both numerically and experimentally. Theoretically, a full-wave self-consistent code to consider the beam-wave interaction in a complex structure consisting of ceramic and metallic rings is currently developed [114, 115]. At KIT, experiments and simulations on fully metallic smooth-wall beam ducts and on beam tunnels with slots are ongoing. Concerning SPC, the implementation of the new transverse-field formulation in the presence of a lossy dielectric layer in the codes TWANG, TWANG-PIC and TWANGlinspread would extend even more the modelling capabilities. Based on the results presented in this thesis, an experiment is foreseen with a fully dielectric SiC smooth-wall beam duct in the KIT 170GHz/1MW short-pulse gyrotron [116]. Comparing these measurements with measurements using the fully metallic smooth-wall beam duct and the corresponding simulation results will be an essential step in the view of including a smooth-wall SiC beam duct in future European high-power gyrotrons.

A Mode conversion calculation

The propagation of a wave in a tapered structure is subject to mode conversion [117]. This mode conversion could be important for the steep wall tapering considered in the smooth-wall beam duct studies. In order to evaluate the mode conversion level, a scattering matrix formalism [101] has been used. The model is approximating the structure by a large number of cylinders with different diameters, each of them represented by a scattering matrix. A Gaussian profile with a given width is considered and the system is solved in the form of an eigenvalue problem. The output mode purity and the resonance frequency are calculated.

The case studied here is the extended spacer plus cavity region of the European 170 GHz gyrotron for ITER [8, 103]. The code TWANGlinspec predicts the excitation of the transverse mode $TE_{-23,7}$ at 150 GHz for a beam current as low as 4 A. The interaction is in the backward regime. The longitudinal field profile as well as the geometry and magnetic field profile for this gyrotron are shown in Figure A.1. As the mode is only situated in the spacer plus cavity region, only this part has been selected for the study, as reported in Figure A.2. Only the transverse modes $TE_{23,p}$ and $TM_{23,p}$, with $p \in [1, 10]$ have been included in the calculation. For each mode, the field reflection and transmission level calculated are reported in Table A.1. The electric field amplitude of the modes are shown in Figure A.3.

The mode conversion level calculated is on the order of 15%, mainly in the two modes $TE_{23,6}$ and $TE_{23,8}$. This moderate level of mode conversion is still acceptable for our studies, using models neglecting the mode conversion.

Appendix A. Mode conversion calculation

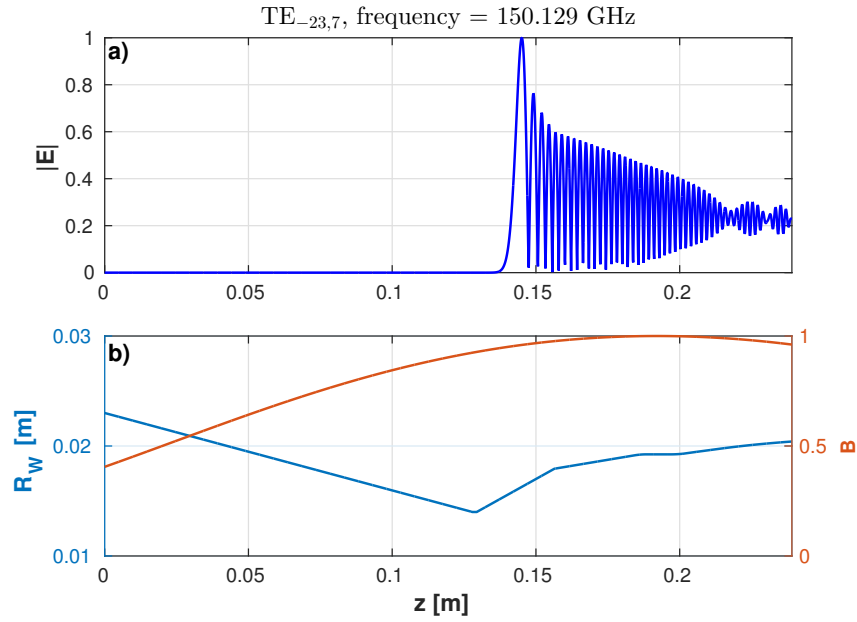


Figure A.1 – a) Amplitude of the electric field profile for the parasitic mode TE_{-23,7} for a current slightly exceeding the starting current. b) Interaction space and magnetic field profiles.

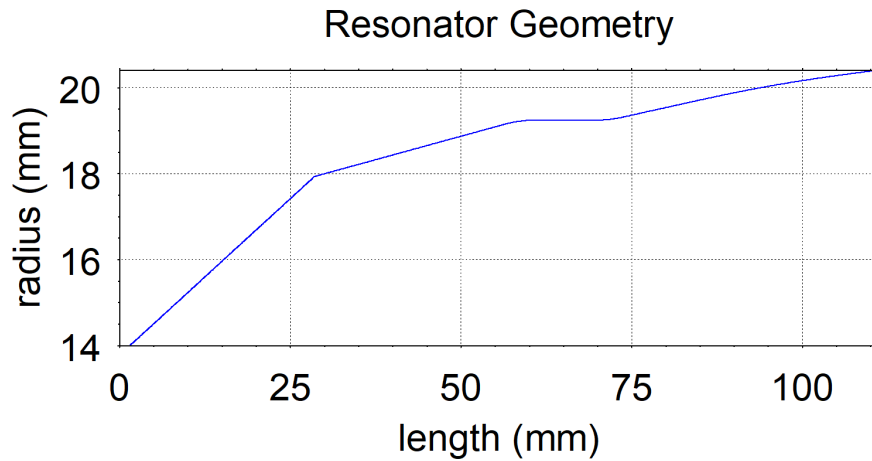


Figure A.2 – Geometry considered in the calculation. As the electric field is only situated in the spacer plus cavity region (cf. Figure A.1), the beam duct part has been removed.

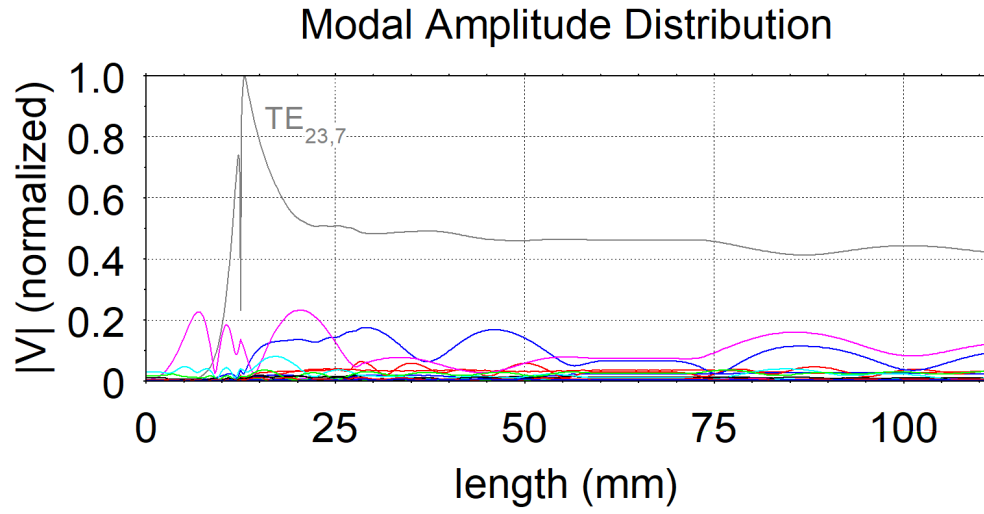


Figure A.3 – Amplitude of the electric field for the different modes.

Table A.1 – Reflection and transmission values for the different transverse $TE_{23,p}$ and $TM_{23,p}$ considered in the calculation.

Mode	Reflection [%]	Transmission [%]
$TE_{23,1}$	< 0.01	0.01
$TE_{23,2}$	< 0.01	0.04
$TE_{23,3}$	0.06	0.02
$TE_{23,4}$	0.12	0.63
$TE_{23,5}$	0.22	0.07
$TE_{23,6}$	< 0.01	7.78
$TE_{23,7}$	< 0.01	84.88
$TE_{23,8}$	< 0.01	3.57
$TE_{23,9}$	< 0.01	0.44
$TE_{23,10}$	< 0.01	< 0.01
$TM_{23,1}$	< 0.01	0.01
$TM_{23,2}$	< 0.01	0.03
$TM_{23,3}$	< 0.01	0.04
$TM_{23,4}$	0.01	0.01
$TM_{23,5}$	0.06	0.59
$TM_{23,6}$	< 0.01	1.13
$TM_{23,7}$	< 0.01	0.16
$TM_{23,8}$	< 0.01	0.07
$TM_{23,9}$	< 0.01	< 0.01
$TM_{23,10}$	< 0.01	< 0.01

B Surface impedance needed to suppress the parasitic oscillations

As a test case the study on the parasitic oscillation occurring in the beam duct, the code TWANGlinspec has been compared with the results presented in [76]. In [76], a spectral code is used to simulate the parasitic oscillations in a smooth-wall conical beam duct. The surface impedance needed to stabilize the parasitic is estimated. The stabilization criteria is found when the wave growth rate changes sign, from a positive to a negative value.

The conical section and the parameters given in [76] are used for the calculations. They are listed in Table B.1 and the geometry and magnetic field profiles are shown in Figure B.1.

The surface impedance needed to suppress the transverse mode $TE_{24,6}$ calculated with TWANGlinspec and the one presented in [76] are in a qualitative good agreement. They are shown in Figure B.2. The discrepancies could be associated with a difference in the profiles considered, as they are not fully described in [76]. As observed several times during the thesis, small variation on some parameters could have large effects on the interactions.

Table B.1 – Parameters used for the calculations.

Parameters	Value
Transverse mode	$TE_{24,6}$
Magnetic field maximum	5.6 – 7.2 T
Beam radius	9 mm
Beam energy	80 keV
Beam current	68 A
Pitch angle	1.5

Appendix B. Surface impedance needed to suppress the parasitic oscillations

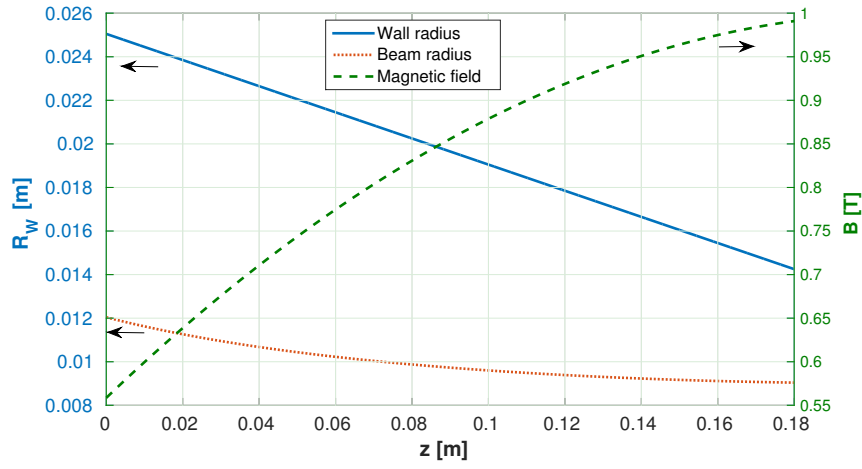


Figure B.1 – Interaction space, magnetic field profile and beam radius considered in the calculation.

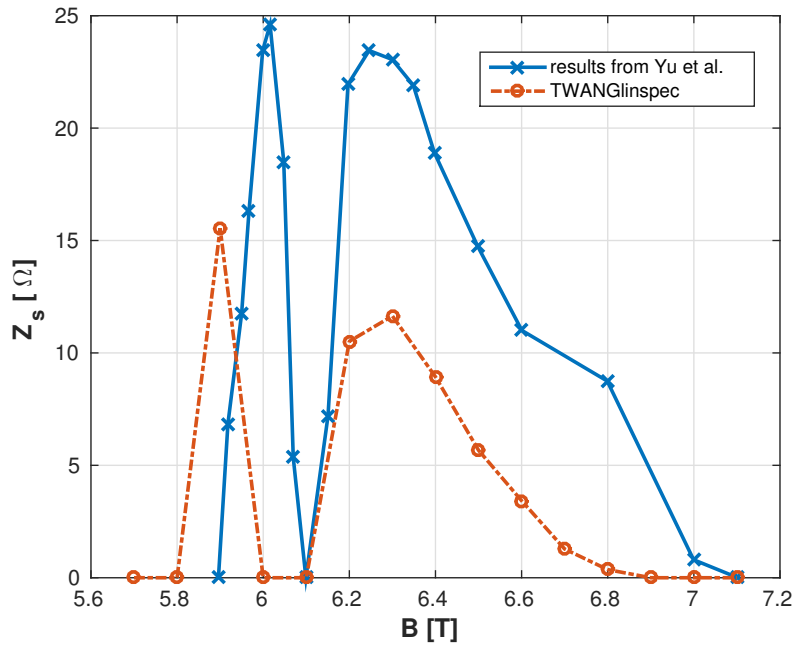


Figure B.2 – Surface impedance needed to suppress the transverse mode $TE_{24,6}$ for the parameters listed in Table B.1. The results from [76] are shown with the continuous blue line while the results from TWANGlinspec are shown with the dashed red line. The local minimum, around $B = 6$ T corresponds to a situation where the mode is stable with a perfectly conducting metallic wall.

C Dielectric permittivity measurements for BeOSiC and SiC materials

In this section, the method used to measure the dielectric properties of BeOSiC and SiC materials are described and the results of the measurements are presented. These measurements are used for the simulations including the dielectric layer in chapter 4. The work has been carried out by Angelica Ottaviano under the supervision of Jean-Philippe Hogge and Stefano Alberti. First the measurement method and the experimental setup are described in section C.1. The measurement results both for BeOSiC and SiC materials are then presented in section C.2 and C.3.

C.1 Measurement method

The method used to measure the complex permittivity is briefly described here. The sample is exposed to an incident electromagnetic field and the reflection and transmission coefficients are measured. The scattering matrix formalism for a two port junction is used and it is represented in Figure C.1. The reflection coefficient (parameter S_{11}) and the transmission coefficient (parameter S_{21}) are measured and the technique described in [118] is used to calculate the complex permittivity values of the sample.

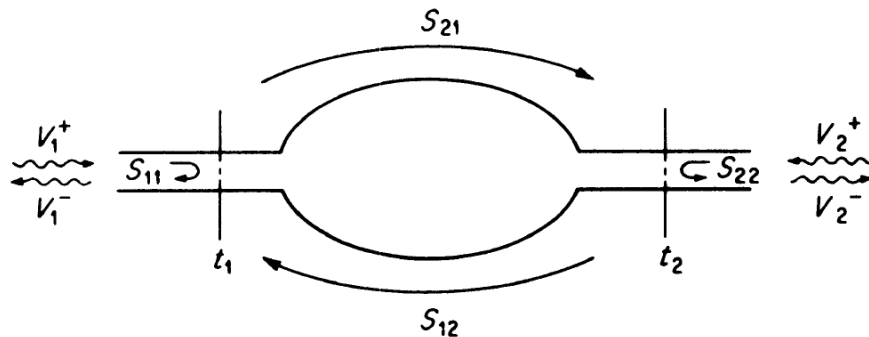


Figure C.1 – A two-port junction. Figure from [119].

C.1.1 Measurement setup

To measure the scattering parameters S_{11} and S_{21} , a commercial vector network analyzer (VNA) is used. VDI extension heads (WR 6.5 110 – 170 GHz) are connected and calibrated to the VNA with the Swissto12 Material Characterization Kit (MCK) connected between the transceiver and receiver modules. The MCK is normalized with a full transmission, when the ports are connected without the sample, and zero transmission when the ports are connected with a short in between.

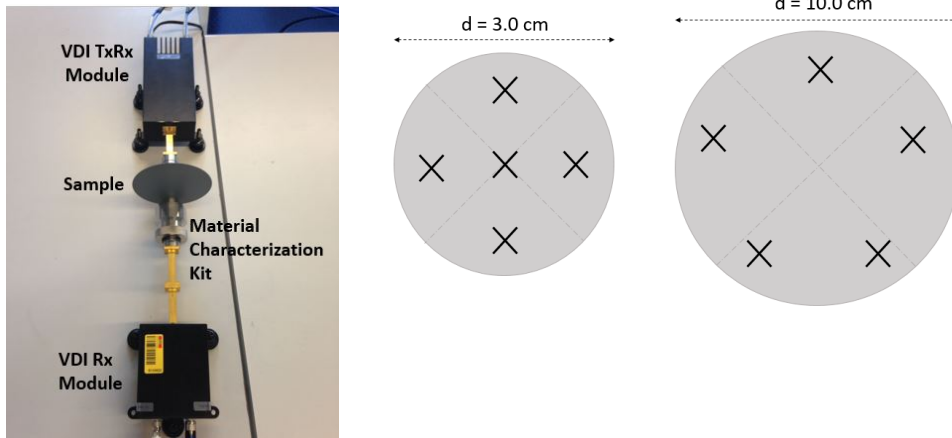


Figure C.2 – (Left) Measurement setup using VDI frequency extension modules and Swissto12 material characterization kit. (Right) Measurement locations for the two different type of samples.

The sample thickness are measured ten times using a micrometer and the transmission and reflection parameters are measured 5 times at 5 different locations. Two types of samples have been measured, with 3 and 10 cm diameter. The measurement locations are shown in Figure C.2b.

C.1.2 Error analysis

The errors are due to the measurements of the S parameters by the VNA, to the sample thickness uncertainty (ΔL), to the sample positioning into the MCK holder and to the sample temperature.

The relative uncertainties introduced by the scattering parameters and by the sample thickness ΔL to the real (ϵ') and imaginary (ϵ'') part of the permittivity are found using a differential uncertainty analysis [118, 120]. The derivatives are calculated explicitly, assuming that the complex relative permeability is $\mu_r = 1$. and using a cutoff frequency $f_c = 90.79$ GHz. The relative uncertainties due to the measurements of S_{11} and S_{21} are first evaluated separately and then combined to find the total error which follows from the equations used to calculate

C.2. Dielectric properties measurements for BeOSiC samples

the permittivity [118].

$$\Delta\epsilon'_{r,11} = \epsilon'_r \sqrt{\left(\frac{\partial\epsilon'_r}{|\partial S_{11}|} \Delta|S_{11}|\right)^2 + \left(\frac{\partial\epsilon'_r}{\partial\theta_{11}} \Delta\theta_{11}\right)^2 + \left(\frac{\partial\epsilon'_r}{\partial L} \Delta L\right)^2}, \quad (\text{C.1a})$$

$$\Delta\epsilon'_{r,21} = \epsilon'_r \sqrt{\left(\frac{\partial\epsilon'_r}{|\partial S_{21}|} \Delta|S_{21}|\right)^2 + \left(\frac{\partial\epsilon'_r}{\partial\theta_{21}} \Delta\theta_{21}\right)^2 + \left(\frac{\partial\epsilon'_r}{\partial L} \Delta L\right)^2}, \quad (\text{C.1b})$$

$$\Delta\epsilon'_{r,\text{tot}} = \sqrt{(\Delta\epsilon'_{r,11})^2 + (\Delta\epsilon'_{r,21})^2}. \quad (\text{C.1c})$$

In these equations θ is the scattering parameter phase. Analogous expressions can be found for the imaginary part of the permittivity (ϵ''). An analysis of each term in the $\Delta\epsilon'$ expressions reveals that on average, 88% of the total permittivity error is due to the uncertainty in magnitude of the S-parameter, 10% is due to the uncertainty in the phase of the S-parameter and only 2% is due to the sample thickness uncertainty. The measured thickness uncertainty is estimated to be 0.2% (variation of 1.5 μm) across the sample area and does not significantly affect the permittivity values. The dominant error therefore is due to S-parameters errors, which can be reduced by time gating on tighter intervals and securing the sample to port connections.

C.2 Dielectric properties measurements for BeOSiC samples

The dielectric properties have been measured for three different BeOSiC samples listed in Table C.1. First, the dependency on the frequency and on the temperature are shown in subsections C.2.1 and C.2.2, then the characteristic penetration depth and reflection coefficients are calculated and shown in subsection C.2.3.

Table C.1 – BeOSiC samples information.

Origin, Lot no.	Material Composition	Diameter [cm]	Thickness [mm]	# Samples
Thales 17988	BeO (60%) SiC (40%)	3.0	0.255±0.001	5
Thales 17195	BeO (60%) SiC (40%)	3.0	0.254±0.001	2
Kit 17711	BeO (60%) SiC (40%)	10.0	0.254±0.002	1

C.2.1 Frequency dependencies

Thales 17988

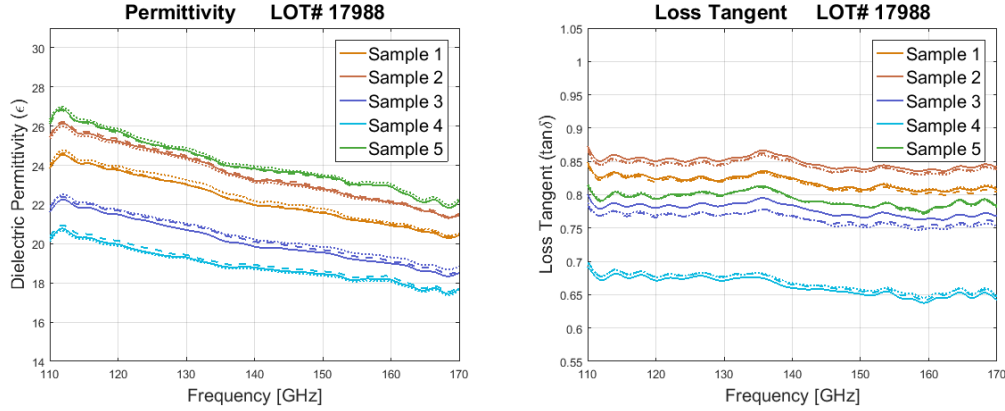


Figure C.3 – (Left) Relative permittivity and (Right) loss tangent measured for the five BeOSiC samples from Lot#17988. For each sample, three of the five measurements are represented by continuous and segmented lines of the same color.

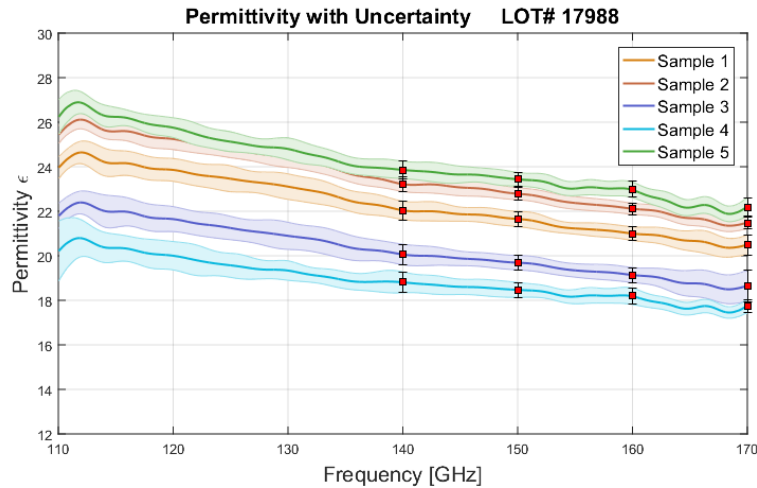


Figure C.4 – Average permittivity values measured for each samples versus frequency. The shaded areas show the uncertainties above and below the average. Red data points are shown at 140, 150, 160 and 170GHz.

Table C.2 – Permittivity measured for lot # 17988

Lot 17988	Mean thickness [μm]	ϵ at 150GHz	% Error of ϵ	ϵ at 170GHz	% Error of ϵ
1	258.6	21.66	1.6	20.47	2.2
2	254.2	22.78	1.2	21.47	1.3
3	254.0	19.69	1.6	18.64	3.8
4	252.8	18.02	1.8	17.74	1.7
5	253.8	23.44	1.3	22.18	1.9

Thales 17195

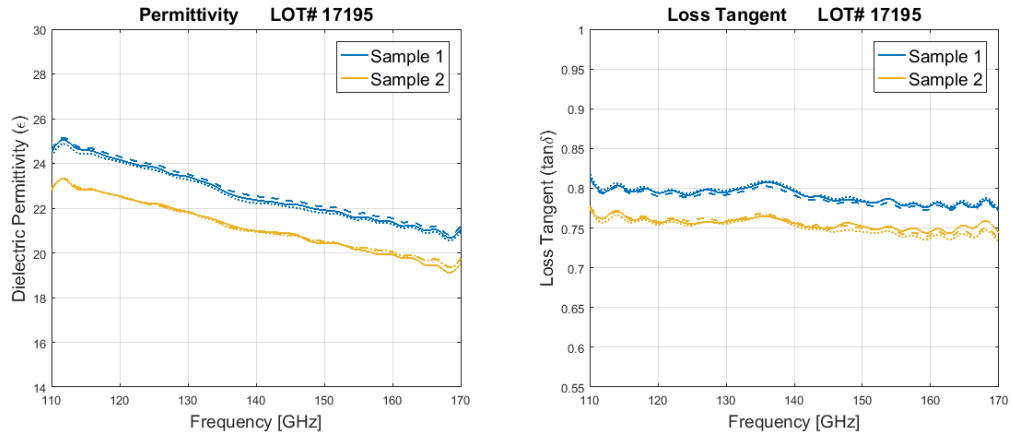


Figure C.5 – (Left) Relative permittivity and (Right) loss tangent measured for the two BeOSiC samples from Lot#17195. For each sample, three of the five measurements are represented by continuous and segmented lines of the same color.

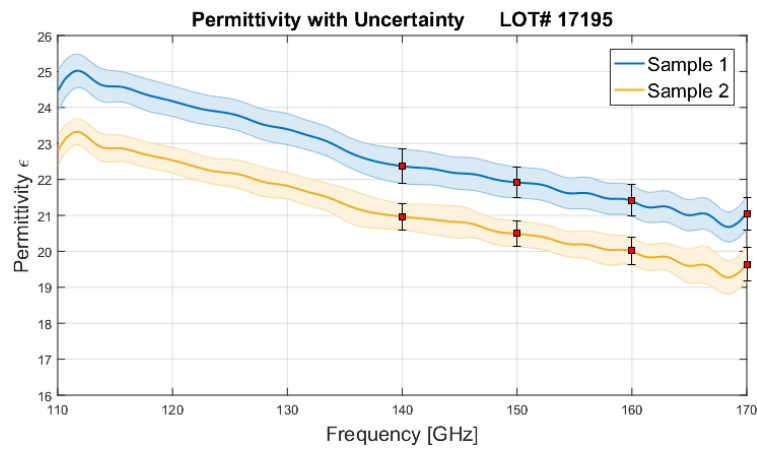


Figure C.6 – Average permittivity values measured for each samples versus frequency. The shaded areas show the uncertainties above and below the average. Red data points are shown at 140, 150, 160 and 170GHz.

Table C.3 – Permittivity measured for lot # 17195

Lot 17195	Mean thickness [μm]	ϵ at 150GHz	% Error of ϵ	ϵ at 170GHz	% Error of ϵ
1	252.6	21.92	1.7	21.04	2.2
2	255.4	20.49	1.8	19.64	2.4

KIT 17711

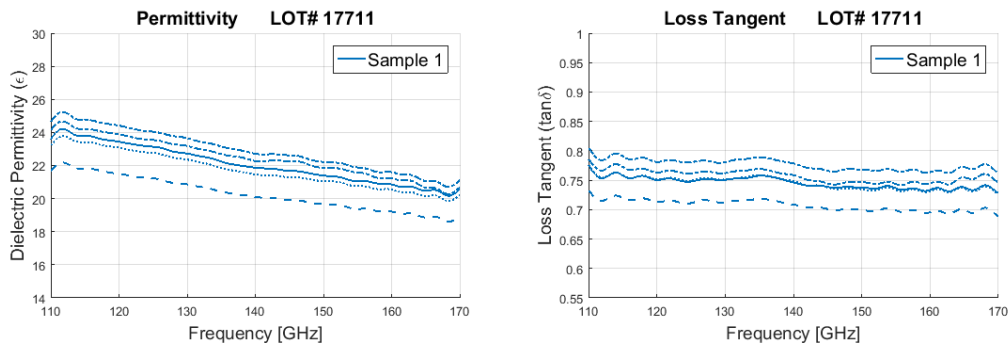


Figure C.7 – (Left) Relative permittivity and (Right) loss tangent measured for the BeOSiC sample from Lot#17711. The five measurements are represented with different line styles.

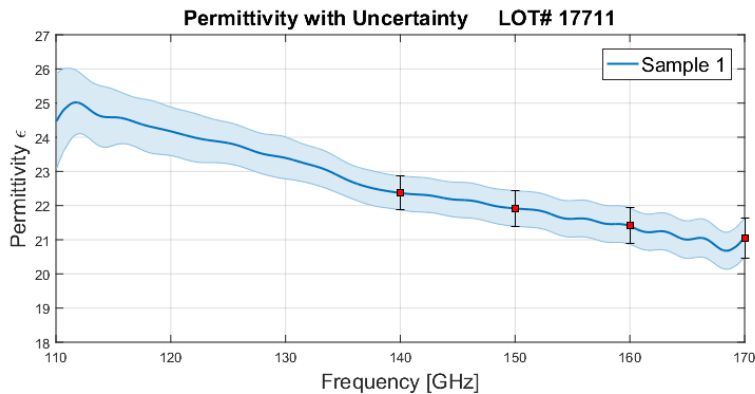


Figure C.8 – Average permittivity value measured versus frequency. The shaded areas show the uncertainties above and below the average. Red data points are shown at 140, 150, 160 and 170 GHz.

Table C.4 – Permittivity measured for lot # 17711

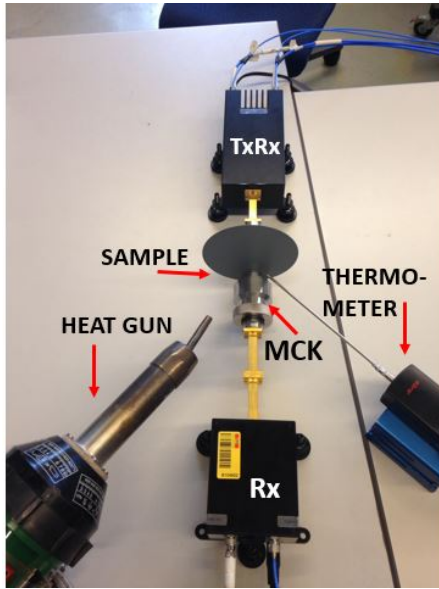
Lot 17711	Mean thickness [μm]	ϵ at 150GHz	% Error of ϵ	ϵ at 170GHz	% Error of ϵ
1	254.4	21.95	2.4	21.10	2.8

Comments on the measurements

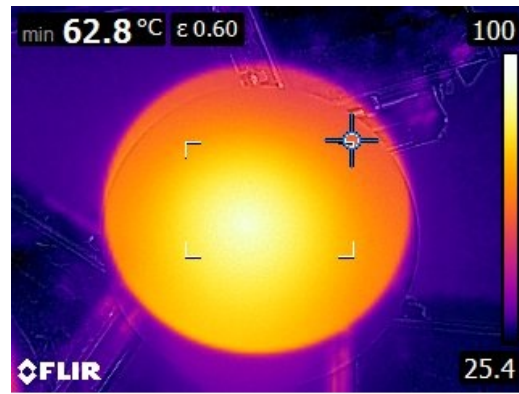
- Time gating was performed on the data around the region connecting the MCK device and the ceramic material. Different time gating may result in smoother raw data and present less errors.
- The spread between measurements of different samples of the same material is real and exceeds the error-bars of measurements taken of the same sample at different locations. This suggests that there is a large variation in material uniformity from one sample to another.
- All the samples show an ϵ in the range of 19 - 24 and decrease with an increase of frequency. Samples from lot 17915 were within a small range of each other, whereas lot 17988 shows the largest range (with most data) which includes 18.93 and 24.13.
- The loss tangent value for all samples averages between 0.70 and 0.80.
- The dominant error was found to be from the S-parameter variation while the error in thickness of the samples only affects the total permittivity error by 2%.

C.2.2 Temperature dependencies

The dielectric properties dependence on the temperature was studied with the same measurement setup. A heat gun with a contact thermometer and infra-red laser thermometer were used to heat the sample and measure the temperature, as well as to monitor the heat distribution across the sample surface as shown in Figure C.9b. Three locations on the edge of the 10cm diameter sample (lot 17711, Thales) were measured and averaged. An initial analysis was made on the heat uniformity of the ceramic by heating the 10 cm diameter BeOSiC sample and measuring the temperature on both surfaces (back and front) of the ceramic as well as using an infra-red camera to visualize heat uniformity. It was found that the temperature on the front and back of the ceramic is uniform within 0.5°C. The temperature was measured from room temperature ($\approx 23^\circ\text{C}$) to 100°C in increments of 10°C .



(a) Measurement setup using VDI frequency extension modules and Swissto12 material characterization kit, heat gun and contact thermometer



(b) 10cm BeOSiC sample shown heated at 62.8°C on its central region through IR camera

As can be seen in Figure C.9, the BeOSiC permittivity increases almost linearly with temperature between 30°C and 100°C from approximately 23.8 to 33.8 at 170 GHz and from 27.7 to 38.3 at 170GHz. The loss tangent decreases by 13.8% between room temperature and 100°C (cf. Figure C.10).

C.2. Dielectric properties measurements for BeOSiC samples

Lot 17711 Thales Sample BeOSiC

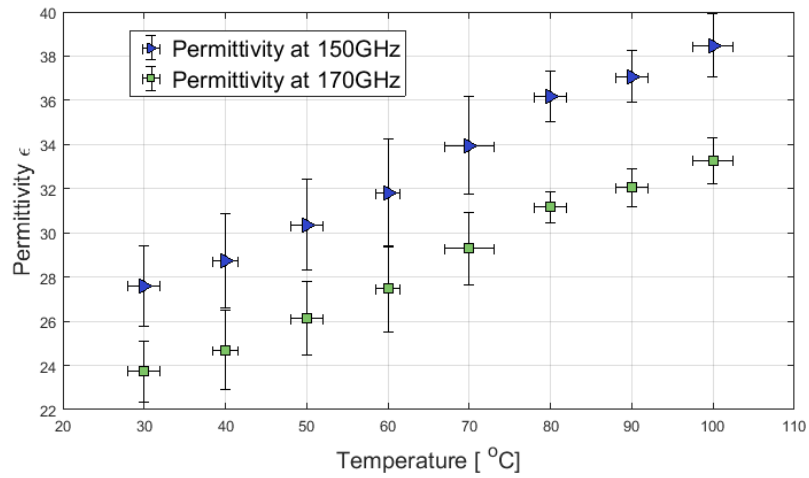


Figure C.9 – Permittivity variation with temperature shown for 150GHz and 170GHz from room temperature to 100°C.

Lot 17711 Thales Sample BeOSiC

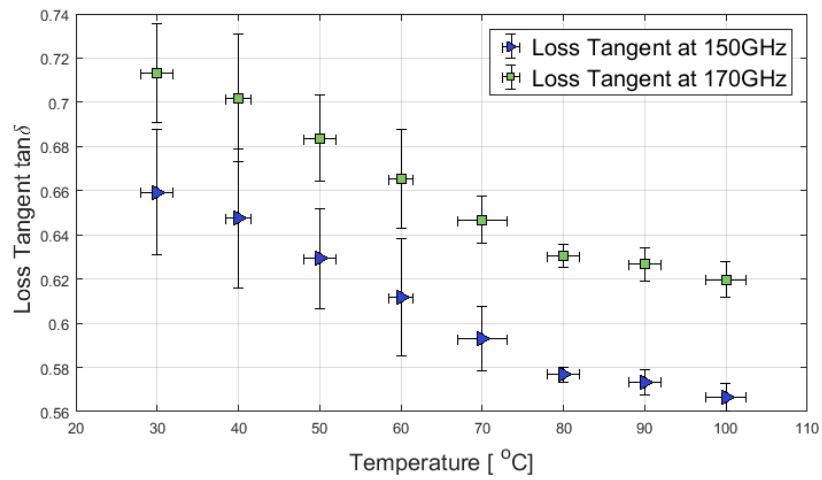


Figure C.10 – Loss tangent variation with temperature shown for 150GHz and 170GHz from room temperature to 100°C.

Table C.5 – Permittivity measured

Temperature [°C]	ε at 150GHz	ε at 170GHz
30	27.80	23.95
60	31.95	27.90
100	38.50	32.25

C.2.3 Characteristic penetration depth and reflection coefficient

The wave penetration depth λ_p is calculated for BeOSiC and SiC using the complex permittivity (real part ϵ_r) and frequency ω .

$$\lambda_p = \left[\frac{2\pi}{\lambda_0} \sqrt{\epsilon_r} \left(\frac{\tan \delta}{2} - \frac{\tan^3 \delta}{16} \right) \right]^{-1}, \quad (C.2)$$

where $\lambda_0 = 2\pi/k$ and $k = \frac{\omega\sqrt{\epsilon}}{c}$. The reflection coefficient R is

$$R = \frac{\sqrt{\epsilon_r} - 1}{\sqrt{\epsilon_r} + 1}. \quad (C.3)$$

The result for BeOSiC is shown in Figure C.11. The penetration depth decreases significantly with temperature, following the fact that the permittivity increases with temperature, while the loss tangent decreases, each by nearly 50%. The penetration depth varies from $195\mu\text{m}$ to $185\mu\text{m}$ showing that the wave is attenuated almost immediately at the interface of the material. This depth is roughly two thirds of the BeOSiC sample thickness. The reflection coefficient increases weakly from 0.65 to 0.70 from RT to 100°C .

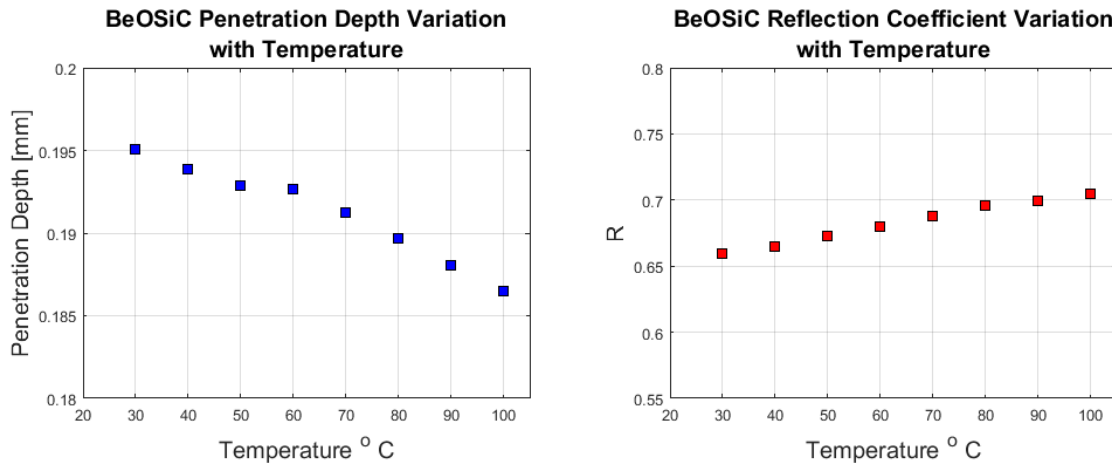


Figure C.11 – Penetration depth (left) and reflection coefficient (right) in function of the temperature for the BeOSiC material.

C.3 Dielectric properties measurements for SiC samples

C.3.1 Frequency dependencies

The same measurements were performed for Cerasic-B Silicon Carbide (SiC) and Thales SiC samples. The sample from Thales has a 5 cm x 5 cm surface and a thickness of approximately 1 cm, while the Cerasic-B sample has a 9 mm thickness. The permittivity and loss tangent measurements are shown in Figure C.12. Both samples have a small dependency on the frequency. For the sample from Thales, 3 different measurements from different locations are shown. The almost identical results show a very consistent material uniformity. The permittivity and loss tangent values between the two samples are comparable.

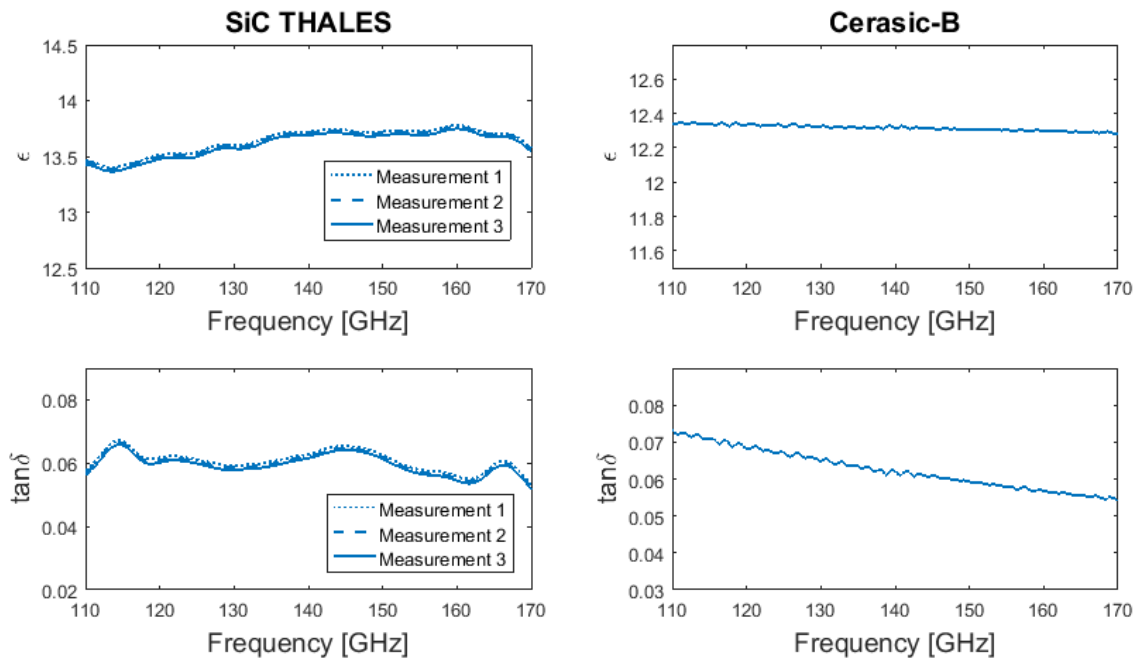


Figure C.12 – Permittivity and loss tangent measurements as function of the frequency for Thales SiC (left figures) and Cerasic-B SiC (right figures). Cerasic-B ϵ is ≈ 12.38 with $\tan\delta \approx 0.062$ while SiC from Thales has $\epsilon \approx 13.6$ and $\tan\delta \approx 0.06$.

Additionally, three types of SiC were ordered from *Ceramids GmbH*. The materials are CS10 (α -SiC), CS10G which has graphite and SiSiC CS11 which has Si infiltrated. The samples are disks with a 5.25 cm radius and 8.5 mm thickness. The results are shown in Figures C.13a, C.13b and C.13c. For the CS10G sample (with Graphite), the results show a large spread in dielectric values for both location across a single sample and between different samples. The largest spread in dielectric properties is found for the CS11 (SiSiC). However, because the VNA data displays almost no transmission in the S_{21} parameter, it is difficult to process the raw data into reliable ϵ and $\tan\delta$ values. The algorithm used to find the results rely on multiple values for S_{21} and S_{11} for different frequencies. For the second sample, the dielectric properties are

Appendix C. Dielectric permittivity measurements for BeOSiC and SiC materials

comparable to the CS10 and CS10G values.

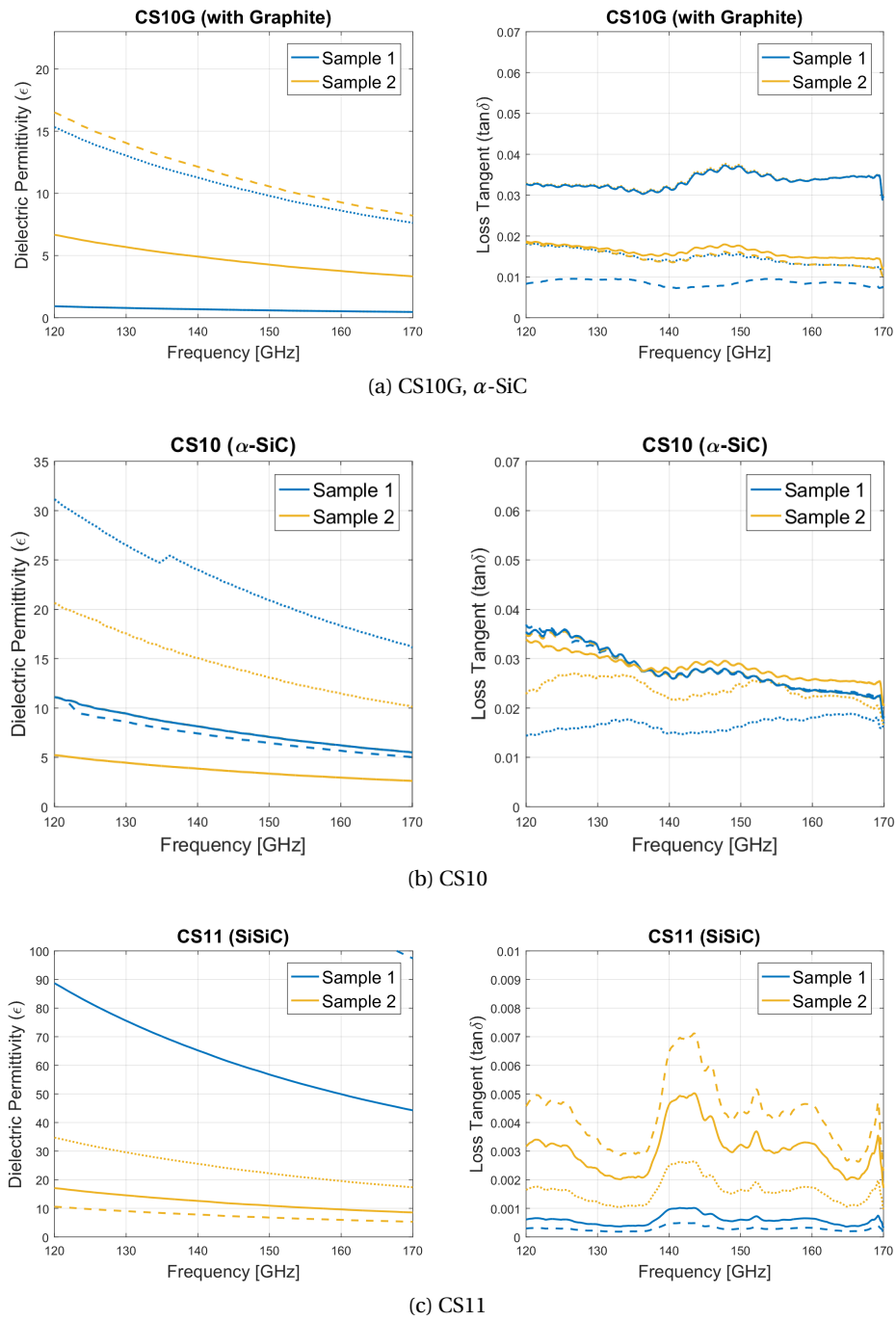


Figure C.13 – Permittivity and loss tangent measurements for two identical samples in each case.

C.3.2 Temperature dependencies

A temperature dependency for the Thales and Cerasic-B SiC was performed. The results are reported in Figure C.14. The temperature dependencies are similar for the two materials. Permittivity in both cases does not show a strong temperature dependence, while loss tangent increases significantly (40% for the Thales SiC and more than 300% for the Cerasic-B SiC).

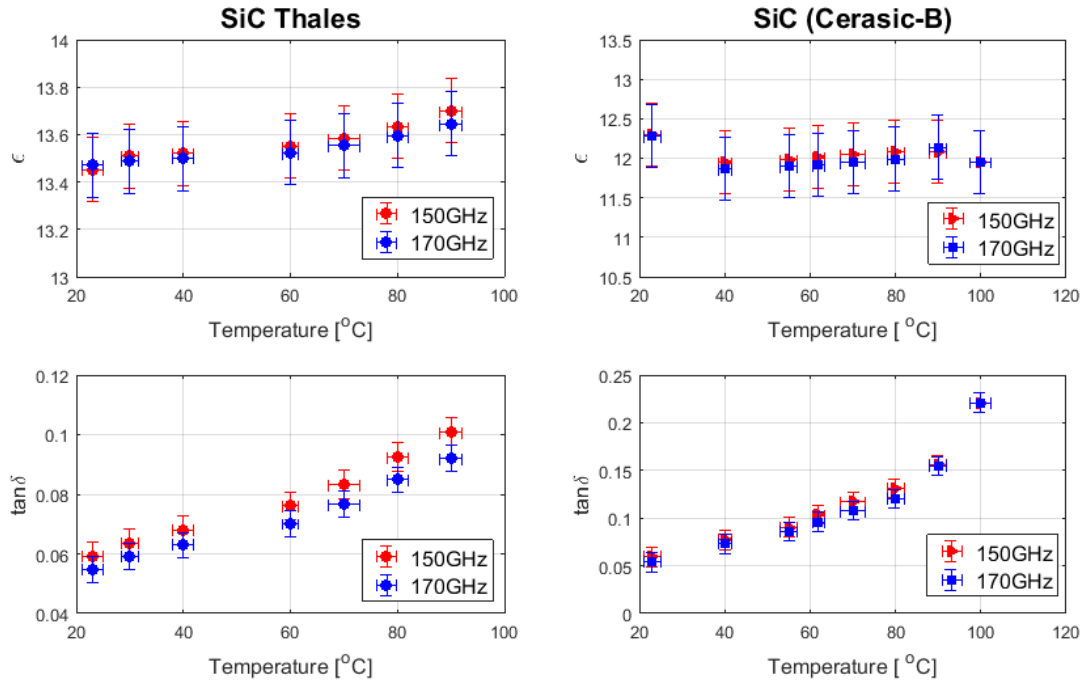


Figure C.14 – Loss tangent variation with temperature shown for 150GHz and 170GHz from room temperature to 90-100°C for the Thales (left) and Cerasic-B (right) SiC samples.

C.3.3 Characteristic penetration depth and reflection coefficient

From these measurements, the characteristic penetration depth and reflection coefficients have been calculated. The values are shown in Figure C.15 for the Cerasic-B SiC. The penetration depth for SiC also decreases significantly with temperature. The penetration depth varies from 3.4 mm to 0.8 mm showing that the wave is attenuated further into the material with respect to BeOSiC. The reflection coefficient is almost constant at 0.55.

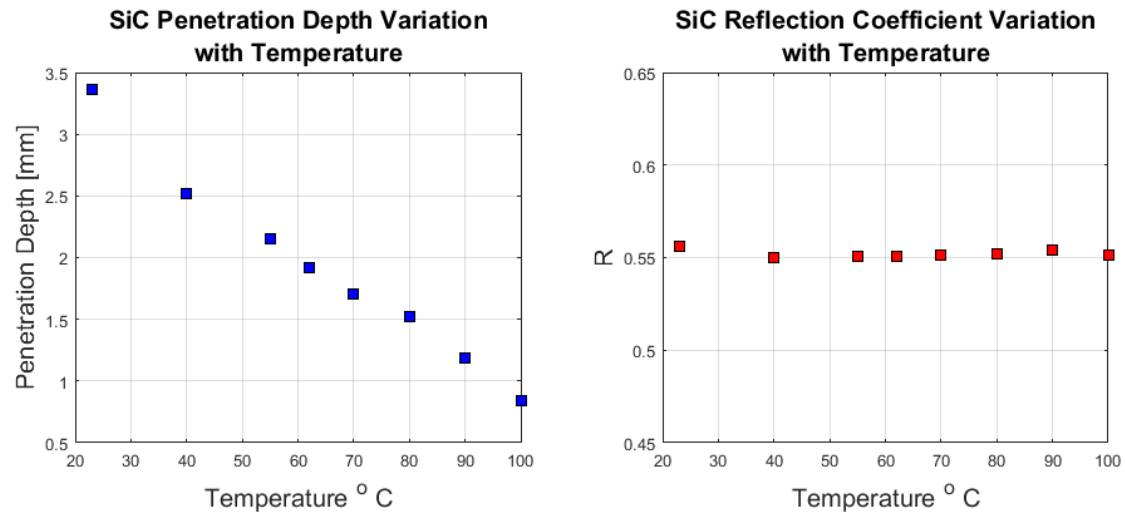


Figure C.15 – Penetration depth (left) and reflection coefficient (right) in function of the temperature for the SiC material.

C.4 Resistivity measurements

To measure the resistivity, a simple circuit was constructed by connecting a power supply to the ceramic sample with an ammeter and voltmeter to measure currents and voltages. A heat gun was also positioned for sample heating to conduct measurements of resistivity with respect to temperature change. The samples were inserted into the circuit by use of copper plates, copper paste and a clamp. To ensure that the entire surface area of the ceramic samples were in contact with the copper plates and minimize error effects in gaps between sample surface and circuit, copper paste was used to mold the sample surface onto the copper plates (sketched in Figure 1). The resistance of the wires, copper plates and copper paste were considered negligible and the resistivity ($\rho = \frac{RA}{L}$) for the ceramic materials was found using:

$$\rho = \frac{VA}{IL} \quad [\Omega \cdot m]. \quad (C.4)$$

The current was varied from 0 - 130mA and the voltage read for each value in steps of ≈ 10 mA. Measurements were also taken as a function of sample temperature: the sample was heated from 0 - 80° and the voltage kept fixed to find how the resistivity varies with T. Each measurement was repeated 4 times for statistical significance and error-bar representation.

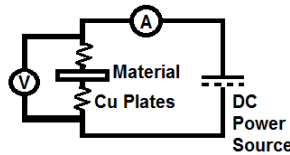


Figure C.16 – Simple DC circuit setup for the resistivity measurements.

Appendix C. Dielectric permittivity measurements for BeOSiC and SiC materials

The resistivity is measured for the three materials listed in Table C.6 and the result is shown in Figure C.17. It is found that for all three materials, the resistivity has comparable values of 1 – 30 kΩm. Furthermore, the resistivity does not have a constant value and a non-Ohmic behaviour is found. Therefore ρ is plotted against voltage. As expected from the materials, there is a temperature dependence showing an increase in conductivity with temperature.

Table C.6 – Samples information.

Manufacturer	Surface Area [cm ²]	Thickness [mm]
SiC (Japan, Ceric-B)	22.09	9.0
SiC (Thales)	18.48	5.0
BeOSiC (Thales)	4.43	3.0

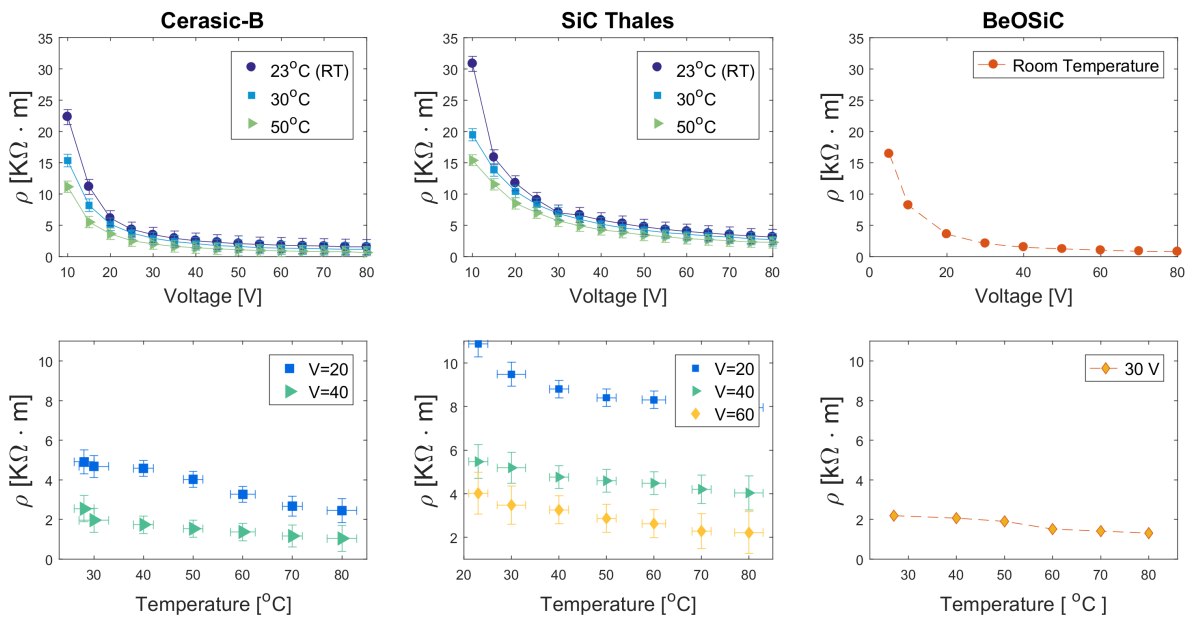


Figure C.17 – Resistivity measured in function of the voltage applied (top figures) and in function of the temperature (bottom figures) for the three materials (Ceric-B SiC on the left, Thales SiC on the middle and BeOSiC on the right).

C.5 Conclusions

In this study, the known and already employed beryllium oxide silicon carbide in stacked dielectrically loaded ring beam duct structures has been characterized at the ITER relevant frequency (170GHz) and compared to the Cerasic-B SiC (or SiC from Thales). Results show significant dielectric difference between the BeOSiC and Cerasic-B materials. In the case of BeOSiC, the ϵ values are higher, and have a stronger dependence on frequency at the WR-6.5 range, decreasing by nearly 20% and presenting errors of up to 4%. The uncertainty analysis made has furthermore shown the principal source of error to derive from S_{11} and S_{21} rather than from sample thickness inconsistencies, which were on the order of $<1\mu m$. Loss tangent values have a weaker frequency dependence and range from 0.68 to 0.9. Furthermore, a larger spread in the measurements is seen for BeOSiC between identical samples and measurements at different sample locations. A temperature dependence of dielectric properties was found for BeOSiC between room temperature and 100°C: the permittivity increases by 60% of its room temperature value while loss tangent decreases by 30% of its room temperature value.

Cerasic-B SiC and Thales SiC have been shown to be dielectrically similar materials by three criteria: good material uniformity (permittivity values within 1% of each other for different measurements), almost no ϵ temperature dependence and weak $\tan\delta$ temperature dependence, and comparable ϵ and $\tan\delta$ absolute values. It is important to note that it is a useful result that temperature dependence is strong for $\tan\delta$ only in the SiC Cerasic and Thales materials, because this could be a useful tool to control or monitor the EM penetration depth into the material in the beam duct. For the Thales SiC samples, the penetration depth is about 3.3mm at room temperature, while for the BeOSiC samples, it is about 0.18mm at room temperature, which is very small compared to the ring thickness in the beam duct structure (≈ 5 mm).

The DC conductivity of all three materials was measured and shown to be comparable and in the range of 5 – 30k Ω m. The SiC materials under analysis are non-Ohmic and have a weak temperature dependence. As expected, conductivity increases with temperature.

SiC materials provided by GoodFellow and Ceramid were also measured and characterized but it was found that the permittivity values are very different from Cerasic-B with almost no material uniformity.

Other considerations are:

- The DC conductivity of all samples presented is being measured as well as X-Ray Spectroscopy to gain more information about material characteristics and specific composition (cf. Figure C.18).
- The dielectric permittivity is measured with no external magnetic field and it is possible that results will vary when analyzed in a 4T magnetic field. The power used from the VNA for these measurements is on the order of 1mW (1 dBm), which is significantly less

Appendix C. Dielectric permittivity measurements for BeOSiC and SiC materials

than the gyrotron power regimes, and temperatures might rise to much larger values than 100°C for those powers.

- Investigation of material properties, such as valence band and conduction band gaps, could be made to better understand the differences between permittivity variation with temperature for SiC and BeOSiC. The behaviour of the two materials is almost opposite; BeOSiC attenuates the incoming waves at the interface of the material and strongly changes properties with temperature. The effect of heat load might be damaging at such an interface. SiC's loss tangent increases weakly from room temperature to 80°C and its permittivity remains almost constant for a large temperature range, which can prove as a useful property for material stability.

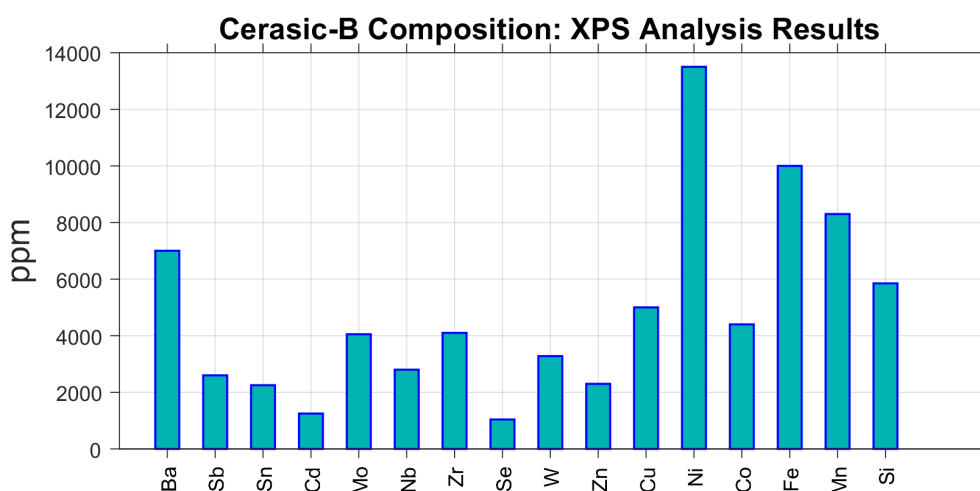


Figure C.18 – XPS performed on Cerasic-B reveals nickel, iron and manganese as the significant dopants.

D Low-power gyrotron for DNP-NMR spectroscopy, the Temperature-Jump experiment

Beside their main application for ECRH and ECCD for fusion reactors, gyrotrons are also used for Dynamic Nuclear Polarization enhanced Nuclear Magnetic resonance (DNP-NMR) spectroscopy [14]. In this application, the electromagnetic radiation permits to transfer the polarization from the electron spins to the nuclear spins, leading to a strong increase in the nuclear magnetization and a stronger NMR signal. As the electron magnetic moment is 660 times larger than for the proton, a comparable enhancement factor in the measured NMR signal could theoretically be reached for DNP-NMR spectroscopy on hydrogen. Experimentally, enhancements on the order of 200 have been reached [121]. Recently at the Ecole Polytechnique Federale de Lausanne (EPFL), the versatility of the gyrotron has been used to further increase this enhancement, either by modulating the radiation frequency [19] or by performing a "Temperature-Jump" DNP [20]. The "Temperature-Jump" DNP consists of combining a hyperpolarization phase at a precise frequency, a thawing phase with a large rf-power in order to melt the sample, and eventually an "off phase", without rf-generation in order to acquire the NMR signal. The transition between the melting phase and the DNP phase has to be more rapid than the nuclear spin relaxation time. The gyrotron allows such fast transition via the cathode and anode voltage control. For a DNP-NMR spectroscopy on ^{13}C sample and with this method, an enhancement as high as 550 has been obtained [20] with the DNP gyrotron designed at the Swiss Plasma Center [16–18]. For this study and as an illustration of the gyrotron flexibility, the Table D.1 contains the parameters in the two phases. The corresponding experimental traces of the cathode and anode voltage as well as the rf-power measured by a Schottky diode are reported in Figure D.1.

Table D.1 – Gyrotron main parameters during the two phases for the DNP-NMR ^{13}C "temperature jump" spectroscopy [20].

Phase	B [T]	I_b [mA]	U_k [kV]	U_a [kV]	P_{rf} [W]	Frequency [GHz]
Melting	9.43	100	14	8	100	260.42
DNP	9.43	100	10	5.5	2	260.63

Appendix D. Low-power gyrotron for DNP-NMR spectroscopy, the Temperature-Jump experiment

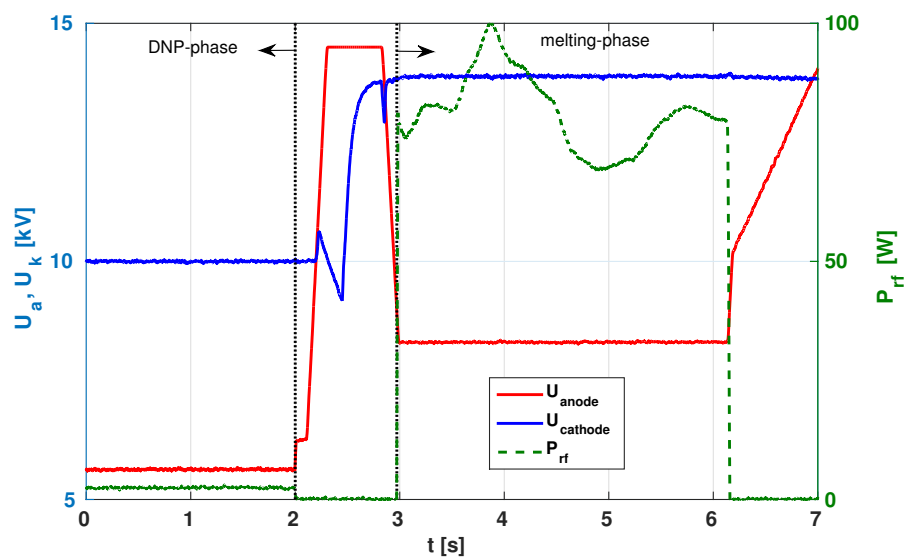


Figure D.1 – Time evolution of the cathode and anode voltages (in blue and red lines) as well as the power measured by a schottky diode (in dashed green) during the two phases of the "temperature jump" DNP-NMR experiment [20].

E Dispersion relation with dielectric layer, formulation with Hankel functions

In the dielectric dispersion relation studies, it has been found that the dispersion relation expressed with Bessel function of the first kind (cf. equation 2.45) are not adequate to treat lossy dielectric layer with large imaginary part of the permittivity constant. A solution has been found by using Hankel functions for the field expressions. The derivation is described here. It follows the derivation in terms of Bessel functions detailed in [43]. First, the definition of the Hankel functions of the first and second kind is recalled, they are a linear combination of Bessel function of the first and second kind:

$$H_n^{(1)}(x) = J_n(x) + iY_n(x), \quad (\text{E.1a})$$

$$H_n^{(2)}(x) = J_n(x) - iY_n(x). \quad (\text{E.1b})$$

The geometry consists in an infinitely long and homogeneous cylinder with a dielectric layer (cf. Figure 2.15). Region 1 is the vacuum region, while Region 2 is the dielectric layer region. For transverse electric TE and transverse magnetic TM modes, the corresponding electric and magnetic vector potential have only a nonzero longitudinal component: F_z and A_z . The Ansatz assumed for F_z , renamed ψ^e , and A_z , renamed ψ^m in both regions are:

$$\psi_n^{m1}(k_{\perp 1} r) = (A_1 H_n^{(1)}(k_{\perp 1} r) + A_2 H_n^{(2)}(k_{\perp 1} r)) \cos(n\phi) e^{-ik_z z}, \quad (\text{E.2a})$$

$$\psi_n^{e1}(k_{\perp 1} r) = (B_1 H_n^{(1)}(k_{\perp 1} r) + B_2 H_n^{(2)}(k_{\perp 1} r)) \sin(n\phi) e^{-ik_z z}, \quad (\text{E.2b})$$

$$\psi_n^{m2}(k_{\perp 2} r) = (C_1 H_n^{(1)}(k_{\perp 2} r) + C_2 H_n^{(2)}(k_{\perp 2} r)) \cos(n\phi) e^{-ik_z z}, \quad (\text{E.2c})$$

$$\psi_n^{e2}(k_{\perp 2} r) = (D_1 H_n^{(1)}(k_{\perp 2} r) + D_2 H_n^{(2)}(k_{\perp 2} r)) \sin(n\phi) e^{-ik_z z}, \quad (\text{E.2d})$$

where k_{\perp} and k_z are the perpendicular parallel wave number and A , B , C and D are the amplitude that have to be determined. The electric field \vec{E} and magnetic field \vec{H} are calculated with the Maxwell's equations:

$$\vec{E} = \frac{1}{i\omega\epsilon} (k^2 \vec{A} + \nabla(\nabla \cdot \vec{A})) - \nabla \times \vec{F}, \quad (\text{E.3a})$$

$$\vec{H} = \nabla \times \vec{A} + \frac{1}{i\omega\mu} (k^2 \vec{F} + \nabla(\nabla \cdot \vec{F})). \quad (\text{E.3b})$$

Appendix E. Dispersion relation with dielectric layer, formulation with Hankel functions

By imposing the continuity conditions in the tangential field components at the interface of region 1 and 2 ($E_{z_1} = E_{z_2}$, $E_{\phi_1} = E_{\phi_2}$, $H_{z_1} = H_{z_2}$ and $H_{\phi_1} = H_{\phi_2}$), the vanishing tangential electric field component at the external metallic boundary ($E_{z_2} = 0$ and $E_{\phi_2} = 0$) and the fact that the field at $r = 0$ must be finite, the system is reduced to two equations for C_1 and C_2 :

$$\alpha C_1 + \beta D_1 = 0, \quad (\text{E.4a})$$

$$\gamma C_1 + \delta D_1 = 0, \quad (\text{E.4b})$$

where

$$\alpha = \frac{k_z n}{\omega \epsilon_2 a} \frac{Q(k_{\perp_2} a)}{H_n^{(2)}(k_{\perp_2} b)} \left(\frac{k_{\perp_2}^2}{k_{\perp_1}^2} - 1 \right), \quad (\text{E.5a})$$

$$\beta = \frac{k_{\perp_2}}{H_n(k_{\perp_2} b)} \left(\frac{k_{\perp_2}}{k_{\perp_1}} \frac{P(k_{\perp_2} a) J'_n(k_{\perp_1} a)}{J_n(k_{\perp_1} a)} - P'(k_{\perp_2} a) \right), \quad (\text{E.5b})$$

$$\gamma = \frac{k_{\perp_2}}{H_n(k_{\perp_2} b)} \left(Q'(k_{\perp_2} a) - \frac{k_{\perp_2} \epsilon_1}{k_{\perp_1} \epsilon_2} \frac{Q(k_{\perp_2} a) J'_n(k_{\perp_1} a)}{J_n(k_{\perp_1} a)} \right), \quad (\text{E.5c})$$

$$\delta = \frac{k_z n}{\omega \mu_0 a} \frac{P(k_{\perp_2} a)}{H_n^{(2)}(k_{\perp_2} b)} \left(1 - \frac{k_{\perp_2}^2}{k_{\perp_1}^2} \right). \quad (\text{E.5d})$$

The functions P and Q have be defined for clarity:

$$P(k_{\perp_2} a) = H_n^{(1)}(k_{\perp_2} a) H_n'^{(2)}(k_{\perp_2} b) - H_n^{(2)}(k_{\perp_2} a) H_n'^{(1)}(k_{\perp_2} b), \quad (\text{E.6a})$$

$$Q(k_{\perp_2} a) = H_n^{(1)}(k_{\perp_2} a) H_n^{(2)}(k_{\perp_2} b) - H_n^{(2)}(k_{\perp_2} a) H_n^{(1)}(k_{\perp_2} b). \quad (\text{E.6b})$$

Solving the system formed by the equation (E.4a) and (E.4b) lead to the dispersion relation reported in section 2.3.3:

$$\frac{Q(k_{\perp_2} a) P(k_{\perp_2} a)}{\epsilon_2 \mu_0 H_m^{(2)}(k_{\perp_2} a) H_m'^{(2)}(k_{\perp_2} a)} \left(\frac{k_z m}{\omega a} \right)^2 \left(1 - \frac{k_{\perp_2}^2}{k_{\perp_1}^2} \right)^2 + \frac{k_{\perp_2}^2}{H_m^{(2)}(k_{\perp_2} a) H_m'^{(2)}(k_{\perp_2} a)} \zeta \lambda = 0, \quad (\text{E.7a})$$

with

$$\zeta = \frac{k_{\perp_2}}{k_{\perp_1}} \frac{P(k_{\perp_2} a) J'_m(k_{\perp_1} a)}{J_m(k_{\perp_1} a)} - P'(k_{\perp_2} a), \quad (\text{E.7b})$$

$$\lambda = Q'(k_{\perp_2} a) - \frac{\epsilon_2}{\epsilon_1} \frac{k_{\perp_2}}{k_{\perp_1}} \frac{Q(k_{\perp_2} a) J'_m(k_{\perp_1} a)}{J_m(k_{\perp_1} a)}. \quad (\text{E.7c})$$

This dispersion relation has to be solved together with the two relations

$$k_{\perp_1}^2 + k_z^2 = \omega^2 \epsilon_1 \mu_0, \quad (\text{E.8})$$

$$k_{\perp_2}^2 + k_z^2 = \omega^2 \epsilon_2 \mu_0. \quad (\text{E.9})$$

Bibliography

- [1] M. Thumm. Recent Advances in the Worldwide Fusion Gyrotron Development. *IEEE Transactions on Plasma Science*, 42(3):590–599, March 2014.
- [2] S. Alberti. Magnetic confinement fusion: Plasma heating with millimetre waves. *Nature Physics*, 3(6):376–377, June 2007.
- [3] M. Shimada, D. J. Campbell, V. Mukhovatov, M. Fujiwara, N. Kirneva, K. Lackner, M. Nagami, V. D. Pustovitov, N. Uckan, J. Wesley, N. Asakura, A. E. Costley, A. J. H. Donné, E. J. Doyle, A. Fasoli, C. Gormezano, Y. Gribov, O. Gruber, T. C. Hender, W. Houlberg, S. Ide, Y. Kamada, A. Leonard, B. Lipschultz, A. Loarte, K. Miyamoto, V. Mukhovatov, T. H. Osborne, A. Polevoi, and A. C. C. Sips. Chapter 1: Overview and summary. *Nuclear Fusion*, 47(6):S1–S17, June 2007.
- [4] R. Prater. Heating and current drive by electron cyclotron waves. *Physics of Plasmas*, 11(5):2349–2376, April 2004.
- [5] O. Sauter. Partial Stabilisation of NTMs with ECCD for standard scenarios in ITER. volume 29C, page 2.059, Tarragona, 2005.
- [6] P. P. Woskov, J. S. Machuzak, R. C. Myer, D. R. Cohn, N. L. Bretz, P. C. Efthimion, and J. L. Doane. Gyrotron collective Thomson scattering diagnostic for confined alpha particles in TFTR. *Review of Scientific Instruments*, 59(8):1565–1567, August 1988.
- [7] C. D. Joye. *Design of a wideband, 100 W, 140 GHz gyrokystron amplifier*. Thesis, Massachusetts Institute of Technology, 2004.
- [8] J.-Ph. Hogge, F. Albajar, S. Alberti, K. Avramidis, W. Bin, T. Bonicelli, F. Braunmueller, A. Bruschi, J. Chelis, P.-E. Frigot, G. Gantenbein, V. Hermann, S. Illy, Z. C. Ioannidis, J. Jelonnek, J. Jin, W. Kasperek, T. Kobarg, G. P. Latsas, C. Lechte, M. Lontano, M. Losert, I. G. Pagonakis, Y. Rozier, T. Rzesnicki, C. Schlatter, M. Schmid, M. Thumm, I. G. Tigelis, M. Q. Tran, J. L. Vomvoridis, and A. I. Zisis. Status and Experimental Results of the European 1 MW, 170 GHz Industrial. In *2016 41st International Conference on Infrared, Millimeter, and Terahertz Waves (irmmw-Thz)*. Ieee, New York, 2016.
- [9] Z. C. Ioannidis, T. Rzesnicki, F. Albajar, S. Alberti, K. A. Avramidis, W. Bin, T. Bonicelli, A. Bruschi, I. Chelis, P.-E. Frigot, G. Gantenbein, V. Hermann, J.-P. Hogge, S. Illy, J. Jin,

- J. Jelonnek, W. Kasperek, G. Latsas, C. Lechte, F. Legrand, T. Kobarg, I. Gr. Pagonakis, Y. Rozier, C. Schlatter, M. Schmid, I. G. Tigelis, M. Thumm, M. Q. Tran, A. Zein, and A. Zisis. CW Experiments With the EU 1-MW, 170-GHz Industrial Prototype Gyrotron for ITER at KIT. *Ieee Transactions on Electron Devices*, 64(9):3885–3892, September 2017.
- [10] G. Gantenbein, V. Erckmann, S. Illy, S. Kern, W. Kasperek, C. Lechte, W. Leonhardt, C. Lievin, A. Samartsev, A. Schlaich, M. Schmid, and M. Thumm. 140 GHz, 1 MW CW Gyrotron Development for Fusion Applications-Progress and Recent Results. *Journal of Infrared Millimeter and Terahertz Waves*, 32(3):320–328, March 2011.
- [11] S. Cauffman, M. Blank, P. Borchard, and K. Felch. Design and testing of a dual-frequency 104/140 GHz megawatt-class gyrotron for fusion plasma heating. In *2016 IEEE International Conference on Plasma Science (ICOPS)*, pages 1–1, June 2016.
- [12] G. G. Denisov, A. G. Litvak, V. E. Myasnikov, E. M. Tai, and V. E. Zapevalov. Development in Russia of high-power gyrotrons for fusion. *Nuclear Fusion*, 48(5):054007, April 2008.
- [13] R. Ikeda, Y. Oda, T. Kobayashi, M. Terakado, K. Kajiwara, K. Takahashi, S. Moriyama, and K. Sakamoto. Development of 170 GHz, 1 MW gyrotron with high-order TE_{31,11} mode oscillation for ITER EC system. *Fusion Engineering and Design*, 128:23–27, March 2018.
- [14] A. Abragam. *The Principles of Nuclear Magnetism*. Clarendon Press, 1961.
- [15] L. R. Becerra, G. J. Gerfen, R. J. Temkin, D. J. Singel, and R. G. Griffin. Dynamic nuclear polarization with a cyclotron resonance maser at 5 T. *Physical Review Letters*, 71(21):3561–3564, November 1993.
- [16] J.-Ph. Hogge, F. Braunmueller, S. Alberti, J. Genoud, T. M. Tran, Q. Vuillemin, M. Q. Tran, J. Ansermet, P. Cuanillon, A. Macor, E. de Rijk, and P. V. Saraiva. Detailed characterization of a frequency-tunable 260ghz gyrotron oscillator planned for DNP/NMR spectroscopy. In *2013 38th International Conference on Infrared, Millimeter, and Terahertz Waves (IRMMW-THz)*, pages 1–2, September 2013.
- [17] S. Alberti, J.-Ph Ansermet, K. A. Avramides, F. Braunmueller, P. Cuanillon, J. Dubray, D. Fasel, J.-Ph Hogge, A. Macor, E. de Rijk, M. da Silva, M. Q. Tran, T. M. Tran, and Q. Vuillemin. Experimental study from linear to chaotic regimes on a terahertz-frequency gyrotron oscillator. *Physics of Plasmas*, 19(12):123102, December 2012.
- [18] S. Alberti, F. Braunmueller, T. M. Tran, J. Genoud, J.-Ph. Hogge, M. Q. Tran, and J.-Ph. Ansermet. Nanosecond Pulses in a THz Gyrotron Oscillator Operating in a Mode-Locked Self-Consistent Q-Switch Regime. *Physical Review Letters*, 111(20):205101, November 2013.
- [19] D. Yoon, M. Soundararajan, P. Cuanillon, F. Braunmueller, S. Alberti, and J.-Ph. Ansermet. Dynamic nuclear polarization by frequency modulation of a tunable gyrotron of 260 GHz. *Journal of Magnetic Resonance*, 262:62–67, January 2016.

-
- [20] D. Yoon, M. Soundararajan, C. Caspers, F. Braunmueller, J. Genoud, S. Alberti, and J.-Ph. Ansermet. 500-fold enhancement of in situ C-13 liquid state NMR using gyrotron-driven temperature jump DNP. *Journal of Magnetic Resonance*, 270:142–146, September 2016.
- [21] G. S. Nusinovich, R. Pu, T. M. Antonsen, O. V. Sinitsyn, J. Rodgers, A. Mohamed, J. Silverman, M. Al-Sheikhly, Y. S. Dimant, G. M. Milikh, M. Yu Glyavin, A. G. Luchinin, E. A. Kopelovich, and V. L. Granatstein. Development of THz-range Gyrotrons for Detection of Concealed Radioactive Materials. *Journal of Infrared Millimeter and Terahertz Waves*, 32(3):380–402, March 2011.
- [22] D. Kim, D. Yu, A. Sawant, M. S. Choe, and E. Choi. First experimental observation of plasma breakdown for detection of radioactive material using a gyrotron in real-time. In *2017 Eighteenth International Vacuum Electronics Conference (IVEC)*, pages 1–2, April 2017.
- [23] G. Denisov, Y. Bykov, A. Ereemeev, M. Glyavin, V. Kholoptsev, G. Kalynova, A. Luchinin, M. Morozkin, I. Plotnikov, and D. Sobolev. High Efficient Gyrotron-Based Systems for Materials Processing. In *2007 IEEE International Vacuum Electronics Conference*, pages 1–2, May 2007.
- [24] M. Takahashi and K. Komurasaki. Discharge from a high-intensity millimeter wave beam and its application to propulsion. *Advances in Physics: X*, 3(1):1417744, January 2018.
- [25] M. Thumm. Progress on Gyrotrons for ITER and Future Thermonuclear Fusion Reactors. *IEEE Transactions on Plasma Science*, 39(4):971–979, April 2011.
- [26] M. Thumm. *State-of-the-Art of High Power Gyro-Devices and Free Electron Masers. Update 2017 (KIT Scientific Reports ; 7750)*. 2018.
- [27] S. Alberti, F. Braunmueller, J. Genoud, J. P. Hogge, T. M. Tran, M. Q. Tran, K. Avramidis, I. G. Pagonakis, J. Jin, S. Illy, G. Gantenbein, J. Jelonnek, and F. Cismondi. Dual-frequency, 126/84 GHz, 1 MW gyrotron for the upgrade of the TCV EC-system. In *2015 40th International Conference on Infrared, Millimeter, and Terahertz waves (IRMMW-THz)*, pages 1–2, August 2015.
- [28] K. R. Chu. The electron cyclotron maser. *Reviews of Modern Physics*, 76(2):489–540, May 2004.
- [29] E. Borie. *Review of gyrotron theory*. Kernforschungszentrum, 1991.
- [30] F. Braunmueller, T. M. Tran, S. Alberti, J.-Ph Hogge, and M. Q. Tran. Moment-based, self-consistent linear analysis of gyrotron oscillators. *Physics of Plasmas*, 21(4):043105, April 2014.
- [31] J. Genoud, T. M. Tran, S. Alberti, F. Braunmueller, J.-Ph Hogge, M. Q. Tran, W. C. Guss, and R. J. Temkin. Novel linear analysis for a gyrotron oscillator based on a spectral approach. *Physics of Plasmas (1994-present)*, 23(4):043101, April 2016.

- [32] J. Genoud, S. Alberti, T. M. Tran, G. Le Bars, P. Kaminski, J.-Ph. Hogge, K. A. Avramidis, and M. Q. Tran. Parasitic Oscillations in Smooth-Wall Circular Symmetric Gyrotron Beam Ducts. *Journal of Infrared, Millimeter, and Terahertz Waves*, 40(2):131–149, February 2019.
- [33] I. G. Tigelis, M. Pedrozzi, P. G. Cottis, and J. L. Vomvoridis. Calculation of eigenmodes in a nonperiodic corrugated waveguide. *IEEE Transactions on Microwave Theory and Techniques*, 45(2):236–244, February 1997.
- [34] G. S. Nusinovich. *Introduction to the Physics of Gyrotrons*. JHU Press, August 2004.
- [35] T. H. Chang, W. C. Huang, H. Y. Yao, C. L. Hung, W. C. Chen, and B. Y. Su. Asymmetric linear efficiency and bunching mechanisms of TM modes for electron cyclotron maser. *Physics of Plasmas*, 24(2):023302, February 2017.
- [36] J. P. Calame, M. Garven, B. G. Danly, B. Levush, and K. T. Nguyen. Gyrotron-traveling wave-tube circuits based on lossy ceramics. *IEEE Transactions on Electron Devices*, 49(8):1469–1477, August 2002.
- [37] C. Du and P. Liu. Linear Full-Wave-Interaction Analysis of a Gyrotron-Traveling-Wave-Tube Amplifier Based on a Lossy Dielectric-Lined Circuit. *IEEE Transactions on Plasma Science*, 38(6):1219–1226, June 2010.
- [38] C. Du, Q. Xue, and P. Liu. Loss-Induced Modal Transition in a Dielectric-Coated Metal Cylindrical Waveguide for Gyro-Traveling-Wave-Tube Applications. *IEEE Electron Device Letters*, 29(11):1256–1258, November 2008.
- [39] C. L. Hung, M. F. Syu, M. T. Yang, and K. L. Chen. Selective mode suppression in a W-band second harmonic coaxial-waveguide gyrotron backward-wave oscillator. *Applied Physics Letters*, 101(3):033504, July 2012.
- [40] Lee, C. S., Lee, S. W, and Chuang, Shun Lien. Normal Modes in an Overmoded Circular Waveguide Coated with Lossy Material. *IEEE Transactions on Microwave Theory and Techniques*, 34(7):773–785, July 1986.
- [41] H. Wang, H. Li, Y. Luo, and R. Yan. Theoretical and Experimental Investigation of a Ka-band Gyro-TWT with Lossy Interaction Structure. *Journal of Infrared, Millimeter, and Terahertz Waves*, 32(2):172–185, February 2011.
- [42] K. Ohmi and F. Zimmermann. Head-Tail Instability Caused by Electron Clouds in Positron Storage Rings. *Physical Review Letters*, 85(18):3821–3824, October 2000.
- [43] C. H. Du and P. K. Liu. *Millimeter-Wave Gyrotron Traveling-Wave Tube Amplifiers*. Springer Berlin Heidelberg, Berlin, Heidelberg, 2014.
- [44] I. I. Antakov, I. G. Gachev, and E. V. Zasyrkin. Self-excitation of spurious oscillations in the drift region of gyrotrons and their influence on gyrotron operation. *IEEE Transactions on Plasma Science*, 22(5):878–882, October 1994.

- [45] K. Sakamoto, A. Kasugai, Y. Ikeda, K. Hayashi, K. Takahashi, S. Moriyama, M. Seki, T. Kariya, Y. Mitsunaka, T. Fujii, and T. Imai. Development of 170 and 110 GHz gyrotrons for fusion devices. *Nuclear Fusion*, 43(8):729–737, August 2003.
- [46] M. Pedrozzi, S. Alberti, J. P. Hogge, M. Q. Tran, and T. M. Tran. Electron beam instabilities in gyrotron beam tunnels. *Physics of Plasmas*, 5(6):2421–2430, June 1998.
- [47] G. Gantenbein, G. Dammertz, J. Flamm, S. Illy, S. Kern, G. Latsas, B. Piosczyk, T. Rzesnicki, A. Samartsev, A. Schlaich, M. Thumm, and I. Tigelis. Experimental Investigations and Analysis of Parasitic RF Oscillations in High-Power Gyrotrons. *IEEE Transactions on Plasma Science*, 38(6):1168–1177, June 2010.
- [48] G. P. Latsas, J. L. Vomvouridis, K. A. Avramides, and I. G. Tigelis. Beam-Wave Interaction in Corrugated Structures in the Small-Signal Regime. *IEEE Transactions on Plasma Science*, 37(10):2020–2030, October 2009.
- [49] G. P. Latsas, M. D. Moraitou, Z. C. Ioannidis, and I. G. Tigelis. Calculations on the Beam-Wave Interactions in Coaxial Gyrotron Beam Tunnels. *IEEE Transactions on Plasma Science*, 38(6):1185–1192, June 2010.
- [50] G. P. Latsas, Z. C. Ioannidis, and I. G. Tigelis. Dependence of Parasitic Modes on Geometry and Attenuation in Gyrotron Beam Tunnels. *IEEE Transactions on Plasma Science*, 40(6):1538–1544, June 2012.
- [51] G. P. Latsas, A. I. Zisis, and I. G. Tigelis. Computational Studies on the Suppression of Parasitic Oscillations in Gyrotron Beam Tunnels. *IEEE Transactions on Electron Devices*, 65(8):3479–3485, August 2018.
- [52] A. Samartsev, G. Gantenbein, S. Illy, S. Kern, G. Latsas, M. Thumm, and I. Tigelis. Numerical simulation of parasitic gyro-BWO interaction in a gyrotron beam tunnel. In *2011 International Conference on Infrared, Millimeter, and Terahertz Waves*, pages 1–2, October 2011.
- [53] M. D. Moraitou, G. P. Latsas, Z. C. Ioannidis, and I. G. Tigelis. Parasitic Oscillations in Coaxial Gyrotron Beam Tunnels. *IEEE Transactions on Electron Devices*, 60(4):1469–1475, April 2013.
- [54] K. Sakamoto, A. Kasugai, K. Kajiwara, K. Takahashi, Y. Oda, K. Hayashi, and N. Kobayashi. Progress of high power 170-GHz gyrotron in JAEA. *Nuclear Fusion*, 49(9):095019, August 2009.
- [55] G. G. Denisov, V. E. Zapevalov, A. G. Litvak, and V. E. Myasnikov. Megawatt Gyrotrons for ECR Heating and Current-Drive Systems in Controlled-Fusion Facilities. *Radiophysics and Quantum Electronics*, 46(10):757–768, October 2003.
- [56] M. Blank, K. Felch, P. Borchard, P. Cahalan, S. R. Cauffman, Tak Sum Chu, and H. Jory. Demonstration of a high-power long-pulse 140-GHz gyrotron oscillator. *IEEE Transactions on Plasma Science*, 32(3):867–876, June 2004.

Bibliography

- [57] D. A. Edwards and M. J. Syphers. Intensity Dependent Effects. In *An Introduction to the Physics of High Energy Accelerators*, pages 172–220. John Wiley & Sons, Ltd, 2008.
- [58] T. Weiland and R. Wanzenberg. Wake fields and impedances. In M. Dienes, M. Month, and S. Turner, editors, *Frontiers of Particle Beams: Intensity Limitations*, Lecture Notes in Physics, pages 39–79. Springer Berlin Heidelberg, 1992.
- [59] I. G. Chelis, K. A. Avramidis, Z. C. Ioannidis, and I. G. Tigelis. Improved Suppression of Parasitic Oscillations in Gyrotron Beam Tunnels by Proper Selection of the Lossy Ceramic Material. *IEEE Transactions on Electron Devices*, 65(6):2301–2307, June 2018.
- [60] G. S. Nusinovich, R. Pu, O. V. Sinitsyn, J. Yu, T. M. Antonsen, and V. L. Granatstein. Self-Excitation of a Tapered Gyrotron Oscillator. *IEEE Transactions on Plasma Science*, 38(6):1200–1207, June 2010.
- [61] M. Yeddulla, G. S. Nusinovich, and T. M. Antonsen. Start currents in an overmoded gyrotron. *Physics of Plasmas*, 10(11):4513–4520, October 2003.
- [62] O. Dumbrajs, T. Idehara, T. Saito, and Y. Tatematsu. Calculations of Starting Currents and Frequencies in Frequency-Tunable Gyrotrons. *Japanese Journal of Applied Physics*, 51(12):126601, December 2012.
- [63] T. H. Chang, K. F. Pao, S. H. Chen, and K. R. Chu. Self-Consistent Effects on the Starting Current of Gyrotron Oscillators. *International Journal of Infrared and Millimeter Waves*, 24(9):1415–1420, September 2003.
- [64] E. M. Khutoryan, G. S. Nusinovich, and O. V. Sinitsyn. Competition between modes with different axial structures in gyrotrons. *Physics of Plasmas*, 21(9):093114, September 2014.
- [65] G. S. Nusinovich, M. Yeddulla, T. M. Antonsen, and A. N. Vlasov. Start-Up Scenario in Gyrotrons with a Nonstationary Microwave-Field Structure. *Physical Review Letters*, 96(12):125101, March 2006.
- [66] A. W. Fliflet, M. E. Read, K. R. Chu, and R. Seeley. A self-consistent field theory for gyrotron oscillators: application to a low Q gyromonotron. *International Journal of Electronics*, 53(6):505–521, December 1982.
- [67] F. Braunmueller, T. M. Tran, Q. Vuillemin, S. Alberti, J. Genoud, J.-Ph Hogge, and M. Q. Tran. TWANG-PIC, a novel gyro-averaged one-dimensional particle-in-cell code for interpretation of gyrotron experiments. *Physics of Plasmas (1994-present)*, 22(6):063115, June 2015.
- [68] K. A. Avramides, I. Gr Pagonakis, C. T. Iatrou, and J. L. Vomvouridis. EURIDICE: A code-package for gyrotron interaction simulations and cavity design. In E. Westerhof and Pwjm Nuij, editors, *Ec-17 - 17th Joint Workshop on Electron Cyclotron Emission and Electron Cyclotron Resonance Heating*, volume 32, page 04016. E D P Sciences, Cedex A, 2012.

-
- [69] S. Kern. *Numerische Simulation der Gyrotron- Wechselwirkung in koaxialen Resonatoren*. PhD thesis, Institut für Höchstfrequenztechnik und Elektronik (IHE), 1996.
- [70] M. Botton, T. M. Antonsen, B. Levush, K. T. Nguyen, and A. N. Vlasov. MAGY: a time-dependent code for simulation of slow and fast microwave sources. *IEEE Transactions on Plasma Science*, 26:882–892, June 1998.
- [71] N. S. Ginzburg, N. A. Zavol'skii, G. S. Nusinovich, and A. S. Sergeev. Self-oscillation in uhf generators with diffraction radiation output. *Radiophysics and Quantum Electronics*, 29(1):89–97, January 1986.
- [72] S. Alberti, T. M. Tran, K. A. Avramides, F. Li, and J.-P. Hogge. Gyrotron parasitic-effects studies using the time-dependent self-consistent monomode code TWANG. *2011 36th International Conference on Infrared, Millimeter, and Terahertz Waves (irmmw-Thz)*, 2011.
- [73] J. L. Hirshfield and J. M. Wachtel. Electron Cyclotron Maser. *Physical Review Letters*, 12(19):533–536, May 1964.
- [74] K. E. Kreischer and R. J. Temkin. Linear theory of an electron cyclotron maser operating at the fundamental. *International Journal of Infrared and Millimeter Waves*, 1(2):195–223, June 1980.
- [75] S. Y. Park, V. L. Granatstein, and R. K. Parker. A linear theory and design study for a gyrotron backward-wave oscillator. *International Journal of Electronics*, 57(6):1109–1023, December 1984.
- [76] J. Yu, T. M. Antonsen, and G. S. Nusinovich. Excitation of Backward Waves in Beam Tunnels of High-Power Gyrotrons. *IEEE Transactions on Plasma Science*, 38(6):1193–1199, June 2010.
- [77] S. H. Chen and L. Chen. Linear and nonlinear behaviors of gyrotron backward wave oscillators. *Physics of Plasmas*, 19(2):023116, February 2012.
- [78] H. Saito, T. M. Tran, K. E. Kreischer, and R. J. Temkin. Analytical treatment of linearized self-consistent theory of a gyromonotron with a non-fixed structure. *International Journal of Electronics*, 61(6):895–903, December 1986.
- [79] M. Garven, J. P. Calame, B. G. Danly, K. T. Nguyen, B. Levush, F. N. Wood, and D. E. Pershing. A gyrotron-traveling-wave tube amplifier experiment with a ceramic loaded interaction region. *IEEE Transactions on Plasma Science*, 30(3):885–893, June 2002.
- [80] I. G. Tigelis, J. L. Vomvoridis, and S. Tzima. High-frequency electromagnetic modes in a dielectric-ring loaded beam tunnel. *IEEE Transactions on Plasma Science*, 26(3):922–930, June 1998.

Bibliography

- [81] K. R. Chu, H. Y. Chen, C. L. Hung, T. H. Chang, L. R. Barnett, S. H. Chen, T. T. Yang, and D. J. Dialetis. Theory and experiment of ultrahigh-gain gyrotron traveling wave amplifier. *IEEE Transactions on Plasma Science*, 27(2):391–404, April 1999.
- [82] K. R. Chu, L. R. Barnett, H. Y. Chen, S. H. Chen, Ch. Wang, Y. S. Yeh, Y. C. Tsai, T. T. Yang, and T. Y. Dawn. Stabilization of Absolute Instabilities in the Gyrotron Traveling Wave Amplifier. *Physical Review Letters*, 74(7):1103–1106, February 1995.
- [83] J.-P. Hogge, S. Alberti, L. Porte, and G. Arnoux. Preliminary results of top launch third harmonic X-mode electron cyclotron heating in the TCV tokamak. *Nuclear Fusion*, 43(11):1353–1360, November 2003.
- [84] M. Shapiro, R. Temkin, I. Mastovsky, and S. Cauffman. Studies of the 1.5-MW, 110-GHz Gyrotron Experiment. May 2004.
- [85] F. Braunmüller. *Gyrotron physics from linear to chaotic regimes: experiment and numerical modeling*. EPFL thesis, no 6959, Ecole Polytechnique Federale de Lausanne, Swiss Plasma Center, Lausanne, 2016.
- [86] G. Le Bars. Velocity spread effects on backward-wave interaction in gyrotron beam ducts. Master thesis, Ecole Polytechnique Fédérale de Lausanne (EPFL): Sciences de Bases - Physique, January 2019.
- [87] D. C. Sorensen, R. B. Lehoucq, C. Yang, and K. Maschhoff. ARPACK - Arnoldi Package, 1996.
- [88] W. H. Press, B. P. Flannery, S. A. Teukolsky, and W. T. Vetterling. *Numerical Recipes: The art of scientific computing*. Cambridge Univ. Press, 1986.
- [89] S. Alberti, T. M. Tran, S. Brunner, F. Braunmueller, J. Genoud, J.-Ph Hogge, and M. Q. Tran. Generalized Radiation Boundary Conditions in Gyrotron Oscillator Modeling. *Journal of Infrared, Millimeter, and Terahertz Waves*, pages 1–16, September 2015.
- [90] D. R. Whaley, M. Q. Tran, S. Alberti, T. M. Tran, Jr. Antonsen, T. M., and C. Tran. Startup Methods for Single-Mode Gyrotron Operation. *Physical Review Letters*, 75(7):1304–1307, August 1995.
- [91] P. Kaminski. High order finite elements discretization of the gyrotron linear spectral model. TPIV project,, Ecole Polytechnique Fédérale de Lausanne (EPFL), Swiss Plasma Center (SPC), Lausanne, 2016.
- [92] F. Brezzi and M. Fortin, editors. *Mixed and Hybrid Finite Element Methods*, volume 15 of *Springer Series in Computational Mathematics*. Springer New York, New York, NY, 1991.
- [93] G. Dahlquist and Å. Björck. *Numerical Methods*. Dover Publications, Mineola, N.Y, reprint edition edition, April 2003.

-
- [94] W. Gropp, E. Lusk, and A. Skjellum. Using MPI Portable Parallel Programming with the Message-Passing Interface Second Edition. page 8.
- [95] B. Davies. Locating the zeros of an analytic function. *Journal of Computational Physics*, 66(1):36–49, September 1986.
- [96] T. M. Tran, D. R. Whaley, S. Merazzi, and R. Gruber. DAPHNE, a 2d axisymmetric electron gun simulation code. *Proc. 6th Joint EPS-APS International Conference on Physics Computing*, 1994.
- [97] J. G. Pagonakis and J. L. Vomvoridis. The self-consistent 3d trajectory electrostatic code ARIADNE for gyrotron beam tunnel simulation. In *Infrared and Millimeter Waves, Conference Digest of the 2004 Joint 29th International Conference on 2004 and 12th International Conference on Terahertz Electronics, 2004.*, pages 657–658, September 2004.
- [98] T. M. Tran and J. S Wurtele. Free-electron laser simulation techniques. *Physics Reports*, 195(1):1–21, November 1990.
- [99] C. K. Birdsall and A. B. Langdon. *Plasma Physics via Computer Simulation*. CRC Press, October 2004.
- [100] S. Coda. Overview of the TCV tokamak program: scientific progress and facility upgrades. *Nuclear Fusion*, 57(10):102011, October 2017.
- [101] D. Wagner, M. Thumm, G. Gantenbein, W. Kasperek, and T. Idehara. Analysis of a Complete Gyrotron Oscillator Using the Scattering Matrix Description. *International Journal of Infrared and Millimeter Waves*, 19(2):185–194, February 1998.
- [102] K. Sakamoto, A. Kasugai, K. Takahashi, R. Minami, N. Kobayashi, and K. Kajiwara. Achievement of robust high-efficiency 1 MW oscillation in the hard-self-excitation region by a 170 GHz continuous-wave gyrotron. *Nature Physics*, 3(6):411–414, June 2007.
- [103] T. Rzesnicki, F. Albajar, S. Alberti, K. A. Avramidis, W. Bin, T. Bonicelli, F. Braunmueller, A. Bruschi, J. Chelis, P.-E. Frigot, G. Gantenbein, V. Hermann, J.-P. Hogge, S. Illy, Z. C. Ioannidis, J. Jin, J. Jelonnek, W. Kasperek, G. P. Latsas, C. Lechte, M. Lontano, T. Kobarg, I. G. Pagonakis, Y. Rozier, C. Schlatter, M. Schmid, I. G. Tigelis, M. Thumm, M. Q. Tran, J. L. Vomvoridis, and A. Zisis. Experimental verification of the European 1 MW, 170 GHz industrial CW prototype gyrotron for ITER. *Fusion Engineering and Design*, 123:490–494, November 2017.
- [104] G. P. Anastasiou, G. P. Latsas, I. G. Tigelis, M. Dehler, P. Queffelec, and N. F. Dasyras. Calculation of the electromagnetic waves in nonperiodic corrugated waveguides With Dielectric loading. *IEEE Transactions on Plasma Science*, 32(3):1310–1317, June 2004.
- [105] A. N. Vlasov and T. M. Antonsen. Numerical solution of fields in lossy structures using MAGY. *IEEE Transactions on Electron Devices*, 48(1):45–55, January 2001.

Bibliography

- [106] M. Thumm, S. Alberti, A. Arnold, P. Brand, H. Braune, G. Dammertz, V. Erckmann, G. Gantenbein, E. Giguet, R. Heidinger, J. Hogge, S. Illy, W. Kasperek, H. P. Laqua, F. Legrand, W. Leonhardt, C. Lievin, G. Michel, G. Neffe, B. Piosczyk, M. Schmid, K. Schworer, and M. Q. Tran. EU Megawatt-Class 140-GHz CW Gyrotron. *IEEE Transactions on Plasma Science*, 35(2):143–153, April 2007.
- [107] D. Wagner, F. Leuterer, J. K. Stober, A. Manini, F. Monaco, M. H. Munich, H. Schutz, H. Zohm, T. Franke, M. Thumm, R. Heidinger, I. Danilov, G. Gantenbein, J. Flamm, W. Kasperek, A. Litvak, L. M. Popov, V. O. Nichiporenko, V. E. Myasnikov, G. G. Denisov, E. M. Tai, E. A. Solyanova, and S. A. Malygin. Present Status of the New Multi-Frequency ECRH System for ASDEX Upgrade. *2007 IEEE 34th International Conference on Plasma Science (ICOPS)*, pages 814–814, 2007.
- [108] K. Kajiwara, A. Kasugai, Y. Oda, K. Takahashi, K. Sakamoto, C. Darbos, and M. Henderson. Reliability Test of the 170-GHz Gyrotron for ITER. *Journal of Infrared, Millimeter, and Terahertz Waves*, 32(3):329–336, March 2011.
- [109] D. R. Whaley, M. Q. Tran, T. M. Tran, and T. M. Antonsen. Mode competition and startup in cylindrical cavity gyrotrons using high-order operating modes. *IEEE Transactions on Plasma Science*, 22(5):850–860, October 1994.
- [110] D. S. Tax, O. V. Sinitsyn, W. C. Guss, G. S. Nusinovich, M. A. Shapiro, and R. J. Temkin. Experimental Study of the Start-Up Scenario of a 1.5-MW, 110-GHz Gyrotron. *IEEE Transactions on Plasma Science*, 41(4):862–871, April 2013.
- [111] S. Alberti. *Etude expérimentale de l'interaction faisceau d'électrons relativistes - onde électromagnétique dans un gyrotron quasi-optique*. Thesis #963, Ecole Polytechnique Federale de Lausanne, Lausanne, 1991.
- [112] A. T. Drobot and K. Kim. Space charge effects on the equilibrium of guided electron flow with gyromotion. *International Journal of Electronics*, 51(4):351–367, October 1981.
- [113] E. Borie and G. Gantenbein. Self consistent theory for gyrotrons including effect of voltage depression. *International Journal of Infrared and Millimeter Waves*, 12(2):65–78, February 1991.
- [114] I. G. Chelis, K. A. Avramidis, and J. L. Vomvoridis. Resonant Modes of Disk-Loaded Cylindrical Structures With Open Boundaries. *IEEE Transactions on Microwave Theory and Techniques*, 63(6):1781–1790, June 2015.
- [115] Chelis, I., et al. Development of a self-consistent simulation code for the electron cyclotron interaction in dielectric-loaded gyrotron beam tunnels. In *proc. 238*, Nizhny Novgorod-Moscow, Russia, July 2017.
- [116] T. Rzesnicki, I. G. Pagonakis, A. Samartsev, K. Avramidis, G. Gantenbein, S. Illy, J. Jelonek, J. Jin, C. Lechte, M. Losert, B. Piosczyk, and M. Thumm. Recent experimental results

- of the European 1 MW, 170 GHz short-pulse gyrotron prototype for ITER. In *2015 40th International Conference on Infrared, Millimeter, and Terahertz waves (IRMMW-THz)*, pages 1–2, August 2015.
- [117] B. Z Katsenelenbaum. *Theory of nonuniform waveguides: the cross-section method*. 1998.
- [118] J. Baker-Jarvis, E. J. Vanzura, and W. A. Kissick. Improved technique for determining complex permittivity with the transmission/reflection method. *IEEE Transactions on Microwave Theory and Techniques*, 38(8):1096–1103, August 1990.
- [119] R. E. Collin. *Foundations For Microwave Engineering, 2nd ed.* Wiley India Pvt. Limited, 2007.
- [120] D. A. Hill. Reflection coefficient of a waveguide with slightly uneven walls. *IEEE Transactions on Microwave Theory and Techniques*, 37(1):244–252, January 1989.
- [121] D. Yoon, A. I. Dimitriadis, M. Soundararajan, C. Caspers, J. Genoud, S. Alberti, E. de Rijk, and J-Ph. Ansermet. High-Field Liquid-State Dynamic Nuclear Polarization in Microliter Samples. *Analytical Chemistry*, 90(9):5620–5626, May 2018.

Publications and Conferences

Journal publications as first author

- J. Genoud, T. M. Tran, S. Alberti, F. Braunmueller, J.-Ph Hogge, M. Q. Tran, W. C. Guss, and R. J. Temkin "Novel Linear Analysis for a Gyrotron Oscillator Based on a Spectral Approach." **Physics of Plasmas (1994-Present)**, vol. 23, no. 4, Apr. 2016, p. 043101.
- J. Genoud, S. Alberti, T. M. Tran, G. Le Bars, P. Kaminski, J.-Ph. Hogge, K. A. Avramidis, and M. Q. Tran. "Parasitic Oscillations in Smooth-Wall Circular Symmetric Gyrotron Beam Ducts." **Journal of Infrared, Millimeter, and Terahertz Waves**, vol. 40, no. 2, Feb. 2019, pp. 131–49.

Journal publications as co-author

- Y. Dongyoung, A. I. Dimitriadis, M. Soundararajan, C. Caspers, J. Genoud, S. Alberti, E. de Rijk, and J.-Ph. Ansermet. "High-Field Liquid-State Dynamic Nuclear Polarization in Microliter Samples." **Analytical Chemistry**, vol. 90, no. 9, May 2018, pp. 5620–26.
- Y. Dongyoung, M. Soundararajan, C. Caspers, F. Braunmueller, J. Genoud, S. Alberti, and J.-Ph. Ansermet. "500-Fold Enhancement of in Situ ¹³C Liquid State NMR Using Gyrotron-Driven Temperature-Jump DNP." **Journal of Magnetic Resonance**, vol. 270, Sept. 2016, pp. 142–46.
- S. Alberti, T. M. Tran, S. Brunner, F. Braunmueller, J. Genoud, J.-Ph. Hogge, and M. Q. Tran. "Generalized Radiation Boundary Conditions in Gyrotron Oscillator Modeling." **Journal of Infrared, Millimeter, and Terahertz Waves**, Sept. 2015, pp. 1–16.
- F. Braunmueller, T. M. Tran, Q. Vuillemin, S. Alberti, J. Genoud, J.-Ph. Hogge, and M. Q. Tran. "TWANG-PIC, a Novel Gyro-Averaged One-Dimensional Particle-in-Cell Code for Interpretation of Gyrotron Experiments." **Physics of Plasmas (1994-Present)**, vol. 22, no. 6, June 2015, p. 063115.

- S. Alberti, F. Braunmueller, T. M. Tran, J. Genoud, J.-Ph. Hogge, M. Q. Tran, and J.-Ph. Ansermet. "Nanosecond Pulses in a THz Gyrotron Oscillator Operating in a Mode-Locked Self-Consistent Q-Switch Regime." **Physical Review Letters**, vol. 111, no. 20, Nov. 2013, p. 205101.

Conference contributions

- Conference paper and Poster: "Linear and non-linear studies of spurious backward-wave instabilities in a smooth-wall gyrotron beam duct" **International Conference on Infrared, Millimeter, and Terahertz Waves (IRMMW-THz)**, Cancún, 27 August-1 September, 2017.
- Conference paper and Presentation: "Start-up scenario studies in gyrotron oscillator using a novel linear and spectral code." **International Conference on Infrared, Millimeter, and Terahertz Waves (IRMMW-THz)**, Copenhagen, 25-30 September, 2016.
- Conference paper and Presentation (by S. Alberti): "Novel self-consistent linear theory of a gyrotron oscillator and experimental validation." **International Conference on Infrared, Millimeter, and Terahertz Waves (IRMMW-THz)**, Hong-Kong, September 23-28, 2015.
- Presentation: "Novel self-consistent linear theory for a gyrotron oscillator based on a spectral approach". **Joint Annual Meeting of the Austrian Physical Society and the Swiss Physical Society**, Vienna, September 01, 2015.

Remerciements

Avec ces quelques lignes, que j'espère pas trop maladroites, j'aimerais remercier toutes les personnes que j'ai côtoyées durant ces 4 dernières années très enrichissantes et qui ont contribué, de près ou de loin, au bon déroulement de la thèse.

Premièrement, un grand merci à mon directeur de thèse Stefano. Son aide et son soutien durant cette thèse sont inestimables. Malgré sa charge de travail, Stefano était toujours disponible et a toujours pris le temps de répondre à mes nombreuses questions, avec sa bonne humeur, son calme et sa motivation contagieuse. Sa pédagogie, toujours habilement ciblée, est incomparable. Minh est la deuxième personne que je veux remercier et je tiens à lui rendre hommage. Il nous a quitté il y a maintenant une année et demie. Même si ce n'est pas officiellement écrit sur la première page de cette thèse, Minh est mon deuxième superviseur. Sans lui cette thèse n'existerait pas. Son expertise en ce qui concerne la théorie et la modélisation numérique étaient sans égal. Sa rigueur et sa dévotion dans la transmission de son savoir m'ont toujours épaté. C'est un honneur pour moi d'avoir pu travailler avec Stefano et Minh, des personnes aussi brillantes scientifiquement que riches humainement.

Je tiens également à remercier Falk, qui m'a appris énormément durant la première partie de cette thèse, Jean-Philippe, pour la lecture de la thèse et pour tous les précieux conseils qu'il m'a apportés. Merci également à Quang pour son aide, ses questions et conseils tout au long de la thèse. J'ai eu la chance de travailler avec deux excellents étudiants de master, Patryk et Guillaume. Leur travail a été impeccable et j'ai pu en tirer profit directement pour ma thèse, je leur en suis reconnaissant. Merci à Philippe Cuanillon, qui m'a aidé à de multiples reprises lorsque quelque chose ne tournait pas rond avec le gyrotron DNP.

Je souhaite également remercier les membres du jury, Ioannis Tigelis, Sudheer Jawla et Stephan Brunner, pour avoir lu et amélioré mon manuscrit par leurs corrections et commentaires.

Mes tâches d'assistantat ont aussi été très enrichissantes. C'est pourquoi je veux remercier Jean-Philippe, Stephan et Jon, avec qui j'ai eu le plaisir de travailler. J'admire l'effort qu'ils mettent sans cesse à parfaire leur enseignement.

Merci à Ambrogio et Yves à la direction du SPC, ainsi que toutes les personnes impliquées dans le bon fonctionnement du labo, Edith, Roxane, Thushi, Christine, Christian et Pierre.

Remerciements

A côté du travail même, j'ai eu la chance d'être entouré de véritables amis, avec lesquelles j'ai partagé des moments magnifiques. J'aimerais remercier particulièrement Emmanuel, Noé et Stéphane pour toutes nos pauses cafés/réunions/repas, mais aussi Matteo, Marta, Dahye, Samuel, Oulfa, Mathilde, Mengdi et Madhu pour ces nombreuses sorties mémorables. Merci aux "anciens", Himank, Fabio, Christoph, Gabriele mais aussi aux "nouveaux", Arsène et Lorenzo à qui je souhaite bonne chance et merci à tous les autres que je ne cite pas ici. Bien sur je veux aussi remercier mes amis de longue date, particulièrement Jean-François, Denis, Lionel, Patrick, Stéphane, Janik et Francesco.

Je souhaite conclure avec mes remerciements pour ma famille et surtout mes deux frères et ma maman. Je ne pourrais jamais la remercier assez pour tout ce qu'elle a fait pour moi avant et pendant la thèse ainsi que pour son soutien total. Sans elle je ne serais pas là où je suis aujourd'hui, merci infiniment.

Lausanne, le 08.04.2019.

J.G.

Jérémy Genoud

Address	Rue des Billonnaires 9B 1957 Ardon Switzerland	Date of Birth	28 th June 1988
		Nationality	Swiss
		Email	jerem.genoud@gmail.com

Education

2014-2019 Doctoral student at the Swiss Plasma Center, École Polytechnique Fédérale de Lausanne:
Advanced linear models for gyro-backward wave instabilities in gyrotrons

2008-2014 BSc and MSc in physics at the École Polytechnique Fédérale de Lausanne
- Master thesis at the Swiss Plasma Center:
Self-consistent linear analysis of a gyrotron oscillator: spectral approach
- Semester project at the Swiss Plasma Center:
Analysis of nonstationary and chaotic regimes in gyrotrons

Journal Publications (first author)

2016 "Novel linear analysis for a gyrotron oscillator based on a spectral approach"
J. Genoud, T.M. Tran, S. Alberti, F. Braunmueller, J.-Ph Hogge, M.Q. Tran, W.C. Guss and R.J. Temkin.
Physics of Plasmas 23(4):043101, April 2016

2019 "Parasitic Oscillations in Smooth-Wall Circular Symmetric Gyrotron Beam Ducts"
J. Genoud, S. Alberti, T.M. Tran, G. Le Bars, P. Kaminski, J.-Ph Hogge, K.A. Avramidis and M.Q. Tran.
Journal of Infrared, Millimeter, and Terahertz Waves 40(2):131-149, February 2019

Work experience

2013-2014 Internship at MétéoSuisse (6 months)
Intercomparison of different precipitation type measurements
Development of automatic tools for extracting and displaying measured data.
Quality control and recommendations for the choice of new operational measurement devices.

Special skills

■ Languages

French: Native speaker

English: Fluent

German: B1-B2

■ Programming Languages and IT skills

C++, Fortran

Matlab

LaTeX, Office Suite

